

# **High Resolution X-Ray Spectroscopy of Laboratory Sources.**

**by**

**James Dunn**

A thesis submitted to the University of Leicester for the degree of  
Doctor of Philosophy.

1990.

Department of Physics

University of Leicester

UMI Number: U546116

All rights reserved

INFORMATION TO ALL USERS

The quality of this reproduction is dependent upon the quality of the copy submitted.

In the unlikely event that the author did not send a complete manuscript and there are missing pages, these will be noted. Also, if material had to be removed, a note will indicate the deletion.



UMI U546116

Published by ProQuest LLC 2015. Copyright in the Dissertation held by the Author.  
Microform Edition © ProQuest LLC.

All rights reserved. This work is protected against  
unauthorized copying under Title 17, United States Code.



ProQuest LLC  
789 East Eisenhower Parkway  
P.O. Box 1346  
Ann Arbor, MI 48106-1346



7500 49168x

y 251645035

## **Abstract.**

### **High Resolution X-Ray Spectroscopy of Laboratory Sources.**

**James Dunn.**

A detailed programme of research is presented to design, build and operate a high resolution  $\lambda/\Delta\lambda \geq 5000$  curved crystal Johann-type x-ray spectrometer for the waveband below  $13\text{\AA}$ . The spectrometer is used to observe line emission features from different laboratory x-ray sources. Characteristics of the Johann geometry are described with emphasis given to the properties of sensitivity, dispersion, resolving power and waveband. The tolerance of the instrumental parameters is defined for successful high spectral resolution operation. The key feature of the spectrometer is the unique crystal bending device which can generate a high quality cylindrical curvature of radius  $R=150 \rightarrow 5000\text{mm}$ . The crystal focusing alignment and testing procedures are evaluated. Choice of crystals suitable for the observation programme is discussed together with analysis techniques for interpretation of the x-ray spectral line profiles.

The instrument is optimised for time-integrated and time-resolved ion temperature measurements of UKAEA DITE Tokamak at the Culham Fusion Laboratory. X-ray line emission results from medium Z He-like and H-like impurity ions are presented for different plasma conditions.

Density sensitive He-like and Li-like Aluminium ion satellite emission features are studied for intense transient laser produced plasmas at the Central Laser Facility, SERC Rutherford Appleton Laboratory. The peak plasma electron density of 0.1 times solid density is estimated from these line intensity ratios and is in good agreement with Stark line width measurements.

X-ray emission from beam-foil interactions is observed on the Folded Tandem accelerator of the Nuclear Physics Department, Oxford University. The proposed improvement in the intrinsic spectral line broadening due to the accelerator is investigated by high resolution axial beam measurements of the He-like Silicon and H-like Neon  $n=2$  transitions.

The Lyman- $\alpha$  intensity  $\beta$ -ratio and wavelength separation  $\Delta\lambda_{\text{FS}}$  is studied for the fine-structure of Hydrogenic Neon, Magnesium, Aluminium and Silicon. The fine-structure separation is compared with the Dirac theory and other experimental data, while the possible mechanisms giving rise to the non-statistical value of the  $\beta$ -ratio are analysed.

---

# Acknowledgements

I would like to thank Drs. Kenton Evans and Nicol Peacock for the opportunity to work in this field and acknowledge the receipt of a scholarship from the UKAEA Fusion Laboratory, Culham.

I am indebted to Nicol Peacock for his continued encouragement and advice in all areas of this work. I enjoyed many stimulating conversations with him, and his wide knowledge of plasma spectroscopy was invaluable.

Special thanks go to my colleague and friend Robin Barnsley for making many suggestions and contributions to this research. Much of my present understanding of experimental x-ray techniques has been built on numerous discussions at the Jomuna Research Institute, Oxford.

I would like to thank Dr. Richard Willingale for his comments on part of this thesis; and Dr. Francis Keenan of Queen's College, Belfast for his advice on opacity calculations and his unpublished data on the  $\alpha$ -ratios.

This work has depended on the scientific collaboration with physicists at various laboratories. Thanks go to Nick Hawkes, Steve Fielding, Josh Silver, Martin Laming, Mike Key, Greg Tallents and Peter Norreys.

I have benefited a great deal from the assistance provided by staff of the mechanical workshop headed by John Hennessey and other members of the Physics Department. I would like to thank Jim McGowan for his skill in machining the various components of the spectrometer. Many thanks also go to Harry Jones and Paddy for continued technical support at Culham Laboratory and to Tony Damerell at Rutherford Appleton Laboratory.

Finally, it is a pleasure to acknowledge the high quality of word-processing on an Apple Macintosh by Joy Milsom in the face of rapidly approaching deadlines. I would like to thank Ann Crane for tracing the figures with great skill.

# Contents

## Part I

### Chapter 1 Introduction.

1.1	Thesis Objective.	2
1.2	Spectroscopy.	2
1.2.1	Laboratory Plasmas.	4
1.2.2	X-ray Spectroscopy.	4
1.2.3	High Resolution X-ray Spectroscopy.	5
1.3	Research Programme	5
1.4	Thesis Layout.	7

### Chapter 2 X-Ray Crystal Spectrometers.

	Introduction.	10
2.1	Bragg Diffraction.	10
2.1.1	History of X-Ray Diffraction.	10
2.1.2	Bragg's Law.	10
2.1.3	Diffraction Models.	13
2.1.4	Refractive Index Calculations.	14
2.2	X-Ray Crystal Spectrometers.	17
2.2.1	Instrument Parameters.	17
2.2.2	Plane Crystal Spectrometers.	17
2.2.3	Curved Crystal Spectrometers.	24
2.3	The Johann Geometry.	25
2.3.1	Waveband.	25
2.3.2	Sensitivity.	30
2.3.3	Dispersion Relation.	31
2.3.4	Instrumental Resolving Power.	38
2.4	Conclusions and Instrumentation Specification.	41

### Chapter 3 Spectrometer Design.

	Introduction.	44
3.1	Spectrometer Description.	44
3.1.1	Basic Spectrometer Design.	44
3.1.2	Vacuum System.	44

---

3.2	Curved Crystal Devices.	48
3.2.1	Review of Curved Crystal Methods.	48
3.2.2	Principle of Four Bar Beam Bending.	49
3.3	The Leicester Crystal Bending Jigs.	52
3.3.1	Bending Jig Description.	52
3.3.2	The MarkIII Crystal Bending Jig.	56
3.4	Crystal Focusing and Alignment Procedure.	57
3.4.1	The Crystal Focusing Procedure.	57
3.4.2	The Crystal Alignment Procedure.	60
3.5	Optical Testing Procedure.	62
3.5.1	Objective.	62
3.5.2	Method.	62
3.5.3	Focus Quality Interpretation.	66
3.6	Thermal and Mechanical Stability Testing.	67
3.7	Conclusions.	68

#### **Chapter 4 Instrumentation and Techniques.**

	Introduction.	70
4.1	Crystals.	70
4.1.1	Crystals for $1 \rightarrow 25\text{\AA}$ .	70
4.1.2	Practical Information About Bending Crystals.	74
4.2	X-Ray Films.	77
4.2.1	Kodak X-Ray Films for $1 \rightarrow 25\text{\AA}$ .	77
4.2.2	Kodak DEF 392 Film Response.	78
4.2.3	Densitometry and Optimisation of Signal/Noise.	80
4.2.4	Digitisation Process.	83
4.3	Filters and Transmission Calculations.	84
4.4	Instrument Sensitivity.	89
4.5	Line Profiles and Analysis.	92
4.5.1	Natural Line Broadening.	92
4.5.2	Doppler Broadening.	93
4.5.3	The Voigt Profile.	94
4.5.4	Spectral Line Profile Fitting.	97
4.6	Discussion.	99

## Part II

### Chapter 5 Tokamak Plasmas.

	Introduction.	106
5.1	Introduction to Atomic Processes.	106
	5.1.1 The Emission Spectrum.	106
	5.1.2 Ionization, Recombination and Excitation Processes.	107
5.2	Line Emission.	108
	5.2.1 Introduction.	108
	5.2.2 Electron Impact Excitation.	109
	5.2.3 Dielectronic Recombination - Satellite Lines.	110
	5.2.4 Inner-Shell Excitation - Satellite Lines.	111
5.3	Plasma Models.	112
	5.3.1 Coronal Equilibrium Model.	112
	5.3.2 Local Thermodynamic Equilibrium Model.	114
	5.3.3 Collisional Radiative Equilibrium Model.	114
5.4	Controlled Nuclear Fusion and Tokamaks.	115
	5.4.1 Nuclear Fusion Programme.	115
	5.4.2 Tokamak Devices.	121
5.5	Ion Temperature Measurements.	122
	5.5.1 Different Methods.	122
	5.5.2 Instrument Description for DITE Measurements.	126
	5.5.3 He-like Ion Emission.	132
	5.5.4 Toroidal Rotation during Neutral Beam Injection.	144
5.6	The Bragg Rotor 2-Crystal Spectrometer.	145
	5.6.1 Instrument Description and Experiment.	145
	5.6.2 Results and Analysis.	145
5.7	Time-resolved Spectra Using a CCD Detector.	149
	5.7.1 Description.	149
	5.7.2 Results.	150
5.8	Discussion and Conclusions.	154

### Chapter 6 Laser Produced Plasmas.

	Introduction.	157
6.1	Introduction to Laser Produced Plasmas.	157
	6.1.1 High Power Lasers: Brief History to the Present day.	157
	6.1.2 Plasma Production.	158

6.1.3	X-Ray Emission and Comparison with Other Sources.	160
6.1.4	Applications of Laser Plasmas.	160
6.2	Line Broadening Mechanisms.	161
6.3	Experimental Section.	163
6.3.1	High Power Lasers at the Central Laser Facility.	163
6.3.2	Description of Instrumentation.	163
6.3.3	Optimisation of the Johann Spectrometer.	164
6.3.4	Suprathermal Electron Transport Experiment.	166
6.4	Experimental Results from the Johann Spectrometer.	167
6.4.1	He-like Aluminium Ion $1s^2$ - $1s2p$ Spectrum and Satellites.	167
6.4.2	H-like Aluminium Ion $1s$ - $2p$ Spectrum and Satellites.	182
6.5	Opacity Calculations.	182
6.5.1	Escape Factor Model.	183
6.5.2	He-like Aluminium $1s^2$ - $1s2p$ Resonance Line.	184
6.5.3	H-like Aluminium Lyman- $\alpha$ Resonance Line.	186
6.5.4	He-like Dielectronic Satellite Lines.	192
6.6	Electron Density Measurements.	193
6.6.1	H-like and He-like $n=2$ Resonance Lines.	193
6.6.2	Density Sensitive Dielectronic Satellite Lines.	194
6.7	Discussion and Conclusions.	200
6.7.1	Comparison of Density Measurements.	200
6.7.2	Observed Anomalous Spectral Features.	201
6.7.3	Instrumentation and Future Experiments.	204
<b>Chapter 7 Fast Ion Beam Spectroscopy.</b>		
	Introduction.	207
7.1	Introduction to Fast Ion Beam Spectroscopy.	207
7.1.1	General Description.	207
7.1.2	Beam Ionization and Excitation.	208
7.1.3	Ion Charge State Distribution.	209
7.2	Lamb Shift in the $1s$ Ground State of Hydrogenic Ions.	209
7.3	Axial Observation.	213
7.4	Experimental Description and Method.	213
7.4.1	Instrumentation.	214
7.4.2	Instrument Alignment to Source.	214
7.4.3	MWPC Detector for Experiment.	215

7.5	Silicon XIII Axial Observation.	217
	7.5.1 Experimental Details.	217
	7.5.2 Results.	218
7.6	Neon X Axial Observation.	224
	7.6.1 Experimental Details.	224
	7.6.2 Results.	224
7.7	Conclusions and Future Experiments.	225
	7.7.1 Discussion on Present Experiment.	225
	7.7.2 Application to Different Beam-Target Interactions.	228
	7.7.3 Instrumentation and Techniques for Future Experiments.	229
<b>Chapter 8 Fine-Structure Measurement.</b>		
	Introduction.	232
8.1	Interest in Fine-Structure Measurements.	232
8.2	Theory for Fine-Structure Splitting.	234
8.3	Experiments and Dispersion Calibration.	235
	8.3.1 Experimental Details.	235
	8.3.2 Spectrometer Wavelength Calibration.	236
	8.3.3 Results.	238
8.4	Fine-Structure Intensity Ratio.	243
	8.4.1 Collisional Mixing of the n=2 Levels.	243
	8.4.2 Non-collisional Effects.	244
	8.4.3 Experimental Data.	246
8.5	Review of Fine-Structure Splitting Measurements.	248
	8.5.1 Discussion of Measurements from Other Sources.	248
	8.5.2 Satellite Lines.	252
	8.5.3 Satellite-Free Spectra.	254
8.6	Conclusions.	254
<b>Final Conclusions</b>		256
<b>Appendices</b>		257
<b>Publications</b>		
<b>References</b>		

# **Part I**

# Chapter 1 Introduction.

1.1	Thesis Objective.	2
1.2	Spectroscopy.	2
	1.2.1 Laboratory Plasmas.	4
	1.2.2 X-ray Spectroscopy.	4
	1.2.3 High Resolution X-ray Spectroscopy.	5
1.3	Research Programme	5
1.4	Thesis Layout.	7

# Chapter 1 Introduction.

## 1.1 Thesis Objective.

The main aim of this research is to demonstrate and define the successful use and optimisation of a high precision Johann<sup>1</sup> curved crystal spectrometer. High resolving power  $\lambda/\Delta\lambda \geq 5000$  in the waveband below  $13\text{\AA}$  has been applied to three different laboratory x-ray sources: Tokamak plasmas, laser produced plasmas and beam-foil interactions. Whilst high resolution curved crystal spectrometers are commonly employed to interpret Tokamak ion temperatures from Doppler broadening, to the author's knowledge, no single instrument design has previously been used to observe such diverse sources.

The key feature of this versatile spectrometer, which has determined high spectral resolution and sensitivity over the specified waveband, has been the ability to vary the crystal radius as a free parameter. A specially designed crystal bending device has been demonstrated here for crystal curvatures  $R=300 \rightarrow 2500\text{mm}$ . Interpretation of the source parameters has been possible through the revelation of fine spectral features difficult to achieve with other instrument geometries. This has been most fully illustrated on beam-foil sources which have high intrinsic spectral resolution. The measurements of the Neon X Lyman- $\alpha$  and Silicon XIII resonance lines represent the best resolved x-ray spectra to be recorded between  $6\text{\AA}$  and  $13\text{\AA}$  on this source.

## 1.2 Spectroscopy.

A brief introduction to x-ray spectroscopy of astrophysical and laboratory, plasma and non-plasma sources is given. The reader is guided to several excellent reviews of spectroscopic diagnostics by De Michelis and Mattioli: "Soft-X-Ray Spectroscopic Diagnostics of Laboratory Plasmas"<sup>2</sup> and "Spectroscopy and Impurity Behaviour in Fusion Plasmas"<sup>3</sup>. Further information on non-plasma sources can be found in the recently published text "Astrophysical and Laboratory Plasmas" edited by Brown and Lang<sup>4</sup>.

Spectroscopy has always been considered an important method for observing and understanding plasmas and their properties: this is a consequence of the electromagnetic radiation emitted from such sources. The initial development of these techniques stemmed from fundamental research of astrophysical sources (including the solar corona) whose remoteness made non-spectroscopic methods impossible. In recent times, soft x-ray spectroscopy has become increasingly relevant to high temperature plasmas developed for the nuclear fusion programme. They emit intense x-radiation in the soft x-ray waveband, defined here as being  $1 \rightarrow 25\text{\AA}$ . These methods are useful because they are passive and do not interact with the plasma.

While the origins of laboratory spectroscopy lie in early astrophysical work, current laboratory plasma research is useful for interpreting non-terrestrial sources.

## Laboratory Plasma Sources

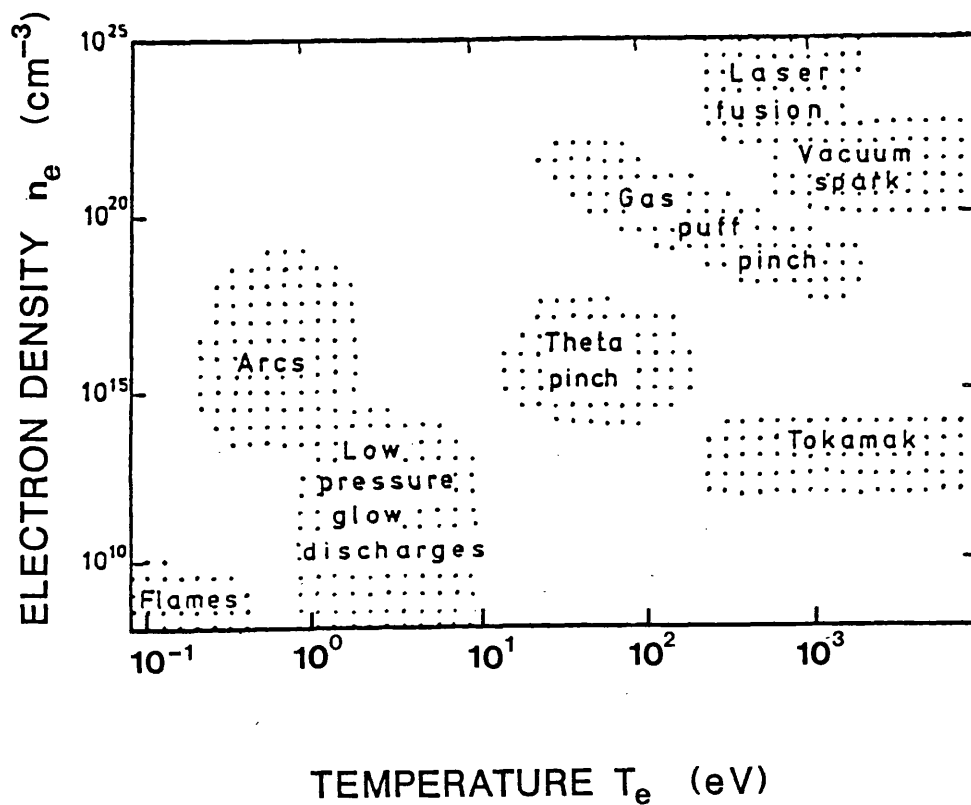


Figure 1.1 shows the  $n_e$  and  $T_e$  parameter range for some laboratory plasma sources.

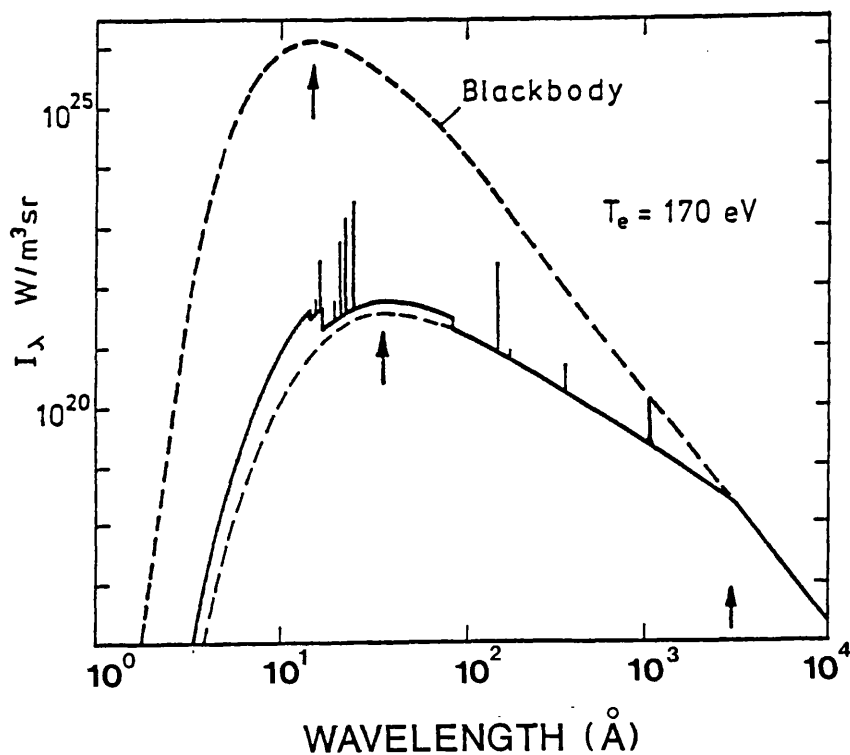


Figure 1.2 Emission spectrum showing resonance lines and continua for a typical plasma source.

### 1.2.1 Laboratory Plasmas.

Laboratory plasmas, emitting x-radiation, differ in many ways: plasma dimensions and duration, methods of production and characteristics vary from one source to another. Figure 1.1, after Kunze<sup>4</sup>, shows schematically the electron density and temperature parameters for some plasma sources. They range from low density Tokamaks and  $\theta$ -pinches to high density plasma foci, gas puff pinches, low inductance vacuum sparks, exploding foils and laser produced plasmas. The observed thermal electron temperature  $T_e$  for these plasmas is usually in the range of two orders of magnitude between 100eV and in excess of 10keV (for large Tokamaks like JET). The electron density  $n_e$  range, however, is much greater with dilute Tokamak plasmas of  $\sim 2 \times 10^{12} \text{cm}^{-3}$  to more than  $10^{24} \text{cm}^{-3}$  for laser produced compression cores. The plasma duration can last from seconds in Tokamak discharges to picoseconds for laser plasmas.

### 1.2.2 X-Ray Spectroscopy

The main interest in the x-ray band lies in the increasing proportion of electromagnetic radiation emitted as continuum and resonance lines at shorter wavelengths (higher energies) as the plasma electron temperature  $T_e$  rises. For example, the relation:

$$\lambda = \frac{6200}{T_e} \quad (1.1)$$

shows the maximum intensity of the continuum emission due to bremsstrahlung occurs at a wavelength  $\lambda$  (Å) where  $T_e$  is measured in eV. Resonance line emission comes from impurities of varying degrees of ionization. The ionization potential for Hydrogenic impurity ions scales as  $Z^2 \chi_H$ , where  $Z$  is the nuclear charge and  $\chi_H (=13.6\text{eV})$  is the ionization potential of Hydrogen. Thus the wavelength of resonance line emission scales as  $Z^{-2}$  and the strongest  $n=2$  transition may be written as:

$$\lambda = \frac{16500}{Z^2 \chi_H} \quad (1.2)$$

This is a fair indication that electrons of energy  $E(\text{eV}) = 12400/\lambda$  are being generated in the plasma.

Figure 1.2, after Kunze<sup>4</sup>, shows a typical emission spectrum observed from a plasma. Further discussion on atomic processes giving rise to lines and continua in plasmas can be found in Chapter 5.1.

The role of x-ray spectroscopy and problems faced by spectroscopists are very much dependent on these source parameters, and availability of other diagnostic techniques. Active methods such as Thomson scattering and interferometry, both laser and microwave, have been used extremely effectively to measure  $T_e$  and  $n_e$  of low density plasmas. They have better spatial and temporal resolution and are generally more accurate than spectroscopic techniques. X-ray spectroscopy, however, becomes increasingly important at higher

densities where laser probing of the plasma becomes ineffective due to refraction and finally unuseable because of total reflection of the propagating beam.

The following information can be gained by studying spectral features including continuum, resonance line emission and profile shape from the x-ray source:

- (1) The thermal  $T_e$  and suprathreshold  $T_H$  electron temperature can be measured from the continuum and line emission.
- (2) The electron density  $n_e$  can be determined by Stark broadening of spectral profiles or line intensity ratios.
- (3) The ion density  $n_i$  (or impurity abundance) can be derived from absolute line intensities.
- (4) The ion temperature  $T_i$ , or large scale bulk motion of an ablation plasma, for a particular ion species can be measured by Doppler broadening or shifting of the emitted spectral lines.
- (5) The energy balance, of particular importance to nuclear fusion plasmas, can be determined. The energy loss through x-radiation of multiply ionised high  $Z$  impurities can be established from absolute intensities of emission lines and continuum. Impurity transport and its influence on the plasma stability can be studied.
- (6) The degree of ionization of the plasma and its dynamics can be readily observed by time-resolved measurements of the relative line intensities from different charge states.

### **1.2.3 High Resolution X-Ray Spectroscopy.**

High resolution x-ray spectroscopy can play an important role in virtually all of the above parameters; ion temperature  $T_i$  and electron density  $n_e$  from profile studies in low and high density plasmas, respectively are obvious candidates. In the case of the former this is the standard method of measuring high plasma temperatures above  $10^6\text{K}$ . There are additional features for example opacity which can be measured: the optical thickness or self-absorption of any emission line can be measured by study of the profile shape or through the line intensity ratio of adjacent transitions with different absorption oscillator strengths. In some cases, for example density sensitive satellite line ratios discussed later, medium to high resolution is needed to resolve the individual transitions of interest to utilise their diagnostic potential.

### **1.3 Research Programme.**

Initially, the main aim of this research was to develop a high resolution x-ray spectrometer for the Tokamak experimental programme of the UKAEA Culham Fusion Laboratory. The new instrument primarily would provide information about the ion temperature of the various constituent high  $Z$  plasma impurities and investigate its characteristics under different plasma conditions. This would complement the existing Bragg rotor spectrometer

from Leicester designed to give low resolution, time-resolved survey spectra of DITE (Divertor Injection Tokamak Experiment) from  $1 \rightarrow 25 \text{ \AA}$ . A 500mm (crystal radius) Johann instrument had previously been built at Culham and recorded the x-ray spectrum above  $10 \text{ \AA}$ . The Leicester high resolution instrument while still being a Johann-type spectrometer, would be completely different and a more versatile design.

This was a new research topic for the spectroscopy group at Leicester; although expertise in x-ray crystal spectroscopy and techniques for solar physics and astronomy had been achieved within the department in the previous two decades, no experience in high resolution curved crystal spectrometers had been developed. The instrument, starting from the drawing board, would be designed and built at Leicester, followed by commissioning at Culham Laboratory. Initial time-integrated photographic operation would be replaced with a time-resolved, photo-electric readout system at a later date.

The Johann spectrometer produced high quality spectra (below  $10 \text{ \AA}$ ) from DITE in early 1986. An exposure of more than 10 shots was needed to generate sufficient signal intensity, but DITE vacuum restrictions limited the output to only one spectrum per day. Although the results were interesting for atomic spectroscopy, and produced ion temperature measurements, they were felt to be less useful as a plasma diagnostic because they were time-integrated. Financial constraints and lengthy machine non-operational periods prevented both rapid detector development and acquiring a sufficient data base of results.

The opportunity became available during one of these periods to investigate the intrinsic spectral line broadening mechanism of the Folded Tandem accelerator in the Nuclear Physics Department, Oxford University. The instrument was optimised for axial observation of x-rays produced by foil-excitation of high Z ion beams. This was a successful collaboration with Josh Silver's group and involved three short experimental runs in late 1986/early 1987.

The Johann instrument in photographic mode was ideally suited for use with the constant x-ray emission of beam-foil or similar sources and opened up exciting possibilities for future experiments with very high resolution.

Shortly after, in September 1987, there was an informal invitation from Mike Key (Division Head) to work at the Laser Division, Rutherford Appleton Laboratory. This was a challenge to achieve high resolution spectroscopy on a small scale, intense, transient x-ray source. The instrument trial occurred in a three week experiment on VULCAN during December studying electron transport phenomena in layered planar targets. The outcome was successful, producing interesting results of useful diagnostic significance not obtained by the other instruments. (The potential to use a Johann instrument on a regular basis on laser produced plasma experiments in this country is still to be exploited).

The final stage of this experimental programme was to demonstrate the feasibility of CCDs as x-ray detectors with the Johann spectrometer on DITE Tokamak.

To summarise, the Johann spectrometer has been optimised to observe x-radiation below  $10\text{\AA}$  with high spectral resolution from three different laboratory sources.

## **1.4 Thesis Layout.**

This thesis is divided into two parts; the first relates to the instrumental and quantitative x-ray techniques whilst the experimental section deals with Tokamak plasmas, laser produced plasmas and beam-foil interactions, with results and interpretation.

### **Part I**

**Chapter 2** discusses x-ray crystal spectrometers, and choice of instrument for the particular experimental programme. The Johann spectrometer is described in detail as are the properties of sensitivity, dispersion, resolving power and waveband. The tolerance on the instrumental parameters is defined for successful high spectral resolution operation.

The practical implementation of the instrument is indicated in **Chapter 3**. The main spectrometer component is the crystal bending jig and the important features are listed; optical and mechanical testing procedures are presented and its performance is evaluated. The crystal focusing and alignment techniques are outlined.

**Chapter 4** deals with the practical considerations, observations, and use of crystals, filters and x-ray film. Full optimisation and data retrieval are included, together with the interpretation of spectral profiles and analysis codes. Thermal and natural spectral line broadening mechanisms are introduced. A discussion of a very high resolution spectrometer with CCD detector readout concludes this chapter and the instrumentation section.

### **Part II**

The second experimental section starts with **Chapter 5** which introduces the atomic processes giving rise to resonance line and continuum emission. Tokamaks and controlled nuclear fusion by magnetic confinement are described. A search for the best waveband for ion temperature observations on DITE below  $10\text{\AA}$  is shown. Ion temperature measurements are made with two different spectrometers. Some results for spatially-scanned ion temperature measurements are also presented. An initial feasibility study using a commercial TV format CCD chip is reported.

**Chapter 6** describes the production and applications of laser plasmas. Additional line-broadening mechanisms are mentioned. The "Suprathermal Electron Transport" experiment is outlined, where the Johann spectrometer is optimised to the source, and observes the H-like and He-like  $n=2$  transitions from the buried Aluminium diagnostic layer. Methods are devised to measure the optical depth of the main resonance and satellite lines. He-like and Li-like satellite lines are used to estimate the peak plasma electron density. The results of 0.1 times solid density are in good agreement with the Stark width measurements. A brief comparison with the commonly used flat crystal spectrometers rounds off this chapter.

---

The final experimental programme of beam-foil interactions is introduced in **Chapter 7**. There follows an outline of the current topical interest in QED (Quantum Electrodynamics) effects on the Hydrogenic ion ground state in high  $Z$  beams by direct measurement of the radiative transitions. The proposed improvement in the intrinsic spectral line broadening due to the accelerator is investigated by high resolution axial beam measurements of the He-like Silicon and H-like Neon  $n=2$  transitions. The use of the technique for future experiments is summarised.

Finally, precision measurements of the Lyman- $\alpha$  fine-structure separation  $\Delta\lambda_{FS}$  and intensity ratio  $\beta$  for medium  $Z$  elements is given in **Chapter 8**. The results for  $Z=12\rightarrow 14$  (Magnesium, Aluminium and Silicon) are observed on DITE Tokamak, but also the  $Z=10$  (Neon) beam-foil measurement is included for completeness. The fine-structure separation is compared with the Dirac theory and other experimental data, while the possible mechanisms giving rise to the non-statistical value for  $\beta$  are analysed.

Conclusions relevant to a chapter are discussed in that chapter as they arise. The **Final Conclusions** section following Chapter 8 draws together the main achievements of high resolution spectroscopy in each x-ray source.

# Chapter 2 X-Ray Crystal Spectrometers

	Introduction.	10
2.1	Bragg Diffraction.	10
	2.1.1 History of X-Ray Diffraction.	10
	2.1.2 Bragg's Law.	10
	2.1.3 Diffraction Models.	13
	2.1.4 Refractive Index Calculations.	14
2.2	X-Ray Crystal Spectrometers.	17
	2.2.1 Instrument Parameters.	17
	2.2.2 Plane Crystal Spectrometers.	17
	2.2.3 Curved Crystal Spectrometers.	24
2.3	The Johann Geometry.	25
	2.3.1 Waveband.	25
	2.3.2 Sensitivity.	30
	2.3.3 Dispersion Relation.	31
	2.3.4 Instrumental Resolving Power.	38
2.4	Conclusions and Instrumentation Specification.	41

## Introduction.

The following topics are discussed in this chapter:

- Bragg's law, x-ray diffraction and its effect on observed crystal properties, and the calculation of refractive index corrections.
- Description of different Bragg crystal spectrometer geometries and definition of the main instrumental parameters.
- The optimisation of sensitivity, waveband and resolving power of a Johann spectrometer to different sources. The dispersion relation is verified with experimental observations.
- The spectrometer specification is defined for high resolving power.

## 2.1 Bragg Diffraction.

### 2.1.1 History of X-Ray Diffraction.

Diffraction of x-rays by crystals in transmission mode, was discovered by von Laue<sup>5</sup> in 1912 and, later in the same year, confirmed for reflection off a Mica crystal surface by W L Bragg<sup>6</sup>. This early work demonstrated the wave-like nature of x-rays and concentrated mainly on the geometry of diffraction and the study of crystal and atomic structure. However, it did not yield quantitative information on the diffraction intensity or profile shape. This was to follow in 1914 by Darwin<sup>7</sup> who presented a diffraction theory based on Bragg reflection. This theory was dynamical and considered the interaction between incident and reflected waves inside the crystal. It was able to describe the crystal diffraction profile and allow for refraction of the x-rays within the crystal. It was flawed in one respect by the omission of the absorption process in the crystal. Ewald<sup>8</sup> introduced a more general dynamical theory in 1917. Prins (1930)<sup>9</sup> improved Darwin's theory by including a complex refractive index to account for absorption within the crystal. This gave a good quantitative description of Bragg reflection.

### 2.1.2 Bragg's Law.

A crystal may be considered as a three dimensional array of atoms consisting of an identical arrangement of atoms, known as the unit cell, repeated at regular intervals. The crystal can be easily described as a repeating lattice of points with the unit cell associated at each point. For a uniform crystal, parallel lattice or reflecting planes separated by a distance known as the "d-spacing" can be easily defined for the crystal geometry. In the case of the simple (face-centred) cubic symmetry, the lattice spacing  $d_{hkl}$ , for Miller indices (h,k,l) are related to the unit cell dimension  $a_0$  by:

$$d_{hkl} = \frac{a_0}{\sqrt{h^2 + k^2 + l^2}} \quad (2.1)$$

Since the crystal lattice spacings are dimensionally the same as x-ray wavelengths, they will scatter the radiation and behave like a three dimensional diffraction grating. Thus a

plane wave incident on a crystal lattice (Figure 2.1) will be scattered in all directions, but diffraction maxima will only occur in the directions where the waves scattered from the lattice points have zero phase difference. Bragg's law predicts that the condition for constructive interference of radiation from successive planes is satisfied when the path difference is an integral number of wavelengths  $\lambda$ :

$$n\lambda = 2d_T \sin\theta_B \quad (2.2)$$

where  $\theta_B$  is the Bragg reflection angle and  $n$  is the order of diffraction. The (hkl) subscript has been dropped and  $d_T$  refers to the crystal lattice spacing at a temperature  $T$  ( $^{\circ}\text{C}$ ). The lattice spacing varies with temperature where  $\alpha$  is the linear expansion coefficient:

$$d_T = d_{18} (1 + \alpha \{ T - 18 \}) \quad (2.3)$$

The crystal dispersion can be derived from equation (2.2) as:

$$\frac{d\theta}{d\lambda} = \frac{n}{2d_T \cos\theta_B} \quad (2.4)$$

Equations (2.2) and (2.4) can be combined to give the crystal resolving power:

$$\frac{\lambda}{\Delta\lambda} = \frac{\tan\theta_B}{w_c} \quad (2.5)$$

where  $w_c$  (radians) is the FWHM of the diffraction profile.

Bragg's law is not exact due to refraction of the x-ray beam within the crystal material (Figure 2.2). From Compton and Allison<sup>10</sup>, the refractive index of the crystal material defined as  $\mu=1 - \delta$  is very close to (but less than) unity. X-rays are therefore refracted away from the normal and travel an extra distance thus changing the condition for constructive interference. The measured peak diffraction angle  $\theta$  differs from  $\theta_B(=\sin^{-1}(n\lambda/2d_T))$  by an amount:

$$\theta = \theta_B + \Delta\theta \quad (2.6)$$

The unit decrement of the refractive index, in the range  $10^{-5} \rightarrow 10^{-6}$ , is related to  $\Delta\theta$  by:

$$\delta = \Delta\theta \sin\theta_B \cos\theta_B \quad (2.7)$$

(The distinction between  $\theta$  and  $\theta_B$  is unimportant in equation (2.7)). Thus equation (2.2) can be rewritten as:

$$n\lambda = 2d_T \left[ 1 - \left\{ \frac{2d_T}{n} \right\}^2 \frac{\delta}{\lambda^2} \right] \sin\theta \quad (2.8)$$

It can be seen from the previous equation that the maximum wavelength which can be reflected is  $2d$  corresponding to  $\theta=90^{\circ}$ . Also, refractive index corrections are significant at high Bragg angles but reduce as  $n^{-2}$  with increasing diffraction order.

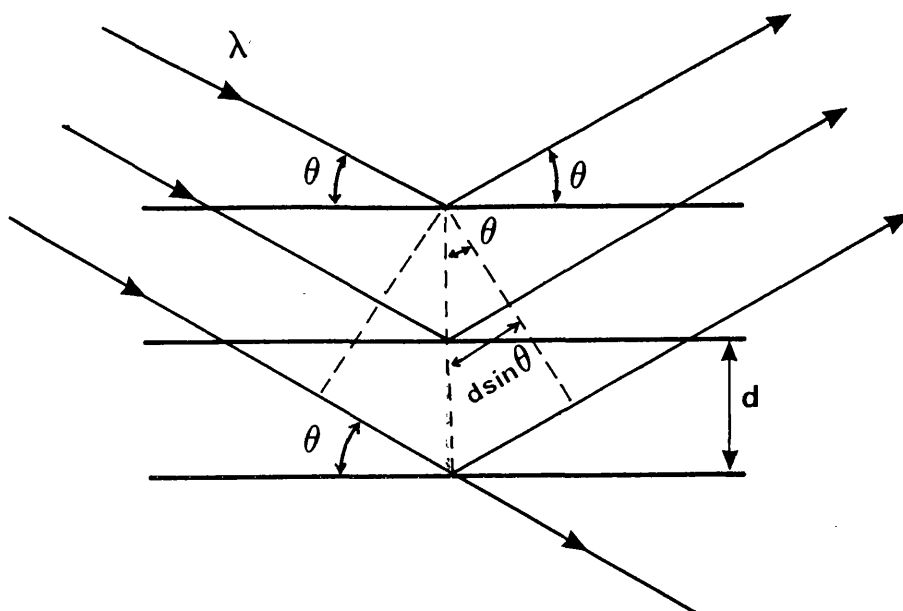


Figure 2.1 Schematic showing Bragg Reflection.

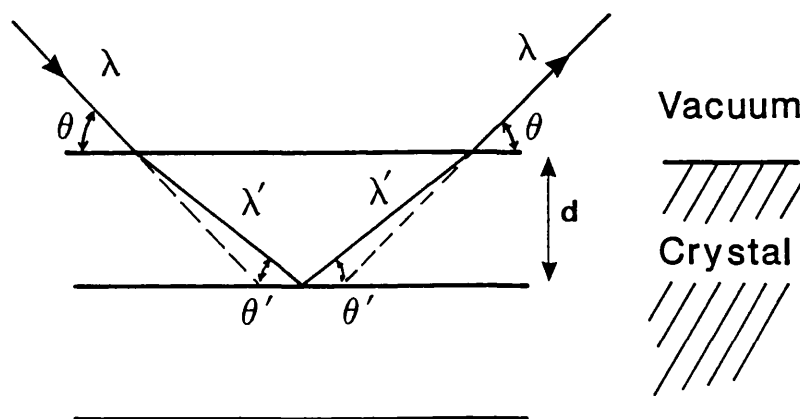


Figure 2.2 Refractive index effects for x-rays within crystal.

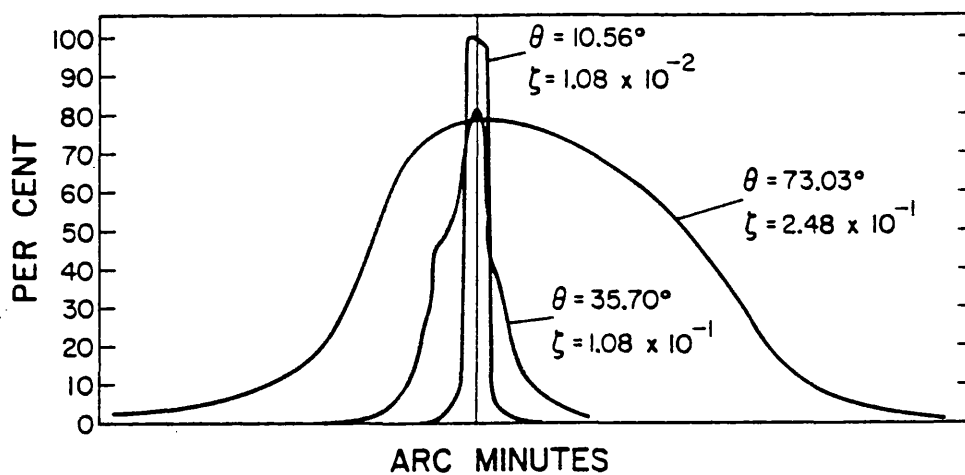


Figure 2.3 Variation of crystal diffraction profile for PET (002) as a function of Bragg angle, calculated from Darwin-Prins (after Burek<sup>12</sup>).

### **2.1.3 Diffraction Models.**

The following is a brief account of the diffraction theories used to describe the reflection process for different crystals. A complete account may be found in Hall<sup>11</sup> or Burek<sup>12</sup> or the references therein. The research of Hall is of particular interest as it documents the change in crystal properties with ageing, atmospheric and chemical attack.

Two different crystal models are:

- The mosaic or ideally imperfect model described by the kinematical theory of x-ray diffraction.
- The perfect crystal or the ideally perfect crystal model described by the dynamical theory of diffraction.

The results of the two models converge at shallow Bragg angles.

#### **Mosaic Model**

This model was proposed by Darwin, neglecting absorption, to describe crystals with imperfections using the kinematical theory. This assumes there is negligible interaction between the scattered and incident beams and the intensity of the incident beam remains constant for a thin crystal. This latter point is referred to as zero-extinction, where primary extinction in thick crystals describes the phenomenon of reduced incident beam intensity in lower crystal planes due to reflection in the upper planes.

The measured diffraction profiles of real crystals are usually broader than the Darwin perfect crystal as a result of imperfections in the lattice. Darwin suggested that most crystals are made from smaller individual blocks or mosaic pieces where each block may be considered as a perfect or ideal crystal. The orientation of the blocks relative to each other have angular deviations which are greater than the diffraction width of a single block. The individual blocks reflect independently, so that the reflected beam energy is proportional to the number of blocks in the beam. The diffraction profile characteristics also depend on the block size, shape and angular distribution.

The mosaic model is not completely accurate and does not cover all crystal defects like dislocations and strains. Also, departure from ideal mosaicity occurs when the block orientation becomes comparable with the diffraction width.

#### **Perfect Crystal**

The dynamical theory or Darwin-Prins theory is more complex and always includes the absorption process. It applies to large perfect crystals where primary extinction and the interaction of the incident and scattered beams cannot be ignored within the crystal material.

Figure 2.3 from Burek<sup>12</sup> shows the calculated diffraction profile using a Darwin-Prins model for PET (002) with various Bragg angles. The different profile shapes are a consequence of the variation of primary extinction and absorption with Bragg angle. At shallow angles, absorption is low and the profile takes on the characteristic flat-topped,

symmetrical Darwin shape with 100% peak reflectivity. Absorption increases with  $\theta$  resulting in reduced peak reflectivity and a broader, asymmetric diffraction profile. The diffraction width also increases as  $\tan\theta$  due to the increase of extinction with Bragg angle.

Generally, mosaic crystals have greater diffraction widths  $w_c$ , lower peak reflectivity  $P_c$  and higher integrated reflectivity  $R_c$  than the corresponding perfect crystal.

### Reflection Integral

It may be predicted from crystal diffraction theory that the Bragg reflection of a parallel and monochromatic x-ray beam happens over a small angular range due to the finite width of the crystal line profile. The reflected intensity  $I(\theta)$ , for an incident intensity  $I_0$  at a glancing angle  $\theta$  for a flat crystal can be written as (Evans and Leigh<sup>13</sup>):

$$I(\theta) = P_\lambda(\theta) I_0 \quad (2.9)$$

where  $P_\lambda(\theta)$  is the fractional reflection of the beam by the crystal (known as the Prins function) at the wavelength  $\lambda$ . The diffraction profile can be determined from the variation of  $P_\lambda(\theta)$  with  $\theta$ . The crystal may be rotated at a constant rate  $\omega = d\theta/dt$  such that the total reflected x-rays  $E$  integrated over limits  $\theta_1 \rightarrow \theta_2$  (much greater than the angle of appreciable Bragg reflection) is:

$$E = \int_{\theta_1}^{\theta_2} \frac{P_\lambda(\theta)}{\omega} d\theta \quad (2.10)$$

The Bragg reflection integral or integrated reflectivity  $R_c$  can be written as:

$$R_c = \int_0^{\pi/2} P_\lambda(\theta) d\theta \quad (2.11)$$

and by using the previous results can be expressed as:

$$R_c = \frac{\omega E}{I_0} \quad (2.12)$$

The most significant factors for the diffraction profile may be defined as the integrated reflectivity  $R_c$ , the FWHM  $w_c$  and the peak reflectivity  $P_c$ . As discussed previously, the diffraction profile changes over the crystal waveband.

### 2.1.4 Refractive Index Calculations.

The parameter  $\delta$  may be written in terms of the unit cell scattering factor  $F$ , known as the crystal structure factor, which is the ratio of the scattering amplitude due to all the electrons in the cell to that due to a single electron<sup>10</sup>:

$$\delta = \frac{\lambda^2 r_0 F}{2\pi V} \quad (2.13)$$

where  $r_o$  is the classical electron radius:

$$r_o = \frac{e^2}{m_e c^2} \quad (2.14)$$

$V$  is the volume of the unit cell. Equation (2.13) can be expressed as:

$$\frac{\delta}{\lambda^2} = \frac{n_e e^2}{2\pi m_e c^2} \quad (2.15)$$

where  $n_e$  is the electron density of the crystal material:

$$n_e = \frac{N_A \rho Z_m}{M} \quad (2.16)$$

where  $N_A$  is Avogadro's constant,  $\rho$  is the crystal density and  $Z_m$ ,  $M$  are the number of electrons/molecule and the gram molar weight, respectively. For  $\delta/\lambda^2$  in  $\text{\AA}^{-2}$  units:

$$\frac{\delta}{\lambda^2} = \frac{N_A \rho e^2 Z_m}{2\pi 10^{18} m_e c^2 M} \quad (2.17)$$

which simplifies to:

$$\frac{\delta}{\lambda^2} = 2.7008 \times 10^{-6} \frac{\rho Z_m}{M} \quad (2.18)$$

Table 2.1 lists  $\rho$ ,  $Z_m$  and  $M$  for various crystal materials.

### Corrections for Wavelengths near Absorption Edges

Equation (2.13) indicates that  $\delta/\lambda^2$  is constant and independent of wavelength for a given crystal. Generally this method should be accurate to better than 5→10% provided the diffracting wavelength region is far from crystal absorption edges. There are, however, variations and discontinuities near absorption edges of the atoms within the crystal material. This anomalous dispersion can be corrected in the refractive index calculation. Equation (2.13) from Compton and Allison<sup>10</sup> can be expressed as:

$$\frac{\delta}{\lambda^2} = \frac{N_A \rho e^2}{2\pi 10^{18} m_e c^2 M} \left[ Z_m + Z_K \left\{ \frac{\lambda}{\lambda_K} \right\}^2 \ln \left[ 1 - \left\{ \frac{\lambda_K}{\lambda} \right\}^2 \right] \right] \quad (2.19)$$

for radiation of wavelength  $\lambda$  near an absorption edge  $\lambda_K$  where  $Z_K$  is the number of electrons in the K-shell of the absorbing atom. The above equation applies for wavelengths to the long wavelength side of the absorption edge. On the short wavelength side, the sign of the argument of the logarithm is simply reversed.

**Table 2.1 Crystal Properties for Refractive Index Calculations**

Crystal	$\rho$ (g/cm <sup>3</sup> )	$Z_m$	M
ADP	1.80	60	115.0
PET	1.39	74	136.0
Si	2.33	14	28.08
Ge	5.33	32	72.6
KAP	1.636	104	204.2
NaAP	1.504	96	188.1
CsAP	2.178	140	298.0
TIAP	2.7	166	369.5
NH <sub>4</sub> AP	1.415	96	183.2
CaCO <sub>3</sub>	2.710	50	100.1
SiO <sub>2</sub>	2.66	30	60.1

$\rho$  Crystal material density  
 $Z_m$  Number of electrons/mole  
M Molar weight in gram

## 2.2 X-Ray Crystal Spectrometers.

### 2.2.1 Instrument Parameters.

An x-ray crystal spectrometer is a device which uses the principle of diffraction for monochromating the polychromatic radiation emitted from the source. The instrument in its most basic form is usually constructed from an entrance aperture or window through which the radiation is viewed or collimated, a dispersion element (the crystal) and a detector for recording the dispersed radiation or spectrum. Various spectrometer geometries have been established in the last eighty years which use plane or curved crystals (concave or convex) in transmission or reflection mode. Such instruments can be complicated using doubly curved crystals or may use multiple reflections from two or more crystals.

The choice of the geometry primarily depends on the experimental objective and the source characteristics. Thus, the following factors should be examined:

- Spectral features to be studied.
- Spectral resolution needed.
- Intensity of emitted radiation.
- Spatial dimensions of x-ray source.
- Temporal variations in source emission and repeatability of emission features.

This should enable the spectroscopist to define and optimise the main instrument parameters of:

- Waveband,  $\lambda_1 \rightarrow \lambda_2$  where  $\lambda_1$  and  $\lambda_2$  define the lower and upper wavelength limits.
- Resolving Power,  $\lambda/\Delta\lambda$ , where two adjacent lines are resolved if their separation is equal to the full width at half-maximum FWHM of the instrument function.
- Spectrometer sensitivity, which includes the crystal reflectivity  $R_c$ , solid angle collection  $\psi_x\psi_y$ , filter and optics transmission  $T(\lambda)$  and detector efficiency  $\eta$  factors.

The additional parameters of time and space resolution may be achieved by adjusting the balance of the primary instrument characteristics. The choice of the final instrument geometry should reflect these different considerations.

In this section, some of the basic instrument designs are described and examples are given to illustrate the diversity of crystal spectrometers. While space prevents a discussion and detailed comparison of the different geometries for each studied source, instrumental resolving power is mentioned in keeping with the main theme of this research. The observed spectral resolution from the different sources has been in the range  $\delta\lambda/\lambda=2 \times 10^{-4} \rightarrow 8 \times 10^{-4}$ , and so high resolving power is defined here as  $\lambda/\Delta\lambda \geq 5 \times 10^3$ .

### 2.2.2 Plane Crystal Spectrometers.

Different types of flat or plane crystal instruments have been designed for x-ray sources.

#### 1. The Bragg Rotor Spectrometer for Tokamak Plasmas.

The Bragg rotor spectrometer<sup>14</sup> (Figure 2.4) was designed by R Barnsley for diffuse Tokamak

plasmas. The instrument design has evolved from the scanning  $\theta \rightarrow 2\theta$  sounding rocket spectrometers<sup>15</sup> built at Leicester and is a true monochromator; the main difference is the completely rotating crystal and fixed detector. The main features are the slotted or gridded collimator defining the resolving power, the crystal rotor and the static Multi-Wire Proportional Counter (MWPC) for collecting the diffracted x-rays. An absolute angle encoder with 2.6 minute of arc resolution on the Bragg rotor gives absolute wavelength calibration. The crystal rotation thus sequentially records different parts of the spectrum with time. The hexagonal rotor holds six crystals which can be chosen to observe the waveband  $1 \rightarrow 25\text{\AA}$  in a single rotation. Different modes of operation allow the crystal to be  $\lambda$ -locked for maximum time resolution and monochromatic sensitivity, scanned slowly or rotated up to 10Hz. Maximum count rates of 10MHz can be sustained before driving the detector into saturation. Time resolution of  $\sim 100\mu\text{sec}$  is possible when  $\lambda$ -locked to a single line or 20 msec in scanning survey mode. The vacuum chamber can be tilted to allow spatial scans at  $\sim 2\text{cm}$  intervals of the minor plasma radius. The resolving power is determined by the collimator angular divergence which is  $3'$  for the grid and  $7'$  for the soller slots; for Bragg angles up to  $65^\circ$ ,  $\lambda/\Delta\lambda=500 \rightarrow 1200$  is possible with the coarse collimator.

The number of integrated counts  $N$  in a spectral line for the crystal rotating at constant angular velocity  $\omega$   $\text{rads}^{-1}$  is expressed as (from Barnsley et al<sup>16</sup>):

$$N = E_\lambda \Delta z \frac{\psi_x \psi_y}{4\pi} \frac{R_c}{\omega} h_x h_y \eta_\lambda \eta_s \quad (2.20)$$

(see Figure 2.4(a)), where  $E_\lambda$  is the plasma emissivity ( $\text{photons cm}^{-3}\text{s}^{-1}$ )  $\Delta z$  is the plasma depth while  $h_x, h_y$  are the crystal/collimator height and width, respectively. The parameters  $\psi_x, \psi_y$  are the collimator acceptance angles in the plane and perpendicular to the plane of dispersion. The former defines the instrumental resolving power. Finally,  $\eta_\lambda, \eta_s$  refer to the filter and detector efficiency and the transmissions of the spectrometer structural elements.

This is a versatile instrument which has been used primarily for studying low resolution, time-resolved survey spectra. It can be converted to a high resolution 2-crystal spectrometer, discussed in Chapter 5.

## 2. The Flat Miniature Spectrometer for Laser Plasmas.

Figure 2.5 shows the main features of the miniature space resolving x-ray spectrometer<sup>17</sup>. X-rays from the plasma are dispersed by the crystal onto the film plane. Different parts of the crystal reflect different wavelengths. The waveband is determined by the incident angles of the radiation to the crystal surface. No collimator is necessary as the small spatial extent of the plasma (typically  $50\mu\text{m}$ ) and the plasma/crystal separation distance ( $\sim 20\text{mm}$ ) define the angular divergence of the x-ray beam. Resolving power of  $\lambda/\Delta\lambda \sim 500$  is usual which is sufficient to measure the Stark widths of high series members of the H- and He-like ion resonance lines. Large wavelength coverage  $\Delta\lambda/\lambda \sim 0.5 \rightarrow 0.8$  is possible, making this design ideal as a low resolution survey spectrometer.

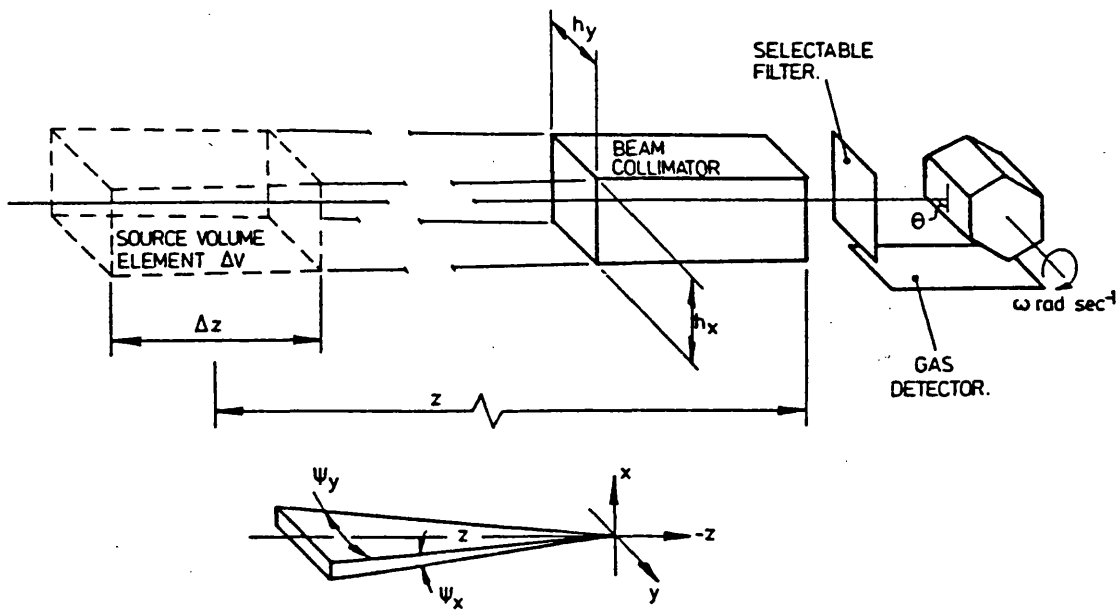


Figure 2.4(a) Geometry of a plane crystal spectrometer for diffuse x-ray sources.

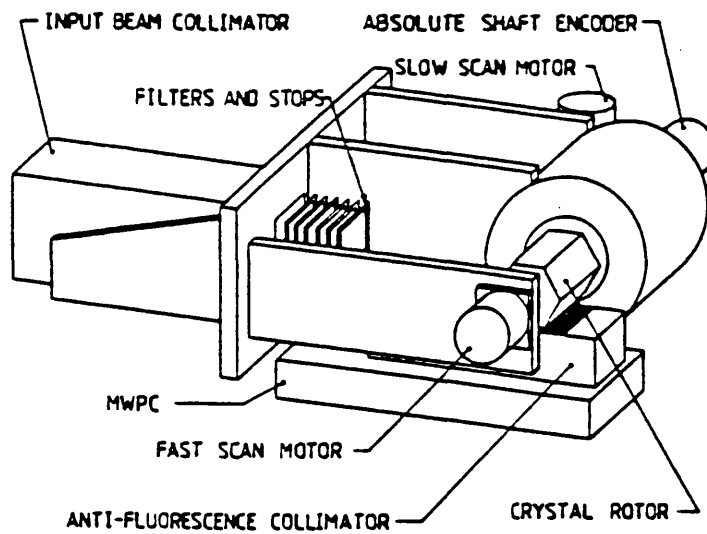


Figure 2.4(b) Schematic of the Bragg Rotor Spectrometer.

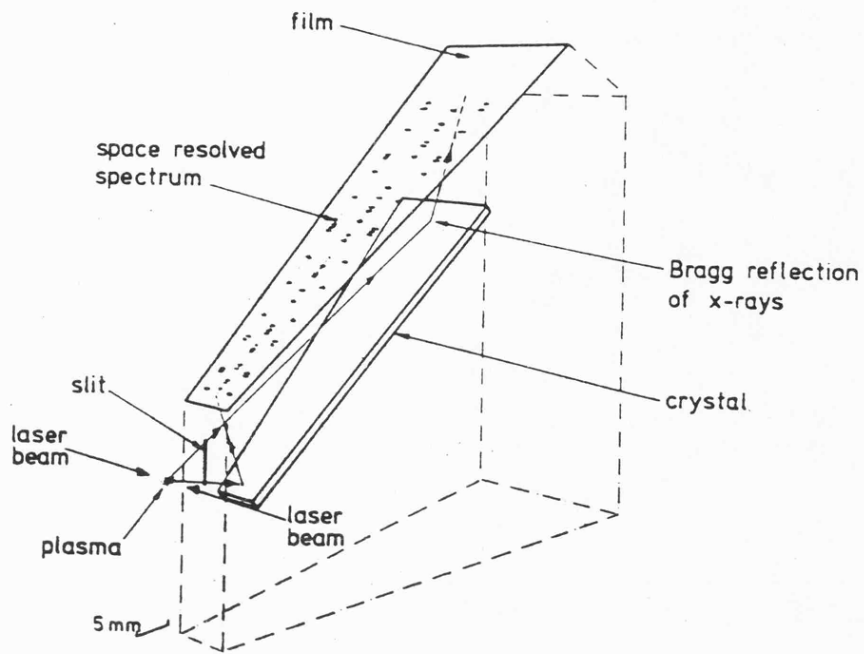


Figure 2.5 Flat crystal miniature x-ray spectrometer for laser produced plasmas, after Kilkenny et al<sup>17</sup>.

### Von Hamos Geometry

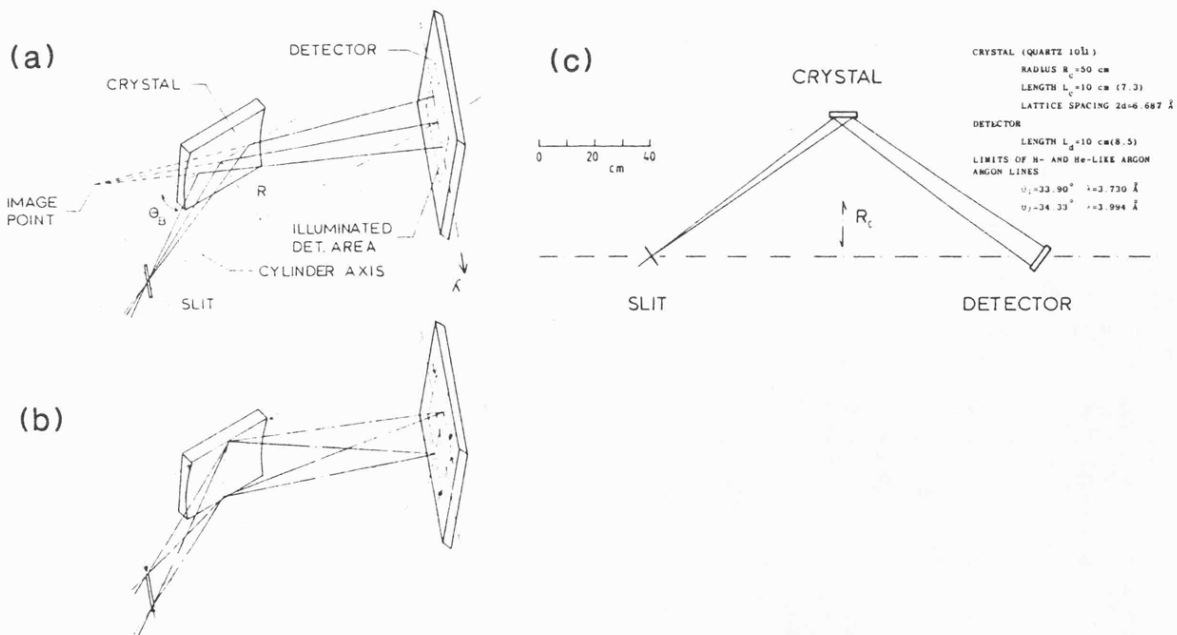


Figure 2.6 Von Hamos geometry after Källne et al<sup>19</sup>.

## The de Broglie Convex Crystal Spectrometer

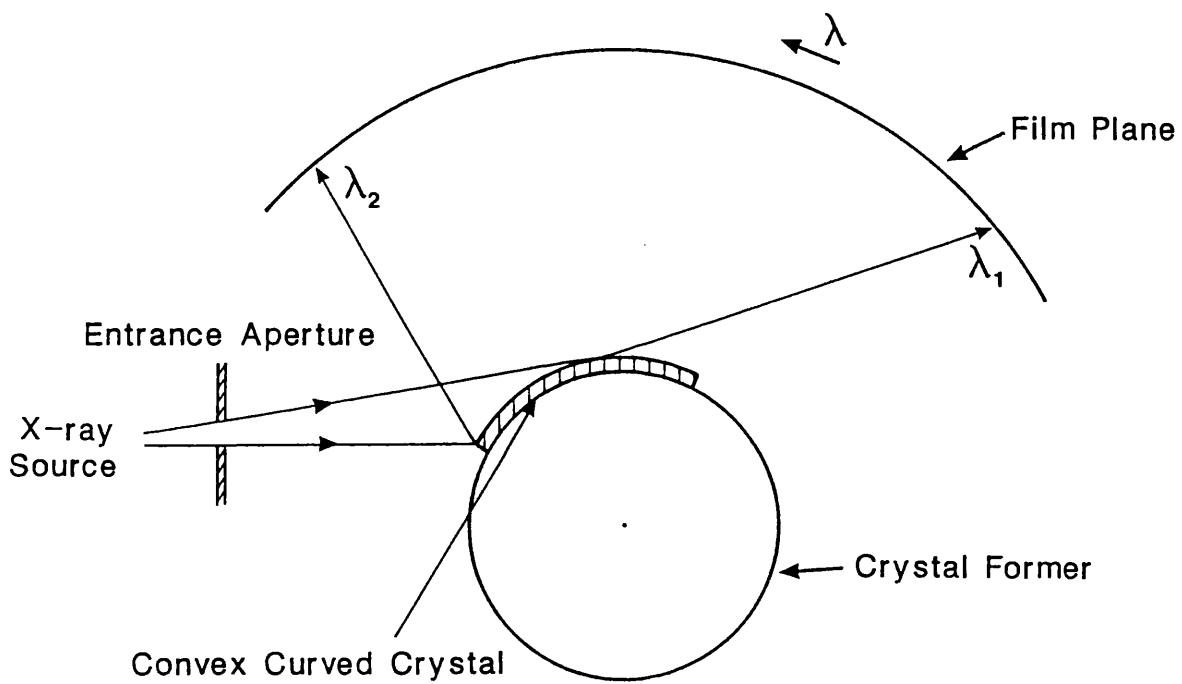


Figure 2.7 The de Broglie convex crystal spectrometer.

# The Johann Curved Crystal Spectrometer

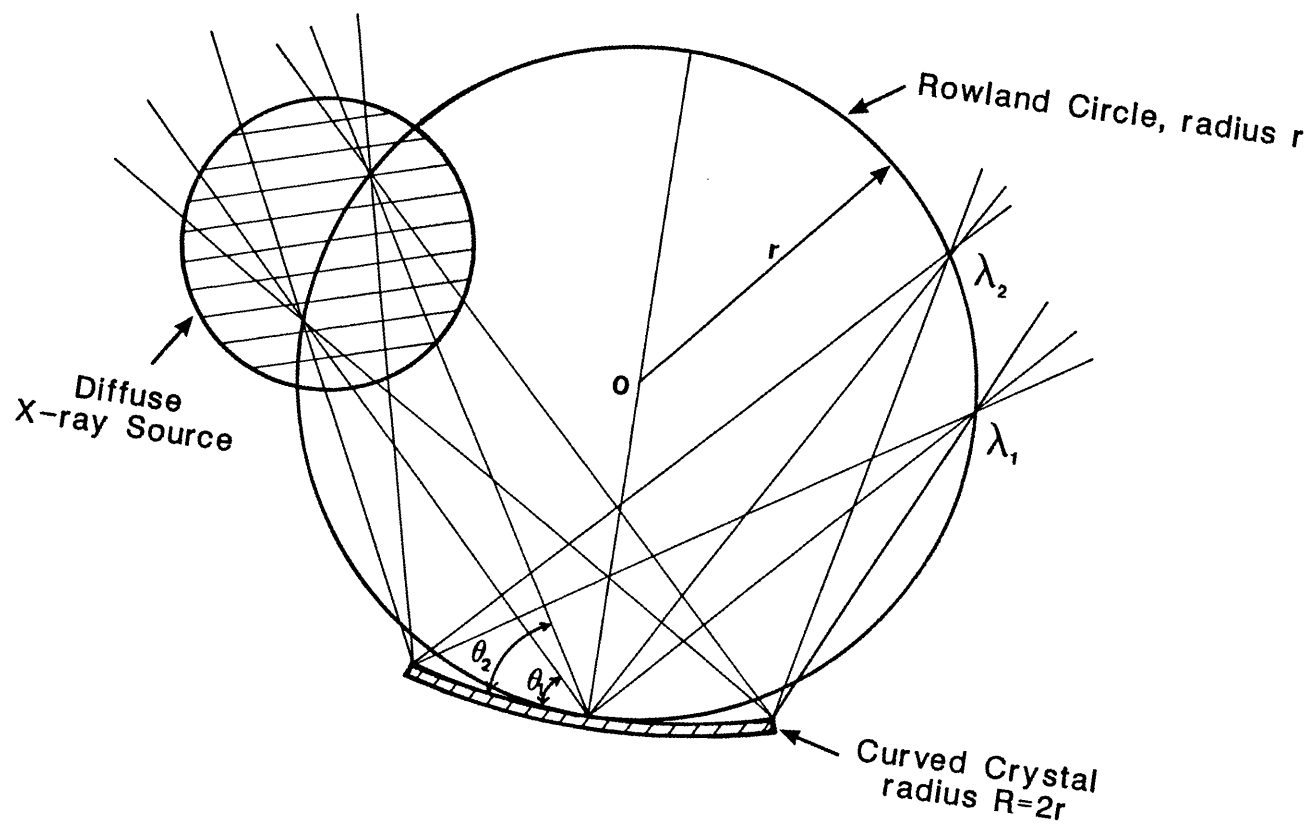


Figure 2.8 The Johann curved crystal spectrometer.

## The Johansson Curved Crystal Spectrometer

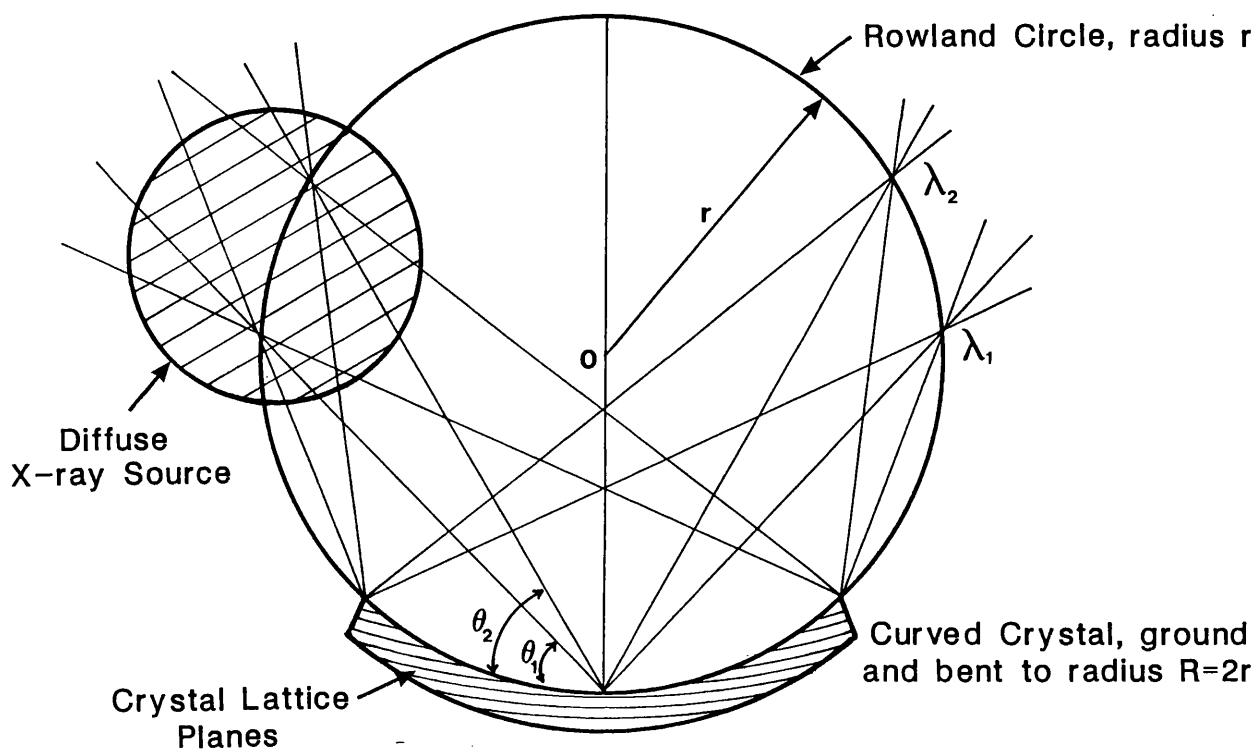


Figure 2.9 The Johansson curved crystal spectrometer.

The plasma/crystal distance may be increased to improve the instrumental resolving power; the measured x-ray flux, however, falls according to the inverse square law and so sensitivity considerations limit the separation to 50mm. The range of incident crystal angles is reduced, and consequently the waveband, with increasing separation. The spectrometer is aligned approximately to the plasma, with only a rough estimate of the Bragg angle, and so wavelength calibration relies on the identification of known lines in the spectrum.

A slit (10→20 $\mu$ m wide) may be introduced, as shown in the figure, to give spatial resolution of the plasma perpendicular to the plane of dispersion. Time-resolved spectra can be recorded if the film is replaced with a streak camera.

### **3. The Von Hamos Spectrometer.**

The von Hamos spectrometer<sup>18</sup> although using a curved crystal, is still in principle a flat crystal instrument. Figure 2.6 from Källne et al<sup>19</sup> illustrates the spectrometer geometry. It can be seen that the crystal curvature is normal to the crystal dispersion plane and is not a true focusing design of the Johann or Johansson arrangement. For use with a Tokamak source, an entrance aperture or slit is needed which effectively determines the crystal resolving power ( $\lambda/\Delta\lambda=3000$  for the Källne instrument). The loss of instrumental sensitivity, by using a single slit instead of a Soller slot collimator in the Bragg rotor design, is partly compensated by the focusing of the beam, perpendicular to the dispersion plane, onto the detector. The range of incident angles allow a simultaneous polychromatic observation which is achieved using a MWPC detector with 1-dimensional spatial resolution. The latter contribution must be taken into account for the overall instrument resolving power.

## **2.2.3 Curved Crystal Spectrometers.**

### **1. The de Broglie Convex Crystal Spectrometer.**

The de Broglie<sup>20</sup> spectrometer, shown in Figure 2.7, consists of a convex crystal which disperses the incident x-radiation onto the film plane. It has been used extensively with x-ray sources of small spatial extent such as the plasma focus, laser plasmas and spark plasmas (see Peacock et al<sup>21</sup> and Gordon<sup>22</sup> for example). The instrument can readily observe a large waveband simultaneously, depending on the incident angles of the radiation on the crystal, but needs a detector with spatial resolution. Resolving power is in the range  $\lambda/\Delta\lambda=500\rightarrow 1500$ . The instrument has been used on DITE Tokamak (Barnsley<sup>23</sup>) but needs an entrance slit. The slit setting while defining the instrumental resolving power, also restricts the collection angle of the spectrometer

### **2. The Johann Spectrometer.**

This spectrometer was reported by Johann<sup>1</sup> in 1931, and was the first focusing crystal x-ray spectrometer. Figure 2.8 indicates the arrangement; the crystal is curved in a uniform cylinder of radius R around an imaginary circle of radius  $r=R/2$ , referred to as the Rowland circle (RC). The concave crystal is tangential to RC at only one point, called the crystal pole.

If the x-ray source is placed on the Rowland circle, then a wavelength  $\lambda_1$  satisfying Bragg's law will be reflected from the full crystal area and focused onto the opposite side as indicated. A similar process is repeated for another wavelength  $\lambda_2$  coming from a different part of the source, so that the spectrum is dispersed round the Rowland circle. A position sensitive detector is needed to record the focused spectrum.

The main point to be stressed here is no entrance slit is necessary to define the instrumental resolving power. One can think of the crystal diffraction profile as an imaginary aperture on the RC. A large increase in sensitivity is possible due to the increased collection angle of the spectrometer. Chapter 2.3 discusses the parameters of waveband, sensitivity, dispersion and resolving power.

### 3. The Johansson Geometry.

The Johansson spectrometer<sup>24</sup>, illustrated in Figure 2.9, uses a concave crystal geometry very similar to the Johann case. Much of the discussions concerning the latter in the previous and next sections equally apply. The main difference is with the crystal, ground and bent to a radius R so that the crystal surface lies on the Rowland circle of radius  $r=R/2$ . The crystal planes are still at radius R. For ideal grinding and bending, this crystal arrangement has perfect x-ray focusing and does not suffer from the Johann width de-focusing error. In practice, the combination of grinding and bending the crystal has deterred many spectroscopists from using this geometry. However, a small Rowland circle Johansson instrument for observing laser produced plasmas would be expected to show a significant increase in sensitivity, with no loss in resolving power, over a similar Johann arrangement; this should be investigated. Large Rowland circle geometries used in Tokamak experiments have negligible width aberrations and so no advantage in sensitivity or resolving power is expected with the Johansson design.

## 2.3 The Johann Geometry.

Waveband, sensitivity and resolving power for the Johann spectrometer are interlinked and depend on the spatial dimensions of the x-ray source.

### 2.3.1 Waveband.

#### 1. Tokamak Sources.

The usual procedure when operating Johann spectrometers with large x-ray sources like Tokamaks is to place the region of x-ray emission on the Rowland Circle RC. This optimises the throughput of the spectrometer where each element of the crystal diffracts equally a wavelength increment  $\delta\lambda$  of the radiation in the waveband  $\Delta\lambda$  in accordance with Bragg's law. The spatial extent of the plasma subtends an angle to the crystal which defines the maximum range of Bragg angles  $\Delta\theta$  (measured in radians) with limits  $\theta_1, \theta_2$  centred on the mean angle  $\theta$ . This defines the wavelength region of interest  $\Delta\lambda$  when used with the dispersion relation, ignoring higher orders and refractive index effects:

$$\Delta\lambda = 2d \cos\theta \Delta\theta \quad (2.21)$$

where  $2d$  is the crystal lattice spacing.

Figure 2.10 shows a large source of spatial extent  $x$  at position A on the RC. This subtends an angle of  $x/r$  to the RC centre O and an angle  $x/R$  to the crystal centre C. The sagittal field angle  $\psi_x$  may be defined as:

$$\psi_x = \frac{x}{R} \quad (2.22)$$

This angle  $\psi_x$  remains independent of  $\theta$  because the cross-section of the source which scales as  $\sin\theta$  is exactly matched by the separation distance AC which also varies as  $\sin\theta$ . The crystal radius  $R$  should be chosen to optimise the waveband so that  $\psi_x = \Delta\theta$ .

If the source is defined by an aperture perpendicular to the Bragg angle then  $\psi_x$  can be modified from equation (2.22):

$$\psi_x = \frac{x}{R \sin\theta} \quad (2.23)$$

The instrument "f-number" for an incremental source element on the RC, with the condition that the radiation filling the crystal aperture  $W$  makes an angle with the lattice within the rocking curve angle  $w_c$ , can also be written:

$$f_{no} = \frac{W \sin\theta}{R \sin\theta} = \frac{W}{R} \quad (2.24)$$

## 2. Optimisation for Small X-Ray sources

It is clear from the above equations that as the source size becomes smaller, the waveband will reduce linearly unless the Rowland Circle can also be reduced. There comes a point, at  $R = 150\text{mm}$  in the present study, where the reduction of the RC will become difficult to achieve with a crystal bending device. It is then likely to reduce the instrumental resolving power without increasing the waveband. To observe small x-ray sources of less than 1mm diameter, like laser produced plasmas, the spectrometer is used in the de-focus mode by moving the source inside the Rowland Circle. For the case of a point source at B in Figure 2.10, a distance  $b$  from the crystal, it is clear that it subtends a larger angle (and therefore waveband) from the crystal than at the corresponding point A on RC. Assuming the condition  $R \gg W$ , the angle  $\phi$  is:

$$\phi = \frac{W \sin\theta}{b} \quad (2.25)$$

However, the Bragg angle range  $\Delta\theta$  is less than  $\phi$  because of the concave crystal curvature between DE. This can be shown clearly by looking at the Bragg angle of a pencil ray diffracting at the points C, D and E. The angle between the tangent to C and BC is the Bragg angle  $\theta$ . The point D should make the highest angle and so the ray from BD intersects with the tangent to D at:

$$\theta_2 = \theta + \frac{\phi}{2} - \frac{W}{2R} \quad (2.26)$$

## Waveband for Different Source Geometries

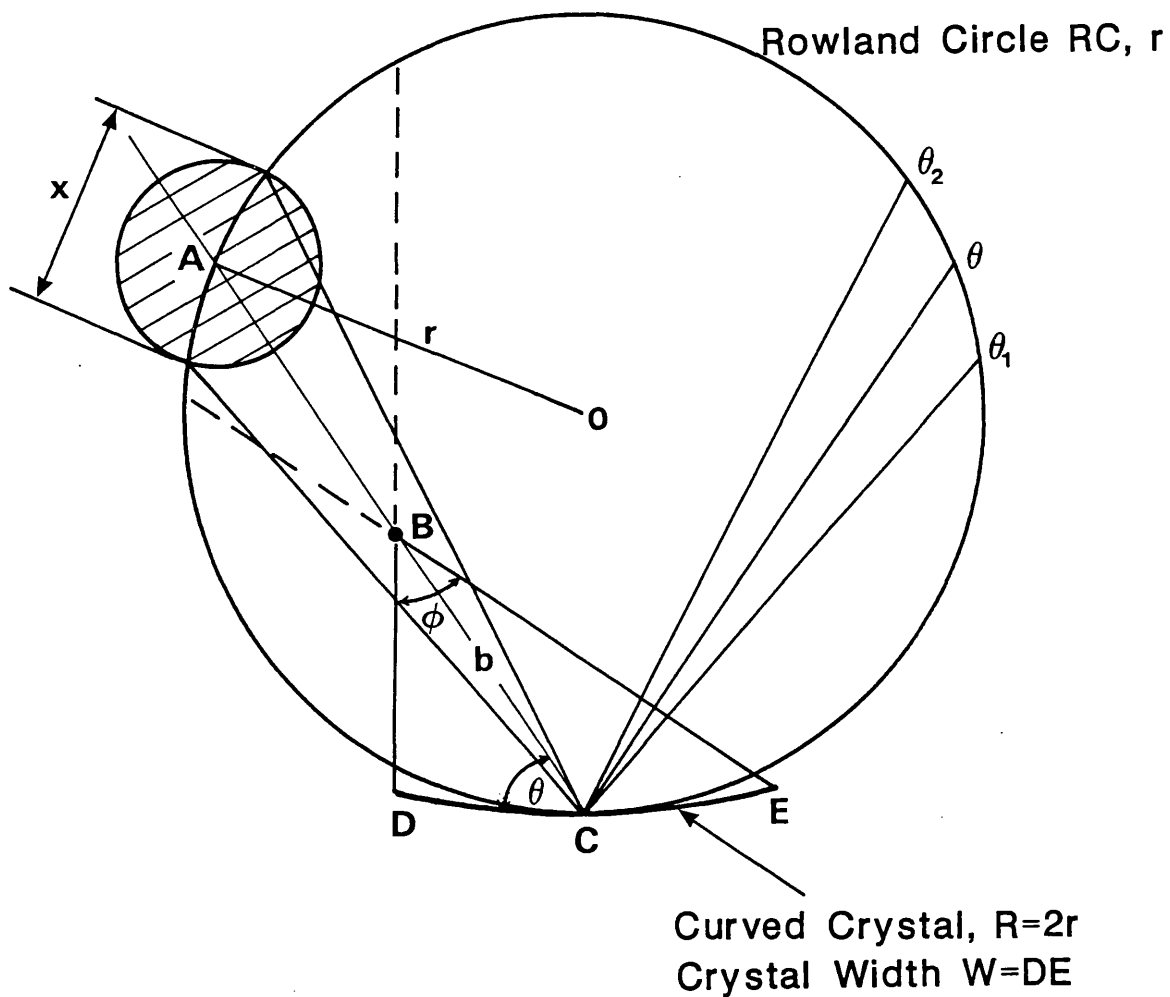


Figure 2.10 Optimising waveband for different source geometries with a Johann spectrometer. Diffuse source A of spatial extent  $x$  defines waveband. Point-like source B must be placed within the RC to achieve useful waveband.

## Waveband for Spectrometer in De-focused Mode

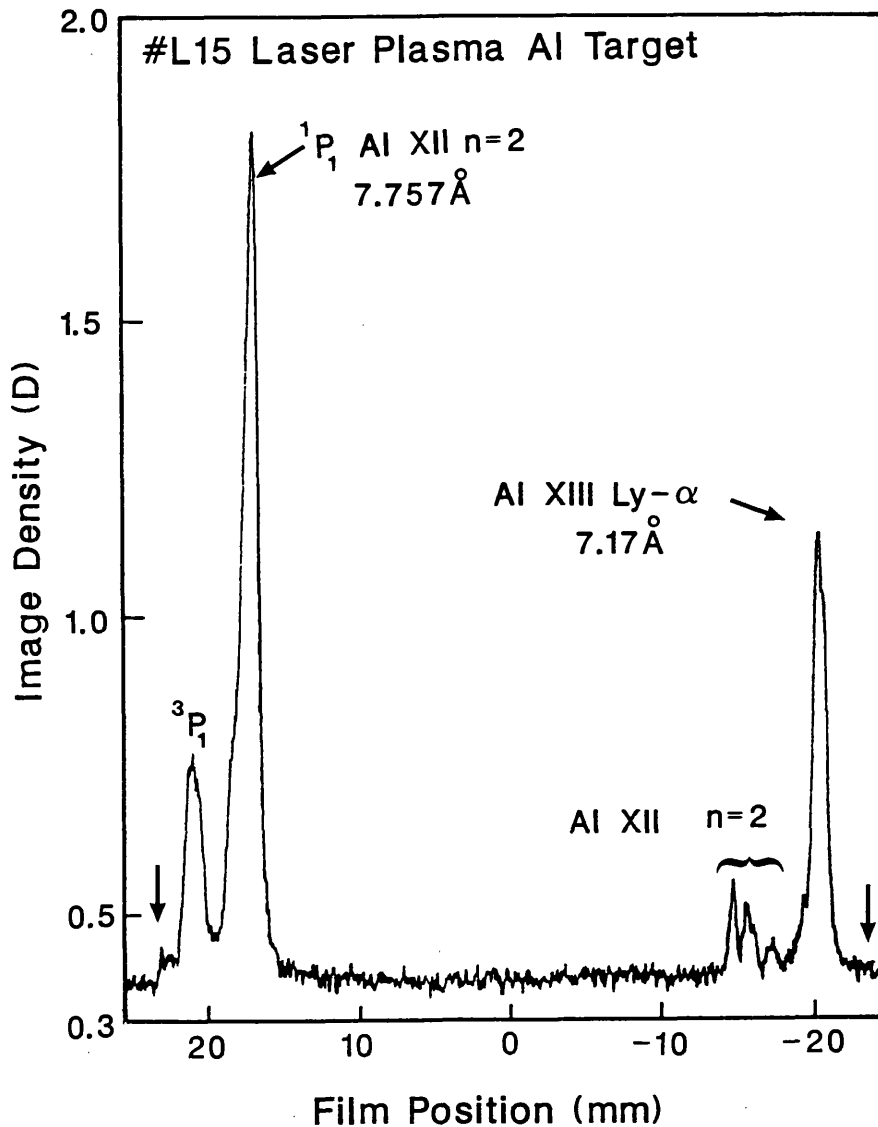


Figure 2.11 The recorded waveband using the Johann spectrometer in de-focus mode for a small laser produced plasma source. The waveband is determined from continuum intensity on the short wavelength side of the Al XIII Ly- $\alpha$  at 7.17 Å and the long wavelength side of the Al XII 2p  $^3P_1$  intercombination line at 7.80 Å. The arrows indicate waveband limit, though the short wavelength side does not have good contrast with background noise.

Similarly at point E, the lowest Bragg angle is increased due to the curved nature of the crystal by:

$$\theta_1 = \theta - \frac{\varphi}{2} + \frac{W}{2R} \quad (2.27)$$

Bragg angle range  $\Delta\theta$  is:

$$\Delta\theta = \theta_2 - \theta_1 = \varphi - \frac{W}{R} \quad (2.28)$$

The above result is verified by allowing the point source to approach the Rowland Circle. Neglecting finite effects due to the crystal diffraction width, then as expected  $b \rightarrow R \sin\theta$  and so  $\Delta\theta \rightarrow 0$ .

Another modification is the replacement of a point source with a finite source of dimension  $x$ . This will change the Bragg angle range almost in proportion to  $x$ . Assuming that the source presents a uniform cross section perpendicular to the crystal and  $R \gg W$  so that  $BD=BC=BE$ , then the additional contribution to  $\Delta\theta$  is  $\Delta\varphi$  where:

$$\Delta\varphi = \frac{x}{b} \quad (2.29)$$

By letting  $b$  increase to the RC we get the value obtained in equation (2.22). The total Bragg angle range  $\Delta\theta$  can be written:

$$\Delta\theta = \frac{W \sin\theta}{b} - \frac{W}{R} + \frac{x}{b} \quad (2.30)$$

It can be noted that a consequence of the increased waveband is reduced sensitivity. The full crystal aperture  $W$  is no longer diffracting the incremental wavelength  $\delta\lambda$ , but is multiplied by a factor  $\kappa \leq 1$  which falls more rapidly than  $b/R \sin\theta$ . The principle for reflection, stated earlier requires the incident radiation to be within the diffraction width  $w_c$  of the crystal for Bragg's law to be satisfied. Ray tracing techniques show that the angle of incidence satisfies  $\delta\theta \leq w_c$  for a small fraction of the crystal width for  $b$  less than the chord length  $R \sin\theta$ . This problem, like the Johann width aberration, is due to the crystal not lying on the Rowland Circle. This effect is not expected to happen with the perfectly focusing geometry of the Johansson type spectrometer.

### 3. Experimental Verification.

The above equation (2.30) is verified by looking at experimental results for a laser produced plasma. The spectrum, shown in Figure 2.11, #10 15/12/87 L15 is a record of the  $n=2$  transitions of H- and He-like Aluminium generated by irradiating a solid target with an intense  $2\omega$  (green) laser beam. The illuminated area on the film, as measured by the continuum emission on either side of the two resonance lines, is 47.5mm in the plane of dispersion, neglecting the departure of the flat film plate from the Rowland Circle. For a crystal curvature of  $R=300\text{mm}$  the measured Bragg angle range is  $\Delta\theta=0.158\text{rad}$ . The spectrometer and source parameters are:

Crystal curvature radius:	R	300mm
Crystal width:	W	26 ± 1mm
Source/crystal separation:	b	90mm
Mean Bragg angle:	θ	59.7°
Source dimensions:	x	Ø50µm

Putting the values into the equation for  $\Delta\theta$  gives  $0.158 \pm 0.006$ rad. This agrees very well with the measured result, the main error arising from the approximate crystal aperture setting. It can be noted that the contribution to the angle range from the small source dimensions is almost negligible, the x-ray emission being well approximated to a point source. Finite sources like beam-foil targets with  $x=\text{Ø}4$ mm have also given good agreement with the above derivation.

### 2.3.2 Sensitivity.

The sensitivity equation for a Johann instrument can be written as (from Barnsley et al<sup>25</sup>) the total signal N (photons) recorded by the detector in an observation period t over the band  $\Delta\lambda$ :

$$N = \kappa \frac{W}{R} \psi_y R R_c \sin\theta H \eta_\lambda t \left[ \frac{E_\lambda \Delta z}{4\pi} \right] \quad (2.31)$$

where W, H are the the crystal width and height dimensions respectively. R is the crystal radius,  $\psi_y$  is the angle subtended by the source perpendicular to the dispersion plane,  $R_c$  is the crystal integrated reflectivity,  $\eta_\lambda$  describes the detector and filter efficiency,  $E_\lambda$  is the plasma emissivity (photons  $\text{cm}^{-3}\text{s}^{-1}$ ) and  $\Delta z$  is the plasma depth. The assumption that the source is dimensionally large enough to observe the specified band  $\Delta\lambda = \lambda_2 - \lambda_1$ , for chosen diffractor width W and radius R, must hold. The wavelengths  $\lambda_1, \lambda_2$  correspond to angles  $\theta_1, \theta_2$  respectively on the Rowland Circle such that in the optimum situation the sagittal field angle  $\psi_x$  may be defined as:

$$\psi_x = \theta_2 - \theta_1 \quad (2.32)$$

In this case, as can be seen from equation (2.31), R can be cancelled completely, indicating that the signal sensitivity to emissivity ratio is independent of R. The R-dependence is in fact contained in the other variables. As stated in section 2.3.1, the parameter  $\kappa$  is introduced to modify the instrument f-number ( $= W/R$ ), and therefore the sensitivity, where the source spatial dimensions do not satisfy the bandpass considerations. It can be written as:

$$\kappa = \frac{\psi_x}{\theta_2 - \theta_1} \quad (2.33)$$

This effect should not be ignored as the value of  $\kappa$  may be small ( $0.1 \rightarrow 0.005$ ) for the instrument used in "de-focused" mode with laser plasma sources. The monochromatic sensitivity should be maximised by placing the source in the correct position for the specified bandpass.

### 2.3.3 Dispersion Relation.

#### 1. Curved Detector on Rowland Circle.

If the curved photographic film or position sensitive detector lies exactly on the RC, then it can be trivially shown that any position on RC a distance  $\delta x$  from the fiducial position  $x_0$ , corresponding to the setting angle  $\theta_0$ , for wavelength  $\lambda_0$ , subtends an angle  $\delta\theta$  from the crystal pole where:

$$\delta x = R \delta\theta \quad (2.34)$$

The wavelength increment  $\delta\lambda$ , ignoring refractive index effects and higher orders for the moment, corresponding to  $\delta\theta$  can be expressed as:

$$\delta\lambda = 2d \cos\theta \delta\theta \quad (2.35)$$

from equation (2.4). The plate factor D, otherwise known as the inverse linear dispersion, can be defined from (2.34) and (2.35):

$$D = \frac{\delta\lambda}{\delta x} = \frac{2d \cos\theta}{R} \quad (2.36)$$

and the Bragg equation for  $\lambda_1 = \lambda_0 + \delta\lambda$ :

$$\lambda_1 = 2d \sin \left[ \theta_0 + \frac{\delta x}{R} \right] \quad (2.37)$$

#### 2. Flat Detector Tangential to the Rowland Circle.

For a flat tangential detector touching the Rowland circle at one point, see Figure 2.12, the position  $\delta x$ , from the fiducial point  $x_0$ , on the detector corresponding to an angle  $\delta\theta$  is:

$$\delta\theta = \tan^{-1} \left[ \frac{\delta x \sin\theta'}{R \sin\theta_0 + \delta x \cos\theta'} \right] \quad (2.38)$$

where  $\theta'$  is the tangential angle of rotation and  $\theta_0$  is the reference angle corresponding to  $x_0$ . The convention is adopted where  $\delta x$  is positive if it is to the long wavelength side of  $x_0$  and negative for the short wavelength side. The simple Bragg law is written:

$$n\lambda_1 = 2d \sin(\theta_0 + \delta\theta) \quad (2.39)$$

#### 3. Experimental Verification.

A spectrum with a suitable number of identified resonance lines was analysed in some detail to verify the derived expression for the spectrometer dispersion. Figure 2.13, a DITE Tokamak spectrum #20 22/5/86, shows strong x-ray lines in the 6.6→7.2Å waveband emitted from intrinsic Magnesium, Silicon impurities and laser ablated Aluminium.

## Schematic of Flat Detector Tangential to Rowland Circle

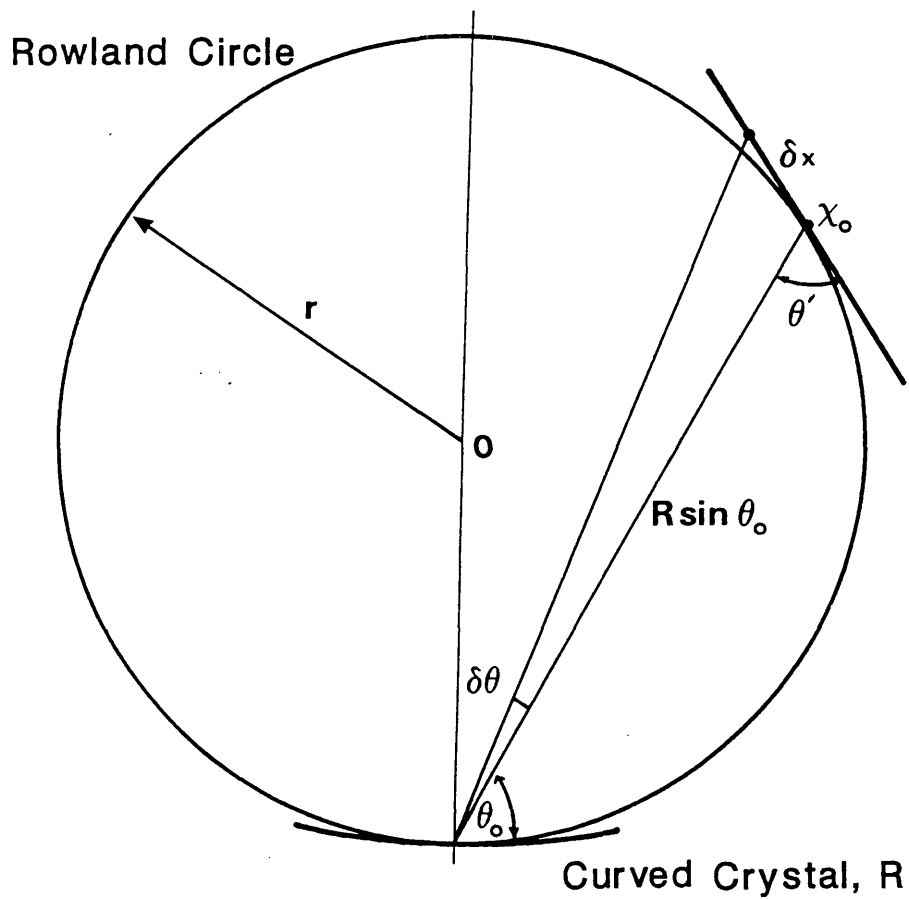


Figure 2.12 Flat detector plate tangential to the Rowland circle.

DITE Spectrum #20 for Dispersion Check

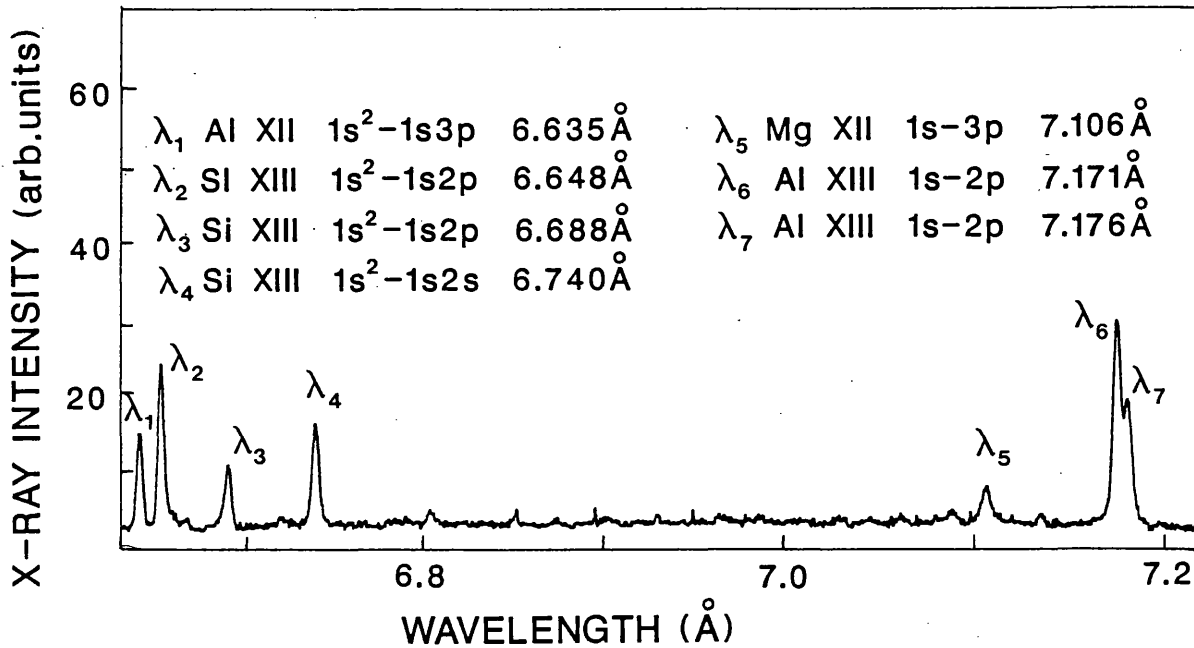


Figure 2.13 DITE spectrum #20 for the 6.6→7.2Å waveband emitted from intrinsic Magnesium XII, Silicon XIII impurity ions and Aluminium XII and XIII ions from laser ablation. The theoretical wavelengths in Table 2.2 can be compared with the values calculated from the dispersion equation.

The resolved lines labelled  $\lambda_1 \rightarrow \lambda_7$  in Table 2.2 as well as adjacent unresolved lines were assigned wavelengths from Drake<sup>26</sup>, Mohr<sup>27</sup> and Garcia and Mack<sup>28</sup>. The unresolved components were carefully considered:

- The Al XII  $1s^2 \ ^1S_0 - 1s3p \ ^3P_1$  resonance line is blended with  $\lambda_2$  but is expected to be weak.
- The Si XIII  $1s^2 \ ^1S_0 - 1s2p \ ^3P_2$  line, blended with  $\lambda_3$  with an intensity ratio of 1:5 (from later spectra with higher resolution) and contributing line centroid shifts of less than 0.1mÅ.
- The Mg XII  $1s \ ^1S_{1/2} - 4p \ ^2P$  resonance line occurs close to  $\lambda_4$  and has ~40% the intensity of the resolved Mg XII  $1s \ ^1S_{1/2} - 3p \ ^2P$  line at 7.1Å.
- Mg XII 1s-3p line has an unresolved fine structure component which is assumed to be statistically weighted 2:1 for  $^2P_{3/2}; ^2P_{1/2}$ . The two components were modelled with Gaussian profiles for a range of spectral resolution and a mean value adopted.
- The Al XIII Lyman- $\alpha$  doublet profiles were modelled with Gaussians and it was shown that for spectral resolution of 1:1800 the measured line centroids were shifted slightly together. This was taken into account in Table 2.2.

Low intensity Iron L-shell emission was expected to have little effect on the reference line centroids. Low intensity satellite structure to the He-like Al and Si lines could be neglected because:

- The line intensity is low, scaling with atomic number as  $Z^4$ .
- The plasma temperature  $T_e$  is high from additional heating.

The theoretical wavelength values in Table 2.2 are accurate to better than 0.05mÅ (7ppm). The line positions on film, listed in the last column of Table 2.2, relative to the reference mark defining the setting Bragg angle  $\theta_0$ , were carefully determined using a plate measuring instrument with digital readout accurate to  $\pm 5\mu\text{m}$ . They were also confirmed by measurements from a calibrated densitometer. Repeated measurements allowed the mean values of the strongest lines to have a tolerance approaching the readout accuracy, but the other lines like  $\lambda_5$  with low S/N were a factor of three higher. An upper limit of  $\pm 20\mu\text{m}$  (corresponding to 0.15mÅ) was estimated for the line position accuracy. (This could be improved by digitising the film in 2-D onto computer and compressing to 1-D to improve the S/N ratio by a factor of five).

Most of the spectrometer parameters needed in the dispersion relation were determined during the alignment procedure. These were the crystal radius  $R=1200\pm 1\text{mm}$ , the setting Bragg angle  $\theta_0=40.5^\circ$  and the detector angle tangent to the Rowland Circle  $\theta'=40.5^\circ$ . (These two angles should be identical with a tolerance of 1 or 2 minutes of arc, but they are independent variables and have a different effect on the dispersion function).

A literature search for the lattice spacing of the crystal used in the experiment, Ammonium Di-Hydrogen Phosphate ADP (101), gave three values. These were experimental

measurements by Deslattes et al<sup>29</sup>, Blake et al<sup>30</sup> of  $2d=10.640\text{\AA}$  and Wyckoff<sup>31</sup> of  $2d=10.658\text{\AA}$ , see Chapter 8. The values differed by 1 part in 500, ostensibly too large an error for checking the dispersion accurately.

It may be noted that ADP is a synthetic, inorganic crystal where the properties would be dependent on the growing conditions to a greater degree than crystals of high purity Silicon and Germanium. The refractive index of  $\delta\lambda^2=(2.40\pm 0.24) \times 10^{-6}\text{\AA}^{-2}$  was calculated from section 2.1.

The five parameters  $R$ ,  $\theta_0$ ,  $\theta'$ ,  $2d$  and  $\delta\lambda^2$  were used in the dispersion equations (2.8), (2.38) and (2.39) and optimised within the given tolerances to fit the line positions by method of least squares to the theoretical wavelengths of Table 2.1. Several important points were found to hold:

- (a) A minimum for the least squares could always be found for a combination of fixed or floating parameters with the exception of (c) below.
- (b) The mean wavelength discrepancy from theory was  $\delta\lambda=0.17\text{m\AA}$  (25ppm) and the values for  $\lambda_1 \rightarrow \lambda_7$  remained stable to  $\pm 0.05\text{m\AA}$  even when only two line positions were used in the fit instead of the seven.
- (c) The  $2d$  spacing, when allowed to vary, consistently gave a value of approximately  $10.66\text{\AA}$ . When held fixed at  $10.6402\text{\AA}$ , no minimum was found and the resultant wavelength discrepancy was about two orders of magnitude greater than (b). The lattice spacing of  $10.658\text{\AA}$  was therefore chosen.
- (d) A tolerance of  $\pm 10\%$  in the refractive index  $\delta\lambda^2$ , introduced a small change of  $\pm 0.015\text{m\AA}$  (about 2ppm) for  $\lambda_1 \rightarrow \lambda_7$ . This was negligible when compared with the errors in (b) above.

Table 2.3 shows the results of the optimised dispersion curve, giving the spectrometer parameters and wavelengths corresponding to the line positions. The numbers in brackets show the wavelength discrepancy, in  $\text{m\AA}$ , from the theoretical values of Table 2.2. The third column shows the stability of the measured wavelengths when only two line positions are used in the optimisation fit. The accuracy of the measured wavelengths, using two lines as references, was mainly limited by the statistical errors in the line positions and unresolved lines in  $\lambda_4$  and  $\lambda_5$  for example.

The data above has demonstrated the strength of using the geometrical expression for calculating the dispersion function. Knowledge of the spectrometer parameters from the crystal alignment and focusing procedure is crucial in this regard. The achieved result also confirms the high accuracy of the crystal curvature which affects the observed spectral resolution and dispersion equally.

More precise wavelength measurements, of interest for the work of Chapter 7, could be obtained by a combination of the following:

- (a) Higher spectral resolution, revealing the extent of unresolved lines.

**Table 2.2 Theoretical wavelengths and corresponding measured line positions for DITE#20**

Line	Identification		Wavelength Å		Adjusted Wavelength (Å)	Position (mm)
$\lambda_1$	Al XII $1s^2 1S_0 - 1s3p 1P_1$	§	6.63476		6.63476	$-41.020 \pm 0.007$
	Al XII $1s^2 1S_0 - 1s3p 3P_1$	§	6.64468			
$\lambda_2$	Si XIII $1s^2 1S_0 - 1s2p 1P_1$	§	6.64795		6.64795	$-39.270 \pm 0.005$
	Si XIII $1s^2 1S_0 - 1s2p 3P_2$	§	6.68499			
$\lambda_3$	Si XIII $1s^2 1S_0 - 1s2p 3P_1$	§	6.68819		6.68819	$-33.834 \pm 0.011$
	Mg XII $1s 2S_{1/2} - 4p 2P_{3/2}$	†	6.73775	◇		
	Mg XII $1s 2S_{1/2} - 4p 2P_{1/2}$	†	6.73819	◇		
$\lambda_4$	Si XIII $1s^2 1S_0 - 1s2p 3S_1$	§	6.74029		6.74029	$-26.782 \pm 0.005$
$\lambda_5$	Mg XII $1s 2S_{1/2} - 3p 2P_{3/2}$	†	7.10577	•	7.10614	$+27.531 \pm 0.017$
	Mg XII $1s 2S_{1/2} - 3p 2P_{1/2}$	†	7.10691	•		
$\lambda_6$	Al XIII $1s 2S_{1/2} - 2p 2P_{3/2}$	‡	7.17091	*	7.17096	$+37.961 \pm 0.004$
$\lambda_7$	Al XIII $1s 2S_{1/2} - 2p 2P_{1/2}$	‡	7.17632	*	7.17616	$+38.820 \pm 0.007$

**Key:**

- § Drake<sup>26</sup>. The estimated error due to higher order uncalculated terms is 0.3ppm.  
NB: Drake's previous calculations for the transition frequencies of He-like ions differed from the above by a systematic factor of 1.4ppm.
- † Garcia and Mack<sup>28</sup>.
- ‡ Mohr<sup>27</sup>. The values for Al Ly- $\alpha$  agree to 0.3ppm.
- ◇ The Mg XII 1s-4p lines were modelled to give a mean value of 6.73790Å.
- Similarly, the ratio of the Mg XII 1s-3p  $P_{3/2}:P_{1/2}$  was expected to be 2:1. The two lines were modelled with Gaussian functions and by averaging the results for spectral resolution ranging from 1300 to 1700 gave a mean value of  $\lambda=7.10614\text{Å}$ .
- \* The Al XII Ly- $\alpha$  doublet was modelled with Gaussians, as above, where a shift in the centroid of each line was found and adjusted accordingly.

**Table 2.3 Results from Optimised Dispersion Curve.**

Parameter	Fitting Results			
	7 Line Fit		2 Line Fit	
	$\delta\lambda$ (mÅ)		$\delta\lambda$ (mÅ)	
$\theta_0$ (°)	40.55		40.55	
$\theta'$ (°)	40.47		40.60	
2d (Å)	10.658 <b>F</b>		10.658 <b>F</b>	
$\delta/\lambda^2$ (Å <sup>-2</sup> )	$2.40 \times 10^{-6}$ <b>F</b>		$2.40 \times 10^{-6}$ <b>F</b>	
R (mm)	1199.0		1201.0	
$\lambda_1$	6.63480	(0.04)	6.63476	(0)
$\lambda_2$	6.64795	(0.002)	6.64790	(-0.05)
$\lambda_3$	6.68839	(0.20)	6.68834	(0.15)
$\lambda_4$	6.73998	(-0.31)	6.73993	(-0.36)
$\lambda_5$	7.10636	(0.22)	7.10638	(0.24)
$\lambda_6$	7.17086	(-0.09)	7.17092	(-0.04)
$\lambda_7$	7.17610	(-0.06)	7.17616	(0)
Mean Square Difference, $\Delta\lambda$	0.17mÅ		0.18mÅ	

This table shows the wavelength results from optimising the spectrometer parameters in the dispersion equation, based on the theoretical wavelengths of Table 2.2 and their respective measured line positions. See the text for parameter description.

The second column shows optimum fit for parameters and wavelengths from measured line positions.

The third column in parentheses in units of mÅ, gives the discrepancy with theory.

The mean square wavelength discrepancy  $\Delta\lambda$  is 0.17mÅ shown in the last row.

The fourth and fifth columns show the stability of the measured wavelengths when only two wavelengths  $\lambda_1$ ,  $\lambda_7$  are used in the fit.

N.B: **F** beside 2d and  $\delta/\lambda^2$  refers to fixed parameter.

- (b) Crystal properties would have to be known more exactly. For crystals not described in the literature, calibration on the 2-crystal spectrometer instrument at Leicester would be worthwhile.
- (c) Improved rotation stages and crystal alignment for accurate spectrometer parameters.

### 2.3.4 Instrumental Resolving Power.

The crystal resolving power was defined earlier in equation (2.5). A similar function may be defined for the instrumental resolving power where the total angular resolution of the spectrometer  $\Delta\theta$  replaces  $w_c$  in equation (2.5). Usually  $\Delta\theta$  is determined by the main components of the instrument where  $\Delta\theta_1=w_c$ ,  $\Delta\theta_2$  denote the crystal rocking curve width and the angular resolution of the detector system, respectively. The chosen crystal depends on the waveband of interest while the latter is defined by the inherent spatial resolution  $\Delta x$  of the detector and its distance from the crystal:

$$\Delta\theta_2 = \frac{\Delta x}{R \sin\theta} \quad (2.40)$$

For photo-electric detectors,  $\Delta\theta_2$  may only be reduced to an acceptable level by increasing the crystal radius  $R$ . No restrictions are needed on  $R$  for the use of photographic film with high spatial resolution.

There are further contributions to  $\Delta\theta$  due to a variety of focusing and geometrical effects. The most significant is the quality of the generated crystal curvature or x-ray focus  $\Delta\theta_3$ . This can be measured directly (see Bitter et al<sup>32</sup>) or equally can be interpreted from the optical focus in visible light. Discussion of this point is reserved to Chapter 3.

#### Johann Aberrations

These focusing defects, labelled as the width and height errors, arise from the interaction of the x-ray source and the Johann geometry. The crystal does not remain tangential to the Rowland circle at all points and thus is not perfectly focusing. The deviation from RC increases with crystal width, and the associated focusing error defined by Johann<sup>1</sup> is:

$$\Delta\theta_4 = \frac{W^2}{8R^2 \tan\theta} \quad (2.41)$$

The width error  $\Delta\theta_4$  is often misinterpreted as an angular width, whereas in fact it is an angular displacement to the short wavelength side of the line. A convolution of the spectral profile with each crystal element over the total width would be needed to calculate the overall broadening effect. Since  $\Delta\theta_4$  is proportional to  $W^2$ , more than half of the peak intensity is within  $\Delta\theta_4/4$  and this may be a better estimate. The crystal radius may also be increased to reduce the width error. The Johansson geometry has perfect focusing and therefore the width error is ignored.

The Johann height error is due to the superposition of a series of parabolic line foci displaced vertically; each parabola is associated with an incremental point source perpendicular to the plane of dispersion. This may be illustrated in Figure 2.14 where  $\Delta x$  is the line broadening first reported by Johansson. Assuming the detector, crystal and source are all the same height  $H$ , then the height error may be written as:

$$\Delta\theta_5 = \frac{H^2}{8R^2 \sin\theta \cos\theta} \quad (2.42)$$

Sandström<sup>33</sup> makes an estimate of this effect for general crystal geometries. He states that the radius of curvature  $\rho$  of the reflected beam at the detector plane is due to the law of selective reflection of monochromatic radiation from a point source at A, illustrated in Figure 2.15. This may be written:

$$\rho = (l + a) \cos\theta \quad (2.43)$$

where  $l$  is the crystal/detector separation and  $a$  is the crystal/source separation. For two point sources displaced vertically by a distance  $h$ , a lateral displacement  $b$  of the curves in the plane of dispersion is noted where:

$$b = \frac{h^2}{8(l + a) \cos\theta} \quad (2.44)$$

For the Johann geometry,  $l=a=R\sin\theta$  in which case a functional form similar to equation (2.42) can be derived but is a factor of two less than the calculation of  $\Delta\theta_5$ . It is not obvious where this discrepancy arises from.

It may be noted that the curvature is towards the long wavelength side. For small point-like laser plasma sources, the crystal height aberration is negligible and the spectral line curvature is clearly visible;  $\rho$  decreases with increasing  $\lambda$ . Diffuse Tokamak sources should be considered carefully as  $\Delta\theta_5$  is likely to be larger than  $\Delta\theta_4$  and may need aperturing of the source or crystal height.

The error due to the tangential film plate deviating from RC at all points except the film pole will be greatest for the extreme long and short wavelength limits. If the overall length of the tangential plate is  $x$ , then the greatest angular divergence  $\Delta\theta_6$  will depend on the instrument f-number  $W/R$  where:

$$\Delta\theta_6 = \frac{x^2 W}{8R^3 \sin^2 \theta} \quad (2.45)$$

Similarly, a defocusing error  $\Delta\theta_7$  will occur if the film pole is displaced by an amount  $\Delta d$ , where the crystal/film separation is  $d=R\sin\theta$ :

$$\Delta\theta_7 = \frac{\Delta d W}{d R} = \frac{\Delta d W}{R^2 \sin\theta} \quad (2.46)$$

It may be noted that other defocusing errors, setting angle misalignment or finite depth effects in MWPC for example, may be calculated from the equations listed above.

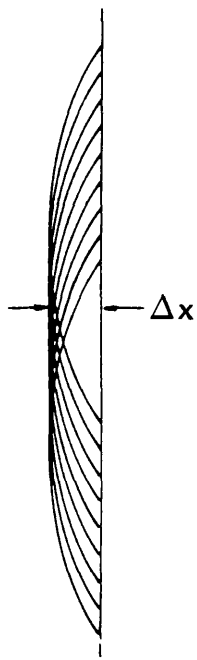


Figure 2.14 Each curve shown here represents the same wavelength but from a different part of the source perpendicular to the plane of dispersion. The superposition of all curves leads to a broadening  $\Delta x = R\Delta\theta_s$ , which depends on the crystal height, radius and Bragg angle.

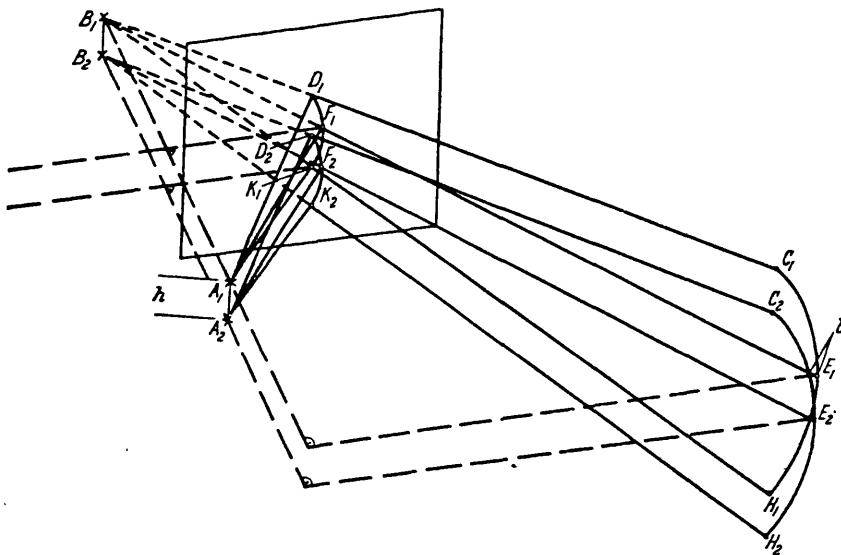


Figure 2.15 Sandström<sup>33</sup> gives a schematic of the influence of the source/crystal height on the width and shape of the x-ray line. Note that the observed line curvature indicates a similar crystal diffraction area for monochromatic rays. Broadening of lines will decrease as source/detector separation increases.

## 2.4 Conclusions.

It can be concluded that the Johann spectrometer may be optimised for high resolving power with good signal throughput. It has the advantage over other spectrometer geometries of requiring no aperture stop, thus not incurring a loss of sensitivity. This is in addition to simultaneous observation over the specified bandpass.

For Tokamak plasmas, the waveband is limited by the viewing port dimensions,  $\varnothing 100\text{mm}$  for DITE, and crystal radius  $R \sim 1000\text{mm}$  from resolving power considerations below. The maximum useable waveband is  $\lambda/\Delta\lambda = 0.05 \rightarrow 0.09$  and requires a detector of length  $\sim 100\text{mm}$ .

The dispersion function has been derived and shown to give relative wavelength measurements accurate to  $\lambda/\delta\lambda = 4 \times 10^4$  from known spectral lines in the band  $6.6 \rightarrow 7.2\text{\AA}$ . Higher accuracies are possible for adjacent spectral lines in a smaller waveband (see Chapter 8). While the dispersion function is useful for identifying unknown lines, the accurate wavelength calibration is also essential for measuring line widths in profile analysis.

The instrumental resolving power is determined by many factors as shown in section 2.3, and large diffuse sources like Tokamak plasmas present the most serious problems to achieving high spectral resolution. The equations in Chapter 2.3.4 may be used to choose the instrument specification more precisely. The crystal diffraction profile ultimately sets the resolving power, but from Table 4.1 (Chapter 4), crystal examples are available offering  $\lambda/\Delta\lambda \sim 10^4$  in the soft x-ray band  $6 \rightarrow 13\text{\AA}$ . The Johann errors and other defocusing effects may be held low by suitable aperturing of the crystal/source dimension or choice of crystal radius. In this respect, crystal curvature  $R$  must exceed  $1000\text{mm}$ . Using this as the starting point, the following instrument parameters may be suggested:

R	$1300 \pm 1\text{mm}$	associated tolerance is given.
W x H	$20 \times 15\text{mm}^2$	crystal aperture.
x	90mm	total length of tangentially mounted detector.
$\Delta x$	100 $\mu\text{m}$	detector spatial resolution.
$\theta$	$50 \pm 0.167^\circ$	approximate Bragg angle and alignment tolerance.

The associated defocusing errors are:

$\Delta\theta_2$	detector resolution	$\lambda/\Delta\lambda = 1.2 \times 10^4$
$\Delta\theta_4$	Johann width error	$\lambda/\Delta\lambda > 4.8 \times 10^4$
$\Delta\theta_5$	Johann height error	$\lambda/\Delta\lambda = 3.5 \times 10^4$
$\Delta\theta_6$	defocusing at ends of tangential detector	$\lambda/\Delta\lambda = 1.6 \times 10^4$
$\Delta\theta_7$	error in radius setting	$\lambda/\Delta\lambda = 3.2 \times 10^4$
$\Delta\theta_7$	Bragg angle misalignment	$\lambda/\Delta\lambda = 1.3 \times 10^4$

It can be seen immediately that the detector spatial resolution, the crystal diffraction width and the Bragg angle alignment contribute equally to the final instrumental resolving power. The final figure would be a convolution of these angular widths. The resolving power

should be maximised with the following procedures. The error  $\Delta\theta_g$  may be reduced by using the central part of the detector frame. The radius R can be increased if there is no further improvement in the detector spatial resolution or angle alignment. Ultimately, the instrumental resolving power will converge to the limit set by the crystal diffraction width. The other defocusing errors have negligible contribution for the listed spectrometer parameters at the specified  $\lambda/\Delta\lambda=10^4$  level.

The one error so far ignored, which the author feels is the most fundamental to this instrument is the generation of the crystal curvature. The quality of the crystal radius not only affects the resolving power, but has consequences for the dispersion relation and signal throughput. An equally high specification ( $\lambda/\Delta\lambda=4\times 10^4$ ) must be set in line with the other aberrations. The process of choosing the crystal focusing method, alignment and testing are described in Chapter 3.

# Chapter 3 Spectrometer Design.

	Introduction.	44
3.1	Spectrometer Description.	44
	3.1.1 Basic Spectrometer Design.	44
	3.1.2 Vacuum System.	44
3.2	Curved Crystal Devices.	48
	3.2.1 Review of Curved Crystal Methods.	48
	3.2.2 Principle of Four Bar Beam Bending.	49
3.3	The Leicester Crystal Bending Jigs.	52
	3.3.1 Bending Jig Description.	52
	3.3.2 The MarkIII Crystal Bending Jig.	56
3.4	Crystal Focusing and Alignment Procedure.	57
	3.4.1 The Crystal Focusing Procedure.	57
	3.4.2 The Crystal Alignment Procedure.	60
3.5	Optical Testing Procedure.	62
	3.5.1 Objective.	62
	3.5.2 Method.	62
	3.5.3 Focus Quality Interpretation.	66
3.6	Thermal and Mechanical Stability Testing.	67
3.7	Conclusions.	68

## **Introduction.**

In the previous chapter, the Rowland circle geometry was chosen because it satisfied the main objectives of high spectral resolving power and high signal throughput over a useful waveband. This chapter describes:

- The experimental apparatus and specification required for the Johann configuration.
- The four bar crystal bending jig is explained in detail; the principle of operation and its performance are compared to other bending devices.
- The procedures for focusing and aligning the crystal are outlined.
- Methods are devised for testing the thermal and optical stability of the device.

## **3.1 Spectrometer Description.**

Two versions of the spectrometer were designed for use with various laboratory sources and although having different features, both were based on the same principle. A vacuum version was first built, for Rowland circle diameters generally greater than 1m, for observing Tokamak plasmas (see Chapter 5) and was also used with fast ion beam sources (see Chapter 7). The spectrometer in its vacuum system was bolted externally to these x-ray sources. Most of the vacuum chamber, which was an integral part of the spectrometer, was designed by R Barnsley. A second vacuum-less spectrometer for Rowland circles in the range  $R = 0.15 \rightarrow 0.5\text{m}$  was designed for laser produced plasma x-ray sources (Chapter 6) and was mounted inside the laser target chamber, dimensions  $\sim \text{Ø}1\text{m}$ .

### **3.1.1 Basic Spectrometer Design.**

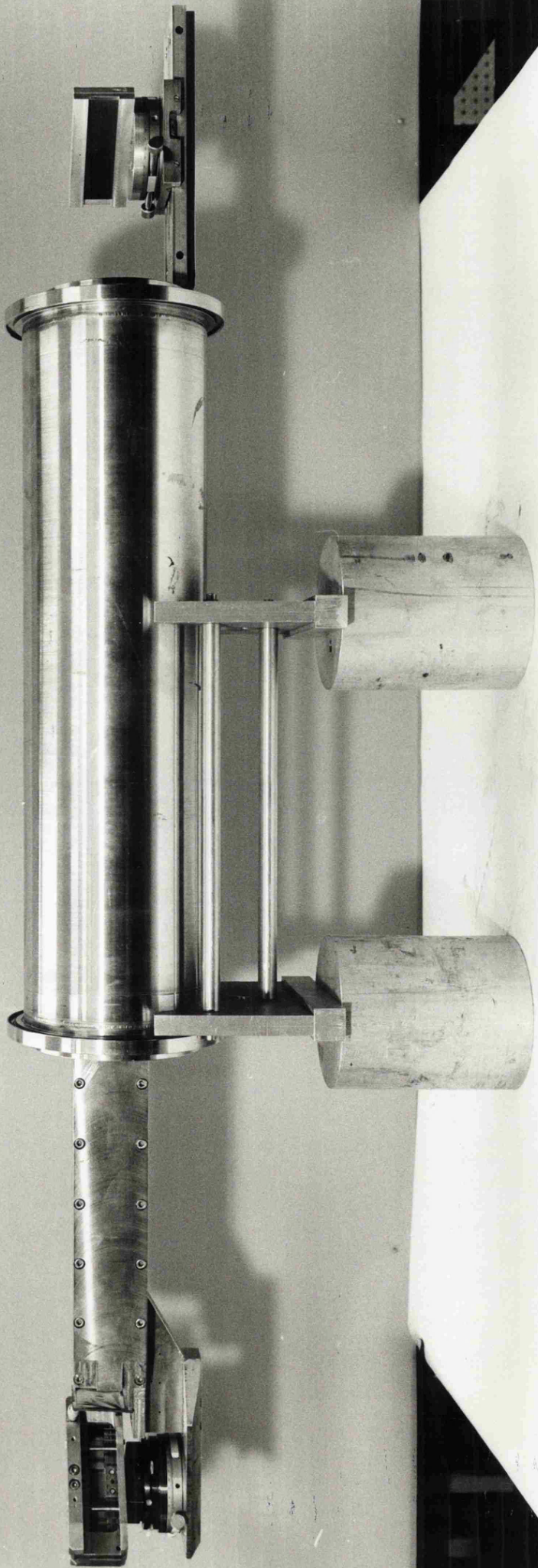
The basic spectrometer consisted of the crystal bending jig and detector/film holder mounted on high precision tilt, translation and rotation stages, supplied by Micro Controle<sup>34</sup>, at opposite ends of a rigid structure. Figure 3.1 is a photograph of the large Rowland Circle vacuum spectrometer. For the large spectrometer, this was a rigid steel tube of internal diameter 150mm by 600mm long and 4mm wall thickness, which also formed part of the vacuum system. This provided good mechanical stability and allowed the crystal to be focused and aligned on a flat metrology bench prior to placing in the main chamber. The small instrument, see Figure 3.2, used a commercial Ealing "continuous cast" Iron triangular optical bench<sup>35</sup> for the spectrometer structural support.

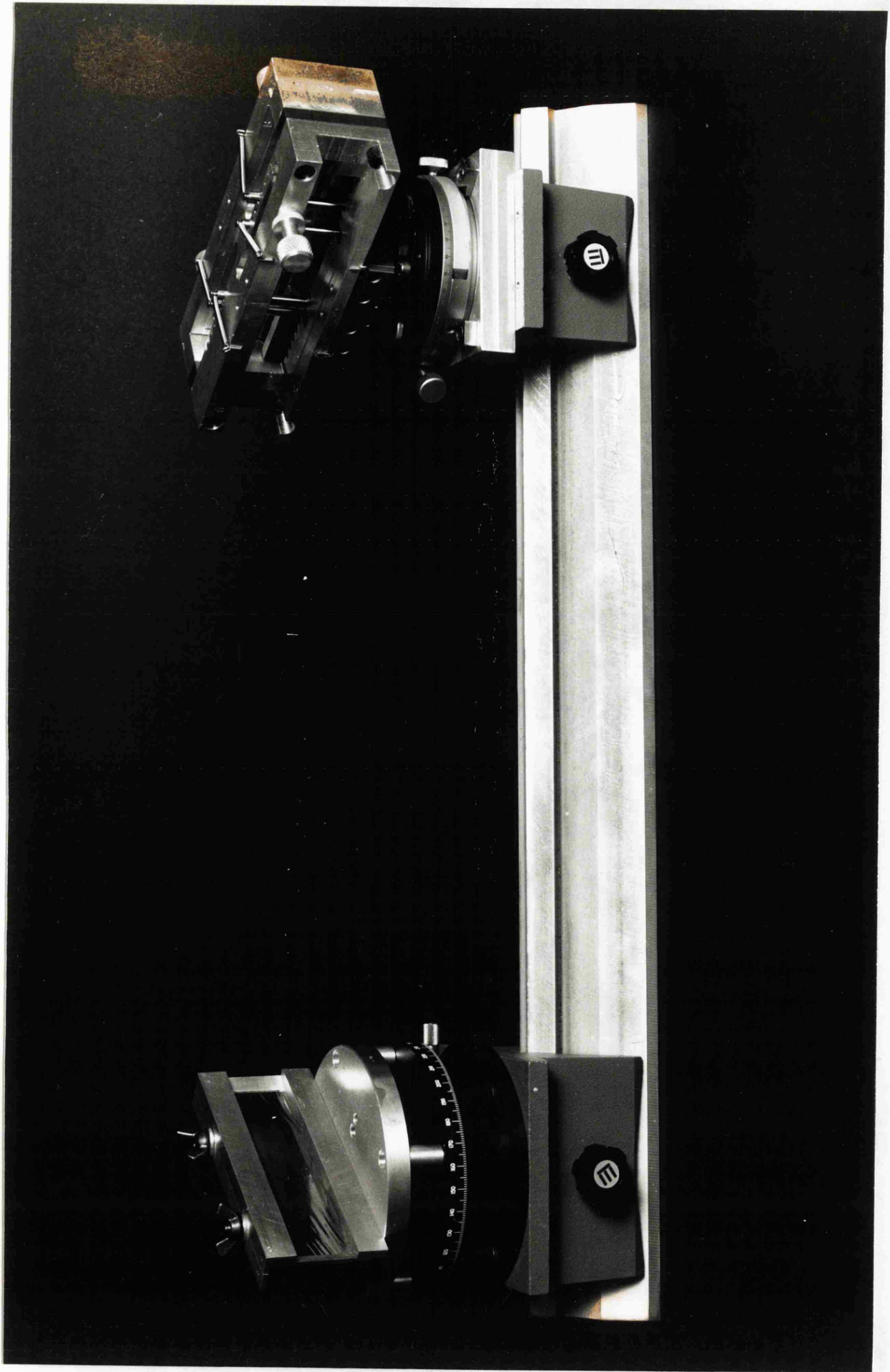
### **3.1.2 Vacuum System.**

The main chamber for the vacuum version consisted of a ported cylinder having two Ø100mm ports for observing the source and two Ø150mm ports angled at 10° and 30° for receiving the spectrometer tube. The crystal was then aligned with the source using the flexible bellows as indicated in Figure 5.4. The combination of angled ports, which could be re-configured relatively easily, allowed a range of Bragg angles from 24°→66°. Access to

Figure 3.1 The vacuum version of the Johann spectrometer is shown in the photograph (next page). The vacuum tube gives the spectrometer its structural rigidity; the crystal and detector platforms are mounted directly from the tube. The crystal bending jig is mounted to platform via the alignment stages. The detector platform, beside the spectrometer, is normally mounted inside the tube. The cradle holding the rotation stage and film plate, can be positioned onto the Rowland Circle by the slide mechanism.

Figure 3.2 (on the page after next) indicates the vacuumless version for laser plasma x-ray sources. The features are as described in Figure 3.1 except the triangular optical bench replaces the vacuum tube for structural support.





the spectrometer when in situ could be achieved via the large top and bottom lids. The tank was evacuated by a turbo-molecular pump bolted onto the unused 150mm port. A second set of bellows gave radial scans of DITE, Figure 5.4, (Chapter 5), though most results presented here were for central chord measurements.

The sightline to the Tokamak was separately pumped and isolated from the spectrometer tank vacuum by a thin unsupported window; 2 $\mu\text{m}$  Mylar for an observation waveband  $\lambda < 10\text{\AA}$  and 1 $\mu\text{m}$  Polypropylene for  $\lambda > 10\text{\AA}$ . A hand valve allowed the spectrometer to be brought up to atmosphere without disturbing the sightline pressure. Under typical operating conditions, the sightline pressure was  $10^{-8}$ Torr and the spectrometer tank pressure was  $10^{-6}$ Torr. Although the vacuum was several orders of magnitude lower than that needed for x-ray transmission, the main criterion was to limit the influx of impurities into the Tokamak vacuum vessel. These may affect the performance of the plasma and lead to disruptions.

Such vacuum considerations were not necessary for the laser experiment target chambers where  $10^{-3}$ Torr was the usual pressure, improved to  $10^{-5}$ Torr if micro channel plate detectors or streak cameras were being operated.

## **3.2 Curved Crystal Devices.**

The performance of the Johann type spectrometer is critically dependent on generating a cylindrically curved crystal, to a high tolerance, in the plane of dispersion. It is immediately obvious that the instrumental resolving power suffers as a consequence of a poor quality or incorrect crystal curvature, but equally affected are both the wavelength dispersion and the signal intensity. Therefore, it is essential to use the best method available for forming curved crystals. It is worth reviewing the range of methods at this stage.

### **3.2.1 Review of Curved Crystal Methods.**

Broadly speaking, curved crystals devices employed by various laboratories world-wide in the last 50 years fall into two categories:

- Beam bending devices, where the crystal is bent between three or preferably four bars to the desired curvature.
- Formers, where the crystal is held or glued against one or two machined mandrils of exact curvature.

(Not all curved crystals fall into these two broad categories; for example a crystal cantilever principle<sup>36</sup> can be used). Both methods are common as shown by the following examples.

#### **Crystal Beam Bending Devices for Johann Geometry.**

The main high resolution spectrometers, where  $\lambda/\Delta\lambda=15000$  for Fe XXV ion x-radiation at 1.85 $\text{\AA}$ ,  $\lambda/\Delta\lambda=23000$  for Ti XXI ions at 2.6 $\text{\AA}$  and  $\lambda/\Delta\lambda=15000$  for Ni XXVII ions at 1.6 $\text{\AA}$ , used at

the Princeton Plasma Physics Laboratory on the Tokamaks PLT (Princeton Large Torus), PDX (Poloidal Divertor Experiment)<sup>32,37</sup> and recently TFTR (Tokamak Fusion Test Reactor)<sup>38</sup> have used four bar beam bending devices. This work was influenced in the early stages by a four bar crystal bending design for generating cylindrical and logarithmic curvatures by Feser and Faessler<sup>39</sup>. Similarly, the high resolution spectrometers on the FT (Frascati Tokamak)<sup>40</sup> and on JET (Joint European Torus)<sup>41</sup>, where  $\lambda/\Delta\lambda=20000$  for Ni XXVII ions at 1.6Å, have used the same Princeton design. This group of instruments generate large radii of curvature in the range  $R=3\rightarrow 25\text{m}$  in conjunction with position sensitive gas filled MWPC detectors.

#### **Crystal Formers for Johann Geometry.**

Other spectrometers in the second category, see for example the Plasma Group at Fontenay-aux-Roses, Platz et al<sup>42</sup> where  $\lambda/\Delta\lambda=15000$  for Cr XXIII ion radiation at 2.2Å, use a grooved holder precisely machined to a set radius. The crystals are held to this by atmospheric pressure when the back of the holder is evacuated. It can be noted that this design cannot be used in a vacuum system and so therefore needs a Helium gas environment. For a 1m Rowland circle diameter, the absorption of x-radiation in a 2m Helium column at atmospheric pressure would be 40% and would limit the spectrometer operation to the waveband below 8Å. Once the effects of windows and support meshes are included in the x-ray transmission calculation, in practice the waveband is reduced to below 4Å. This would preclude most of the x-ray line emission from a small Tokamak like DITE with an electron temperature  $T_e < 1000\text{eV}$ .

#### **Crystal Formers for Other Geometries.**

Examples have been shown for crystals glued to formers; Källne et al<sup>19</sup> have used von Hamos geometry<sup>18</sup> with some degree of success on Alcator C. Resolving power of  $\lambda/\Delta\lambda=3000$ , determined by the entrance slit, has been used for Ar XVII and Ar XVIII lines at 3.7→4.0Å. Similar methods have been used with more elaborate crystal geometries, where toroidally curved crystals by Hauer et al<sup>43</sup>,  $\lambda/\Delta\lambda=1000$  for Si XIII lines at 4.0→6.8Å, and elliptically curved crystals Henke et al<sup>44</sup> have been developed for use with laser produced plasmas. In some cases no bonding medium is needed and a thin crystal wafer can be wrung to a curved optically finished substrate of the same material<sup>45</sup>.

### **3.2.2 Principle of Four Bar Beam Bending.**

The methods used to bend crystals often depend on the desired specification of the spectrometer. However, the four bar beam bending technique has some clear advantages which are not only based on superior performance but also added versatility in the use of the spectrometer. Firstly, the principle of bending a beam to generate a cylindrical curvature by applied loads is a well established technique, for example<sup>46</sup> shown for a three

bar device in Figure 3.3. This may be explained generally, but for a more detailed account see the text "Elements of Strength of Materials" by Timoshenko and Young<sup>47</sup>.

Figure 3.4(a) shows the beam (or crystal) AB subjected to transverse loads at positions A,B,C and D together with the shear force V and bending moment M diagrams below. The condition called pure bending occurs in the middle portion CD when the bending moment is uniform and the shear force is zero. This also depends on the internal stresses produced within the material of the beam. Therefore, the beam must be prismatic, homogenous, obey Hooke's law and be symmetrical in the axial plane.

The applied loads generally cause bending only in this plane. There will be some transverse curvature which may be estimated from the elastic constants of the crystal. This can be minimised by clamping, but was found to be unnecessary here. It can be shown that because the bending moment,  $M=Pa$ , is constant between C and D, the bending deformation is also uniform producing a cylinder in CD, Figure 3.4(b). The resultant deformation causes compression of the material on the concave side and elongation on the convex side. There is a layer which remains unchanged referred to as the neutral surface (shown in the diagram as a dashed line). For soft x-radiation, Bragg reflection occurs in the surface layer and the changes in the lattice spacing can be ignored. Two adjacent cross-sections mn and pq will intersect at O, where the angular element  $\delta\theta$  between these planes is  $\delta\theta=\delta x R$ , where R is the curvature of the neutral surface of the beam. It can be shown that:

$$\frac{1}{R} = \frac{M}{EI} \quad (3.1)$$

where E is the modulus of elasticity of the crystal material and I is the moment of inertia of the crystal cross-section in the axis towards O, illustrated in Figure 3.4(b). The curvature is directly proportional to the the bending moment M and inversely proportional to EI, known as the flexural rigidity of the beam. This quantity reflects the crystal stiffness E and cross-sectional area is indicated by I.

This should be compared with the technique of glueing or supporting the crystal to a former. The final crystal curvature will be affected by the former quality, the glue bond, the crystal surface quality and uniformity. There is no underlying principle for producing an accurately formed crystal curvature and no degree of adjustment if it is unsuccessful. The result also tends to have the curvature over a smaller crystal aperture thus reducing the signal intensity and waveband. This method is also limited in meeting the requirements for different experimental programmes.

#### **Versatility of the Four Bar Bending Method.**

This point was clearly illustrated by the author while trying to optimise the crystal spectrometer from Tokamak plasmas to laser produced plasmas. An ADP (101) crystal was

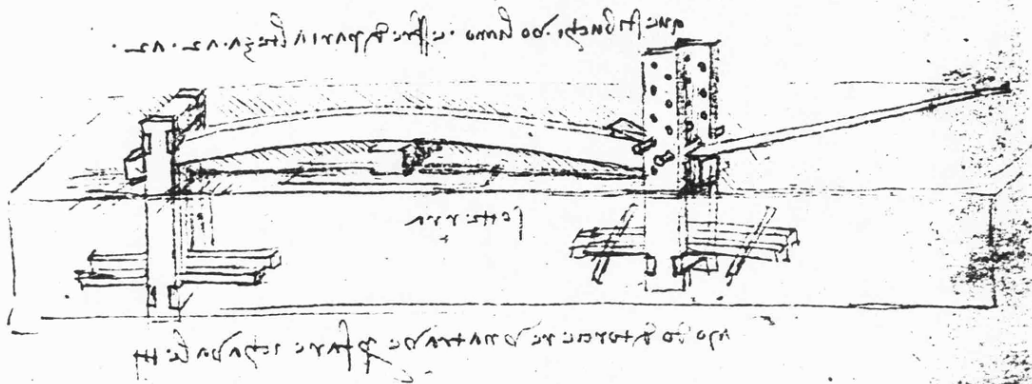


Figure 3.3 A three bar beam bending device invented by Leonardo da Vinci<sup>46</sup> circa 1488.

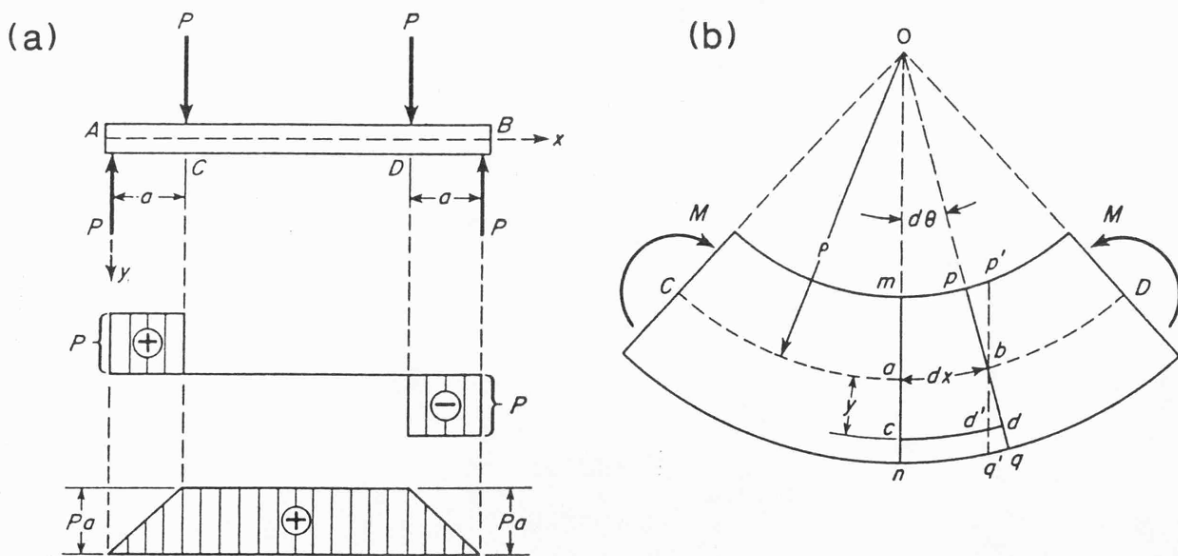


Figure 3.4 (a) indicates the resultant shear force (middle) and bending moment (bottom) diagrams for a uniform beam (top) under four identical loads  $P$  at points A, B, C and D. Uniform bending occurs in the middle section CD if the shear force is zero and bending moment  $M$  is constant. (b) shows uniform curvature in CD directly proportional to the bending moment  $M$ .

routinely used with crystal radius  $R=1200 \rightarrow 1500\text{mm}$  for Tokamaks, but to increase the sensitivity and bandpass for laser sources a smaller radius was required. The same crystal sample was first bent successfully to  $R=500\text{mm}$ , but reduced laser pulse energy caused a rapid drop in the emitted x-ray flux. A PET (002) crystal with higher integrated reflectivity, used initially at  $R=500\text{mm}$ , was quickly substituted and the spectrometer was operational again within a few hours. Further improvements in the spectrometer sensitivity were gained by reducing the radius to  $300\text{mm}$ . This process could have been continued to  $150\text{mm}$ . One crystal bending jig and two crystals were sufficient where the crystal/former method would have needed five different crystal holders, with an associated time penalty.

In summary, the crystal bending jig to be explained in the next section is the ideal device for optimising the spectrometer parameters resolving power, sensitivity and bandpass to any particular experiment where moderate to high resolving power is needed. The long term stability of the device is described in subsequent sections.

### **3.3 The Leicester Crystal Bending Jigs.**

There have been three crystal bending jigs designed and manufactured at Leicester; all are based on the same principle, with later versions modified to give improved performance. The first two jigs referred to as MkI and MkII, designed by R Barnsley, were machined from an Aluminium alloy. The present author modified the MkII and designed the MkIII, machined from stainless steel, to include further features.

#### **3.3.1 Bending Jig Description.**

In practise four rollers replace the loads  $P$  in Figure 3.4(a), see Figure 3.5. The inner two remain fixed and define the crystal aperture  $CD$ , while the crystal curvature is generated by correctly positioning the outer two. The elastic property of the uniform and homogenous crystal is necessary to create the constant desired deflection. Figure 3.6 is an engineering drawing of the MkIII crystal bending device. Figure 3.7 is a photograph of the MkII and MkIII jigs.

##### **Front Clamp-Face.**

The device consists of a front clamp-face bolted to the main body. The clamp face supports the front (or inner) rollers and the radiation passes to and from the crystal surface through a slotted aperture. The size of this aperture is mainly determined by the crystal dimensions. The inner side of the top and bottom webbing is grooved at  $5\text{mm}$  centres to position the steel rollers. The tolerance on the parallelism of the grooves, top to bottom, is generally better than  $5\mu\text{m}$ . Material behind the machined grooves on one side of the thicker webbing is removed to create one front cantilever which can be controlled by a threaded screw. The two front rollers are then aligned parallel by metrology during assembly and no further tuning is necessary during the crystal focusing procedure.

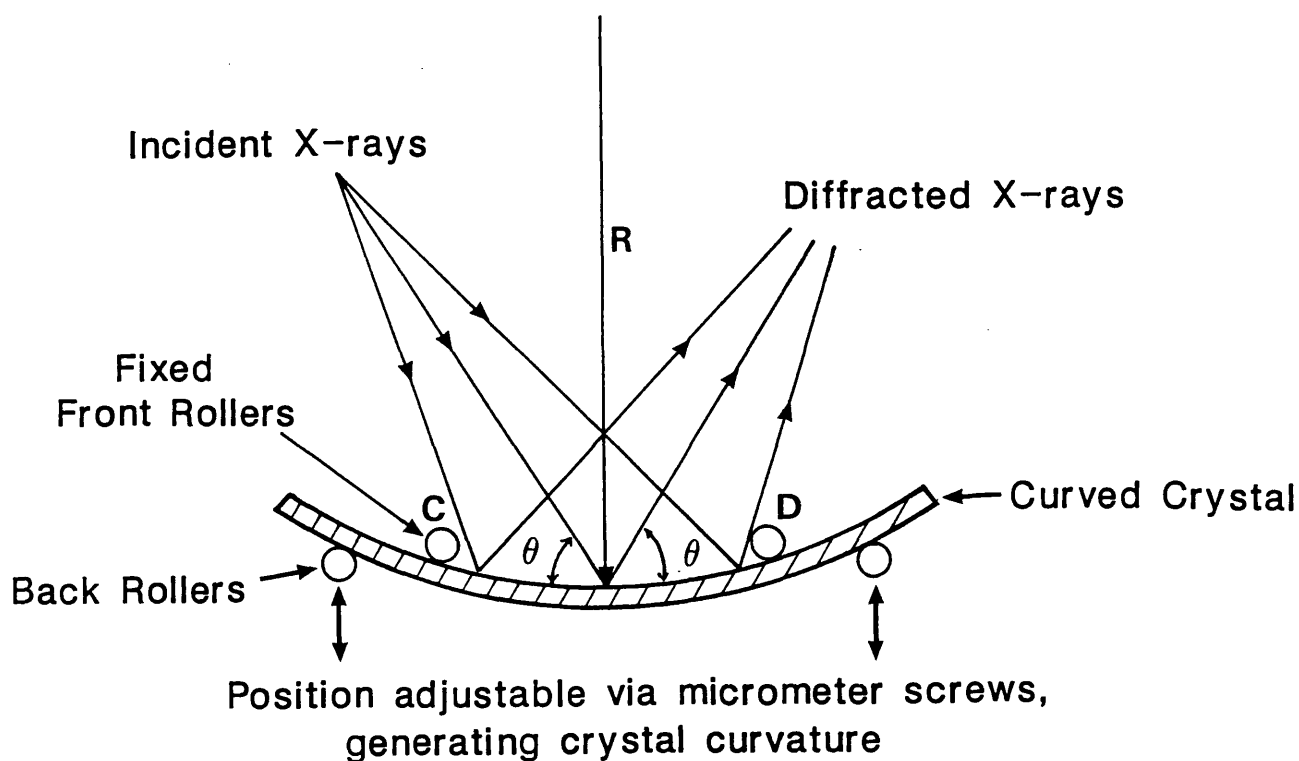


Figure 3.5 Curvature  $R$  in the section  $CD$  of the crystal lamina is generated by adjusting the position of the back rollers. The crystal bending jig is a device which allows fine movement of the roller positions.

Figure 3.6 (over the page) is an engineering drawing giving different views of the MkIII crystal bending jig. The main components are clearly visible. The back micrometers are angled in order that the spectrometer can move freely within the crystal chamber.

Figure 3.7 (on page after next) is a photograph of the MkII and MkIII crystal bending jigs.

USED ON  
ON DND

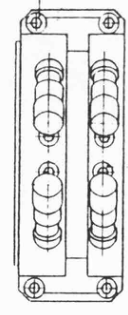
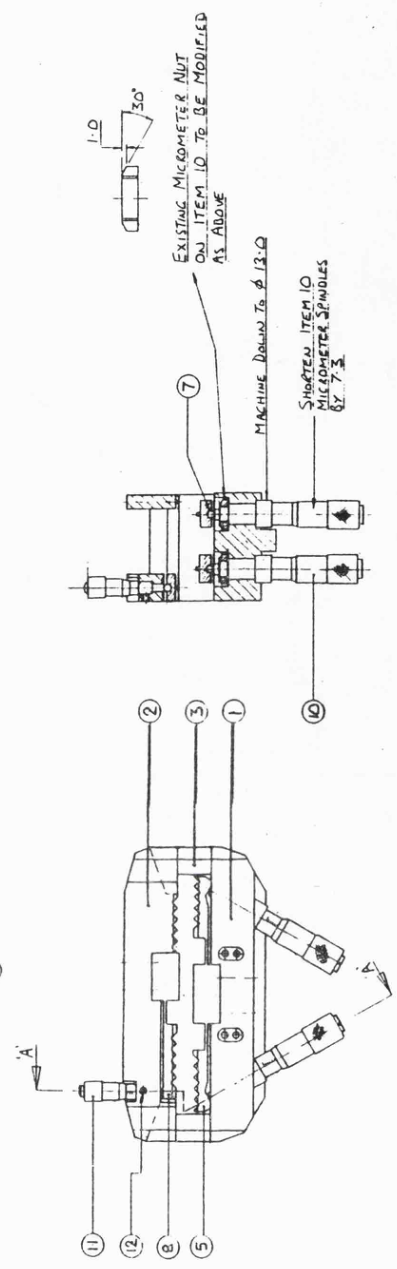
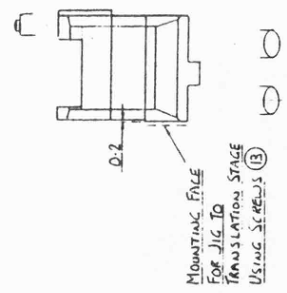
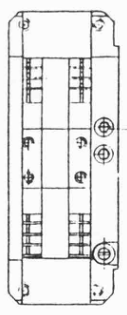
DO NOT SCALE

REMOVE ALL BURRS

10  
9  
8  
7  
6  
5  
4  
3  
2  
1



ITEM	DETAILS	MAT'L	REMARKS	QTY
1	BODY	DAG D.C.B.J.3067		1
2	CLAMP FRAME	"		1
3	SPACER BLOCKS	"		2
4	SOCKET CAP SCREWS	ST	M5 x 10	4
5	DOUBLE ARM	DAG C.C.B.T.3070		2
6	SOCKET CAP SCREW	ST	M5 x 25	4
7	BALLS	ST	φ 3	5
8	SINGLE ARM	DAG B.C.B.T.3071		1
9	SOCKET CAP SCREW	ST	M5 x 18	2
10	MICROMETER	TYPE SM-05 (EX. NEWPORT)		4
11	MICROMETER	TYPE 148-201 (EX. NEWPORT)		1
12	SOCKET SET SCREW	ST	M3 x 3 LG.	1
13	SPECIAL SCREW	ST	DAG A.C.B.T.3072	2



NO.	DATE	ALTERATION	BY	CHK'D

UNIVERSITY OF LEICESTER  
DEPARTMENT OF PHYSICS

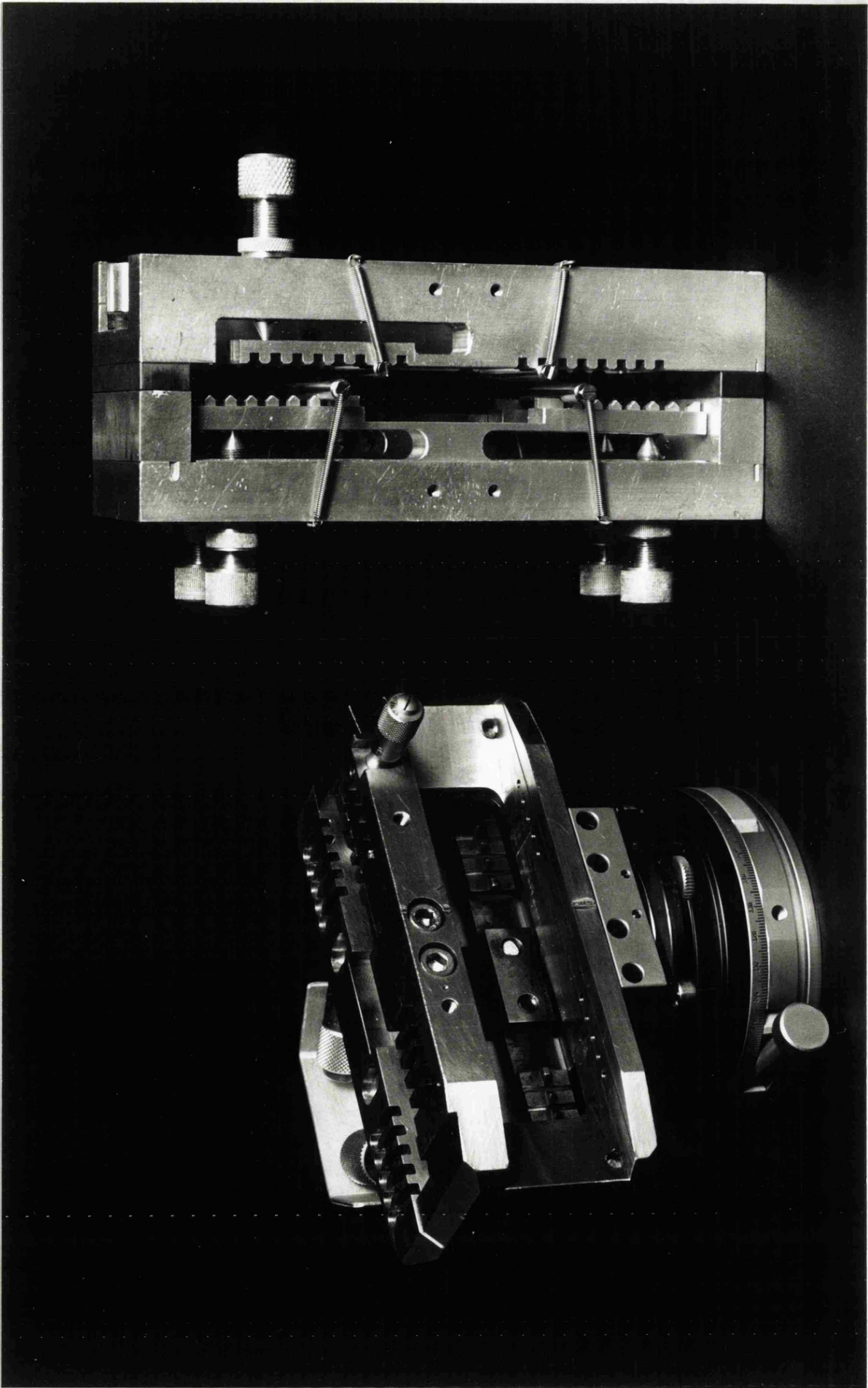
TOLERANCES EXCEPT WHERE OTHERWISE STATED  
DIMENSIONS ARE IN MILLIMETERS

SCALE 1/1

DRAWN BY W.P.R./C2 DATE 20.7.55  
DESIGNED BY W.P.R./C2  
CHECKED BY D.M.  
APPROVED BY D.M.

TITLE APPARATUS FOR CRYSTAL BENDING JIG  
PART No. D.C.B.J.3073

10  
9  
8  
7  
6  
5  
4  
3  
2  
1



### **Main Body.**

The crystal curvature is generated by the back (or outer) rollers which are supported top and bottom from the main body by two pairs of grooved cantilevers. The cantilevers are adjusted directly by four screws, set to the correct position for the chosen crystal curvature. This is done by a process of iteration using optical methods outlined in section 3.4. A locking collar on the adjusting screw secures each cantilever after the final focus. The bending jig body locates onto the spectrometer structure via the crystal alignment tables.

### **Side Pieces.**

The assembly of the two halves is done on a metrology bench; they are held rigidly together (with the back rollers parallel to the front rollers) by bolts through side pieces. The latter incorporate several independent features:

- They are spacers so that the rollers are in the correct position for a chosen crystal radius without exceeding the yield point of the cantilevers and causing damage. This is likely to occur for small radii of curvature  $R=150 \rightarrow 300\text{mm}$ .
- The spacer material and thickness can be varied to tune the thermal control mechanism of the jig which maintains the mechanical stability during temperature variations (section 3.6). Several metals with different thermal expansion coefficients are used to keep the correct back/front roller separation.

### **Rollers**

The rollers giving the best results are commercially available precision ground stainless steel shafting or hardened roller bearings of  $\text{Ø}4 \rightarrow 5\text{mm}$ . Tolerance for straightness is better than  $7\mu\text{m}$  along the 50mm length. Better contact between the rollers and cantilever grooves can be achieved if the rollers are pulled onto the grooves. In this respect, the shafting is preferred because it can be tapped easily at both ends and light springs attached. This makes the crystal focusing process much easier: the rollers tend to drop out at the early stages of focusing until friction from the crystal surface supports them.

### **3.3.2 The MarkIII Crystal Bending Jig.**

The stainless steel MkIII jig has some further important differences which are considered to give it better performance over the MkII version:

- The back cantilevers are machined from separate bars of spring steel to give the best flexure, but are hardened at the grooves for contact with the rollers. The cantilevers are bolted in a location slot in the main body with no resultant degradation of performance. The MkII main body was machined from one block.
- The grooves are also thinned to a "knife-edge"; the rollers then only make contact with 1mm width each end instead of the previous  $2 \rightarrow 10\text{mm}$  range of contact.
- The increased top/bottom separation of the grooves gives better leverage and so finer adjustment of the rollers on the crystal.

- Commercial micrometers<sup>48</sup> with reading accuracy to  $1\mu\text{m}$  replace the back adjusting screws. The front screw is replaced with a smaller micrometer<sup>49</sup> with reading accuracy to  $10\mu\text{m}$ . The micrometer threads have a finer pitch and smoother action. Although they have no locking mechanism, a guard plate protects them while handling the spectrometer.
- The front clamp face is made more rigid by using steel while keeping the dimensions similar. The logical step of bracing the clamp face to the back section would interfere with the thermal compensation.
- The aperture height is increased from 25mm to 30mm to improve the signal throughput when using large crystal curvatures.

The main disadvantage of the MkIII jig is increased machine and assembly time by an order of magnitude as a result of the added complexity and material hardness. However, there is a marked improvement in the crystal focusing through the combination of these factors. The increased cost of manufacture is felt to be justified.

### **3.4 The Crystal Focusing and Alignment Procedure.**

#### **3.4.1 The Crystal Focusing Procedure.**

##### **Basic Focusing Principle.**

The basic idea for generating a high quality crystal curvature of any chosen radius depends on the following principle, shown schematically in Figure 3.8. If monochromatic visible light passes through a slit placed on the Rowland circle of radius  $r$  and illuminates a crystal of radius  $R=2r$ , then the light will be reflected from the crystal surface and focused onto a similar position on the opposite side of the Rowland circle. There, a sharp image of the slit will be produced with only the additional features of Fraunhofer diffraction for visible light due to the finite aperture of the crystal. The diffraction is produced as a result of coherent illumination across the crystal width aperture by a quasi-monochromatic source<sup>50</sup>. Inspection of the image using a microscope eyepiece or ground glass screen will reveal information about the quality of the crystal curvature and show departures from cylindricity. The reflection condition for visible light does not depend on the angle of incidence to the crystal in the same way as Bragg reflection for x-radiation. The similarity remains where the diffraction width of the crystal acts as a virtual slit on the Rowland circle. It follows that a flat crystal can be bent to the desired cylindrical curvature, using a bending jig, when the chosen Rowland circle configuration is defined by placing the points of illumination, observation and the crystal surface in the correct positions.

##### **Spectrometer Preparation.**

The crystal focusing and alignment procedures are performed on a flat metrology surface like a granite slab or optical bench. The tilt table is set parallel to the metrology surface to  $\sim 1 \rightarrow 2$  minutes of arc before the jig is placed on the alignment stages. The crystal jig is

thoroughly cleaned, and dust removed from the rollers. The crystal is handled with similar care and is lightly dusted with a photographer's lens brush. It is then placed between the rollers, and rests on supports to keep it horizontal within the jig.

### **Defining the Rowland Circle.**

The Rowland circle diameter is measured relative to the crystal surface. An illuminated slit and eyepiece, set to the same height as the crystal, are placed on triangular optical benches at the correct positions on the RC. This is a straight forward triangulation exercise which is simplified by pivoting the triangular benches about the crystal pole. The optical alignment angle is chosen close to the normal position, usually  $\theta_v=85^\circ$ .

### **Initial Focusing.**

The slit is set fairly wide at 1mm to check that the crystal surface is evenly illuminated. This is guaranteed by placing a lens between the filtered Tungsten light and the slit. Maximum light throughput is needed to look for the low intensity, unfocused, reflected image. The back micrometers are moved systematically to put the crystal under tension while observing the focused image on a ground glass screen or white card. This could be achieved in a minute or so, the image being easily visible even when crudely focused.

The next stage is to reduce the slit width while correcting the back micrometers for any noticed defects. The image at this point should look uniformly wide, not much greater than the slit width at a few hundred microns, and parallel to the slit. Since it is essential to observe the image while adjusting the micrometers, if the Rowland circle diameter is larger than 0.5m a metrology flat is introduced into the optical path. The reflected image can be observed close to the crystal bending jig.

### **Final Focusing.**

For the final focusing the ground glass screen is replaced with a high quality, calibrated microscope eyepiece. Various focusing defects can be seen around the intense central image. This indicates that parts of the crystal are not at the correct curvature. Progressively finer adjustments to the micrometers are needed in the same iterative way to improve the image. For perfect settings, the slit width should be reduced to a few tens of microns and the observed image should be effectively a fine image of the slit convolved with a diffraction pattern. In practice, this is achieved by reducing the crystal aperture to exclude the parts of the crystal which are contributing aberrations to the image. Masking selected parts of the crystal will quickly confirm areas of imperfection. These are usually concentrated close to the inner rollers where the stress in the crystal is non-uniform.

### **Settling Period.**

At this stage the crystal jig is usually given a light tap to let the device and crystal settle down. The observed image usually defocuses slightly, requiring some fine tuning of the micrometer screws. The crystal is left for a period of an hour before repeating the final

# SCHEMATIC OF CRYSTAL FOCUSING ARRANGEMENT

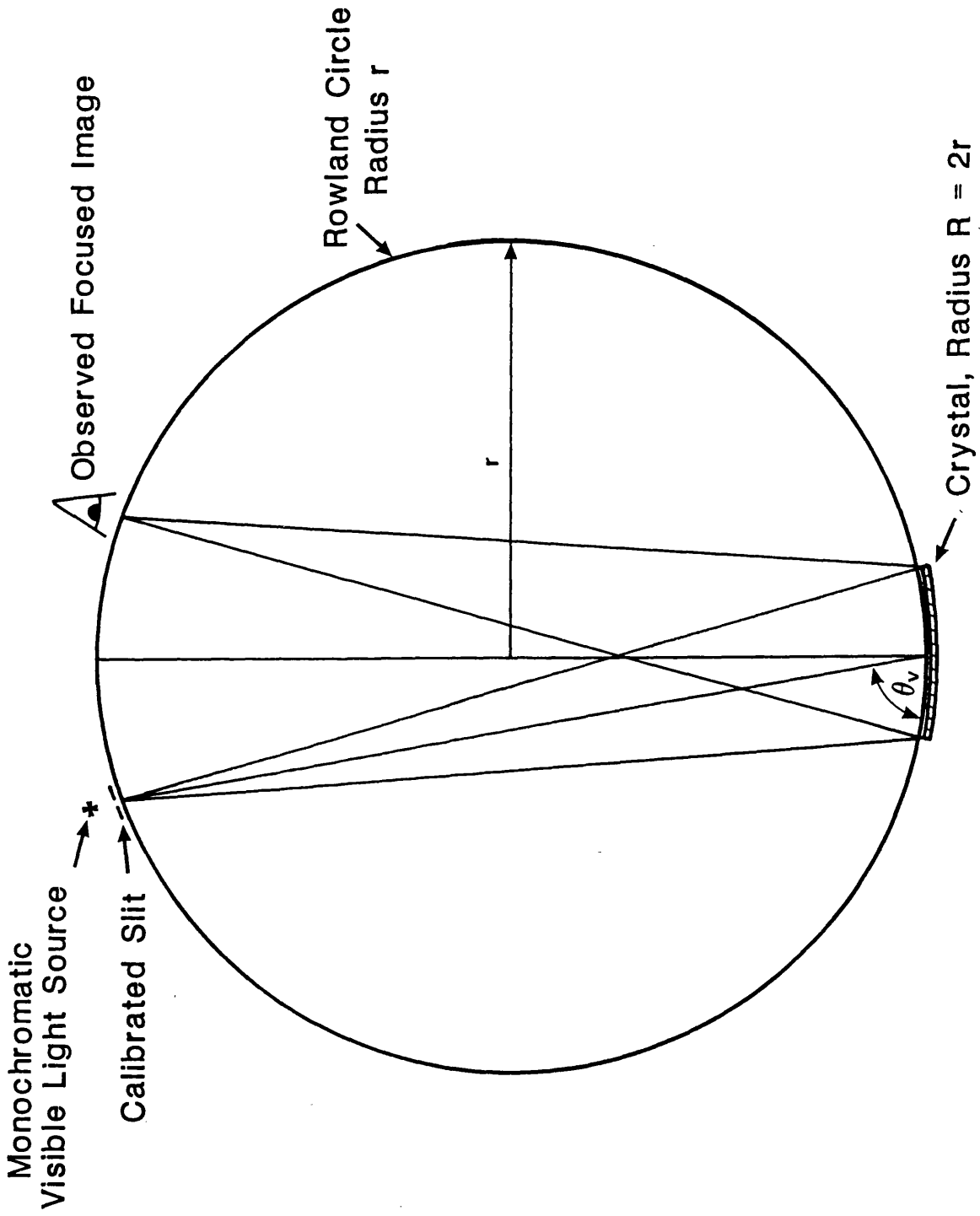


Figure 3.8 Schematic of crystal focusing arrangement.

focusing step. A two-axis travelling microscope is then used to inspect the position of the crystal pole relative to the rotation axis. The calibrated translation stage can correct for any difference to an acceptable tolerance of  $50\mu\text{m}$ . This can almost be set by dead reckoning since the maximum displacement of the crystal from the front rollers can be trivially calculated. The instrument should now be completely focused and ready for the angle alignment stage.

### **3.4.2 The Crystal Alignment Procedure**

#### **Alignment Principle.**

The objective of the angle alignment is to set the spectrometer to the correct Bragg angle.

This involves:

- Defining the reference or optical axis as the line between the the crystal and detector poles. This is analogous to the angle alignment procedure for flat crystal spectrometers with collimators, where the optical axis is defined by the ray path through the collimator.
- Aligning the crystal surface perpendicular to the optical axis in the plane of dispersion. The Bragg angle  $\theta_B=90^\circ$  is referenced when the crystal surface is normal to this axis.
- Measuring the Bragg angle relative to the optical axis using the calibrated rotation stages.

The precision of the absolute Bragg angle calibration then depends on the accuracy of the  $\theta_B=90^\circ$  setting and the tolerance of the rotation stages.

#### **Defining the Optical Axis.**

The crystal jig is rotated until it is approximately normal to the optical axis. The film holder backplate contains an aperture plus a set of cross-wires which define the horizontal mid-plane of the spectrometer and the vertical detector rotation axis, respectively. The film holder is set to the correct position on the Rowland circle corresponding to the chosen x-ray Bragg angle and radius of curvature. The film holder is tangential to the Rowland circle, having been referenced against a vacuum bulkhead. An illuminated pinhole, mounted upon a two axis translation stage, is placed behind the film holder and co-linear with the optical axis at a distance  $R$  from the crystal surface. The light from the pinhole casts an image of the film holder cross-wires onto the plane of the crystal where there is a second set of cross-wires defining the crystal pole. In practice, these cross-wires are a few millimeters in front of the crystal pole. Adjusting the pinhole translation, the pinhole can be positioned precisely on the optical axis where the shadow projected from one set of cross-wires falls on the second set.

#### **Finding $\theta_B=90^\circ$ .**

The next sequence then involves rotating the crystal surface until the image of the pinhole

# SCHEMATIC OF ALIGNMENT PROCEDURE

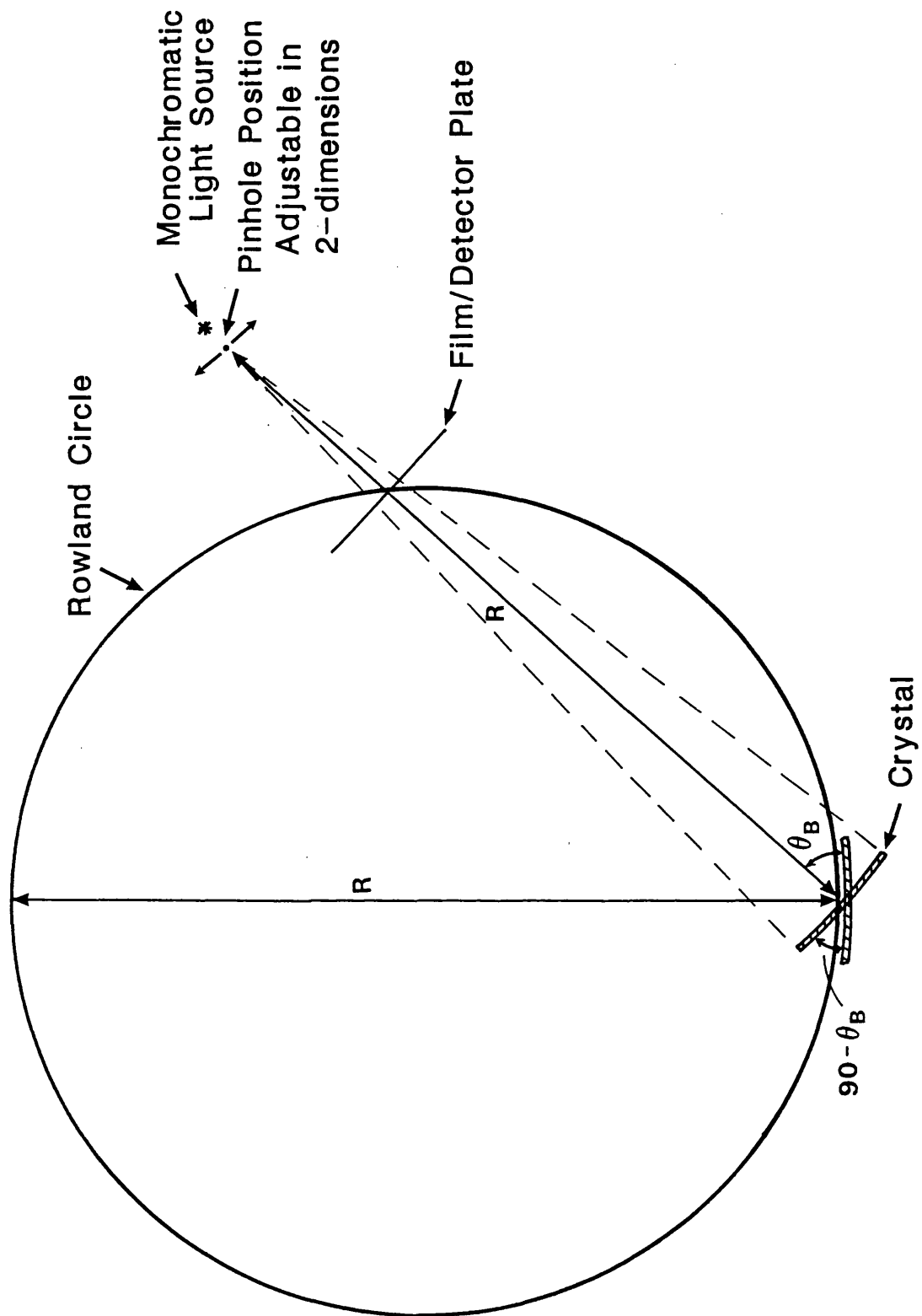


Figure 3.9 Diagram for crystal angle alignment.

(now a vertical line) is reflected back onto itself. This and the previous sequence are repeated iteratively, though usually twice is sufficient, because of the small transverse movement of the crystal cross-wires when the crystal is rotated. The crystal reference angle  $\theta_R$  is noted on the crystal rotation stage. The crystal tilt table can be adjusted to ensure that the crystal surface is normal to the optical axis perpendicular to the plane of dispersion to within a few minutes of arc. The setting angle  $\theta_S$  is then chosen for the Bragg angle  $\theta_B$  from the angle  $\theta_R$ :

$$\theta_S = \theta_R + (90 - \theta_B) \quad (3.2)$$

This effectively returns the crystal onto the Rowland circle. Figure 3.9 shows a schematic layout for the alignment procedure.

Generally, this method works extremely well and is repeatable to 1 minute of arc, limited by the vernier scale of the rotation stage. This corresponds to 300 $\mu$ m transverse displacement from the optical axis for a crystal radius of 1000mm. For this or larger Rowland circles, the method is accurate to ~15 seconds of arc with the use of more accurate rotary stages. This is at the level of the positional tolerance of the crystal pole on the axis of rotation.

## 3.5 Optical Testing Procedure

### 3.5.1 Objective.

The following methods were devised for measuring optically the crystal curvature quality. This was done initially with thin, aluminised glass slides and later with various crystal samples. The objective was to get a numerical value for the quality of the line focus over a range of crystal radii, apertures and angles. Having performed the test extensively, the aim would be to replace it with a quicker method which could be employed routinely in the focusing procedure. A very brief description is given concerning the use of photographic film to record the spatial information of the crystal focus. The reader is recommended to consult the excellent texts of "From Dry Plates to Ektachrome Film" by Mees<sup>51</sup> and "The Theory of the Photographic Process" edited by James<sup>52</sup>.

### 3.5.2 Method.

A 35mm format camera was substituted for the microscope eyepiece on the Rowland circle after final focusing. Fine grain emulsion Ilford PanF black and white film was used to record the images for different exposure times. The film was developed in Ilford ID-11 at 20°C for 8 minutes according to the manufacturer's recommendations. The film response for image optical density D as a function of the logarithm of the exposure  $E=It$ , where I is the irradiance and t the exposure time, was characterised as follows.

### **Iford PanF Calibration.**

A Kodak step wedge with increasing density from 0.05D→3.05D in 0.3D steps, each step reducing the optical transmission from the previous by 50%, was placed on a strip of film and directly exposed to diffuse light. Various exposure times indicated that reciprocity failure was negligible. A 1-dimensional Joyce-loebl MkIII micro-densitometer with influx/efflux optics of 0.16NA/0.25NA converted the photographic images into optical density as a function of position. The instrument slit setting was constrained between maximising the S/N ratio by increasing the scanning area but also minimising the contribution to the image width due to convolution of the slit function with the image profile. For line images, the slit was usually set to 0.1→0.2FWHM.

Figure 3.10 expresses the measured film response function for PanF. This is a typical response of film emulsion to visible light: the toe region A to B, the linear slope B to C and the shoulder part C to D are all evident. The region B to C is the preferred range of operation because of the almost linear relationship between density and logE. Emulsion saturation occurs above this and the response becomes non-linear.

### **Fraunhofer Diffraction.**

By calibrating all exposures in this way, the image density and thus the FWHM can be measured accurately. As noted in the previous section, Fraunhofer diffraction<sup>53</sup> is the dominant feature of a high quality focused image. Poorly focused images have distorted and asymmetric fringe patterns. It is clear that diffraction ultimately limits the focusing of crystals in visible light. Therefore, a comparison between the generated and theoretical diffraction patterns is the best way of measuring the focus quality. The FWHM  $\omega$  of the central fringe of the Fraunhofer diffraction pattern can be written as:

$$\omega = \frac{0.8859 d \lambda}{W} \quad (3.3)$$

where  $d$  is the crystal to observation plane separation,  $\lambda$  is the wavelength of the visible light and  $W$  is the width of illuminated crystal. Also the separation of the  $n$ th minima  $S_n$  can be written as:

$$S_n = \frac{2n d \lambda}{W} \quad (3.4)$$

### **Results.**

Figure 3.11 shows the measured line focus by using a 200:1 expansion lever in the densitometer. Table 3.1 shows a comparison of the measured FWHM with the theoretical values from equation (3.3) for three different crystal aperture widths of the same crystal focus. It is evident that the measured line widths are determined by Fraunhofer diffraction. At the very least this shows that for crystal widths of 15→30mm, the crystal curvature is good to 1 part in 50000. Further agreement with the predicted diffraction pattern is given by

# Measured Film Response of Ilford Pan F

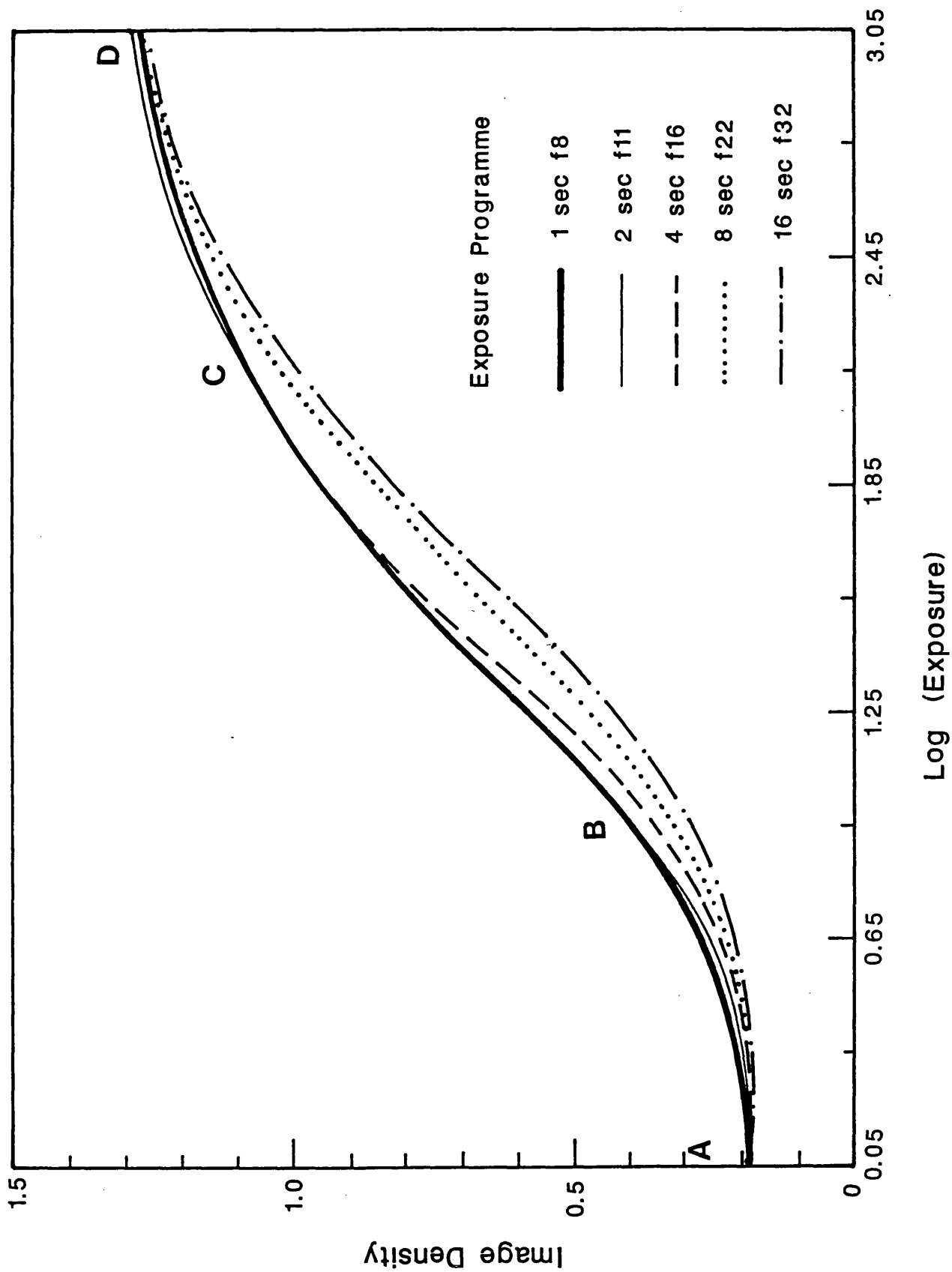


Figure 3.10 This shows the measured film response for Ilford PanF film under different exposure conditions. Identification of the linear region B→C is necessary for finding the half intensity and therefore measuring the FWHM of the crystal focus image.

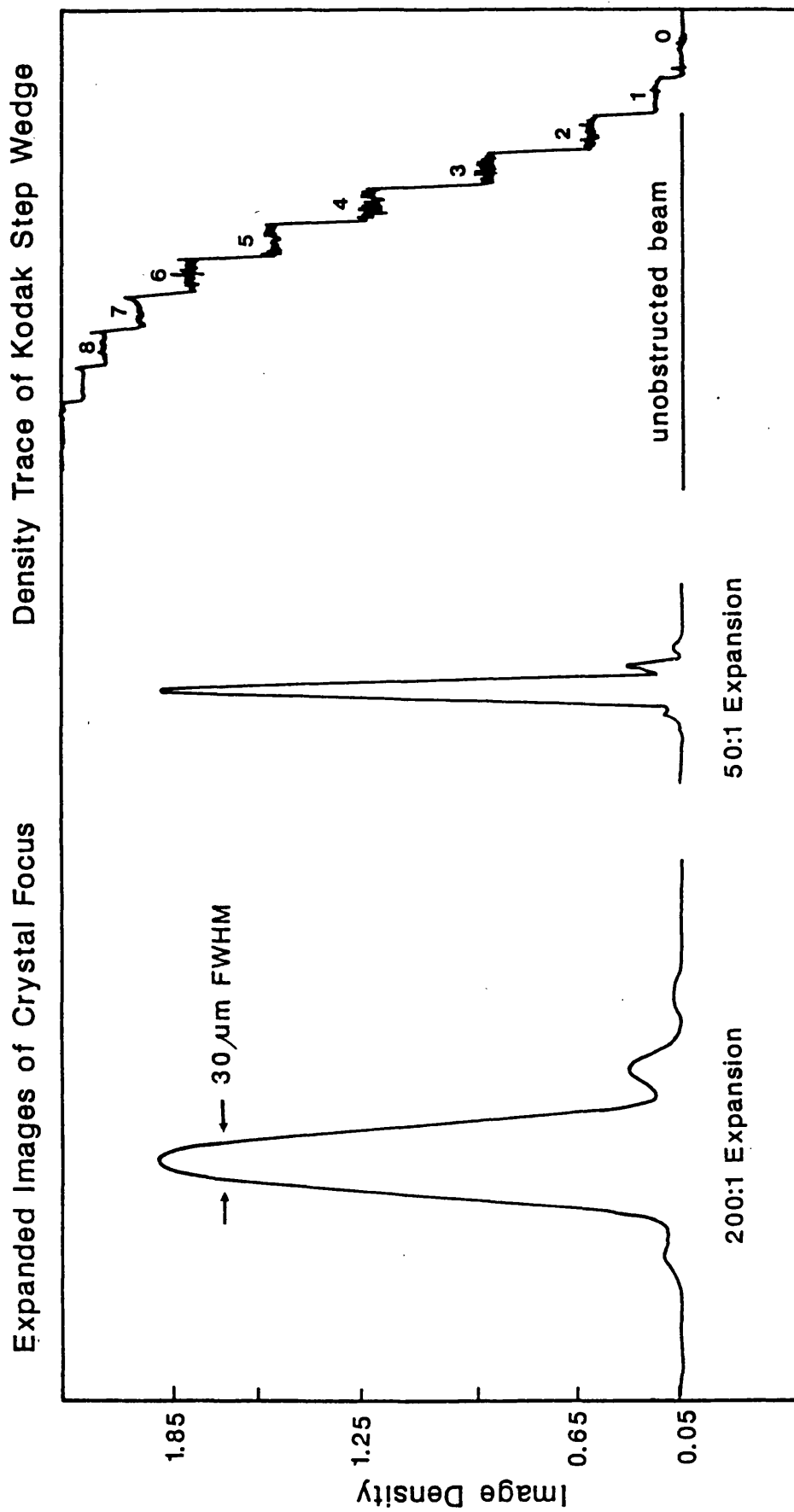


Figure 3.11 Typical calibrated densitometer trace of the crystal focus image. A FWHM of 30μm over 1 metre can usually be obtained with good crystal samples.

studying the fringe positions. Table 3.2 compares the measured and theoretical separation values of the 1st and 2nd minima for the aperture 29 x 20 mm<sup>2</sup>. The alignment parameters are  $\theta_v=85.4^\circ$ ,  $\lambda=5893\text{\AA}$  for Sodium light,  $d=1000\text{mm}$  and the focusing slit width for the maximum crystal aperture is set to  $2\mu\text{m}$ . The intensity of the fringe maxima is considerable less than 5% of the central peak; the film has to be over-exposed to generate significant optical density.

**Table 3.1 Measured and Theoretical Fraunhofer Diffraction Line Widths**

Crystal Aperture W x H (mm <sup>2</sup> )	FWHM, $\omega$	
	Measured ( $\mu\text{m}$ )	Theory ( $\mu\text{m}$ )
29.1 x 20	23	18
14.6 x 20	33	36
4.8 x 20	105	108

### 3.5.3 Focus Quality Interpretation.

The agreement in both these cases is extremely good, with the only deviations being in the relative intensity of the fringe maxima. This is probably due to a combination of scattered light from the crystal surface and low intensity wing features associated with the focused image profile. When the diffraction width is minimised by using either the maximum working crystal aperture or lower wavelength visible light, for example blue light at  $\lambda=4600\text{\AA}$ , the focused image becomes apparent. Therefore, by subtracting the diffraction width  $\omega$  quadratically from the measured width, a worst case estimate can be calculated for the focusing profile width  $\Delta l$ . The film and slit contributions are assumed negligible here. This will contribute to the instrumental resolving power and can be expressed as the measured optical width  $\Delta\theta_{\text{opt}}$ :

$$\Delta\theta_{\text{opt}} = \frac{\Delta l}{d} \quad (3.5)$$

**Table 3.2 Separation of Fringe Minima.**

	Separation of Minima, $S_n$	
	Measured ( $\mu\text{m}$ )	Theory ( $\mu\text{m}$ )
Separation of 1st Minima	50	40.6
Separation of 2nd Minima	95	81.3

### X-ray Focus Quality.

The measured optical width  $\Delta\theta_{\text{opt}}$  for the spectrometer is related to the angular width or de-focusing error  $\Delta\theta_3$  (from Chapter 2) for x-rays by:

$$\Delta\theta_3 = \frac{\Delta\theta_{\text{opt}}}{2} \quad (3.6)$$

This can be explained as follows<sup>54</sup>. If a small crystal element has an angular deviation  $\delta\theta$  from uniform crystal curvature then it will lead to a deviation  $2\delta\theta$  in the reflected visible beam from a point source on the Rowland circle. However, for x-rays under Bragg reflection

a slightly different wavelength will be selected coming from a different part of the source. The deviation of the reflected x-ray beam is  $\delta\theta$ . This result was confirmed in Chapter 5 where the accidentally de-focused crystal optical profiles could be directly compared with the de-focused x-ray profiles.

#### **Quick Focus Quality Estimate.**

Having gone through this elaborate procedure, a much simpler way is obvious. Table 3.2 indicates that by measuring the image width directly with the calibrated microscope eyepiece, the FWHM  $\omega$  can be calculated quickly from the separation  $S_1$  of the first minima. Equations (3.3) and (3.4) give:

$$\omega = 0.443 S_1 \quad (3.7)$$

This is the technique that was regularly used to measure the crystal curvature quality.

### **3.6 Thermal and Mechanical Stability Testing**

The last and perhaps the most important property of the bending device was to check its reliability, principally the long term mechanical and thermal stability. It was noted that the focal length of the curved crystal seemed to vary by several centimeters over a day. An initial study showed that the crystal curvature was proportional to temperature changes in the room but was not accompanied by a reduction in the image quality. This suggested that the de-focusing process was occurring symmetrically and was not due to some inherent instability of the design.

A rigorous test programme was performed to measure the mechanical changes of the device, attribute the cause and find a solution to improve the stability. This was carried out in three different ways:

- (a) Firstly, the crystal jig was uniformly heated in an oven to 50°C, removed then insulated with a polystyrene jacket and allowed to cool to room temperature. The insulation minimised temperature gradients across the jig during cooling. The crystal curvature was measured optically at regular intervals and the corresponding temperature, accurate to  $\pm 0.1^\circ\text{C}$ , noted. This took a few hours and was repeated for different roller configurations. The large temperature range, more than normal for the spectrometer's expected use of  $22.0 \pm 5.0^\circ\text{C}$ , gave enough readings to determine the focus changes accurately. A linear expansion of the crystal curvature with temperature was found to vary with the roller settings. No hysteresis was detected and the crystal curvature would return to its original setting on cooling to room temperature.
- (b) Attention was next turned to measuring the roller movement directly. This was achieved by measuring changes either with a sensitive dial gauge or an autocollimator, the latter giving the more accurate results. Small movements of

0.1 $\mu\text{m}/^\circ\text{C}$  were measured which confirmed that the changes in the crystal curvature were a consequence of the differential movement in the back and front rollers.

- (c) The final step involved the thermal modelling of the crystal bending device. This took account of all the different materials, thicknesses and geometries which linked the back and front rollers. This model corroborated the direct measurements taken in (b), above.

It was then possible to tune the thermal control mechanism to keep the radius fairly constant during temperature changes. The adjusting screws for the back cantilevers were machined from Aluminium alloy in order that most of the Mk II jig was of uniform material. The final adjustment came by using spacers of thermally different material in the side pieces. This reduced the crystal curvature expansion from  $\sim 7\text{mm}/^\circ\text{C}$  to considerably less than  $0.5\text{mm}/^\circ\text{C}$ . The spectrometer then remained stable for a number of months, partly confirmed by the result in Chapter 7. Very high spectral resolution was achieved for Neon Lyman- $\alpha$  despite the long integration time of 30 hours.

### 3.7 Conclusions.

This chapter has described the salient points of the four bar beam bending device and how it can be applied to a Johann spectrometer. The Leicester crystal bending jigs use this principle to create high precision crystal cylinders of any chosen radius.

Methods have been developed for focusing, aligning and testing the curved crystal instrument. Thermal modelling of the device has been introduced to preserve the optical focus quality under temperature variations.

The final specification of the instrument may be outlined:

- The range of possible Bragg angles are  $\theta_B=24\rightarrow 66^\circ$  for the vacuum spectrometer, though angles up to  $75^\circ$  are possible for the vacuumless version.
- The Bragg angle alignment is  $\pm 1\rightarrow 2$  minutes of arc ( $\pm 0.017\rightarrow 0.034^\circ$ ) as determined by the present rotational stages. This corresponds to an absolute wavelength calibration of  $\lambda/\delta\lambda=2000, 5000$  for  $\theta_B=45^\circ, 65^\circ$  respectively. At this level, de-focusing effects due to angle alignment errors are low. The present alignment method should be accurate to  $\pm 15$  seconds of arc.
- The optical crystal focus has been routinely set to 1:50000, giving an equivalent x-ray resolving power  $\lambda/\Delta\lambda\sim 10^5$ . Crystal samples need to be homogenous and uniformly thick to achieve this.
- The thermal and mechanical stability is extremely good. An optical focus once set, following the guidelines given in the focusing procedure, should remain unchanged for periods of a month or more. Thermal testing reveals that the instrument specification should not be compromised for temperature cycling of  $\pm 5^\circ\text{C}$ .

## Chapter 4 Instrumentation and Techniques

	Introduction.	70
4.1	Crystals.	70
	4.1.1 Crystals for $1 \rightarrow 25\text{\AA}$ .	70
	4.1.2 Practical Information About Bending Crystals.	74
4.2	X-Ray Films.	77
	4.2.1 Kodak X-Ray Films for $1 \rightarrow 25\text{\AA}$ .	77
	4.2.2 Kodak DEF 392 Film Response.	78
	4.2.3 Densitometry and Optimisation of Signal/Noise.	80
	4.2.4 Digitisation Process.	83
4.3	Filters and Transmission Calculations.	84
4.4	Instrument Sensitivity.	89
4.5	Line Profiles and Analysis.	92
	4.5.1 Natural Line Broadening.	92
	4.5.2 Doppler Broadening.	93
	4.5.3 The Voigt Profile.	94
	4.5.4 Spectral Line Profile Fitting.	97
4.6	Discussion.	99

## Introduction

The main points discussed in this chapter are:

- Crystals available for studying the 1→25Å waveband, the emphasis being on high resolving power. Some properties of the more useful crystals, including lattice spacing, reflectivity and refractive index are tabulated. Relevant comments are added.
- Practical considerations of crystal dimensions, specifying finish quality and focusing properties.
- Choice of x-ray films, giving an analytical function for the film response and ways of optimising the signal to noise ratio S/N.
- Use of filters and calculation of the transmission function  $T(\lambda)$ .
- Calculation of the relative instrumental sensitivity for line intensity ratio analysis.
- Line profile analysis. This includes a quantitative summary of expected intrinsic and Doppler line widths for x-ray resonance lines. Voigt profile synthesis is introduced as a means to de-convolve instrumental and other contributions from the measured line envelope.
- Some general conclusions about these topics.

## 4.1 Crystals

### 4.1.1 Crystals for 1→25Å

Crystals for astronomical x-ray spectroscopy have been reviewed by Burek<sup>12</sup>, and the reader is directed there for a more complete background of the subject. Most of the information presented here comes from a few selected references; all crystals in general from Burek, mainly acid phthalates from Barrus et al<sup>30</sup> and Lewis<sup>55</sup>, Beryl and Lead Stearate from Willingale<sup>56</sup> and ADP, PET and EDdT from Hall<sup>11</sup>. Table 4.1 gives a representative selection of crystals in this waveband and some of their important properties are defined as:

- (1)  $2d_{1\theta}$ , the usual convention is adopted where the crystal lattice spacing  $d$  is quoted as  $2d$  in Å, measured at 18°C.
- (2)  $\lambda/\Delta\lambda$ , the resolving power as calculated from the single crystal rocking curve width.
- (3)  $R_c$ , the integrated reflectivity in radian units.
- (4)  $\delta/\lambda^2$ , refractive index in Å<sup>-2</sup> units.
- (5)  $\alpha$ , the linear thermal expansion coefficient in K<sup>-1</sup> units.
- (6)  $\rho$ , the crystal material density in g/cm<sup>3</sup>.

The values of integrated reflectivity  $R_c$  and resolving power  $\lambda/\Delta\lambda$  quoted below, are only approximations and the original texts should be consulted for variation with wavelength. Theoretical resolving power for ADP (101) and PET (002) is plotted as a function of wavelength for the first four orders later in this chapter. The useful waveband range for

Table 4.1 Selected Crystals and Properties for the 1-25Å Waveband

Crystal	Lattice Plane	Lattice Spacing $2d_{1g}(\text{Å})$	Resolving Power $\lambda/\Delta\lambda$	Integrated Reflectivity $R_c$ (radians)	Refractive Index $\delta/\lambda^2(\times 10^{-6}\text{Å}^{-2})$	Thermal Expansion $\alpha$ ( $\times 10^{-6}/\text{K}$ )	Density $\rho$ ( $\text{g}/\text{cm}^3$ )
KAP †	(001)	26.6242±0.0005 [57]	1500 [55]	7×10 <sup>-5</sup> [55]	2.30§ [57]	40.5 [60]	1.64 [61]
	(002)	13.3121±0.0002 [57]	9000 [12]	5×10 <sup>-6</sup> [55]			
RbAP	(001)	26.1083±0.0007 [30]	1200 [55]	10 <sup>-4</sup> [55]	2.41§ [30]	37.0 [30]	1.94 [12]
ADP †	(101)	10.6402±0.0012 [30]	9000 [11]	7×10 <sup>-5</sup> [11]	2.52§ [11]	21.6 [62]	1.80 [12]
EDdT	(020)	8.8034±0.0001 [30]	9800 [11]	1.1×10 <sup>-4</sup> [11]	2.25§ [30]	18.8 [30]	1.54 [12]
PET †	(002)	8.7358±0.0006 [11]	6000 [11]	2.2×10 <sup>-4</sup> [11]	1.98§ [11]	110 [11]	1.39 [12]
Si	(111)	6.27110 [59]	7600 [12]	1.2×10 <sup>-4</sup> [12]	3.14 [63]	4.0 [64]	2.33 [64]
Ce	(220)	4.00053 [59]	9000 [12]	2.3×10 <sup>-4</sup> [12]	6.20 [65]	6.0 [64]	5.33 [64]
SiO <sub>2</sub>	(2023)	2.749 [12]	10 <sup>5</sup> [12]	1.5×10 <sup>-5</sup> [12]	3.64 [10]	14.2 [64]	2.66 [12]

1. NB:-Numbers in square brackets indicate references. See main text reference list.

2. Some values of refractive index  $\delta/\lambda^2$ , labelled § are calculated from the referenced data by the present author; all numbers above are generally accurate to ±5%. Large departures outside these tolerances may occur for wavelengths in the vicinity of a crystal absorption edge. The above values are in good agreement with the method outlined in Chapter 2.

3. The linear expansion coefficients  $\alpha$  are accurate to ±5%. The expansion coefficient for Germanium is based on a sample purity of 99.999%. For samples of 99.99% purity or less, assume an expansion coefficient 10% higher.

4. Crystals labelled † have been used in this work.

Table 4.1 gives a representative selection of crystals in the waveband 1-25Å and lists some of their important properties. A full description of the crystals is given in the text.

each crystal has been defined for the Bragg angle  $\theta: 5 \rightarrow 75^\circ$ . However, when using crystals in the Johann geometry, the instrumental resolving power can be considerably reduced by Johann errors at shallow angles, as discussed in Chapter 2. In practice, angles above  $40^\circ$  are preferred. Starting with highest lattice spacing, further relevant comments are added for individual crystals. It is worth mentioning a group of pseudo-crystals first, more appropriate for the longer wavelength region.

**Lead Stearate:**  $2d=100\text{\AA}$ ,  $[\text{CH}_3(\text{CH}_2)_{16}\text{COO}]_2\text{Pb}$ , and multilayers (usually constructed from alternate layers of Tungsten and Carbon) are synthetic crystals. They allow the observable soft x-ray waveband by crystal techniques to be extended longer than  $25\text{\AA}$ , the limit normally reached by acid phthalates. They have good first order reflectivity  $R_c \sim 10^{-3}$  rad, and good higher orders, but very low resolving power  $\lambda/\Delta\lambda=100$ . In this latter respect they cannot compete with gratings, but do have an application for studying short wavelength Carbon transitions or where high resolving power is not desired.

**Acid Phthalates:** are a group of organic crystals grown from aqueous salts, with a large lattice spacing  $2d=26\text{\AA}$ , moderately high reflectivity and resolving power  $\lambda/\Delta\lambda \sim 1000$ . They usually have a transparent, colourless, flat appearance and cleave along the main diffraction plane. They are noted for use in the waveband where crystal spectroscopy properly begins. For these reasons, they have been used extensively in soft x-ray spectroscopy and solar x-ray spectroscopy in the  $5 \rightarrow 26\text{\AA}$  band for the last twenty years. The phthalic salts of Potassium (KAP) and Rubidium (RbAP), both described below, are commonly used. Others have different properties and merits for particular applications, including Thallium (TIAP), Caesium (CsAP), Ammonium ( $\text{NH}_4\text{AP}$ ) and Sodium (NaAP). Burek reports a trend for improved crystal integrated reflectivity by choosing a metal ion with a high atomic number, usually at the expense of resolving power.

**KAP (001):**  $2d_{10} = 26.6242\text{\AA}$ ,  $(\text{C}_6\text{H}_4(\text{COOH})(\text{COOK}))$ , useful waveband  $2.3 \rightarrow 25.7\text{\AA}$ . A crystal which cleaves readily along the (001) planes, has good vacuum properties and long term stability. Good integrated reflectivity  $R_c \sim 7 \times 10^{-5}$  rad and moderate resolving power  $\lambda/\Delta\lambda \sim 1500$  are the main qualities, though the latter is probably the best available for  $15\text{\AA}$  and above. The crystal has a useable second order reflectivity and resolving power (see Chapter 7), but has extremely low third and fourth order reflectivity<sup>57</sup>. A good crystal for observing the H-like and He-like Oxygen series. Several absorption edges are present; Potassium K-edge at  $3.44\text{\AA}$  and Oxygen K-edge at  $23.3\text{\AA}$ .

**RbAP (001):**  $2d_{10} = 26.1083\text{\AA}$ ,  $(\text{CH}_6\text{H}_4(\text{COOH})(\text{COORb}))$ , Rubidium acid phthalate has a useful waveband  $2.3 \rightarrow 25.2\text{\AA}$  and is isostructural to KAP with a Rubidium ion substituted for a Potassium ion. RbAP has higher reflectivity than KAP though lower resolving power; it has useful applications for low signal x-ray sources. Second order reflection is suppressed. It is stable under vacuum, but does not age as well as KAP. Several absorption edges occur in

waveband; Oxygen K-edge at 23.3Å and complicated Rubidium L-edge structure  $L_I$  at 6.00Å,  $L_{II}$  at 6.65Å and  $L_{III}$  at 6.87Å.

**Mica (002):**  $2d=19.84\text{Å}$ , ( $K_2O \cdot 3Al_2O_3 \cdot 6SiO_2 \cdot 2H_2O$ ), has useful waveband 1.7→19Å. A mineral crystal with natural cleavage plane; Muscovite is one common type. Bends easily and is often used in curved crystal spectrometers. Generally, chemical composition and structure may not be uniform. It has low reflectivity  $R_c \sim 2 \times 10^{-5} \text{rad}$  and moderate resolving power  $\lambda/\Delta\lambda \sim 1400$ . Good higher order reflectivity and resolving power are possible, extending to the tenth order or more. Second order offers better resolving power and can be used for He-like Magnesium resonance lines at 9.2Å. Several absorption edges are present; Potassium K-edge at 3.44Å, Silicon K-edge at 6.74Å and Aluminium K-edge at 7.95Å.

**Beryl (10 $\bar{1}$ 0):**  $2d=15.955\text{Å}$ , ( $3BeO \cdot Al_2O_3 \cdot 6SiO_2$ ), useful waveband 1.4→15.4Å. A robust mineral crystal, though good specimens are difficult to find. Colour and  $2d$  spacing may vary depending on impurity concentration<sup>56</sup>. Medium reflectivity  $R_c \sim 6 \times 10^{-5} \text{rad}$  with very useful resolving power  $\lambda/\Delta\lambda = 2500 \rightarrow 3000$  above 12Å. Like Mica, Aluminium and Silicon, K-absorption edges present.

**ADP (101):**  $2d=10.64\text{Å}$ , Ammonium Di-hydrogen Phosphate ( $NH_4H_2PO_4$ ), useful waveband 1→10Å. An inorganic crystal grown from solution which does not cleave along the reflecting plane; surface must be cut and chemically polished. Reflecting properties and spectral resolution are therefore affected by the surface quality. Large specimen sizes are available, and used on several solar corona observing missions eg SMM (Solar Maximum Mission)<sup>58</sup>. Good resolving power  $\lambda/\Delta\lambda = 9000$  with moderate reflectivity  $R_c = 4 \times 10^{-5} \text{rad}$  make it a useful crystal for studying the H-like and He-like series of Magnesium and Aluminium. Extensive measurements of crystal properties by Hall<sup>11</sup> show very little change with ageing process. Phosphorus K-absorption edge is present at 5.79Å.

**EDdT (020):**  $2d=8.8034\text{Å}$ , Ethylenediamine d-tartate ( $C_6H_{14}N_2O_6$ ) is a useful crystal for the 0.8→8.5Å region; large specimens can be grown. Like ADP, EDdT does not cleave along the (020) plane and therefore its properties depend on the sample preparation. Together with PET (002) which has a similar lattice spacing, these crystals complement each other in this waveband; resolving power of EDdT  $\lambda/\Delta\lambda \sim 10^4$  is 60% higher than PET, but the integrated reflectivity  $R_c \sim 1.1 \times 10^{-4} \text{rad}$  is approximately 40% lower than PET. EDdT changes very little with ageing<sup>11</sup> and appears to be stable under normal laboratory conditions. No absorption edges are present.

**PET (002):**  $2d=8.74\text{Å}$ , Pentaerythritol,  $C(CH_2OH)_4$ , is an organic crystal noted for its high integrated reflectivity  $R_c \sim 2 \times 10^{-4} \text{rad}$  for the 0.8→8.5Å band. Large high quality samples can be grown from an aqueous solution and it readily cleaves along the commonly used (002) plane. It has good resolving power  $\lambda/\Delta\lambda = 6000$  and is free from absorption edges. Crystal properties are likely to change with age under normal laboratory conditions<sup>11</sup>. Cleaving to

expose a fresh surface will return crystal to new condition. Very useful for studying the H-like and He-like resonance line series of Aluminium and Silicon.

**Si (111):**  $2d=6.271\text{\AA}$ , has useful waveband of  $0.5\rightarrow 6\text{\AA}$ . A very stable metallic crystal which can be produced with a high degree of purity  $>99.999\%$ . Good resolving power  $\lambda/\Delta\lambda=7000$  and high reflectivity  $R_c=1.2\times 10^{-4}\text{rad}$  are possible as are higher order reflections. However, second order reflections are extremely low. The lattice spacing has been determined to very high accuracy (1ppm) by various authors as reviewed by Hart<sup>59</sup>. This paper and the references therein should be consulted for very slight discrepancies in lattice spacing between samples. The crystal is free from absorption edges over the waveband.

**Ge (220):**  $2d=4.000\text{\AA}$ , has useful waveband of  $0.4\rightarrow 3.8\text{\AA}$ . Like Silicon, Germanium is a very stable metallic crystal which can be manufactured in large sizes to a high degree of purity  $>99.999\%$ . Good resolving power  $\lambda/\Delta\lambda=9000$  and high reflectivity  $R_c=2.3\times 10^{-4}\text{rad}$  can be achieved, together with higher order reflections. Fluorescence will be much higher than lower Z crystals when exposed to intense x-ray sources. Lattice spacing is known to very high accuracy 2ppm, and methods of measurement are reviewed by Hart<sup>59</sup>. The Germanium K-absorption edge appears at  $1.11\text{\AA}$ .

**Quartz and Natural Minerals:** There are a large range of different types of minerals available for x-ray analysis. Quartz ( $\text{SiO}_2$ ) for example, has different cuts with lattice spacing from  $2d=8.350\text{\AA}$  for  $(10\bar{1}0)$  plane to  $2d=1.624\text{\AA}$  for  $(5\bar{0}52)$  plane. Crystals with larger  $2d$  values have medium reflectivity  $R_c\sim 6\times 10^{-5}\text{rad}$  and good resolving power  $\sim 12300$ . Silicon K-absorption edge occurs at  $6.74\text{\AA}$ . An example of low lattice spacing Quartz is given below. Minerals can vary in purity between samples. Other common mineral crystals are Calcite (Calcium Carbonate) eg the (422) cut with spacing  $2d=3.034\text{\AA}$  and the gemstone Topaz (Aluminium Fluorosilicate) eg the (303) cut with  $2d=2.712\text{\AA}$ . Generally, the reflecting properties of Quartz, Calcite and Topaz are well established and have been used consistently in the last sixty years, particularly for precision measurements of x-ray  $K\alpha$  lines.

**Quartz (20 $\bar{2}$ 3):**  $2d=2.75\text{\AA}$ , useful waveband  $0.24\rightarrow 2.6\text{\AA}$ . A mineral crystal which is very stable and rugged. It has low reflectivity  $\sim 1.5\times 10^{-5}\text{rad}$  but very high resolving power  $\lambda/\Delta\lambda=10^5$ . The crystal is free from absorption edges over the waveband of interest.

#### 4.1.2 Practical Information About Bending Crystals

All crystals used in this work were purchased from Quartz et Silice<sup>66</sup> through Ray Handley of the British subsidiary Nuclear and Silica Products Ltd. The samples were delivered unmounted and the finish quality was specified according to whether they naturally cleaved along the chosen diffraction plane. There were two main objectives to consider, in regard to surface quality:

- The crystal preparation should be good enough to ensure a perfect diffraction profile.

- One crystal face should have an optical finish to allow focusing in visible light. The crystals, as described below, were sufficiently reflective in visible light not to require surface silvering.

### **Cleaved Crystals**

PET (002), RbAP (001) and KAP (001) were typical examples, the diffraction plane of interest being parallel to the front surface. These generally had a flat, even, optical finish, except PET which often had a slightly uneven stepped finish when inspected by eye. This would manifest itself as excess scattered light during the focusing operation. It would, however, cleave very easily from large mounted blocks, considerably reducing unit costs. X-ray lines recorded with cleaved crystals were usually uniformly narrow along the film height and repeatably positioned to within the Bragg angle alignment tolerance.

### **Uncleaved Crystals**

Si (111), Ge (220) and ADP (101) for example, did not cleave along the desired plane. Therefore, the face was cut parallel and one side was polished followed by a chemical etching process to remove debris and polishing material. These crystals had the best optical finish, particularly the Silicon and Germanium samples which had a mirror-like surface.

The position of x-ray lines recorded with one sample of ADP (101) were found to be  $\sim 5 \rightarrow 7$  minutes of arc adrift suggesting that there was a similar offset between the diffracting planes and the surface along the length of the crystal. This angular error was not large enough to significantly defocus the line image. However, a considerably larger offset of  $> 30$  arcmin from the diffraction plane to the crystal surface, lying along the rotation pole, made the spectral lines partially wedge shaped along their height. The tilt adjustment of the crystal jig could compensate this more serious defect and highlighted a source of error during the crystal cutting process. In principle, this could be overcome by using a two crystal spectrometer to find the diffraction plane of interest of the crystal block with x-ray light before cutting.

### **Storage of Crystals and Prevention of Ageing**

Barrus et al<sup>30</sup> have reviewed ways of minimising the ageing process of crystals as a result of contact with the atmosphere. The effect often causes changes in the reflectivity, mainly an increase at the lower wavelength region with mosaicity, but also is accompanied by a deterioration in the resolving power.

All crystals should be coated with  $500\text{\AA}$  of Al, or a similar layer impervious to air and water vapour, and should be stored in a dessicator jar. The coating should occur immediately after the cleaving or polishing process. This is expected to reduce the departure from new sample reflectivity for acid phthalates to better than 10% per year.

All crystal samples in this work were normally used shortly after purchase and were stored either in a desiccator or airtight container. Fresh PET samples were cleaved from a block immediately before use.

### **Crystal Sizes and Range of Curvature**

Samples were usually ordered in two sizes:  $80 \times 25 \text{mm}^2$  (length x height) for the MkII jig; and a slightly larger  $105 \times 30 \text{mm}^2$  was used for the MkIII jig. The minimum separation of the outer rollers was 60mm which determined the shortest length of crystal. The crystal height was matched to the aperture of the bending jig. The crystal thickness was chosen according to the crystal properties and the radius of curvature. Samples of PET, KAP, Si and Ge were 0.3mm thick; ADP and RbAP were 0.4mm thick. This thickness allowed a selection of crystal radii from  $R=300 \rightarrow 2300 \text{mm}$ , but was important for smaller radii where the stress in the crystal could exceed the yield point, resulting in breakage.

The smallest radius of  $R=300 \text{mm}$  was achieved using a PET (002) crystal of dimensions  $63 \times 17 \times 0.3 \text{mm}^3$ . This was likely to be the smallest radius for this crystal thickness though no attempt was made to produce a smaller radius or find the breaking point. No such restrictions applied to the upper radius limit. However, a thin crystal at a large radius had to be supported to prevent it slipping from the rollers when the spectrometer was inclined.

### **Observations During Crystal Focusing**

Generally when focusing, the crystal sample quality, which was invariably very good, determined the maximum useable diffraction area. This gave an active crystal area of  $\sim 30 \times 25 \text{mm}^2$  for the 80mm crystal length and  $\sim 55 \times 30 \text{mm}^2$  for the larger size. To some extent, any variations in the thickness or inhomogeneity of the crystal could be compensated by the crystal bending jig.

During focusing some crystals were not as stable as others which seemed to be correlated with using a larger radius  $R > 1200 \text{mm}$  where stress on the crystal was lower. For example, a change in the crystal focus of the inorganic crystals KAP and ADP occurred during sudden increases in temperature and humidity. Even very light breathing on the crystal was sufficient to cause this phenomenon. The original focus quality would not always return if left with no further adjustment. If treated with some caution and a settling period, this was not a serious inconvenience unless the spectrometer had to be transferred some distance from the alignment area to the experiment. A thicker crystal would improve the stability, while mineral and metallic crystals (e.g. Quartz and Silicon) would not expect to be susceptible to this effect.

### **Optimum Crystal Thickness for Radius**

The previous considerations lead to the following suggested thickness for various curvatures of a high resolution crystal spectrometer irrespective of crystal material or cost:

**Table 4.2 Suggested Crystal Thickness For Radius Curvature**

Thickness x (mm)	Radius R (mm)
0.15 → 0.25	150 → 300
0.25 → 0.5	300 → 2000
0.75 →	2000 →

This should be compared with some examples from other researchers:

- Beiersdorfer et al<sup>67</sup>, ADP (101) 100x20x0.5mm<sup>3</sup> for R=570mm.
- Platz et al<sup>42</sup>, Quartz (310) 50x30x0.4mm<sup>3</sup> for R=1380mm.
- Beiersdorfer et al<sup>68</sup>, Quartz (1120) 152x38x0.8mm<sup>3</sup>, for R=2760mm.
- Lieber et al<sup>69</sup>, Quartz (203) 130x55x0.4mm<sup>3</sup>, for R=2970mm.

There is good agreement here, with the previously described tendency of extending the use of thin crystals to larger radii. It may be added that the plane of dispersion for all the above spectrometers was parallel to the horizontal, with one exception<sup>67</sup>. The present spectrometer was used successfully in a range of orientations.

Finally, it is certainly possible to generate radii less than R=100mm with thin wafers of 0.1mm, but such an instrument could not be described as a high resolution instrument for large x-ray sources observed here.

## **4.2 X-Ray Films**

Since most of the results presented in this work were recorded on photographic emulsion, the properties of x-ray film are discussed in some detail. The main emphasis is given to the film sensitivity over the wavelength range of interest, use of the measured film response to convert optical image density into absolute x-ray photon density and ways of improving the signal/noise ratio. Other photo-electric detectors were used namely a Multi-Wire Proportional counter (Chapter 7) and a standard TV compatible CCD (Chapter 5); these are discussed in the relevant chapter. Optimisation of a CCD detector for use with a very high resolution Johann spectrometer is discussed in Chapter 4.6.

### **4.2.1 Kodak X-Ray films for 1→25Å**

There are several commercial x-ray films available for the waveband 1→25Å. The author has used two of the more common Kodak films:

- (1) Kodak 101-01 film is primarily a low energy x-ray/UV film which is composed of a single emulsion monolayer with no protective overcoat, available on glass plate or 35mm plastic backing.
- (2) Kodak DEF film is a double emulsion film, designed for high sensitivity in the 1→10keV band, consisting of a supercoat plus emulsion layer on both sides of a 185µm polyester base. It replaces Kodak No-Screen double emulsion film. DEF film is available in plate or unperforated 35mm (392) format.

The main objective of this research has been to study x-ray spectral lines with instrumental resolving power of  $\lambda/\Delta\lambda \sim 10^4$ . It is apparent from the previous section that crystal availability limits the study to wavelengths below 13Å. Kodak DEF 392 film is the logical choice because of its superior sensitivity. In fact, the two films in the 1→25Å soft x-ray region are complementary, the crossover point being about 13→14Å. Above this wavelength, 101 film has superior sensitivity, without the attenuation of the supercoat, while the emulsion monolayer composition is too thin to register more energetic radiation. The converse is true of DEF 392.

#### **Quick Sensitivity Test for DEF, 101-01 and HP5**

In order to test their performance approximately, Kodak DEF 392 film was compared in turn with 101-01 and Ilford HP5, a commercial fast speed panchromatic black and white film. The two pieces of film, placed in a light tight cassette, were uniformly exposed to monochromatic radiation diffracted from the spectrometer, using the DITE Tokamak as an x-ray light source. The He-like Al ion  $1s^2-1s2p$  resonance lines at 7.8Å were used as a rough guide to prospective lines of interest. The results quickly confirmed that DEF was a factor of about two and three more sensitive than 101 and HP5 respectively. Also, HP5 was more sensitive to visible light than either of the x-ray films, as expected, and needed better optical filtering. It may be noted that HP5 is expected to become more sensitive to shorter x-rays below 4Å and may have some application as a fine grain x-ray film.

#### **4.2.2 Kodak DEF 392 Film Response**

The x-ray response of DEF and other films has been measured experimentally and described theoretically by Henke et al<sup>70</sup> and by references therein. Figure 4.1 taken from this reference shows the sensitivity  $S$ , defined here as the reciprocal of the x-ray intensity, needed to produce a net optical density  $D_{0.1}=0.5$ , as a function of photon energy. The film sensitivity varies by a factor of five with photon energy from 1→10keV while the background grain noise remains constant. The optimum sensitivity, and therefore the best inherent S/N ratio for the film, is for radiation in the 2→6keV (6→2Å) region. The dashed line showing the response of the first emulsion only, demonstrates that the film sensitivity is enhanced for photon energies greater than 4keV for photons registered on the back emulsion coating. This radiation is energetic enough to penetrate the 185µm polyester film base and register on the back layer. The low energy fall-off in the response is due to x-ray absorption in the supercoat while the high energy fall-off is due to incomplete absorption in the two emulsion layers.

For the 1→2keV x-ray region, the photons are completely absorbed in the first (thick) emulsion layer where the image density can be shown to be related to x-ray photon density by equation (4.1) below. For 2→3keV photons, partial absorption takes place in the (thin) emulsion layer and therefore the contribution below the first coat thickness has to be

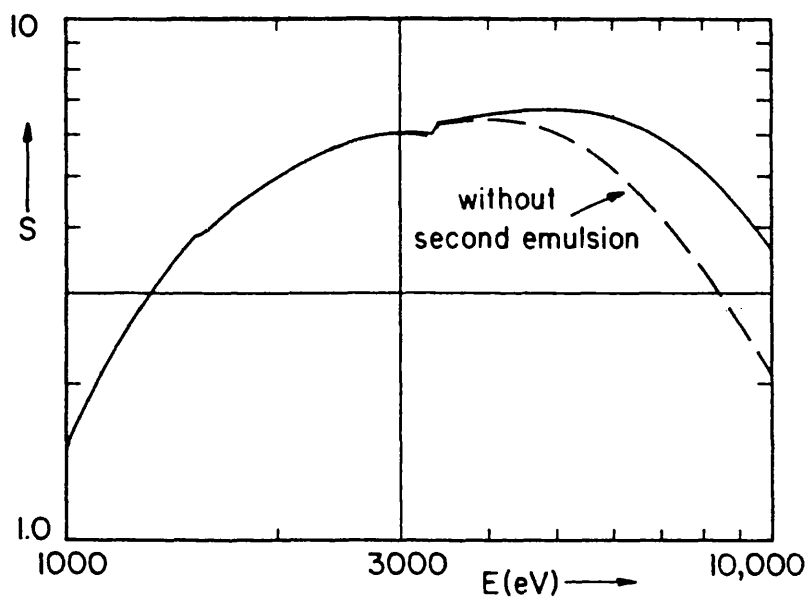


Figure 4.1 The sensitivity  $S$  for DEF x-ray film (after Henke et al<sup>70</sup>) is shown for the 1→10keV energy region.  $S$  is defined here as the reciprocal of photon intensity required to generate an optical density  $D_{0.1}=0.5$ . The dashed curve indicates the sensitivity for the first emulsion only, illustrating the improvement in the DEF sensitivity for photon energies above 4keV.

subtracted. For  $E \geq 3\text{keV}$  photons, the radiation is transmitted through the polyester base and registers on the back emulsion layer giving a double-emulsion response.

### Low Energy Response

Since the detailed analysis of line radiation in this work occurred at energies lower than  $2\text{keV}$  (longer than  $6\text{\AA}$ ) the thick emulsion response alone warrants discussion. Henke<sup>70</sup> describes the film response for a thick (completely absorbing) emulsion as:

$$\alpha D = a \ln (1 + b\beta I) \quad (4.1)$$

where  $D$  is the optical density,  $I$  is the x-ray photon density and  $\alpha$ ,  $a$ ,  $\beta$  and  $b$  are constants depending on the x-ray energy. This can be simplified to:

$$AD = \ln (1 + BI) \quad (4.2)$$

where  $A = \alpha/a$  and  $B = b\beta$ . Table 1 from Henke<sup>70</sup> expresses exposure  $I$  (photons/ $\mu\text{m}^2$ ) against net optical density  $D_{0.1}$ , above the background fog level, as a function of photon energy. The above equation (4.2) was fitted to this tabulation for photon energies of  $1.1 \rightarrow 2.0\text{keV}$  ( $11.27 \rightarrow 6.20\text{\AA}$ ) with an accuracy better than 0.2%. The parameters  $A$  and  $B$  are shown below in Table 4.3 and the film response plotted in Figure 4.2 for the four photon energies. The general form of the film response function is clear from the family of curves, allowing interpolation for any intermediate photon energy.

**Table 4.3 Kodak DEF 392 Low Energy Response Parameters**

$\lambda(\text{\AA})$	A	B
11.27	0.941	1.19
8.27	0.598	1.30
6.89	0.572	1.50
6.20	0.518	1.47

### 4.2.3 Densitometry and Optimisation of Signal/Noise

It may be noted that the optical density mentioned here is net specular density as opposed to net diffuse density. The latter refers to the absolute density of a medium whereas the former depends on the micro-densitometer collection optics and the film granularity. A full account of this phenomenon is given by Tuttle<sup>71</sup> and Weaver<sup>72</sup>. A consequence of this is that, in order to utilise the absolute measurements of Henke et al, all density measurements in this work were recorded with matched 0.1NA/0.1NA (Numerical Aperture) influx/efflux optics using a Joyce-Loebl MkIII densitometer. Likewise, the recipe by Henke for developing and fixing Kodak DEF film was followed and is repeated in Appendix I with some additional comments.

DEF FILM RESPONSE CURVES NET DENSITY/PHOTON DENSITY

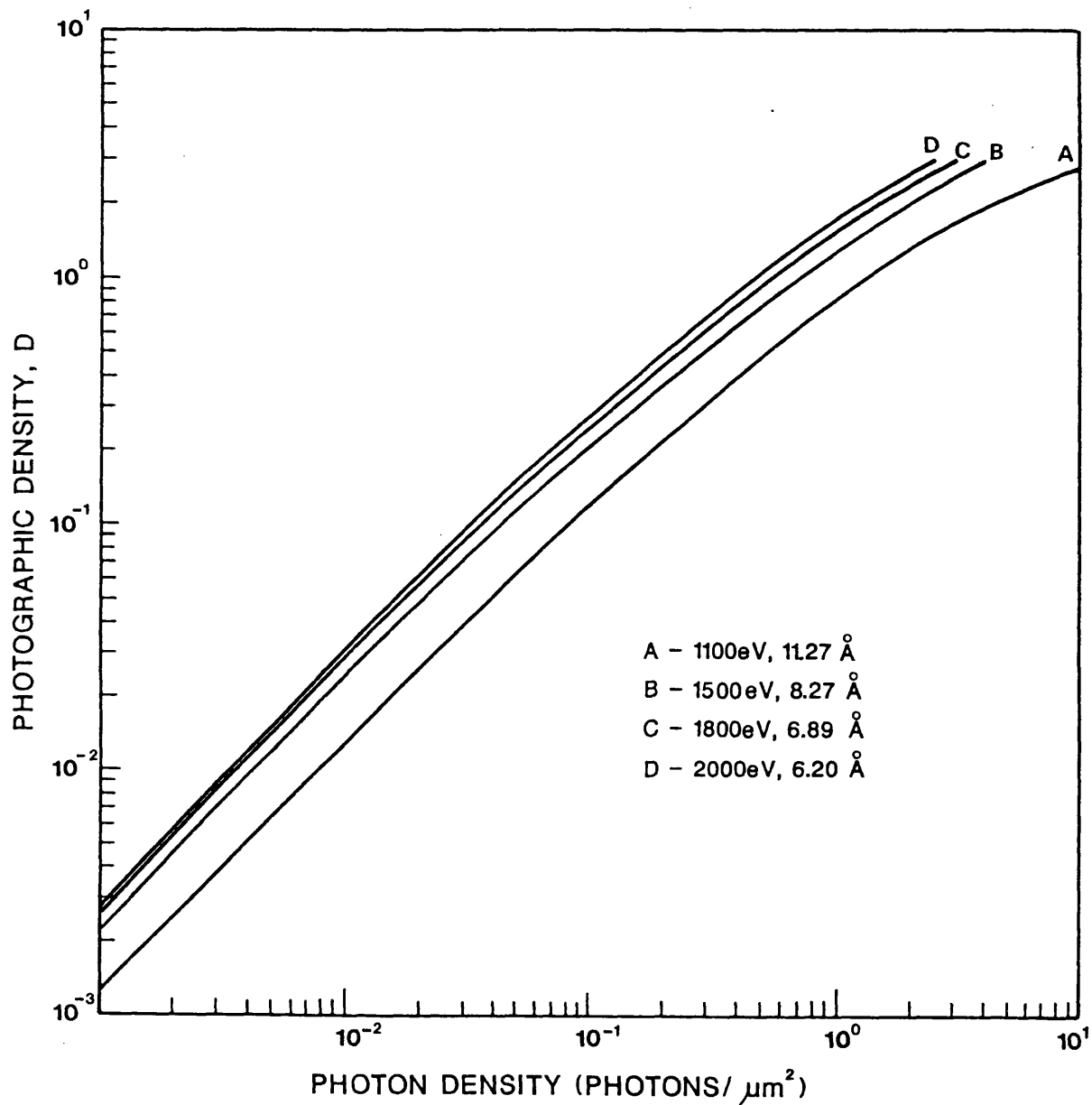


Figure 4.2 DEF film response curves showing net optical density as a function of x-ray photon density for different energies.

The optimal signal retrieval depends on the information required from the spectrum; for the case of line profile measurements the slit width is usually set at 0.1→0.2 line FWHM. This value is chosen to minimise the contribution of the slit convolution with the spectral feature. This places a 1-D restriction on the total scanning area. Since the rms grain noise is inversely proportional to the area, the scanning slit height  $h$  must be maximised in order to improve the S/N ratio. The total number of photons  $N$  included in the scan increases linearly with  $h$ , thus the S/N ratio increases proportionally with  $h^{1/2}$ .

In practice, because the spectral lines are curved or the scanning optics limit the aperture to 1mm or so, only a small number of registered photons can be retrieved from the 25mm film height. Clearly the best results could be obtained by digitising the complete spectrum using a computer-controlled microdensitometer. A 2-D array would be created, followed by a 1-D compression of the height information. This would need a correlation function to combine the individual 1-D slices without losing spectral information. This would be a very successful way of extracting the data and maximising the S/N ratio.

#### **Removing Back Film Emulsion**

The main limit to extracting information from low level spectral features is the background grain noise. Various techniques in the densitometry can be used to minimise the contribution of grain noise, but these are constrained by the optimum signal retrieval. DEF is a double-coated emulsion which suggests that the granularity must be twice that of a single emulsion layer. It is clear that in the region below 4000eV, longer than 3Å, removal of the second emulsion layer does not reduce the signal but results in doubling the S/N ratio by halving the total grain noise.

The present method of removing the unexposed emulsion backing was modified from Gordon<sup>22</sup>. The film was placed on a glass plate with the exposed side face down. The edges of the film were then sealed using a waterproof PVC tape, leaving most of the back emulsion uncovered. A 10% solution of Sodium Hydroxide (NaOH) was poured onto the film back and left for approximately twenty minutes; more solution could be added to keep the film moist. The solution was washed off and the softened emulsion removed from the polyester base using a plastic scraper. (Longer soaking times may be necessary to further soften the emulsion). The PVC tape was discarded and the film washed in distilled water for about ten minutes to remove excess NaOH. The film was dried at room temperature and the emulsion allowed to harden before any further handling.

The main advantage of this method is that the exposed side is protected while the back layer is removed, resulting in no deterioration of the spectral image. Inspection of the backing by eye and with the densitometer show that no scratches or marks are added to the polyester base giving the desired reduction in the overall grain noise.

#### 4.2.4 Digitisation Process

At the time of analysing the data, there was no method at Leicester University for digitising the film spectra directly onto computer. This had to be done in two stages:

- A portion of the film, containing a small group of lines, was densitometered first, with a suitable expansion lever, ~50:1 and the image density calibrated.
- The line profiles were traced by hand using a map digitiser with positional accuracy of 20 $\mu\text{m}$ .

The digitised data could then be converted into x-ray intensity/ $\text{m}\text{\AA}$  using the sensitivity and dispersion functions.

It was important to verify that this digitisation process did not introduce errors in the final line position and therefore wavelength calibration. The individual steps of the complete digitisation and analysis could be tested as follows:

- The densitometer position scale was calibrated and showed deviations of  $5 \times 10^{-4} \rightarrow 10^{-3}$ , ie 5 $\rightarrow$ 10 $\mu\text{m}$  errors in 10mm.
- A synthesised spectrum containing three blended Gaussian profiles was generated and plotted out as a graph from the VAX mainframe computer. The second stage of the digitisation process was repeated in order to simulate the procedure for real spectra density traces. The sampling of the envelope was varied to find out if this was a source of error. The digitised data was then run with the analysis code to try to retrieve the initial synthesised parameters of line width, intensity and position from the three profile envelope. The results were impressive; every parameter agreed with the initial value to better than a tolerance of  $10^{-3}$ . The equivalent line positions could be found to better than ~5 $\mu\text{m}$ . This suggested that the 20 $\mu\text{m}$  map digitiser accuracy did not limit the final accuracy in the profile fitting process. The sampling had little effect once a minimum of 20pts/profile had been exceeded.
- The resonance lines of DITE spectrum #20, used in the dispersion function calibration in Chapter 2, were determined with a plate measuring device, with 2-dimensional readout to  $\pm 5\mu\text{m}$ . The measured position of the first two lines  $\lambda_1$ ,  $\lambda_2$  from Table 2.2 were separated by  $1.750 \pm 0.008\text{mm}$ . These two lines were digitised and analysed using Gaussian profiles (Chapter 5) and the separation of the centroids determined to  $1.743 \pm 0.001\text{mm}$ . When the digitising errors were included, the separation was finally set at  $1.743 \pm 0.004\text{mm}$ . The agreement between the two different measuring techniques was excellent.

The digitisation and analysis processes were further tested when compared to direct digitisation methods at the Laser Division, RAL and the Nuclear Physics Department, Oxford University. In all cases, the final wavelength calibration accuracy was intrinsic to the data and not the digitisation process outlined above.

### 4.3 Filters and Transmission Calculations

Much work was spent early this century in experimentally characterising the absorption properties of different materials<sup>73</sup>. The absorption of x-radiation by a metal layer was observed to be strongly dependent upon the material thickness and its absorption coefficient at that wavelength. For wavelengths less than the K-absorption edge, the mass absorption coefficient  $\mu_a$  can be written empirically as<sup>73</sup>:

$$\mu_a = \mu/\rho = F\lambda^3 + \text{const.} \quad (4.3)$$

where  $\mu$  is the linear absorption coefficient of the absorbing material,  $\rho$  is the density of the material and  $F$  is almost constant. The general absorption law for the attenuation of monochromatic radiation through material of thickness  $x$  can be written as:

$$I = I_0 \exp(-\mu x) \quad (4.4)$$

where  $I_0$  is the incident beam intensity and  $I$  is the filtered beam intensity. The transmission coefficient  $T(\lambda)$ , which is dimensionless, is defined as:

$$T(\lambda) = \frac{I}{I_0} = \exp(-\mu x) \quad (4.5)$$

and is related simply to the absorption coefficient  $A(\lambda)$  by:

$$T(\lambda) = 1 - A(\lambda) \quad (4.6)$$

Generally filters or windows are used with spectrometers to pass or regulate certain wavelengths of interest whilst excluding other radiation outside this band. In practice, the unwanted radiation is not excluded completely, but the intensity can be reduced to an almost negligible level by absorption in the filter material. Possible reasons for using filters are varied and may include:

- Reducing heat load from infra-red and visible radiation on the crystal by placing a filter between the thermal x-ray source and crystal. A thin Aluminium reflecting layer on a plastic base is usually sufficient.
- Minimising crystal fluorescence caused by broad band x-ray emission from source. It is often difficult though, to filter out a "hard" x-ray component without resorting to a geometrical solution.
- Protecting a visible (or ultra-violet) light sensitive detector from scattered or direct radiation from the source.
- Simply reducing the signal intensity to prevent detector saturation.
- Minimising strong higher order reflections or adjacent lines.

Crystal fluorescence was not a problem here because of the choice of low Z crystals and the spectrometer geometry. The x-ray signal intensity was never high enough to drive the film response into saturation, optical densities being less than  $D_{0.1}=2$ . The main use of filters in this work was to prevent film fogging from visible and UV light and to reduce crystal heating.

Some useful formulae can be derived, based on equation (4.5). Two examples are given below.

#### Family of Transmission Curves

A family of transmission curves  $T_2(\lambda)$  of material thickness  $x_2$  can be extrapolated given the transmission  $T_1(\lambda)$  for thickness  $x_1$ . They are related by the expression:

$$T_2(\lambda) = \exp \left[ \frac{x_2}{x_1} \ln(T(\lambda)) \right] \quad (4.7)$$

#### First Order Supression

Another situation, where it may be desirable to suppress a first order wavelength  $\lambda_1$  while looking for the second order  $\lambda_2$ , can be achieved as follows. The transmission, of a material of thickness  $x$ , is  $T_1(\lambda)$  for  $\lambda_1$  and  $T_2(\lambda)$  for  $\lambda_2$  so that a ratio  $R = T_1(\lambda) / T_2(\lambda)$  can be defined for the relative transmission for the two wavelengths. It is then necessary to calculate  $x'$  that will give the suppression ratio  $R'$  where  $R' = T'_1(\lambda) / T'_2(\lambda)$ . Again this is a simple relation:

$$x' = x \frac{\ln(R')}{\ln(R)} \quad (4.8)$$

Where transmission curves were not already available, filter absorption/transmission information was calculated from the atomic cross-section data tabulated in Veigele<sup>74</sup>. Comparisons between calculated and measured transmission data usually agreed to 1→2%. Light-tight filters for the film cassette were made from 2μm Mylar (C<sub>10</sub>H<sub>8</sub>O<sub>4</sub>) coated with 1500Å of Aluminium and were suitable for the x-ray band below 10Å. Thin polypropylene (CH<sub>2</sub>) windows, for above 10Å, could be stretched from an initial 22.5μm thickness to less than 0.5μm, tested by geometrical and x-ray techniques<sup>54</sup>. These were rendered light-tight by a graphite spray which added ~1.5μm carbon to the overall thickness. Transmission curves for these filters are shown in Fig 4.3 (a), (b) and (c) for different thicknesses.

TRANSMISSION OF MYLAR (POLYETHYLENE TEREPHTHALATE)  $C_{10}H_8O_4$

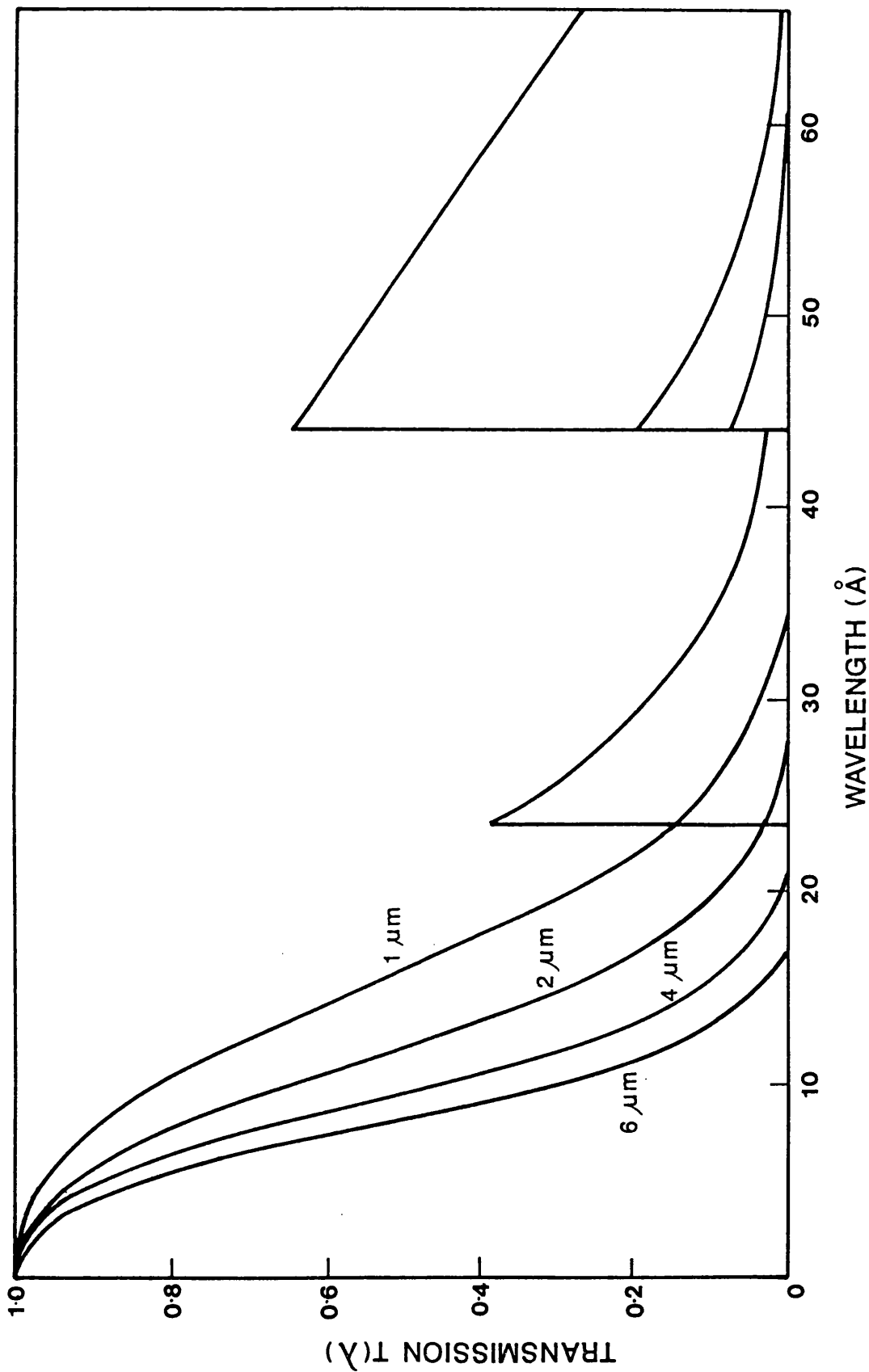


Figure 4.3(a) Transmission curves for Mylar of 1  $\rightarrow$  6  $\mu\text{m}$  thickness.

TRANSMISSION OF POLYPROPYLENE CH<sub>2</sub>

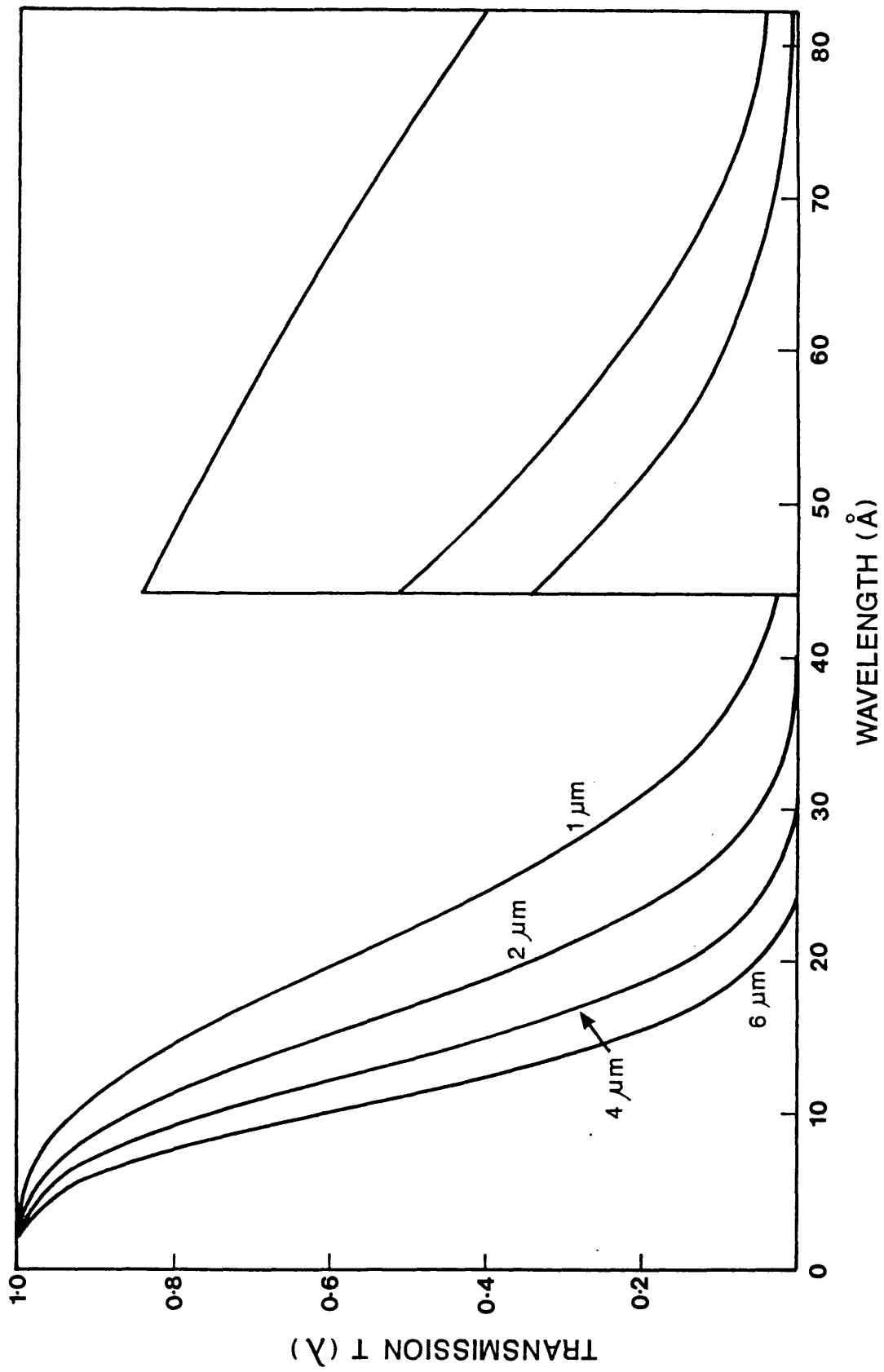


Figure 4.3(b) Transmission curves for Polypropylene of 1→6μm thickness.

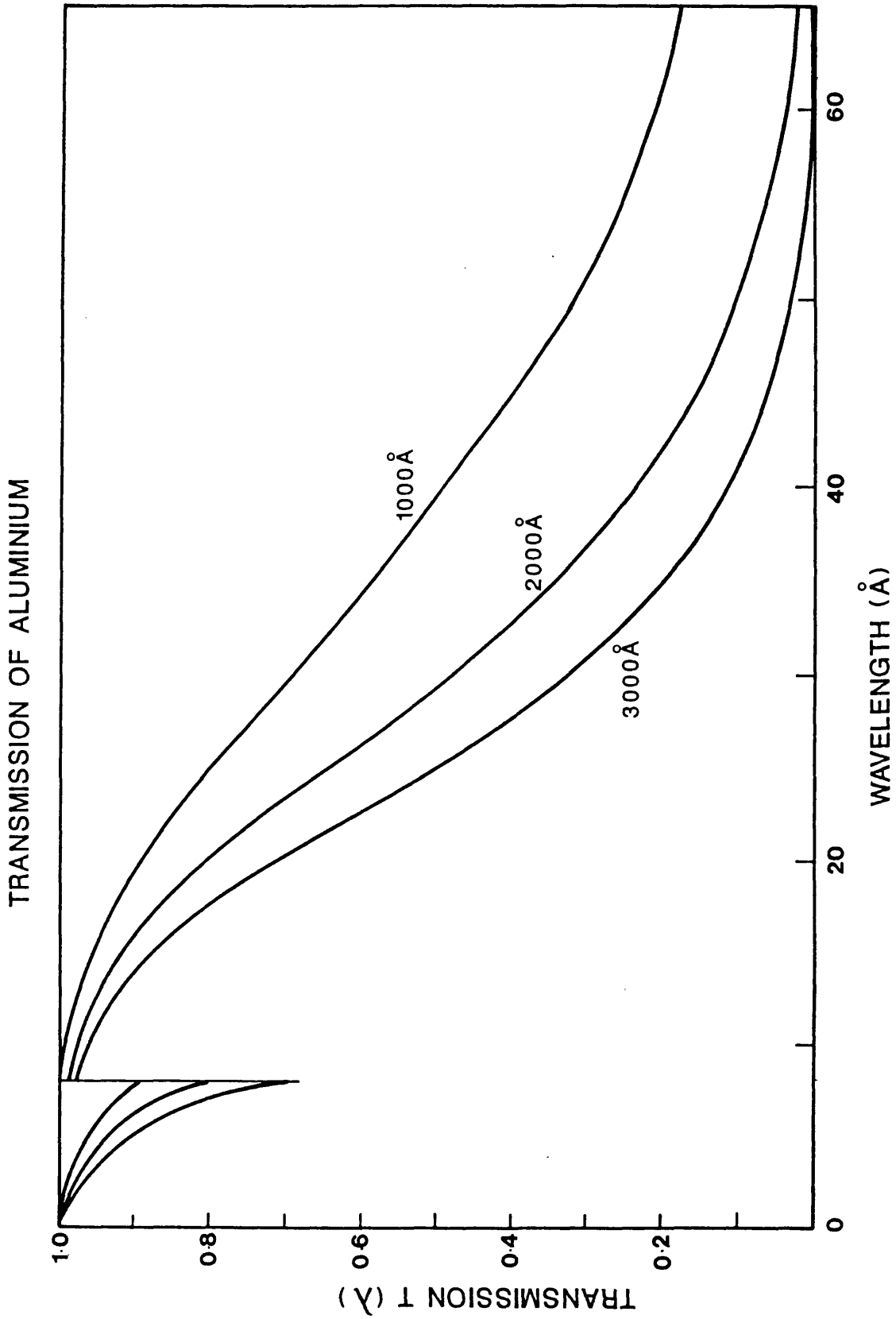


Figure 4.3(c) Transmission curves for Aluminium of 0.1→0.3μm thickness.

## 4.4 Instrument Sensitivity

When analysing the profile of a spectral line, it can be assumed that the instrument response with wavelength effectively remains constant and is free from discontinuities provided the x-ray line is not coincident with absorption edge characteristics of the filters, crystal or detector. The instrument response can vary considerably over the bandpass and is relevant when interpreting resonance line intensity ratios and continuum emission. For an accurate interpretation, the relative instrument response must be calculated. The film response function from Chapter 4.2 can be combined with the dispersion relation in Chapter 2 to determine the total number of photons under any given line regardless of the profile shape. The integrated photon count is directly related to the crystal integrated reflectivity  $R_c$  which together with other factors can be used to define the relative instrumental sensitivity  $S_I(\lambda)$ . This is a modification of the absolute instrumental sensitivity discussed in Chapter 2.  $S_I(\lambda)$  can be written as:

$$S_I(\lambda) = K R_c(\lambda) T(\lambda) F(\lambda) \sin\theta \quad (4.9)$$

The constant  $K$  can be appropriately chosen to include other factors not considered here, like source solid angle collection and crystal radius, to convert the relative sensitivity into an absolute measurement. The other parameters in equation (4.9) include the total filter transmission  $T(\lambda)$  and a factor of  $\sin\theta$  for the geometrical effect on the diffracted crystal area. The film sensitivity  $F(\lambda)$  is defined here as the inverse x-ray photon density in units of  $\text{ph}/\mu\text{m}^2$  needed to register an image optical density of  $D_{0.1}=1$ . The overall uncertainty in the total efficiency is a combination of errors in the above, but is likely to be mainly due to the film and crystal calibration.

The parameter  $S_I(\lambda)$  was calculated for PET (002) and ADP (101) used in the laser and Tokamak work. The integrated reflectivity measurements were taken from the two crystal calibration work of Hall<sup>11</sup> for new and aged crystal samples while the results from Henke et al<sup>70</sup> gave the film sensitivity.  $S_I(\lambda)$  was determined at discrete wavelengths as shown in Figures 4.4 and 4.5. A line is drawn through the points to guide the eye and aid interpolation. Although not shown, some discontinuities at absorption edges are present but are unlikely to vary by more than 5%. The exception to this is the Phosphorous K-edge at 5.79Å for ADP (101). The effect of crystal ageing on the low wavelength region of PET is clearly shown on Fig 4.4.

RELATIVE INSTRUMENTAL SENSITIVITY  $S_I(\lambda)$   
 FOR PET(002) JOHANN SPECTROMETER

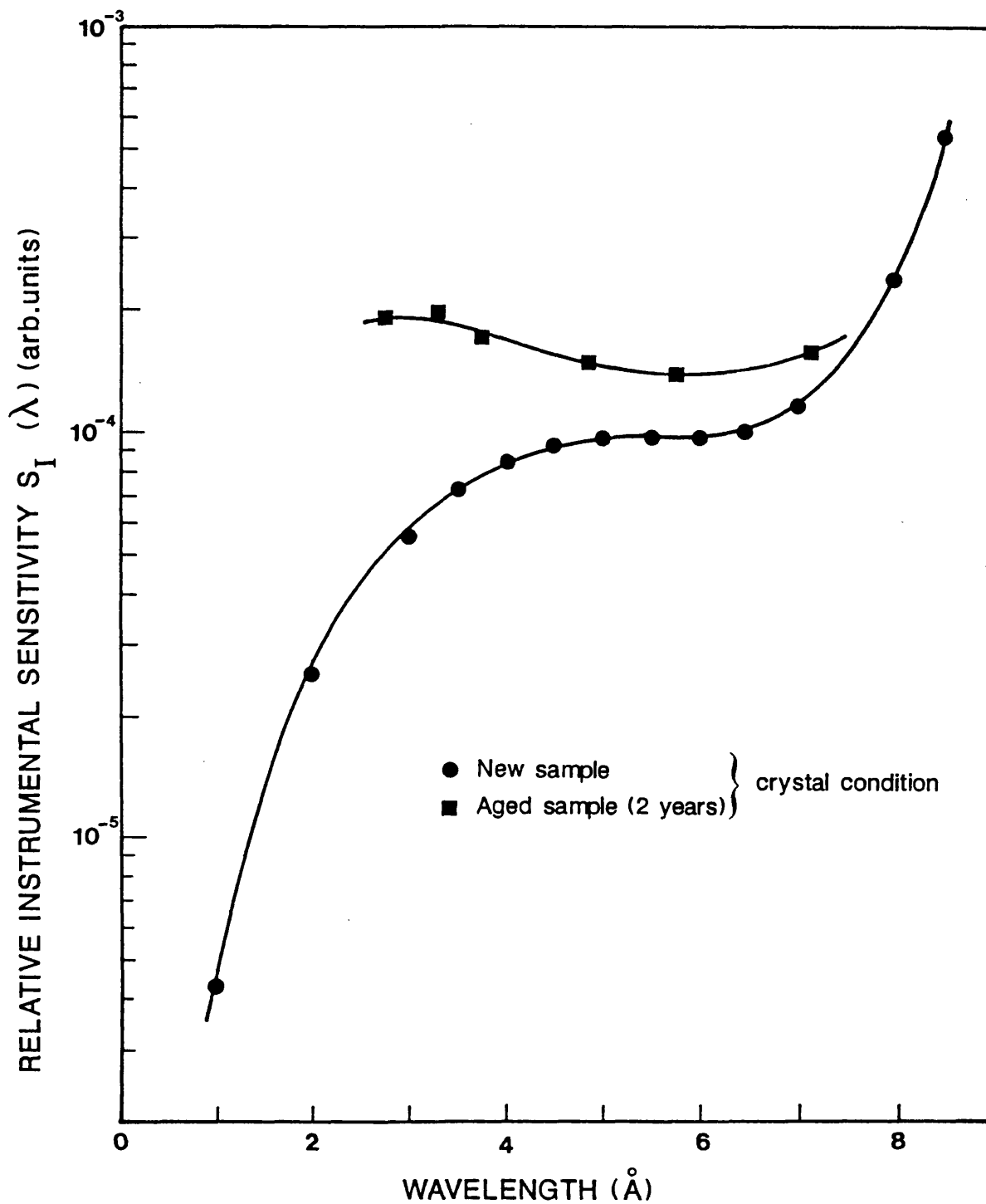


Figure 4.4 Relative sensitivity curve for the PET (002) spectrometer used in the laser produced plasma experiments of Chapter 6 and beam-foil experiment of Chapter 7.

RELATIVE INSTRUMENTAL SENSITIVITY  $S_I(\lambda)$   
FOR ADP(101) JOHANN SPECTROMETER

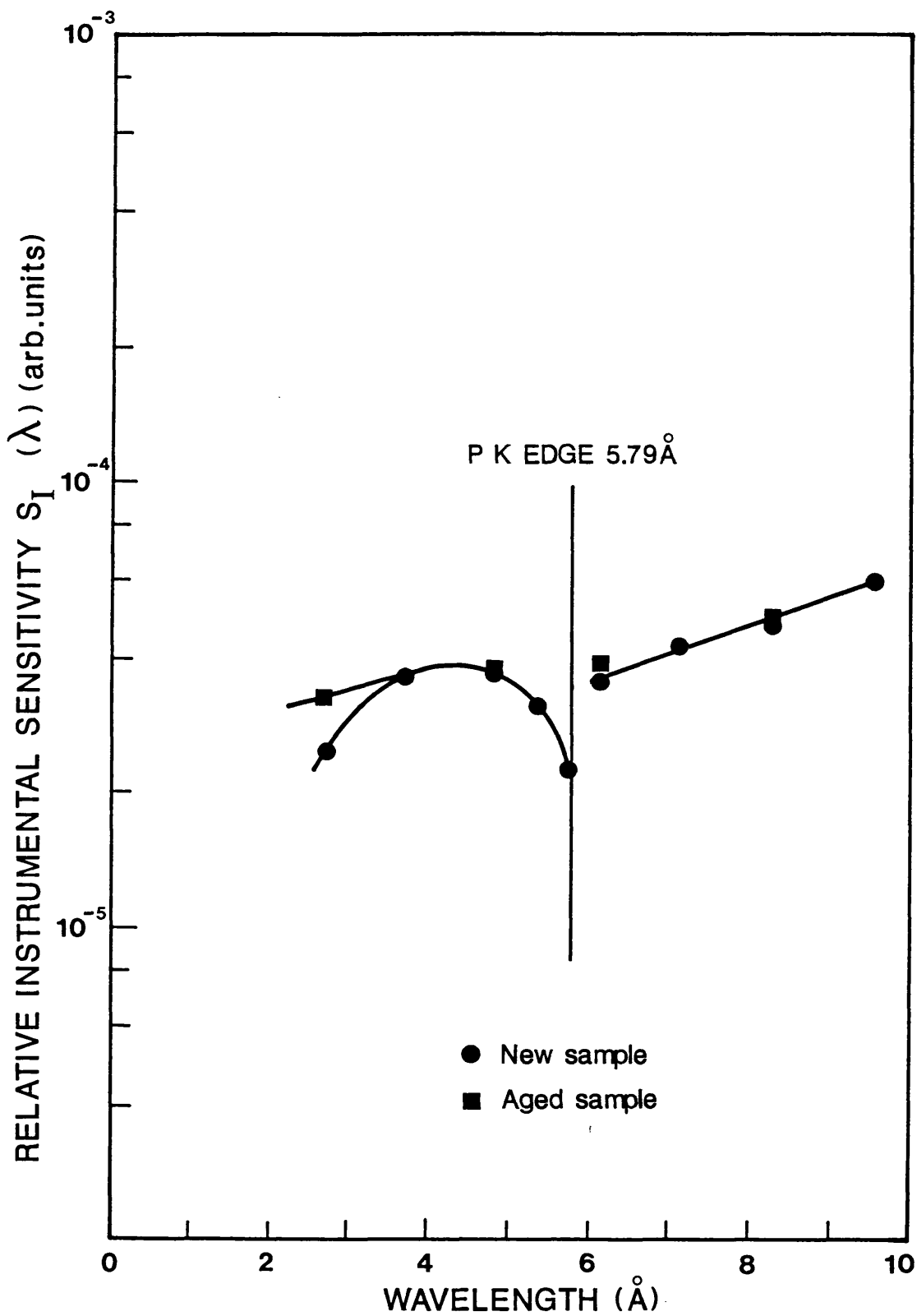


Figure 4.5 Relative sensitivity curve for the ADP (101) spectrometer used in the Tokamak experiments of Chapter 5.

## 4.5 Line Profiles and Analysis

This section deals with the mechanisms which contribute to the overall profile of the x-ray line. Since information concerning the environment of the emitting ion in the plasma can be derived from the line shape, it is important to understand and quantify these processes. Specific topics, for example relevant to high density laser plasmas like Stark broadening and opacity effects, are reserved to Chapter 6. Likewise, broadening effects when observing a Beam-foil source are discussed in Chapter 7.

Before continuing further, a spectral line in general can be described by several parameters:

- (a) The wavelength of the peak intensity.
- (b) Its profile.
- (c) Total line intensity.

The FWHM may warrant special mention under some conditions and can be calculated from (b) and (c).

### 4.5.1 Natural Line Broadening

The natural or radiation line width, due to the radiation process itself, is defined as the intrinsic width of the spectral line emitted by an undisturbed atom or ion at rest. This is linked to the finite energy width  $\Delta E$  of the upper and lower states, but for a transition to the ground state, the line width is equal to the width of the excited state alone. This energy width  $\Delta E$  is related to the lifetime of the state  $\tau$  through the principle of indeterminacy, by:

$$\Delta E \tau = \frac{h}{2\pi} \quad (4.10)$$

$h$  being Planck's constant. The lifetime can also be approximated by the sum of the radiative transition rates  $A_{ji}$  to the lower levels:

$$\frac{1}{\tau} = \sum_{i < j} A_{ji} \quad (4.11)$$

For satellite lines, it may also be necessary to include the autoionization rates.

For Hydrogen, the radiative transition rate for the 1s-2p resonance line is  $A=6.25 \times 10^8 \text{s}^{-1}$  corresponding to a lifetime of  $\tau=1.6 \text{nsec}$ . The line profile is Lorentzian, described analytically in equation (4.21). The radiative transition probabilities scale as  $Z^4$ , therefore by combining the previous equations, the natural line width of the 1s-2p transition for any atomic number can be expressed as:

$$\Delta E = 4.114 \times 10^{-7} Z^4 \quad (4.12)$$

where  $\Delta E$  is the full width at half maximum FWHM energy. Typical examples of high temperature x-ray resonance lines observed in Tokamaks or solar flares below  $10\text{\AA}$  would be from Silicon ( $Z=14$ ) and Iron ( $Z=26$ ). The transition energy scales as approximately  $Z^2$  thus giving a natural line width  $(E/\Delta E)_n=(\lambda/\Delta\lambda)_n$  of  $1.27\times 10^5$  and  $3.7\times 10^4$  respectively. This is considerably smaller than other plasma broadening mechanisms, principally Doppler broadening, and in most cases natural broadening is negligible until  $Z\geq 36$ .

#### 4.5.2 Doppler Broadening

Doppler Broadening of spectral lines is usually the dominant broadening mechanism in most plasma x-ray sources. It can result from the bulk motion of the plasma or from the thermal random motion of the radiating particles. Although the motion occurs in three dimensions, Doppler motion can only be observed when the radiating ion is moving along the line of sight of the spectrometer. For an ion moving with velocity  $v$ , the wavelength of the emitted photon is shifted with respect to the rest frame value  $\lambda_0$  by an amount  $\Delta\lambda$ :

$$\frac{\Delta\lambda}{\lambda_0} = \frac{v}{c} \quad (4.13)$$

where  $c$  is the velocity of light. If the velocities of the ions of mass  $M$  have a thermal Maxwellian distribution of temperature  $T_i$ , the mean thermal velocity  $v_i$  is given by:

$$v_i = \left[ \frac{2kT_i}{M} \right]^{1/2} \quad (4.14)$$

and the velocity distribution function for ion density  $n_i$  is:

$$F(v) = \frac{n_i}{\sqrt{\pi} v_i} \exp \left[ - \frac{v^2}{v_i^2} \right] \quad (4.15)$$

Neglecting the natural line width and substituting for  $v$  and  $v_i$  in (4.15) gives the intensity directly as a function of wavelength:

$$F(\lambda) = A_0 \exp \left[ - \left\{ \frac{\Delta\lambda}{\lambda_0} \right\}^2 \frac{c^2 M}{2kT_i} \right] \quad (4.16)$$

where  $A_0$  is the peak line intensity.  $F(\lambda)$  has the characteristic Gaussian shape where the  $\Delta\lambda$  (FWHM) can be defined as:

$$\Delta\lambda = \frac{2\lambda_0}{c} \left[ \frac{2kT_i \ln(2)}{M} \right]^{1/2} \quad (4.17)$$

This can be conveniently expressed as:

$$\frac{\Delta\lambda}{\lambda_0} = 1.2961 \times 10^{-4} \left[ \frac{M}{T_i} \right]^{1/2} \quad (4.18)$$

where the ion temperature  $T_i$  and the ion mass  $M$  have the units of the eV and amu respectively. Table 4.4 shows the line broadening parameter  $(\lambda/\Delta\lambda)$  as a function of the ion

temperature for elements likely to be found intrinsically or injected into a Tokamak; eg ion temperature  $T_i=1000\text{eV}$ , corresponding to  $11.6 \times 10^6\text{K}$ , gives Doppler broadening  $(\lambda/\Delta\lambda)_D=1841$  for Ne, 2172 for Si and 3063 for Fe. The last two elements were routinely observed as intrinsic impurities in DITE Tokamak.

Measurement of the spectral line Doppler width can determine the thermal ion temperature  $T_i$ . Doppler spectroscopy is one of the standard methods for measuring very high  $T > 10^6\text{K}$  temperatures experimentally. The statistical accuracy of the ion temperature evaluation can also be improved by using all the data points in the line profile to determine the shape and line width of the characteristic Gaussian. Also, contributions from other instrumental, intrinsic or pressure broadening mechanisms must be included in the analysis to extract the thermal broadening.

It is clear that to resolve the line profile in some detail, the instrumental resolving power must be several times greater than the Doppler width, requiring  $\lambda/\Delta\lambda=10^4$  or better. A further criterion is that the chosen line should be intense and separate from adjacent lines.

### 4.5.3 Voigt Profile

The measured profile of the spectral line is often determined by several factors which can be regarded as independent parameters to be mathematically superimposed. Since these different broadening mechanisms have largely Lorentzian  $L(x)$  or Gaussian  $G(x)$  spectral profiles, the combination takes on the properties of both functions and cannot be described easily. The spectral line intensity distribution of the superposition can be written as a folding integral:

$$\psi(x, \eta) = \int_{-\infty}^{+\infty} L(y) G(x-y) dy \quad (4.19)$$

known as a Voigt profile, where the parameters  $x, y$  represent wavelength or energy about the line centroid. The Gaussian profile  $G(x)$ , for example in Doppler broadening, can be represented by:

$$G(x) = A \exp \left[ - \left\{ \frac{x}{\beta_2} \right\}^2 \right] \quad (4.20)$$

where  $\beta_2$  is the Gaussian width and  $A$  is a constant. The Lorentzian profile  $L(x)$  for intrinsic, instrumental and pressure broadening can be described by:

$$L(x) = \frac{B}{1 + \left\{ \frac{x}{\beta_1} \right\}^2} \quad (4.21)$$

where  $\beta_1$  is the Lorentzian width and  $B$  is a constant. The parameter  $\eta$  in (4.19) describes the relative widths of the two functions by  $\eta = \beta_2/\beta_1$ .

**Table 4.4 Doppler Broadening of X-ray Emission Lines for Z=10→42 Ions on DITE and JET, as a Function of Ion Temperature.**

Z	Element	M	IP (eV)	$\lambda$ (Å)	Doppler Broadening $\lambda/\Delta\lambda$															
					10	20	50	100	200	500	700	1000	1200	1500	2000	3000	5000	10000		
10	Neon	20.18	1196	12.13	18412	13019	8234	5822	4117	2604	2201	1841	1681	1503	1302	1063	823	582		
12	Magnesium	24.31	1762	8.419	20208	14290	9037	6390	4519	2858	2415	2021	1845	1650	1429	1167	904	639		
13	Aluminium	26.98	2086	7.171	21289	15054	9521	6732	4760	3011	2544	2129	1943	1738	1505	1229	952	673		
14	Silicon	28.09	2438	6.180	21723	15360	9715	6869	4857	3072	2596	2172	1983	1774	1536	1254	972	687		
16	Sulphur	32.06	3324	4.727	23207	16410	10379	7339	5189	3282	2774	2321	2119	1895	1641	1340	1038	734		
17	Chlorine	35.45	3659	4.185	24403	17256	10913	7717	5457	3451	2917	2440	2228	1992	1726	1409	1091	772		
18	Argon	39.95	4121	3.731	25906	18318	11585	8192	5793	3664	3096	2591	2365	2115	1832	1496	1159	819		
22	Titanium	47.88	6249	2.491	28361	20054	12683	8968	6342	4011	3390	2836	2589	2316	2005	1637	1268	897		
26	Iron	55.85	8828	1.778	30630	21659	13698	9686	6849	4332	3661	3063	2796	2501	2166	1768	1370	969		
28	Nickel	58.69	10289	1.530	31399	22203	14042	9929	7021	4440	3753	3140	2866	2564	2220	1813	1404	993		
32	Germanium	72.59	13557	1.167	34920	24692	15617	11043	7808	4938	4174	3492	3188	2851	2469	2016	1562	1104		
36	Krypton	83.80	17296	0.918	37520	26530	16779	11865	8390	5306	4484	3752	3425	3064	2653	2166	1678	1187		
42	Molybdenum	95.94	23810	0.669	40146	28387	17954	12695	8977	5677	4798	4015	3665	3278	2839	2318	1795	1270		

Z Atomic number of ion.

M Atomic mass in units of amu, quoted accuracy to last significant figure <sup>75</sup>.

IP Ionization energy<sup>75,76</sup>, in electron volts, required to remove one electron from a He-like ion, ie having two electrons before ionization.

$\lambda$  Wavelength of the Lyman- $\alpha_1$  transition<sup>75</sup>.

$\lambda/\Delta\lambda$  Doppler broadened values, where  $\Delta\lambda$  refers to FWHM of spectral line, from equation (4.18); accuracy to one place in fourth significant figure.

$T_1$  Ion temperature expressed in electron volts (eV); 1eV is equivalent to a particle temperature of 11605 K.

### Combining Voigt Profiles

It may be noted that when two Voigt profiles of parameter  $\eta'$  and  $\eta''$  are folded together, then another Voigt profile  $\eta$  is formed where:

$$\beta_1 = \beta_1' + \beta_1'' \quad (4.22)$$

$$(\beta_2)^2 = (\beta_2')^2 + (\beta_2'')^2 \quad (4.23)$$

$$\eta = \frac{\beta_2}{\beta_1} \quad (4.24)$$

Essentially the Lorentzian line widths add linearly while the Gaussian components add quadratically. The overall Lorentzian  $\beta_1$  and Gaussian  $\beta_2$  components give the new Voigt profile. This is an important property which allows the different contributions, for example the Lorentzian function from both the intrinsic and instrumental widths, to be treated quantitatively.

### Voigt Profile Synthesis

Perhaps one major problem with the Voigt profile lies in the computational time needed to produce the function. The various forms of  $\psi(x, \eta)$ , shown below, are integrals which cannot be described analytically, but have to be calculated numerically. This requires the evaluation of an integral over the limits described in equation (4.19) for each point in the spectral profile. Some authors Wertheim et al<sup>77</sup> and Richard et al<sup>78</sup> have proposed the use of a "pseudo-Voigt" profile (this author's description) composed of a linear addition of a Lorentzian and Gaussian functions of the same line width but with relative intensity parameter. Although this function can be quickly synthesised, the composite functions do not have the same meaning as a Voigt profile. It is also only a crude approximation to the voigt line shape. For these reasons, it does not merit further discussion.

An accurate tabulation, better than  $10^{-4}$ , has been calculated by Davies and Vaughan<sup>79</sup> which describes the Voigt profile as a series of widths as a function of the FWHM at various intensities. They do this for a range of Voigt parameters  $\eta=0.1 \rightarrow 10.0$  in logarithmic intervals, based on the following definition of the Voigt integral:

$$\psi(x, \eta) = \frac{1}{\eta\sqrt{\pi}} \int_{-\infty}^{+\infty} \frac{\exp\{-[(x-y)/\eta]^2\}}{1+y^2} dy \quad (4.25)$$

They use the convention of the Lorentzian function of  $(1+x^2)^{-1}$  of FWHM  $\delta=2$  units folded with the Gaussian function  $(\eta\pi^{1/2})^{-1} \exp\{-[x/\eta]^2\}$  of FWHM  $\delta=2\eta(\ln 2)^{1/2}$  units; this defines a Lorentzian/Gaussian width ratio of 1.2112/1 for  $\eta=1$ . This convention is adopted here, also. An alternative form<sup>79</sup> for  $\psi(x, \eta)$  was used in this work and can be written as:

$$\psi(x, \eta) = \int_0^{+\infty} \cos(x\xi) \exp \left\{ -\xi - \frac{(\xi\eta)^2}{4} \right\} d\xi \quad (4.26)$$

A copy of the Fortran computer code with comments is given in Appendix II. The main objective was to create a fast, accurate (better than  $5 \times 10^{-6}$ ) voigt profile code which could synthesise the function for any value of the parameter  $\eta$ . It was tested against the tabulation of Davies and Vaughan, whose accuracy was quoted as being uncertain in the fifth decimal place, and agreed to within  $10^{-5}$  FWHM for any chosen parameter  $\eta$ . Leicester University Computer Centre's DEC Vax8650 with VMS 5.1 software was used for all the data analysis in this work. The code could be run on this machine and duplicate the complete table, containing  $27 \times 21$  entries, within 80 seconds of CPU time. This was thought to be a very respectable time for the calculation, though obviously not as fast as a pure Lorentzian or Gaussian function. Computation times are not listed for similar functions in the literature.

Figure 4.6 gives an example of the Lorentzian, Gaussian and Voigt ( $\eta=1$ ) profiles for comparison. The peak intensity and widths have been normalised and the logarithmic intensity plot in Figure 4.6(b) shows clearly the wing feature of the Voigt and Lorentzian line shapes.

#### 4.5.4 Spectral Line Profile Fitting

Finally, the three profiles: Lorentzian/Holtzmarkian (two specific examples of a power law function); Gaussian and Voigt were all included in a general fitting code. This accepted the experimental data as linear x-ray intensity with position or wavelength. A suitable spectral function could be selected on the grounds of the line shape appearance, leaving the code to optimise the profile parameters of line width, intensity, centroid position, background and possibly Voigt parameter  $\eta$  or power  $n$  if appropriate. A sloping continuum background could be accommodated in the fit. The multi-dimensional parametric space was carefully defined by choosing sensible upper and lower limits for each variable in order that the code would run efficiently.

The effectiveness of the fit could be examined by looking at the residuals, the differences between the code simulation and the actual experimental data. A figure of merit, summing the square of the differences between the data and the fit, was also available for quickly assessing the quality of the fit. As many as twenty spectral lines could be simultaneously fitted with the assumption that each line had the same width and shape. Since the dispersion was constant to within 1% for small wavebands this assumption was acceptable. Linewidths which were different for reasons other than dispersion were fitted

Comparison between Gaussian, Lorentzian and Voigt functions.

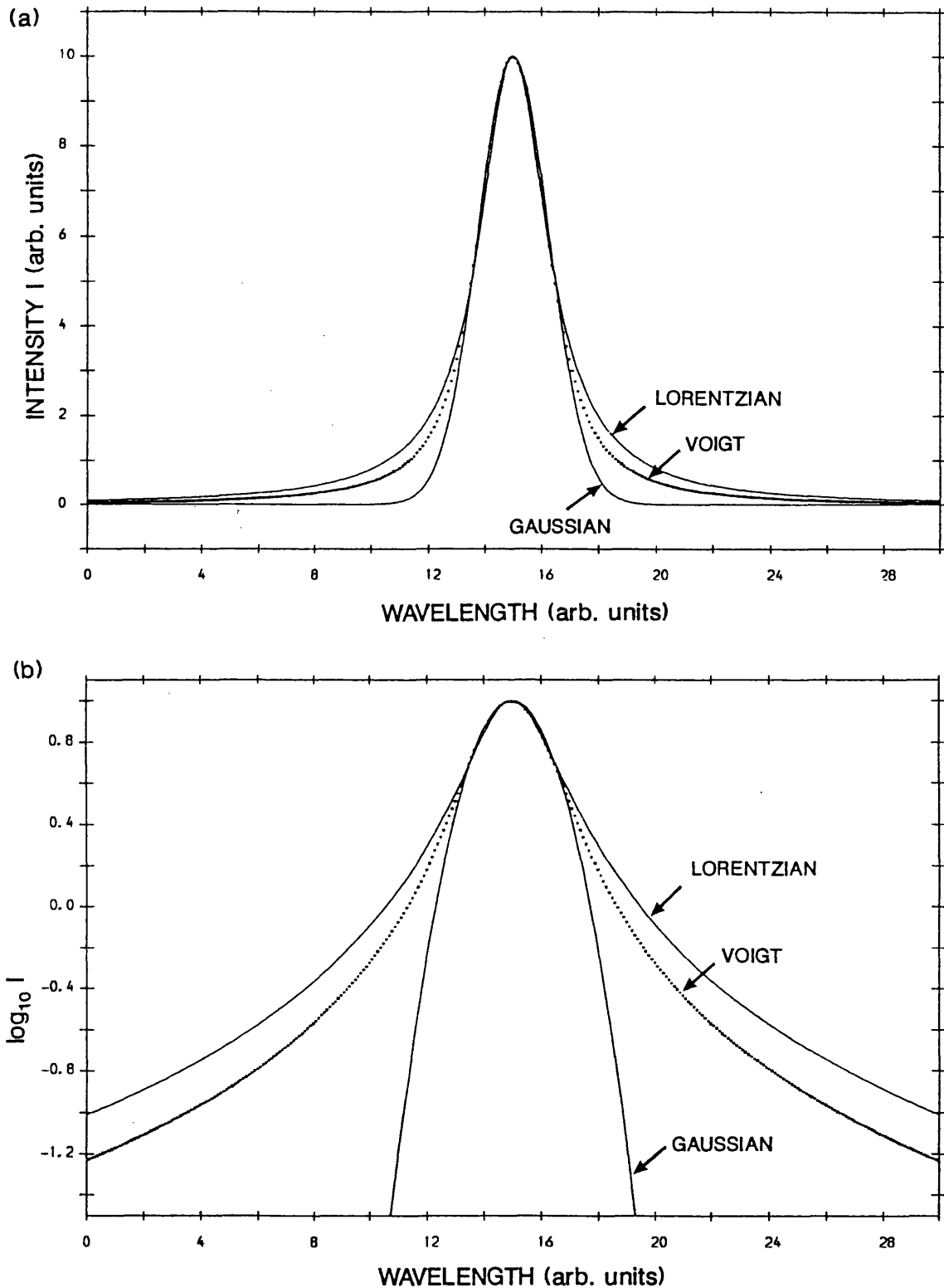


Figure 4.6 The above are examples of Gaussian, Lorentzian and Voigt ( $\eta=1$ ) functions normalised for intensity and FWHM. Intensity and wavelength scales are in arbitrary units. Diagram (b) is the same as (a) but with intensity plotted on a logarithmic scale. The wing features of the Lorentzian and Voigt functions are clearly visible. The Voigt profile should converge to the Gaussian function by increasing the parameter  $\eta$ .

separately. Examples of this were encountered in the laser plasma spectra where resonance lines were optically thick while the satellites remained optically thin.

Complicated spectra of many lines, with varying degrees of blend, were fitted in stages. Single lines, well-resolved or partially blended, were fitted at first to get an accurate profile width and shape. The number of lines was gradually increased to include blended lines. This could be done successfully, provided the most complex envelope was obviously blended, ie asymmetric, and contained no more than three individual lines.

## 4.6 Discussion

Before leaving the instrumentation section of Part I, final comments on instrumental resolving power for any waveband are discussed.

There is some scope for improving the performance of the present Johann spectrometer to achieve a resolving power of  $\lambda/\Delta\lambda \sim 40000$ ; this would be of considerable benefit in precision spectroscopy of Beam-foil sources (see Chapter 7), or ion temperature measurements of Tokamak plasmas (Chapter 5).

In the pursuit of extremely high resolution in any particular x-ray band, a Johann spectrometer is limited in two fundamental areas; namely the diffraction profile of the crystal and the spatial resolution of the detector. The former applies to all Bragg crystal spectrometers, while the latter is often replaced by a requirement for x-ray beam collimation. The other parts of the instrument e.g. the bending jig must also be able to match this performance.

### Overview on Crystal Resolving Power

The main question here is typically what can crystal spectroscopy achieve in resolving power for a particular waveband. An inspection of Table 4.1 or Table V of Burek<sup>12</sup> indicates that there are several likely candidates in the low wavelength region but difficulties occur in the longer band. Starting at the lower end of the  $1 \rightarrow 25\text{\AA}$  band, Quartz crystals with the diffracting planes  $(20\bar{2}\bar{3})$  where  $2d=2.750\text{\AA}$ , and  $(22\bar{4}\bar{3})$  where  $2d=2.028\text{\AA}$ , have resolving power of  $\lambda/\Delta\lambda=10^5$  and  $\lambda/\Delta\lambda=2 \times 10^5$  respectively. The corresponding integrated reflectivities for each plane are  $R_c \sim 1.5 \times 10^{-5}$  rad and  $R_c \sim 6 \times 10^{-6}$  rad. In the first instance, the waveband for very high resolving power appears to be limited to below  $2.5\text{\AA}$ .

Although there are many examples of crystals with moderately high resolving power  $\lambda/\Delta\lambda=10^4$  in the region below  $10\text{\AA}$  eg ADP (101), finding crystals with higher resolving power to apply to the region above  $2.5\text{\AA}$  is difficult. However, theoretical calculations<sup>11</sup>, see Figures 4.7 and 4.8 for the crystals ADP (101) of  $2d=10.6\text{\AA}$  and PET (002) of  $2d=8.74\text{\AA}$ , show that considerably higher resolving powers  $\lambda/\Delta\lambda=5 \times 10^4$  are available in the higher order diffraction planes. This could potentially extend the region up to  $5\text{\AA}$ , or even  $6.2\text{\AA}$  using

Mica (006) with  $2d=6.61\text{\AA}$ , with the proviso that the crystal diffraction profile should be verified by making 2-crystal measurements.

KAP (001) gives medium resolving power  $\sim 1500$  which is as expected for  $10\rightarrow 25\text{\AA}$ , but is not sufficiently high to make ion temperature measurements. There are exceptions to this, and they extend high resolution spectroscopy above  $10\text{\AA}$ . Beryl ( $10\bar{1}0$ ) is extremely useful because it has better resolving power,  $\lambda/\Delta\lambda=2500\rightarrow 3000$  for  $12\rightarrow 15\text{\AA}$ . KAP (002) is reported to have resolving power approaching  $\sim 9000$  to  $13\text{\AA}$  by Burek<sup>12</sup> and this is largely confirmed in Chapter 7.

It can be concluded that high resolution crystal spectroscopy,  $\lambda/\Delta\lambda\geq 10^4$ , is possible below  $13\text{\AA}$ .

### **Spectrometer Geometry**

Perhaps a convenient starting point is the crystal bending jig itself, which was shown to generate crystal curvatures corresponding to  $\lambda/\Delta\lambda\geq 50000$  in Chapter 3. The achieved stability of the crystal jig was of equal importance. Secondly, all Johann and other geometrical aberrations (Chapter 2) have to be held at a negligible level,  $\lambda/\Delta\lambda\geq 10^5$ . This is readily attained by using a crystal curvature greater than  $R=2\text{m}$ , choosing the correct crystal aperture and recording the spectrum at a high Bragg angle  $\theta\geq 60^\circ$  by appropriate choice of crystal lattice spacing. For beam-foil sources, the small source spatial emission profile, regardless of axial or perpendicular observation, also assists here.

### **Optimised Detector System**

The properties of an x-ray film like Kodak DEF 392 when used for recording spatial information can be briefly summarised in Table 4.5. Comparison with other detector systems, show that CCD detectors in particular are superior to film in most of the aspects of the above.

The choice of detector is based ideally on good 2-D spatial resolution  $\Delta x\leq 100\mu\text{m}$ , though 1-D is sufficient, and high quantum detection efficiency coupled to an inherently low S/N ratio. X-ray film satisfies the former, with typically  $\Delta x=5\rightarrow 10\mu\text{m}$ , but is low in sensitivity and S/N ratio. The recent development, however, of CCD detectors for x-ray application<sup>80</sup> have introduced exciting new possibilities, particularly when considered in conjunction with wavelength dispersive spectrometers. They have a large QDE $\sim 50\%$  over the  $1\rightarrow 10\text{\AA}$  band, especially the high resistance large depletion devices, and the pixel size is  $22\times 22\mu\text{m}^2$ .

A full frame of the standard TV compatible devices can be read out every 20msec, an example of a spectrum is shown in Chapter 5. This time resolution can be improved to 1msec by clocking out only part of the frame displaying a small number of spectral lines. This is extremely useful for measuring Tokamak plasma instabilities, for example the saw teeth phenomenon, occurring on the same time scale.

### **Table 4.5 Summary of X-ray Film Properties.**

#### **Advantages:**

- (a) Good spatial resolution, often described as the Modulation Transfer Function MTF and expressed in lines/mm, is unmatched by all present photoelectric systems in 2-D (3-D if film layers are stacked but only for high energy photons or particles).
- (b) Characteristics are well established; accurate photon density as a function of optical density available for most present x-ray films.
- (c) Good dynamic range  $\sim 10^3$  in x-ray photon densities from detection threshold to saturation. In practice, the useful region where profile analysis is needed extends to about a factor of fifty.
- (d) Ease of use; apart from need of light tight filters to stop visible and UV radiation from fogging film. (These filters are also needed in many photo-electric detectors).
- (e) Low cost.
- (f) Large range in exposure time by about sixteen orders of magnitude  $10^{-11} \rightarrow 10^5$  secs for this work.

#### **Disadvantages:**

- (g) No time resolution.
- (h) No photon energy resolution; important in noise rejection and a feature of proportional counters and photon-counting CCDs. It is useful for identifying higher diffraction orders from the spectrum and additional information from the source.
- (i) Low Quantum Detection Efficiency QDE; much less efficient than all photo-electric detectors.
- (j) Low S/N ratio; as with (i), extracting detailed information about the line shape requires considerably larger photon densities when compared with photo-electric detectors. Generally,  $10^6$  photons would be needed in a single spectral line recorded on film where  $10^4$  photons would be sufficient on an optimised detector system. It may be noted that the geometry of the Johann spectrometer is very effective at reducing the background source related noise. The detector does not view the x-ray source directly while x-ray fluorescence from the crystal is very small. Virtually all the spectra presented in this work are limited by inherent film grain noise.
- (k) Non-linear response and procedure needed to digitise information onto computer for analysis, make film an inefficient medium.

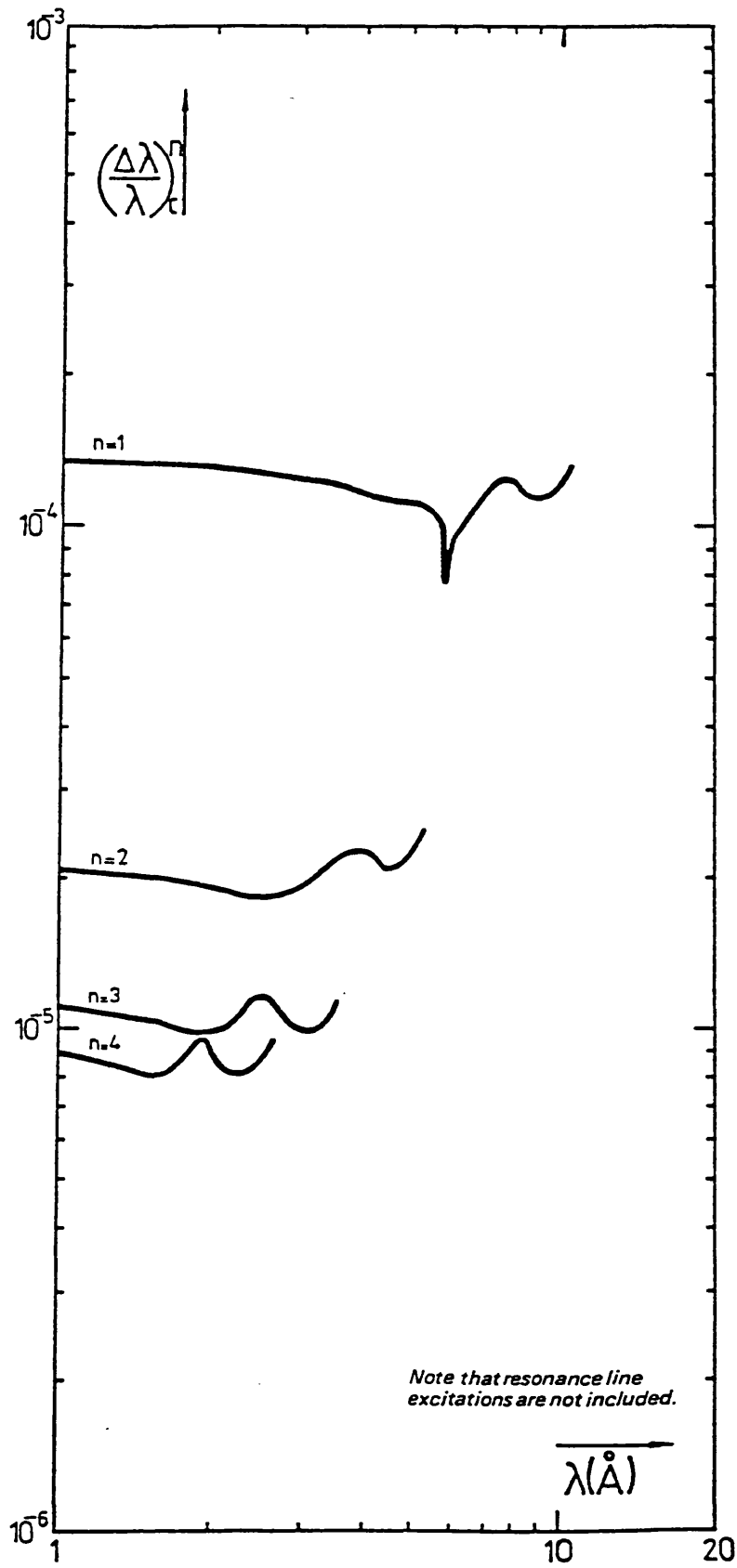


Figure 4.7 1-reflection resolution for reflection orders  $n=1 \rightarrow 4$  of ADP (101), after Hall<sup>11</sup>.

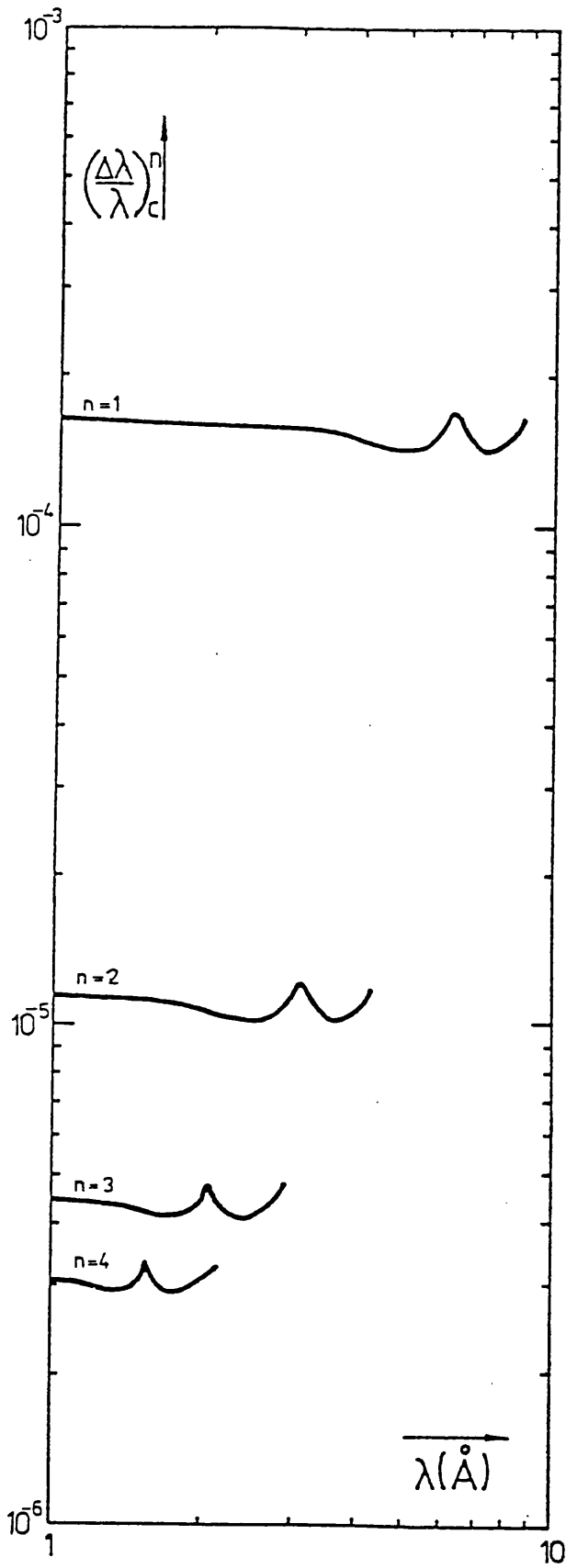


Figure 4.8 1-reflection resolution for reflection orders  $n=1 \rightarrow 4$  of PET (002), after Hall<sup>11</sup>.

When cooled to  $-100^{\circ}\text{C}$  and used with a low photon emission source, count rates of  $0.1\text{ph/pixel}/(\text{integration period})$  over the CCD area, they become an energy dispersive photon counting device with energy resolution of  $\Delta E \leq 200\text{eV}$ . Thus background noise, higher orders and crystal fluorescence can be discriminated. By matching the spectrometer dispersion to the pixel size of the CCD, the instrument can be optimised. For example, high instrumental resolving power of  $\lambda/\Delta\lambda \sim 40000$  could be achieved by allowing  $\sim 4\text{pixels}/\text{FWHM}$ , choosing a  $2\text{m}$  detector/crystal chord length and a Bragg angle  $\theta \sim 60^{\circ}$ .

One criticism concerning CCD devices is their small TV compatible format giving an active area of  $\sim 8 \times 6\text{mm}^2$ , which effectively limits the instrumental bandpass. The advent of large format  $27 \times 25\text{mm}^2$  chips from EEV<sup>81</sup> are beginning to overcome this restriction and therefore are more useful for spectrometer applications.

## **Part II**

## Chapter 5 Tokamak Plasmas.

	Introduction.	106
5.1	Introduction to Atomic Processes.	106
	5.1.1 The Emission Spectrum.	106
	5.1.2 Ionization, Recombination and Excitation Processes.	107
5.2	Line Emission.	108
	5.2.1 Introduction.	108
	5.2.2 Electron Impact Excitation.	109
	5.2.3 Dielectronic Recombination - Satellite Lines.	110
	5.2.4 Inner-Shell Excitation - Satellite Lines.	111
5.3	Plasma Models.	112
	5.3.1 Coronal Equilibrium Model.	112
	5.3.2 Local Thermodynamic Equilibrium Model.	114
	5.3.3 Collisional Radiative Equilibrium Model.	114
5.4	Controlled Nuclear Fusion and Tokamaks.	115
	5.4.1 Nuclear Fusion Programme.	115
	5.4.2 Tokamak Devices.	121
5.5	Ion Temperature Measurements.	122
	5.5.1 Different Methods.	122
	5.5.2 Instrument Description for DITE Measurements.	126
	5.5.3 He-like Ion Emission.	132
	5.5.4 Toroidal Rotation during Neutral Beam Injection.	144
5.6	The Bragg Rotor 2-Crystal Spectrometer.	145
	5.6.1 Instrument Description and Experiment.	145
	5.6.2 Results and Analysis.	145
5.7	Time-resolved Spectra Using a CCD Detector.	149
	5.7.1 Description.	149
	5.7.2 Results.	150
5.8	Discussion and Conclusions.	154

## Introduction

This chapter deals with the following topics:

- Introduction to atomic processes in high temperature plasmas giving rise to continuum and line emission. Models relevant to the plasma density regime are discussed.
- Brief introduction to controlled nuclear fusion and different confinement schemes.
- Description of Tokamaks.
- Ion temperature measurements and observations of DITE during neutral beam injection using the Johann spectrometer.
- Ion temperature measurements of DITE using the Bragg rotor 2-crystal spectrometer.
- Initial time-resolved spectra using a commercial CCD detector.
- Some conclusions and general discussion.

## 5.1 Introduction to Atomic Processes.

### 5.1.1 The Emission Spectrum.

The electro-magnetic spectrum emitted from a high temperature plasma is characterised by resonance lines and continua. The atomic processes which give rise to this spontaneous emission of a photon of energy  $h\nu$  can be described in three categories:

(i) **Free-Free:**



where  $E$ ,  $E'$  refer to the initial and final energies of the electron such that  $E > E'$  and  $E = E' + h\nu$ . This process is called bremsstrahlung and is produced when a free electron makes a transition, without becoming bound, in the presence of an ion  $X$  of charge  $Z$ . Continuum emission is observed for a Maxwellian distribution of initial electron states.

(ii) **Free-Bound:**



where  $E$  is the initial energy of the free electron,  $h\nu = E + \chi_n$  and  $\chi_n$  is the ionization potential for an ion  $X^{+Z}$  in an excited state  $n'$ . This is a recombination process, called radiative recombination (RR), producing continuum emission for electrons in a Maxwellian distribution. Since  $h\nu > \chi_n$ , there are discontinuities in the emission corresponding to the different charge state ionization potentials of the  $n$  levels.

**(iii) Bound-Bound:**

$$X_n^{+z} \Rightarrow X_{n'}^{+z} + h\nu \quad (5.3)$$

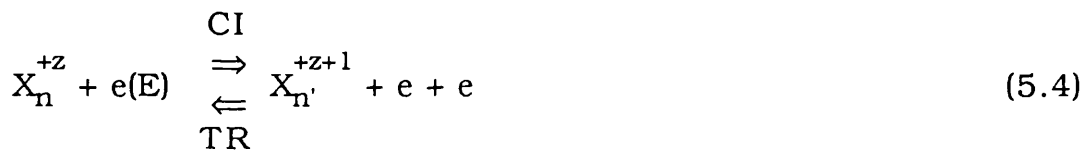
where a bound electron of ion X makes a transition from state n to n'. Spontaneous emission of a photon occurs where  $h\nu = \chi_{n'} - \chi_n$ . Multiple emission from similar ions gives a spectral line.

It can be mentioned here that for bound-bound electron transitions, spontaneous emission is one of several connected processes. Photo-absorption is the reverse process of equation (5.3) and is discussed in chapter 6 for dense laser plasmas. Stimulated emission follows the same form in equation (5.3) but depends on photons of the same energy before the transition and a population inversion in the excited states.

**5.1.2 Ionization, Recombination and Excitation Processes.**

The following processes of ionization, recombination and excitation are described where an ion X of charge z interacts with the free electron gas. Mewe<sup>82</sup> gives a recent survey of current research in this field.

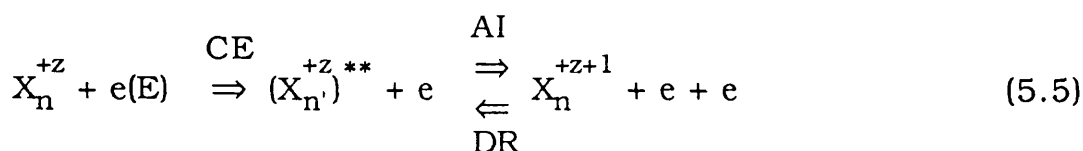
Collisional ionization (CI) occurs when an electron of energy E collides with an ion and removes a bound electron from level n:



The ion positive charge increases to z+1. The above is satisfied if the initial free electron energy E is above the ionization threshold energy  $\chi_n$  for the bound state. The ion may be left in an excited state n'.

The process may be reversed where two free electrons interact with an ion  $X^{+z+1}$  to reduce its charge to +z, leaving one free electron to carry off the excess energy. This is referred to as three-body recombination (TR) and may be neglected for low density Tokamak plasmas.

A two step process is a possible alternative to direct ionization; collisional excitation (CE) followed by autoionization (AI). The electron makes a transition from a lower level through electron impact excitation to a bound doubly excited state (autoionizing level) above the first ionization limit. The excited ion then stabilises through autoionization:



In this instance the excited electron above the ionization limit is ejected leaving the ion of charge z+1 in the ground state.

Photo-ionization is the reverse process of radiative recombination as shown in equation (5.2). It occurs where a photon of energy  $h\nu > \chi_n$  (the ionization potential for excited state  $n$ ) interacts with an ion  $X$  of charge  $z$  to remove one electron, producing the charge state  $z+1$ .

Many of the recombination processes are simply the reverse of the ionization processes; for example CI and TR or RR and PI. There are two other recombination processes, dielectronic and charge exchange recombination, that have not been mentioned.

Dielectronic recombination (DR) is a resonant recombination process which starts with the radiationless capture of a free electron into a doubly excited autoionizing level while simultaneously exciting a bound electron from state  $n \rightarrow n'$ :



The initial state  $n$  is usually the ground state. The recombination is completed when the doubly excited state stabilises either by a radiative transition (or cascades) to a final state below the first ionization limit of ion  $X^{z-1}$  or by radiationless autoionization. For radiative decay, these lines are observed as "satellites" (due to the presence of the spectator electron) to the long wavelength side of the parent resonance line from the ion of charge  $z$ .

Dielectronic recombination requires a bound electron to be excited, therefore the Hydrogenic ion is the highest charge state for any atomic number where this process occurs.

Charge-exchange recombination (CXR) is often observed during neutral beam heating of Tokamak plasmas, where an ion  $X^{+z}$  recombines to  $X^{+z-1}$  by an electron exchange from the neutral Hydrogen atom  $H^0$ . This electron is transferred into a highly excited state  $n'$ :



## 5.2 Line Emission.

### 5.2.1 Introduction

The oscillator strength or  $f$ -number is a dimensionless quantity which can be applied to the process of absorption or emission. For an upper level  $j$  and lower level  $i$  the emission oscillator strength  $f_{ji}$  is related to the absorption oscillator strength  $f_{ij}$  by:

$$f_{ji} = - \frac{g_i}{g_j} f_{ij} \quad (5.8)$$

where  $g_i, g_j$  are the statistical weights of the respective levels. Also the sum of the  $f$ -numbers of all transitions from one state is equal to unity:

$$\sum_k^{\infty} f_{ik} = 1 \quad (5.9)$$

As stated in Chapter 4.5.1, the lifetime of a state is related to the radiative transition probability  $A_{ji}$  ( $s^{-1}$ ) from level  $j \rightarrow i$ . The decay rate  $A_{ji}$  is linked to the absorption oscillator strength  $f_{ij}$ , where  $\lambda_{ji}$  is the transition wavelength ( $\text{\AA}$ ), by<sup>2</sup>:

$$A_{ji} = \frac{6.67 \times 10^{15}}{\lambda_{ji}^2} \frac{g_i}{g_j} f_{ij} \quad (5.10)$$

As an aside, it is useful to relate the transition energy  $E_{ji}$  (eV) to the wavelength  $\lambda_{ji}$  by:

$$E_{ji} \text{ (eV)} = \frac{h c}{\lambda_{ji}} = \frac{12398.521 \pm 0.076}{\lambda_{ji} \text{ (\AA)}} \quad (5.11)$$

where the error bar is largely determined by the accuracy of Planck's constant<sup>75</sup>.

### 5.2.2 Electron Impact Excitation.

The intensity of a resonance line  $I_{ji}$  ( $\text{cm}^{-3} \text{s}^{-1}$ ) can be expressed as:

$$I_{ji} = n_{zj} A_{ji} = n_{zg} n_e C_{gj}(T_e) \quad (5.12)$$

where  $n_{zj}$  is the upper state population density of an ion  $X^{z+}$ , populated by collisions with ions in the ground state  $n_{zg}$  by free electrons  $n_e$  at the collisional excitation rate  $C_{gj}$  ( $T_e$ ) ( $\text{cm}^3 \text{s}^{-1}$ ) from the ground level. Collisional effects on the excited state can be assumed to be negligible which is in fact the conditions for the coronal model (CM) described in the next section. The excitation rate  $C_{ij}$  is determined by the collisional cross-section  $\sigma_{ij}(v)$ :

$$C_{ij} = \langle v \sigma_{ij}(v) \rangle = \int_{E_{ij}}^{\infty} v \sigma_{ij}(v) f(E) dE \quad (5.13)$$

where the product is averaged over the Maxwellian distribution  $f(E)$  of the relative velocity  $v$  of the colliding ion and electron. The ion velocity is usually ignored since the electron velocities are considerably greater. The calculation of  $C_{ij}$  then depends on  $\sigma_{ij}$ . The cross-section for excitation of optically allowed transitions can be approximated by (Van Regemorter<sup>83</sup>, Gabriel and Jordan<sup>84</sup>, and Gabriel<sup>85</sup>):

$$\sigma_{ij} = \frac{8\pi}{\sqrt{3}} \frac{(\chi_H)^2}{E E_{ij}} f_{ij} g(E) \pi a_0^2 \quad (5.14)$$

where  $\chi_H$  is the ionization potential of Hydrogen,  $E$  is the energy of the colliding electron,  $g(E)$  is a semi-empirical factor which varies slowly with electron energy  $E$  and  $a_0$  is the Bohr radius.  $C_{ij}$  can be written as:

$$C_{ij}(T_e) = 2.17 \times 10^{-8} \frac{\Omega_{ij}}{g_i} \left[ \frac{\chi_H}{kT_e} \right]^{1/2} \exp \left[ \frac{-E_{ij}}{kT_e} \right] \quad (5.15)$$

where  $g_i$  is the statistical weight of the initial level and  $T_e$  is the electron temperature of the Maxwellian distribution. The dimensionless parameter  $\Omega_{ij}$  is the average collision strength:

$$\Omega_{ij} = \frac{8\pi}{\sqrt{3}} \frac{\chi_H}{E_{ij}} f_{ij} g_i G \quad (5.16)$$

where  $G$  is the average of the function  $g(E)$  over the Maxwellian distribution.  $G$  has typical values of  $\sim 0.2$  near the threshold<sup>83</sup>, for  $T_e < E_{ij}$ . The previous equations can be combined to give:

$$C_{ij}(T_e) = 3.15 \times 10^{-7} f_{ij} G \frac{\chi_H}{E_{ij}} \left[ \frac{\chi_H}{kT_e} \right]^{1/2} \exp \left[ \frac{-E_{ij}}{kT_e} \right] \quad (5.17)$$

Equation (5.17) is approximate and requires further modification. This is reviewed in de Michelis and Mattioli<sup>2</sup> and Dubau and Volonté<sup>86</sup>. Briefly the oscillator strength is treated as an adjustable parameter depending on the type of transition (allowed or forbidden), temperature and other plasma conditions.

### 5.2.3 Dielectronic Recombination - Satellite Lines.

As discussed in Chapter 5.1 the radiative transition of a dielectronic satellite line corresponds to the stabilisation phase of dielectronic recombination. The satellite state, denoted by the subscript  $s$ , is autoionizing and excited by dielectronic capture from the continuum by the recombining ion  $X^{rz}$  in its ground state. (The other population mechanism is inner-shell excitation discussed in 5.2.4). The population  $n_s$  of the satellite state is balanced between dielectronic capture, autoionization and radiative decay such that:

$$n_{gz} n_e C_d(T_e) = n_s \left( \sum_{k < s} A_{sk} + \Gamma_s \right) \quad (5.18)$$

where  $n_{gz}$  is the ground state population density of the recombining ion,  $C_d(T_e)$  is the rate coefficient for dielectronic capture,  $A_{sk}$  is the radiative decay probability for the transition  $s \rightarrow k$  while  $\Gamma_s$  is the autoionization rate back into the ground level continuum.

The satellite line intensity to a final state  $j$  can be expressed as:

$$I_s(j) = n_s A_{sj} \quad (5.19)$$

which can be combined with the previous equation:

$$I_s(j) = n_{gz} n_e C_d(T_e) \frac{A_{sj}}{\sum_{k < s} A_{sk} + \Gamma_s} \quad (5.20)$$

In coronal equilibrium conditions, detailed balance gives:

$$n_{gz} n_e C_d(T_e) = n_s \Gamma_s \quad (5.21)$$

assuming that radiative decay is negligible in comparison to autoionization. This indicates that local thermodynamic equilibrium (LTE) exists between the continuum and the satellite states. The population  $n_s$  is defined by the Saha-Boltzmann equation:

$$n_s = 3.3 \times 10^{-24} n_{gz} n_e \frac{g_s}{g_g} \left[ \frac{\chi_H}{kT_e} \right]^{3/2} \exp \left[ \frac{-E_s}{kT_e} \right] \quad (5.22)$$

where  $g_s$  and  $g_g$  refer to the statistical weights of the satellite state and the ground state of the recombining ion, and  $E_s$  is the energy difference between them. The dielectronic capture rate can be expressed as:

$$C_d(T_e) = 3.3 \times 10^{-24} \frac{g_s}{g_g} \left[ \frac{\chi_H}{kT_e} \right]^{3/2} \exp \left[ \frac{-E_s}{kT_e} \right] \Gamma_s \quad (5.23)$$

Dubau and Volonté<sup>86</sup> state that since  $C_d$  and  $\Gamma_s$  are atomic coefficients for two exactly inverse processes, equation (5.23) is generally true for a Maxwellian electron distribution in the plasma and is also applicable when the radiative decay rate is non-negligible.

Finally the satellite line intensity can be written as:

$$I_s(j) = 3.3 \times 10^{-24} n_{gz} n_e \frac{1}{g_g} \left[ \frac{\chi_H}{kT_e} \right]^{3/2} \exp \left[ \frac{-E_s}{kT_e} \right] q_s \quad (5.24)$$

where  $q_s$  is the satellite intensity factor defined as:

$$q_s = \frac{g_s A_{sj} \Gamma_s}{\sum_{k < s} A_{sk} + \Gamma_s} \quad (5.25)$$

It may be noted here that the autoionization rate  $\Gamma_s$  remains almost constant along the isoelectronic sequence while the decay rate  $A_{sj}$  increases as  $Z^4$ . Satellite line intensity therefore increases progressively from low values at Oxygen ( $Z=8$ ) to a level comparable with the resonance line at Iron ( $Z=26$ ). The satellite line intensity can be compared directly with the resonance line by combining equations (5.12), (5.17) and (5.24):

$$\frac{I_s(j)}{I_r} = 1.05 \times 10^{-17} \frac{1}{G f_r} \left[ \frac{E_0}{kT_e} \right] \exp \left[ \frac{E_0 - E_s}{kT_e} \right] q_s \quad (5.26)$$

where  $E_0 = E_{ij}$ ,  $f_r = f_{ij}$  in equation (5.17). This intensity ratio is independent of electron density  $n_e$  and ionization equilibrium and is a function only of electron temperature. Therefore, for satellite lines produced only by dielectronic recombination, the electron temperature can be determined from the relative intensity of the dielectronic satellites as long as the radiative decay and autoionization rates are understood. It can be seen that the main temperature dependence in (5.26) comes from the  $T_e^{-1}$  term.

#### 5.2.4 Inner-Shell Excitation - Satellite Lines.

A different way of producing satellite lines is by the process of excitation of an inner shell electron in an ion. The simultaneous excitation of two electrons becomes likely in ions

with three or more electrons, but has very low probability in He-like systems. Thus He-like satellite lines to the long wavelength side of the Lyman- $\alpha$  are produced mainly by dielectronic capture. As in Chapter 5.2.4, the satellite state can decay either by radiative transition or autoionization, and therefore the satellite line intensity depends on the ratio between these processes. Inner-shell excitation gives a line intensity  $I_s(j)$ :

$$I_s(j) = n_{gz'} n_e C_e(T_e) \frac{A_{s'j}}{\sum_{k<s'} A_{s'k} + \Gamma_{s'}} \quad (5.27)$$

where  $n_{gz'}$  is the population density of the ion of charge  $z'=z+1$  in the ground state and  $C_e$  is the rate coefficient for electron impact excitation. An equation similar to (5.26) can be written for the satellite to resonance line intensity ratio:

$$\frac{I_s(j)}{I_r} = \frac{n_{gz'} C_e}{n_{gz} C_r} \frac{A_{s'j}}{\sum_{k<s'} A_{s'k} + \Gamma_{s'}} \quad (5.28)$$

where  $C_r$  is the excitation rate for the resonance line. It may be noted that since the excitation energies are approximately equal, then the ratio  $C_e/C_r$  is largely dependent on the values of the effective oscillator strengths, and has little dependence on  $T_e$ .

The ratio  $n_{gz'}/n_{gz}$  (for example a Li-/He-like ion) is dependent on the electron temperature and the plasma ionization conditions. For coronal plasmas where the ground state population can be considered to represent the total ion population density, this ratio reflects the ion abundance for the charge states. In ionization equilibrium,  $n_{gz'}/n_{gz}$  is a function of electron temperature,  $T_e$ , but strictly speaking is determined by the ionization temperature  $T_z$ . Gabriel<sup>85</sup> defines  $T_z$  as the value of  $n_{gz'}/n_{gz}$  which would exist in a plasma at ionization equilibrium. Thus the conditions  $T_z = T_e$ ,  $T_z < T_e$  and  $T_z > T_e$  correspond to an equilibrium plasma, an ionizing plasma and a recombining plasma. Inner-shell excited satellite lines are therefore useful for determining the parameter  $T_z$  and can provide information of the temporal variation in the plasma ionization.

## 5.3 Plasma Models

Several plasma models have been developed which best describe the charge state distribution and excited level populations of the ions. These allow interpretation of the x-ray emission from the plasma source. The model is chosen from three approximations and is mainly determined by the electron density: the Coronal Equilibrium model (CM), the Local Thermodynamic Equilibrium model (LTE) and the Collisional Radiative Equilibrium Model (CRE).

### 5.3.1 Coronal Equilibrium Model.

The CM model, applied to low density plasmas, is a balance between the processes of collisional ionization and recombination giving the charge state distribution<sup>2</sup> as:

$$n_e n_z S_z(T_e) = n_e n_{z+1} \alpha_{z+1}(T_e, n_e) \quad (5.29)$$

where  $S_z$  and  $\alpha_{z+1}$  are the ionization and recombination rates, respectively for adjacent charge states of ion density  $n_z$  and  $n_{z+1}$ . The ions are mostly in the ground state. The population densities of the excited levels are balanced, for optically thin plasmas, between the collisional excitation rate  $C_{gj}(T_e)$  (from the ground state) and spontaneous radiative decay  $A_{ji}$ :

$$n_{jz} = \frac{n_e n_{iz} C_{gj}(T_e)}{\sum_{i<j} A_{ji}} \quad (5.30)$$

Thus the measured line luminosity  $L_{ji}$  (photons/cm<sup>2</sup>s<sup>-1</sup> sterad<sup>-1</sup>) is:

$$L_{ji} = \frac{1}{4\pi} \int n_e n_z C_{gj}(T_e) \frac{A_{ji}}{\sum_{i<j} A_{ji}} ds \quad (5.31)$$

where the radiation is isotropic, the integration is performed over the plasma depth and  $g, j$  and  $i$  refer to the ground, upper and lower levels of ion  $X^{z+}$ .

The CM model is only appropriate to the low density regime for all excited levels where the probability of de-excitation by radiative decay is considerable greater than by collisional processes:

$$\sum_{i<j} A_{ji} \geq n_e C_j(T_e) \quad (5.32)$$

where  $C_j(T_e)$  refers to the collisional de-excitation rate in cm<sup>3</sup>s<sup>-1</sup>. It may be noted that there will be a value of  $j$  (equivalent to the collision limit  $n_c$ ) even at a low density, where equation (5.32) does not hold as a result of the reduced radiative decay probability with increasing quantum number  $n$ . Using one order of magnitude in equation (5.32) for levels with principal quantum number  $n < 6$  of H-like ions, the CM model is relevant for density conditions (from McWhirter<sup>87</sup>):

$$n_e < 5.9 \times 10^{10} Z^6 T_e \exp \left[ \frac{0.1 Z^2}{T_e} \right] \quad (5.33)$$

for  $T_e$  (eV) and  $n_e$  (cm<sup>-3</sup>). The nuclear charge  $Z$  may be replaced with  $Z+1$  for other isoelectronic sequences. As an example, coronal conditions can be easily calculated for H-like Aluminium at a plasma temperature  $T_e \sim 1000$ eV, typical of the ion emission observed in this work. Coronal conditions still hold for density  $n_e < 10^{19}$ cm<sup>-3</sup>, and may be used for Tokamak plasmas (this chapter) but is not applicable to laser produced plasmas in Chapter 6.

For completeness, dielectronic recombination should be included in the model, though the dielectronic rate coefficient will be reduced by the process of autoionization into an excited state of the recombining ion. Charge exchange recombination may have to be included where it is considered to be a significant recombination scheme (eg where high power neutral hydrogen beams heat Tokamak plasmas).

### 5.3.2 Local Thermodynamic Equilibrium Model.

The LTE approximation is opposite to CM and applies to high density plasmas where excited state populations are effected predominantly by collisional rather than radiative processes. Each atomic process is balanced by the reverse process at equal rates and so the population of excited energy levels are in complete thermodynamic equilibrium. The charge state distribution, for ions impacted by free electrons having a Maxwellian velocity distribution, is described by the Saha equation:

$$n_e \frac{(n_{z+1,g})}{(n_{z,g})} = 2 \frac{(g_{z+1,g})}{(g_{z,g})} \left[ \frac{2\pi m_e kT_e}{h^2} \right]^{3/2} \exp \left[ \frac{-\chi_z}{kT_e} \right] \quad (5.34)$$

where  $\chi_z$  is the ionization potential for charge state  $z$ ,  $g$  refers to the statistical weight of the appropriate charge state and the subscript  $_g$  indicates the ground state level. The excited level populations for an ion of charge  $z$  follow the Boltzmann equation:

$$\frac{n_j}{n_i} = \frac{g_j}{g_i} \exp \left[ \frac{\Delta E_{ji}}{kT_e} \right] \quad (5.35)$$

where  $\Delta E_{ji}$  is the energy separation of the  $i$  and  $j$  levels. The measured line luminosity  $L_{ji}$  is defined as:

$$L_{ji} = \frac{1}{4\pi} \int n_j A_{ji} ds \quad (5.36)$$

where the integration is over the plasma depth along the instrument line of sight. The conditions to satisfy LTE are such that the inequality of equation (5.32) is reversed and collisional processes are at least a factor of ten more likely than radiative processes.

Therefore, the condition for density<sup>2</sup> is:

$$n_e \geq 1.8 \times 10^{14} T_e^{1/2} \Delta E_{ij}^3 \quad (5.37)$$

with  $T_e$  measured in eV. A further condition is needed where  $\Delta E_{ij}$  is the largest separation in the energy scheme. The LTE conditions, for the Aluminium Lyman- $\alpha$  transition for plasma temperature  $T_e=1000$ eV, would require  $n_e \sim 3 \times 10^{25} \text{cm}^{-3}$ .

### 5.3.3 Collisional Radiative Equilibrium Model.

The previous CM and LTE models apply in the low and high density limits where either completely radiative or collisional processes need to be considered. However, in most laser produced plasmas an intermediate density regime requires the Collisional Radiative

Equilibrium model, first proposed by Bates, Kingston and McWhirter<sup>88</sup>, where both collisional and radiative effects must be considered for the population distribution of excited states. The CRE model is based on the CM model with the addition of electron collisions in the upper levels, and the additional processes of three body recombination and radiative recombination. The CRE model must reduce to the LTE model at the high density limit.

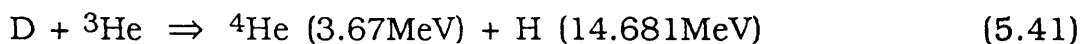
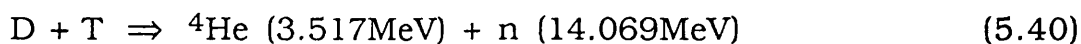
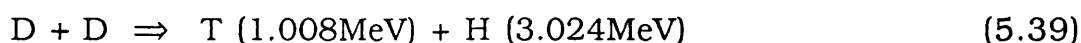
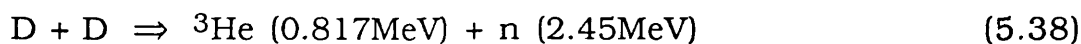
## 5.4 Controlled Nuclear Fusion and Tokamaks.

### 5.4.1 Nuclear Fusion Programme.

The main objective of fusion research is to solve the world's long term energy demands. The nuclear fusion reaction is the opposite of the nuclear fission process; by using isotopes of hydrogen, namely Deuterium (D) and Tritium (T), the nuclei combine together to create a new nucleus at a lower nuclear binding energy. The energy released in the reaction is divided amongst the fusion products and potentially can be harnessed. However, the fusion particles must be confined in some way to overcome the Coulomb repulsion of the positive nuclei for the reaction to take place. In the sun's core, fusion is contained by the gravitational force, but duplication of these conditions is not possible for laboratory devices. Instead, the fusion particles have to be given high enough kinetic energy in a way that non-fusion scattering processes are reduced.

#### Fusion Processes.

There are a large range of fusion processes, but the most promising ones are listed below on account of the high reaction rates and relatively low initial temperature threshold.



The DT reaction in equation (5.40) is the most useful because it has the largest cross-section and at a lower threshold energy than the others. Tritium, however, is radioactive with a short half-life  $\tau_{1/2}=12$  years and therefore occurs only in trace abundances. This disadvantage is outweighed by the fact that 80% of the high reaction energy yield goes to the neutron. The energy can be extracted from the fast neutron which, after slowing, can generate Tritium from Lithium. The universal abundance of Deuterium and Lithium favour this scheme.

The fusion process requires an initial injection of energy to get the reaction going plus sufficient individual reactions to sustain the process by simply adding more fuel. The collision process and high temperatures completely ionize the low Z nuclei producing a

plasma with Maxwellian distribution characterised by temperature T. The "Lawson Criterion" <sup>89</sup> often used as a theoretical benchmark for nuclear fusion, ie the reaction will produce more energy than it consumes, is defined as:

$$n \tau \geq 10^{14} \text{ cm}^{-3} \text{ s} \quad (5.42)$$

where n is the plasma density and  $\tau$  is the time where the plasma delivers nuclear energy. The parameter  $n\tau$  is at a minimum for temperatures  $kT=5 \rightarrow 25\text{keV}$ . Outside this temperature range,  $n\tau$  increases indicating a decrease in the fusion rate coefficient. At high temperatures, plasma losses through bremsstrahlung become significant.

The ignition criteria is a more realistic parameter to judge the fusion reaction. It states that the particles remaining in the plasma after the fusion process, for example the  $\alpha$ -particles from equation (5.40), have sufficient energy to sustain the fusion burn in the event of power losses, after external heating sources have been switched off. This depends on the internal plasma power balance where the input power from the  $\alpha$ -particles balances losses due to conduction, convection, bremsstrahlung, recombination and line radiation. Speth<sup>90</sup> reports the ignition parameter as  $n\tau_E T$ , where  $\tau_E$  is the confinement time for the plasma energy, for a minimum ignition temperature  $T \sim 4.7\text{keV}$  as:

$$n \tau_E T \geq 3 \times 10^{15} \text{ cm}^{-3} \text{ s keV} \quad (5.43)$$

#### Confinement Schemes.

Two schemes have been researched which are practicable and show promise for satisfying the ignition criterion:

- Inertial confinement.
- Magnetic confinement.

**Inertial confinement** utilises the density advantage by starting with solid hydrogen fuel. A small spherical pellet of radius R containing a solid or pressurised D-T mixture is heated and further compressed by a symmetrical irradiation from a particle or laser beam. A characteristic time  $\tau$  for the nuclei to remain in the reaction core, where  $\tau \sim R/v$  for particle velocity v, can be defined to replace equation (5.43) with:

$$\frac{\rho R}{v} T \geq 3 \times 10^{15} \text{ cm}^{-3} \text{ s keV} \quad (5.44)$$

Assuming a Deuterium temperature  $T \sim 10\text{keV}$  and noting that the particle velocity is proportional to  $T^{1/2}$ , then the density radius product  $\rho R$  for ignition is:

$$\rho R \geq 2 \times 10^{22} \text{ cm}^{-2} \quad (5.45)$$

The major thrust of laser plasma fusion has been to increase the density  $\rho$  since the energy needed to heat up the pellet volume scales as  $R^3$  and therefore places a constraint on the radius. A further trend is the use of shorter wavelength laser light to increase the coupling of the laser energy to the target.

Confinement Schemes.

- Magnetic confinement
- ▨ Inertial confinement

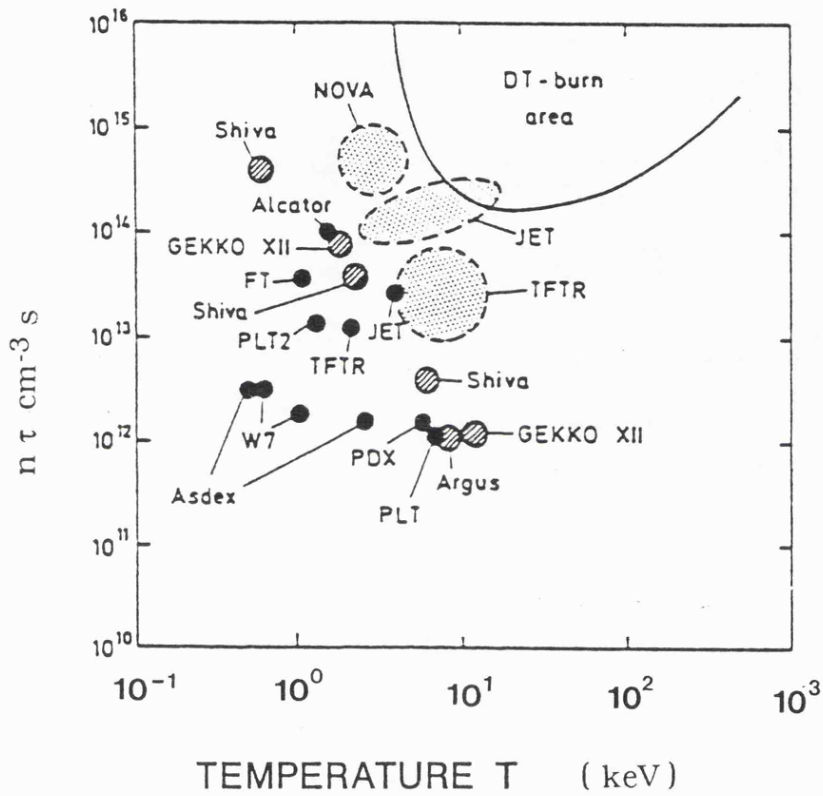


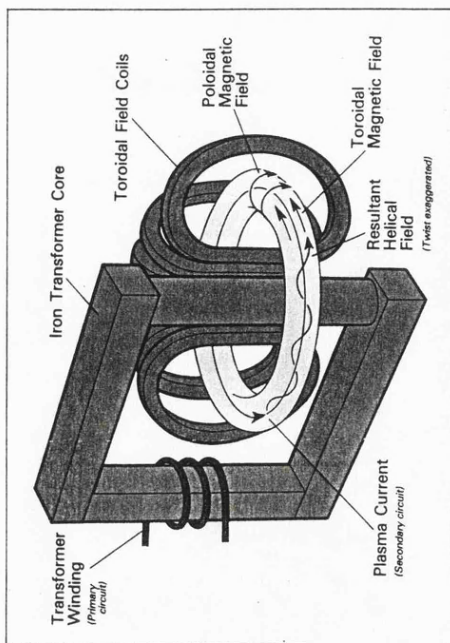
Figure 5.1 Lawson diagram showing confinement parameters for various inertial and magnetic confinement schemes. Solid dots, eg PLT, Asdex, JET indicate Tokamak devices, while hatched areas, eg Gekko XII, Shiva and Argus, are confinement results for high power laser plasmas. Areas surrounded by broken lines represent the potential of present state of the art machines.

Figure 5.2 (next page) is a cut-away schematic of the Joint European Torus (JET). The vacuum chamber is surrounded by the transformer, toroidal and poloidal field coils and the supporting mechanical structure. Not shown are the additional heating supplies or the diagnostic instrumentation. Plasma temperatures in excess of 10keV (120 million degrees Celsius) have been achieved for plasma densities of  $n_e \sim 4 \times 10^{13} \text{ cm}^{-3}$ . Overall pulse lengths last for greater than 15 seconds, with a confinement time of  $\sim 1$  second.

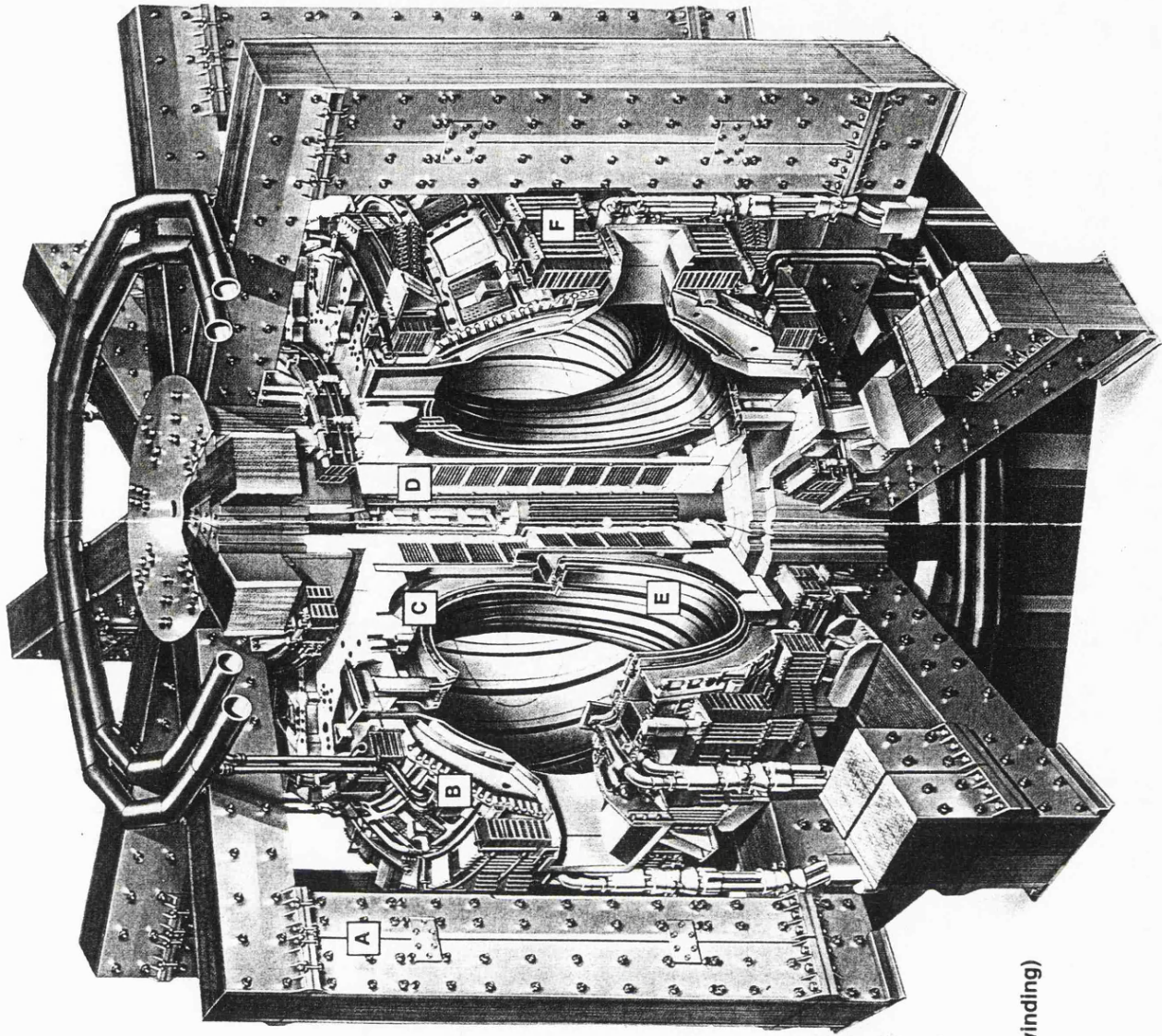
Inset picture is a general diagram of the Tokamak magnetic field configuration.

# JEU

JOINT EUROPEAN TORUS



Tokamak magnetic field configuration.



- A. Transformer limbs
- B. Mechanical structure
- C. Toroidal field coils
- D. Inner poloidal field coils (primary winding)
- E. Vacuum vessel
- F. Outer poloidal field coils

**Table 5.1** The following tabulates the basic parameters of international experiments equipped with neutral injection heating.  $R_0$  is the major radius,  $a$  and  $b$  the minor horizontal and vertical radii, respectively,  $I_p$  the plasma current,  $P_\Omega$  the Ohmic power,  $P_N$  the neutral power and  $E_b$  the beam energy.

Experiment	Location	$R_0$ (m)	$a$ (m)	$b$ (m)	$I_p$ (kA)	$P_{in}^\dagger$ (MW)	$P_N$ (MW)	$E_b$ (keV)	Injection geometry	Remarks
CLEO	Culham, UK	0.9	0.17	0.17	60 $\chi = 0.4$	0.2	0.08	25	tang.	1973 tokamak
ATC	Princeton, USA	0.88	0.17	0.17	70	0.17	0.23	15	tang.	1978 stellarator parameters before com- pression
ORMAC	ORNL, USA	0.8	0.23	0.23	230	0.6	0.36	30	tang.	
TFR 400/600	Fontenay-aux-Roses, France	0.98	0.2	0.2	400/600	0.5	0.65/1.2	39	perp., 10°/15°	
DITE	Culham, UK	1.17	0.27	0.27	280	(0.5)	1.6	28	tang.	divertor tokamak
T-11	Moscow, USSR	0.7	0.18	0.18	110	0.45	1.0	22	tang.	
PLT	Princeton, USA	1.3	0.4	0.4	500	(0.7)	2.4	40	tang.	
ISX	ORNL, USA	0.93	0.27	0.51	200	0.5	3.0	40	tang.	
W VII A	Garching, FRG	2.0	0.1	0.1	35	0.11	1.0	27	perp., 6°	stellarator
PDX/PBX	Princeton, USA	1.43	0.44	0.44	500 $\chi = 0.23$	0	5.0	50	perp., 9°	divertor tokamak
JFT-II	JAERI, Japan	0.9	0.28	0.28	170	0.4	2.0	40	tang.	
JFT-IIIM	JAERI, Japan	1.3	0.35	0.55	500	0.1	2.4	40	tang.	
JIPP-T2	Nagoya, Japan	0.91	0.17	0.17	50	0.1	0.09	22	tang.	
HELIVOTRON-E	Kyoto, Japan	2.2	0.2	0.2	10	(0.1)	2.5	30	perp., 28°	stellarator
ASDEX	Garching, FRG	1.65	0.4	0.4	500 $\chi = 2.2$	0.04	4.2	40/55	tang.	divertor tokamak
DIII	San Diego, USA	1.43	0.44	0.7	1000	(0.5) 0.2	7.5	80	perp., 27°	
TFTR	Princeton, USA	2.5	0.85	0.85	2500	(0.8) 0.36	20	120	tang.	
JET	Culham, UK	2.96	1.25	2.1	5000	(2.0) (5.0)	20	80/140	tang.	
JT-60	JAERI, Japan	3.0	0.9	0.9	2700	(2.0)	20	75	perp., 15°	divertor tokamak

† Values in brackets are without injection.

**Magnetic confinement** deals with low density dilute plasmas and uses the fact that charged particles can move parallel but not perpendicular to a magnetic field  $B$ . A radius of gyration  $r$  about the magnetic field lines due to the Lorentz force may be written as:

$$r = \frac{m v_{\perp}}{e B} \quad (5.46)$$

where  $v_{\perp}$ ,  $m$  and  $e$  are the particle velocity perpendicular to  $B$ , the particle mass and charge.

A consequence of magnetically confined plasmas is that increased plasma kinetic pressure induce plasma currents which modify the externally applied homogenous magnetic fields. The plasma is then confined by a magnetic pressure. Instabilities in the plasma for non-uniform fields then limits the confinement.

Figure 5.1 after Witkowski<sup>91</sup> indicates the confinement parameters versus temperature of various inertial and magnetic confinement schemes.

### 5.4.2 Tokamak Devices.

Magnetic confinement devices include linear and toroidal configurations, the latter being almost universally favoured. There are two main toroidal configurations. The Stellarator utilises external field coils which are suitably shaped to produce the poloidal field. The other design belonging to the "closed" or toroidal configuration is the Tokamak, a Russian acronym for toroidal magnetic chamber. Its main features are shown in Figure 5.2. The main difference from the Stellarator design is the Iron transformer core which couples the primary winding, consisting of the inner poloidal field coils, to the plasma itself which forms the single turn secondary. This plasma current both heats the gas and generates one of the main components of the magnetic field. This current, of up to 5MAmps, produces a poloidal magnetic field which combines with the field from the toroidal coils to confine the plasma. Additional outer poloidal field coils are used to steer the plasma position centrally in the torus away from the vacuum walls.

#### Heating Methods

There are four different ways of heating toroidal plasmas which are combined together in the present large machines such as JET and TFTR:

- **Ohmic heating** as the name suggests comes from Ohm's law where the plasma is produced and heated by the toroidal current. This current acts like a one-turn secondary winding in a transformer as a result of large currents being passed through the (primary) main field coils. The Tokamak has intrinsic Ohmic heating, but the process cannot be used with Stellarators. The effectiveness of Ohmic heating is reduced with increasing plasma temperature because the plasma resistivity scales as  $T_e^{-3/2}$ . The discharge pulse lengths is also limited, with the general conclusion that this heating alone is not sufficient to reach ignition conditions.

- **Adiabatic compression** is similar to the adiabatic compression of an ideal gas. This heating process relies on the conservation of toroidal and poloidal magnetic fluxes in the plasma. Thus, plasma volume reduction (and heating) occurs with the increase in the magnetic field.
- **Radio-frequency RF heating** of the plasma is produced by the absorption of high frequency electro-magnetic waves. The plasma ions and electrons move quickly in a helical trajectory along the magnetic field lines. Energy may be given to the particles if the radio wave frequency matches the gyration frequency: for ions the corresponding radio wave frequency is 20→50MHz referred to as ion cyclotron resonance heating (ICRH) while the frequency range for ECRH is several 10GHz. 15MW of ICRH is used on JET making it one of the major energy input methods, second only to neutral beam injection.
- **Neutral beam heating**, reviewed recently by Speth<sup>90</sup>, utilises high energy >10keV neutral Hydrogen or Deuterium beams which pass easily through the magnetic field to heat the plasma directly. The high energy beam is ionized and energy is distributed to the plasma ions and electrons by collisions. Neutral beam Injection (NBI) is a successful heating method and has been employed on many toroidal devices, see Table 5.1. On JET for example, two injection units produce a total of 20MW heating.

## 5.5 Ion Temperature Measurements.

### 5.5.1 Different Methods.

There are several methods available for measuring the central ion temperature  $T_i$  of Tokamaks:

- Neutral particle analysis (NPA).
- Neutron spectrometry.
- Charge exchange recombination spectroscopy (CXRS).
- X-ray spectroscopy.

Figure 5.3, after Grisham<sup>92</sup>, indicates good agreement between the four diagnostic methods for the central ion temperature in PLT Tokamak.

**NPA** measures the energy distribution of neutral (charge exchange) particles escaping from the plasma. There is always a residual density of neutral hydrogen atoms everywhere in the plasma, whose velocity distribution mirrors the ion velocity distribution due to charge exchange processes. The neutrals are not confined to the plasma and so can be analysed. However, in large plasmas the central neutrals may be attenuated on the way to the plasma edge, thus making  $T_i$  measurements more difficult.

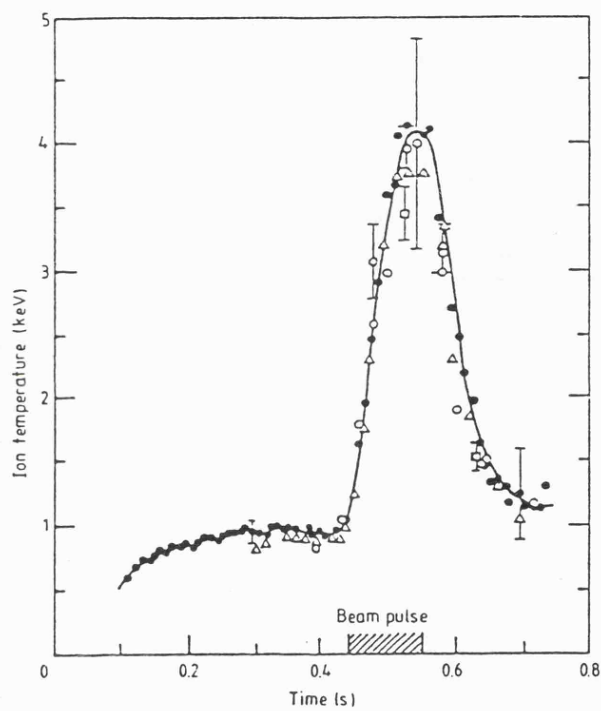


Figure 5.3 Central ion temperature  $T_i$  measurements against time from the four different diagnostic methods (after Grisham<sup>92</sup>). Rise in ion temperature is due to neutral beam heating (shaded area).

Key:

- neutron yield.
- $\Delta$  neutral particle analysis.
- o Fe XX at 2665Å.
- $\square$  Fe XXV 1s2p  $^1P_1$  at 1.85Å.

**Neutron Spectrometry** can be utilised when Deuterium plasmas are studied. A characteristic neutron energy is produced by the fusion reaction, see equations (5.38) and (5.40), and thus the neutron count rate will indicate the Deuterium temperature.

**CXRS** for studying impurity emission in the visible band, requires a neutral beam to populate the high principal quantum number levels of the emitting ion. Doppler broadening of the spectral lines then gives the ion temperature. The use of the fast neutral beam is not a problem since neutral heating is almost a standard feature of large Tokamaks. However, low  $Z$  ions, eg Carbon ( $Z=6$ ), or Oxygen ( $Z=8$ ), are distributed from the core to the plasma edge and emission features from these regions are superimposed. Thus, background emission from the cold plasma edge is always present and manifests itself as a narrow Gaussian profile on the broad shifted Gaussian line of the hot central core.

**X-ray spectroscopy** is also a Doppler spectroscopy technique, but is appropriate to the highly ionized (to the He-like and H-like charge state), high  $Z$  impurities of the plasma core. Doppler broadening of x-ray lines for the determination of the ion temperature in Tokamaks was first measured by the Princeton Plasma Physics Group, see Bitter et al<sup>93</sup>.

The method in principle is straightforward because it only requires knowledge of the instrument dispersion, assuming high instrumental resolving power of course, to interpret the line profiles. No further information is needed from the other plasma parameters. It can also be applied to different plasma conditions; the He-like ion has a high ionization potential and is the most abundant charge state over a large range of electron temperatures. Hydrogenic ions may be studied for higher temperatures. Observation of the appropriate impurity ionized in the hot core gives the peak ion temperature.

A final important point when compared with the other methods, is that x-ray spectroscopy directly measures the plasma impurities which are responsible for power losses through radiative cooling.

#### **Impurity Ion Temperatures.**

It can be noted that the observed Doppler broadening determines the impurity ion temperature which may be different from the bulk Hydrogen ion temperature. This effect, usually small and calculable, occurs when the different ion species are not in thermal equilibrium. The way in which the external heating sources are applied to the plasma, together with the density and temperature conditions, are the dominant factors here.

In Ohmic heating of Tokamak plasmas, the electrons and ions are accelerated by the induced toroidal electric field. The electrons preferentially gain kinetic energy at a rate faster than the ions by a factor of the mass ratio. Thus, the electrons are prevalently heated and electron-ion collisions couple power to the bulk ions. The electron-ion and ion-ion collisions also couple energy to the various impurity ion species.

For neutral beam heating, and ICRH, the converse happens where the beam power is coupled directly to the ion species. The delivered power to the ions is proportional to  $n_i Z_i^2/M_i$ , so although the total power transferred to the impurities is small, the power per ion scales as  $Z_i^2/M_i$ . For low plasma densities and high ion temperatures, the coupling time between the impurity ions and Hydrogen may be sufficiently long for a temperature differential to exist. For low density conditions, the plasma  $Z_{\text{eff}} \sim 3$  mainly due to Carbon and Oxygen, all impurity ions are well coupled to each other so that thermal equilibrium exists giving a common impurity ion temperature.

Some indication of these effects can be gauged from the "self-collision time"  $t_c$  for an ion species. This is defined as the time in which collisions between similar particles change the distribution of kinetic energies to that approaching a Maxwellian distribution. Spitzer<sup>94</sup> writes  $t_c$  as:

$$t_c = \frac{M^{1/2} (3kT)^{3/2}}{8 \times 0.714 \pi n e^4 Z^4 \ln \Lambda} = \frac{11.4 A^{1/2} T^{3/2}}{n Z^4 \ln \Lambda} \quad (5.47)$$

where  $T$  is in °K,  $n$  is the particle density  $\text{cm}^{-3}$  and  $A$  is the atomic mass in amu. For electron collisions,  $A=1/1836$ , and the self-collision time for electrons  $t_{ee}$  requires 0.266 to be substituted for the factor  $11.4 \text{Å}^{1/2}/Z^4$  in the above equation. Thus,  $t_{ee}$  is  $1/43$ ,  $= (A_e/A_p)^{1/2}$ , lower than the proton self-collision time. Spitzer also predicts that the equipartition time  $t_{eq}$  between two groups of particles, say electrons and protons, via electron-proton collisions contains a factor  $(A_e/A_p)^{1/2}$ . It is evident that these collision processes are fairly ineffective at exchanging energy. Therefore,  $t_{eq}$  is 43 times longer than the self-collision time for protons and 1836 times longer than the corresponding self-collision time  $t_{ee}$  for electrons.

#### **DITE Conditions.**

For typical DITE conditions,  $n_e = 5 \times 10^{13} \text{cm}^{-3}$  and  $T_e = 800 \text{eV}$ , the self-collision time for electrons is  $t_{ee} \sim 8 \mu\text{sec}$  and the equivalent parameter for protons  $t_{ep}$ , assuming  $Z_{\text{eff}} = 3$ , corresponds to  $1 \text{msec}$ . Aluminium ions, a representative impurity studied in this work, present at a concentration of  $10^{-4} n_e$ , have a self-collision time calculated to be  $t_{eAl} \sim 1 \text{msec}$ . In the case of Ohmically heated plasmas, the equipartition time  $t_{eq}$  for electron-proton collisions is  $\sim 40 \text{msec}$ . Similarly, proton-Aluminium ion collisions have an equipartition time of  $\sim 5 \text{msec}$  while electron-Aluminium ion collisions have a much longer equipartition time of  $\sim 200 \text{msec}$ .

It is evident that all of the impurity ion species are in thermal equilibrium with each other within a few milliseconds. The electron-proton equilibration time is much longer at  $\sim 40 \text{msec}$  and is the determining time constant for heating the impurity ions. Higher temperatures  $T_i$ ,  $T_e$  with lower impurity concentration and electron density will increase the time for thermalisation between the plasma particles.

### 5.5.2 Instrument Description for DITE Measurements.

An ADP (101)  $2d=10.648\text{\AA}$  crystal,  $R=1200\rightarrow 1300\text{mm}$ , was used on DITE Tokamak in two observing positions as indicated in the plan view of Figure 5.4 and sectional view of Figure 5.5:

- A The spectrometer had a horizontal line of sight through the central chord of the plasma on a port between segments 15 and 16; this intersected the neutral injection beam A. Most of the data from this view were shots with additional heating by neutral beam injection (NBI). The viewing port angle was offset by  $12^\circ$  to the major radius of the machine in the toroidal direction.
- B A vertical line of sight from above DITE observed the central chord of the plasma through a slot port between segments 14 and 15. The view of the plasma was completely radial to the major axis. The slot port allowed a radial scan along the machine minor radius. Additional heating by ECRH is present on some of the data. (The Bragg rotor spectrometer shown at position C in Figure 5.4 had a horizontal line of sight, looking radially to the torus, and could observe the plasma spatially right out to the edge. This instrument was converted for 2-crystal operation with high resolution as discussed in Chapter 5.6).

Where possible, the Rowland circle was placed in the plasma and perpendicular to the toroidal field to maximise the instrumental sensitivity and ensure a uniform source function across a line profile. Bragg angles  $\theta=35\rightarrow 55^\circ$ , corresponding to wavelengths  $6\rightarrow 8.8\text{\AA}$ , were chosen over the whole observation programme. High instrumental resolving power was given priority and crystal apertures of  $5\rightarrow 25\text{mm}$  (in the length and height dimension) were used to minimise Johann defocusing errors. The instrumental resolving power  $\lambda/\Delta\lambda=9000$  was determined by the crystal rocking curve width (Table 4.1). A large waveband  $\Delta\lambda/\lambda=7\rightarrow 9\%$  could be covered and all observed spectral lines were emitted within a region 5cm from the plasma centre for core ion temperature measurements.

#### Choice of Waveband.

Survey spectra of the Bragg Rotor were studied before setting the Johann instrument. The factors considered of importance for choosing the waveband were:

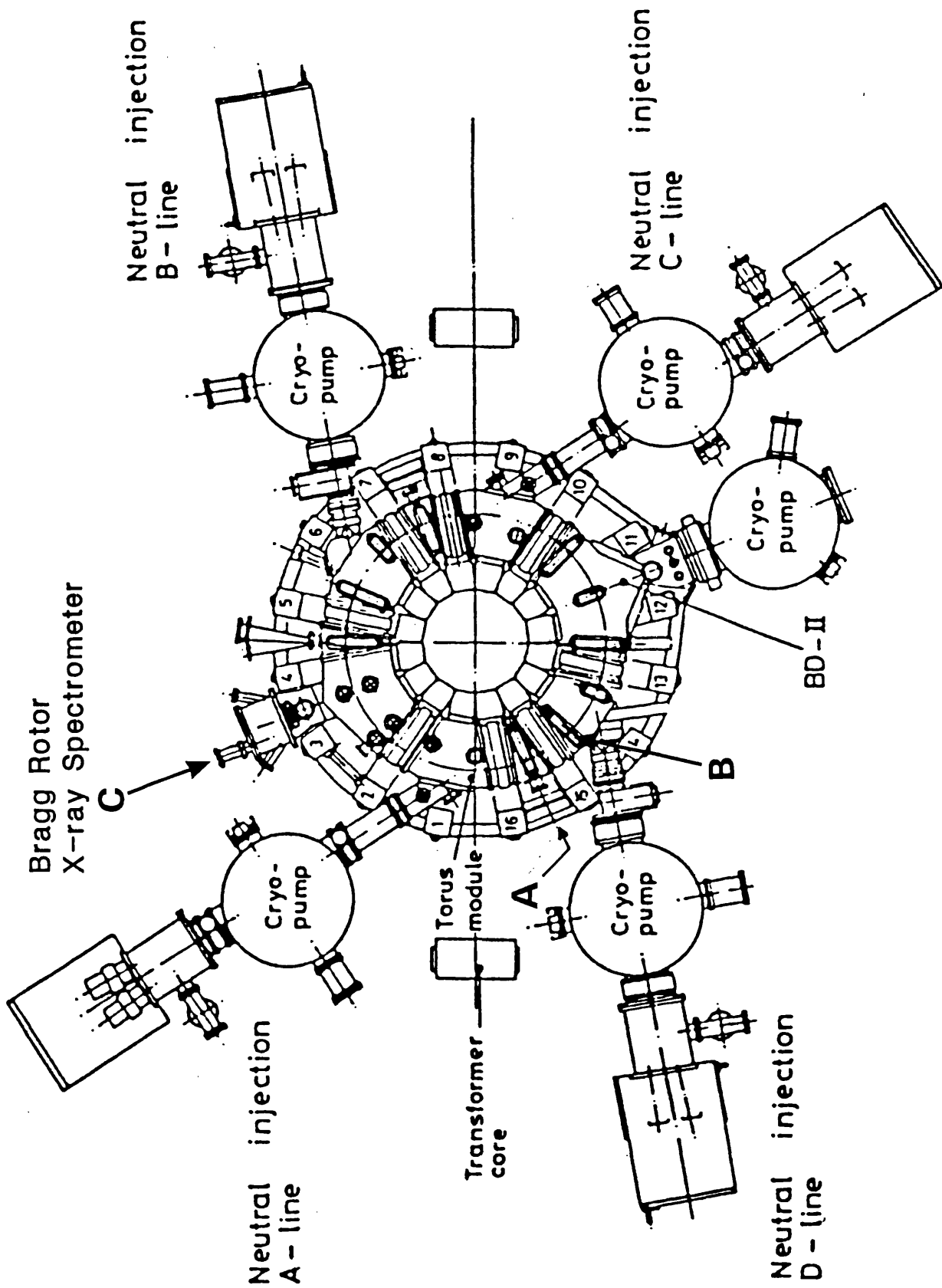
- The ion of interest should be abundant, have a high atomic number and have strong emission below  $10\text{\AA}$ .
- It should be mainly in the high temperature core.
- It should be ionized to the He-like or H-like charge state.

Various intrinsic impurities like Iron, Silicon and Magnesium were usually present but the level of emission changed on a day to day basis as a result of different plasma conditions.

Figure 5.4 (next page) Plan of DITE Tokamak indicating positions A and B for Johann spectrometer. Bragg Rotor spectrometer position is shown at C.

Figure 5.5 Sectional view of DITE Tokamak (page after next); Johann spectrometer has horizontal line of sight (A) and vertical view of plasma at (B). Radial scans of plasma performed at position B.

# Schematic of DITE Tokamak



# JOHANN SPECTROMETER ARRANGEMENT ON DITE TOKAMAK

Vertical Port Set-up:  
Position B

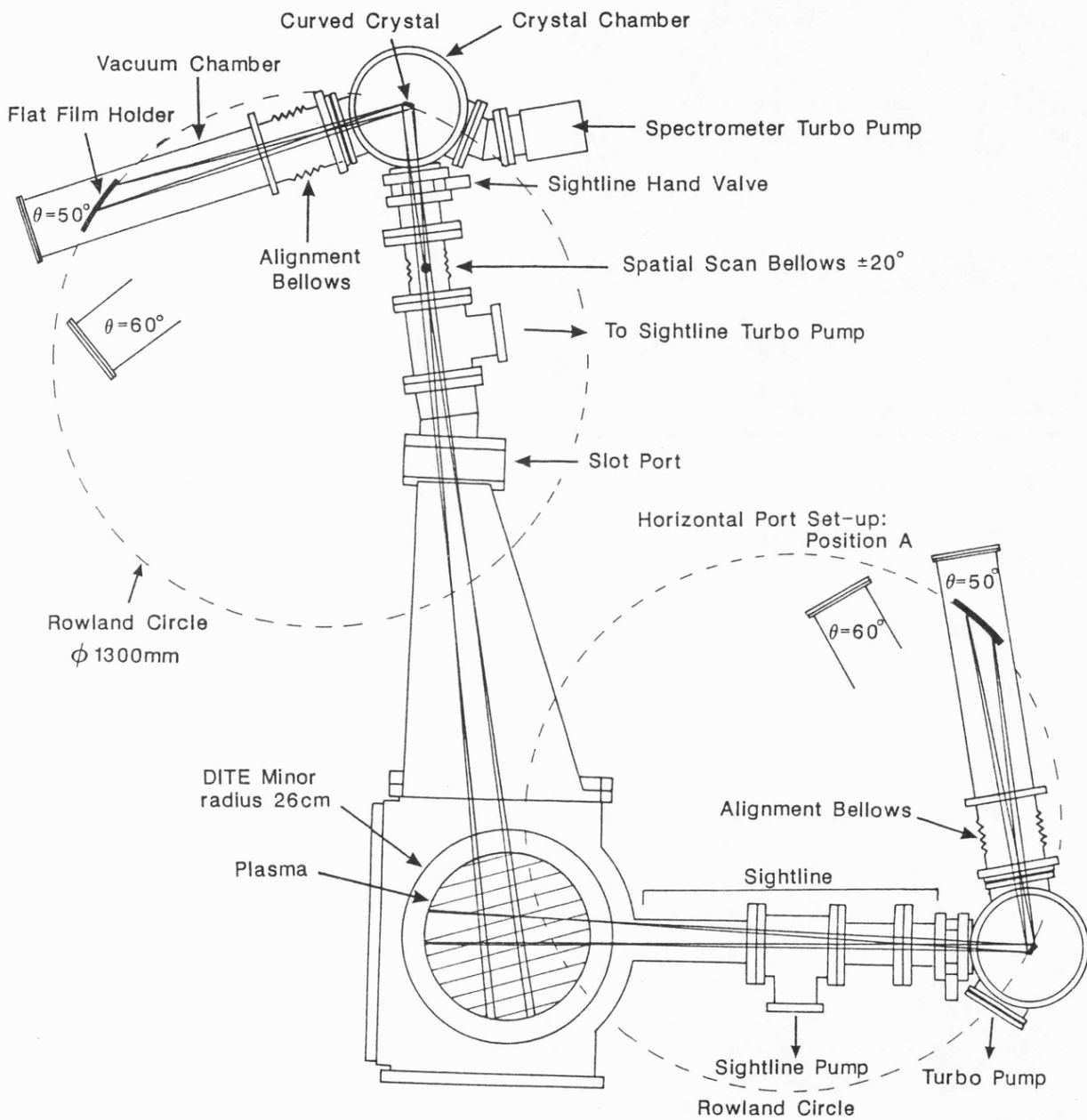
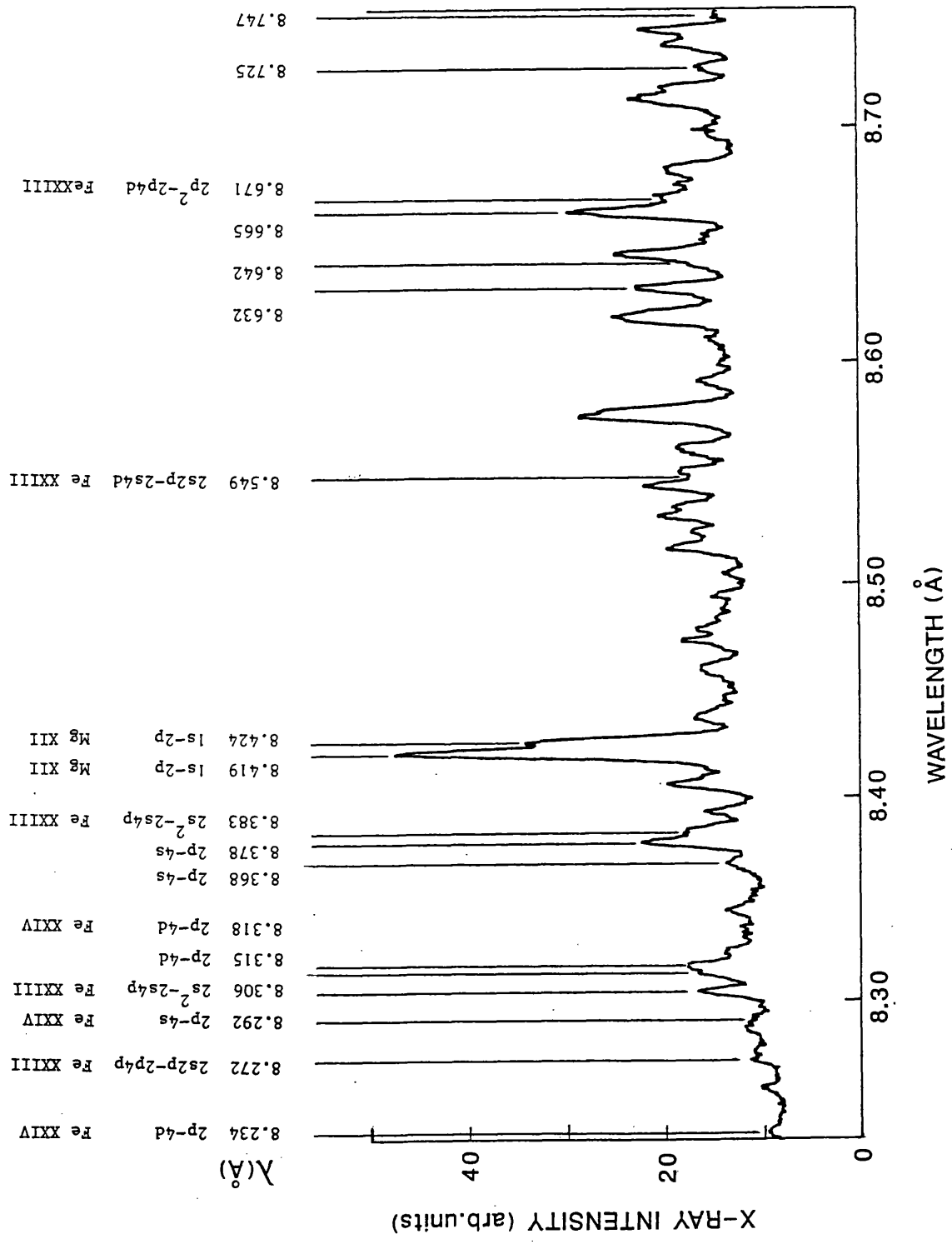


Figure 5.6 (next page) Spectrum of Mg XII Lyman- $\alpha$  and Fe XXIII and Fe XXIV L-shell emission lines 8.2 $\rightarrow$ 8.8 $\text{\AA}$ .

DITE Mg XII Lyman- $\alpha$  and Fe XXIII and XXIV L-Shell Spectrum 8.2 $\rightarrow$ 8.8 $\text{\AA}$



### Iron L-Shell Emission.

Figure 5.6 is a typical spectrum of the 8.2→8.8Å region. The Mg Lyman-α lines are strong but are blended with intense Fe XXIII and XXIV L-shell emission (individual lines are identified from Bromage et al<sup>65</sup>). This spectrum, while interesting for atomic spectroscopy and line identification, is of limited use for  $T_e$  measurements. Unresolved Iron lines form a continuous blend and contribute asymmetries to the Magnesium spectrum. The ionization potential for the Li-like Fe XXIV ion, the highest ionization state observed on DITE, is 2045eV (Kelly and Palumbo<sup>76</sup>) suggests that these L-shell lines continue to 6.06Å. It would be preferable to study x-ray lines below this wavelength but in practice the Iron lines rapidly drop in intensity below 8Å.

### Time Variation of Electron Temperature.

Figure 5.7 from the Bragg Rotor spectrometer<sup>54</sup> gives the temporal emission of the n=2 Mg XII and Mg XI ion lines during Ohmic heating on DITE. The electron temperature can be calculated from the line ratios when the charge state abundances and the excitation rates are considered. It is clear that the electron temperature  $T_e$  rises very quickly (within the first 50msec) to its peak value of 600eV for this shot and remains constant for the rest of the shot. This indicates that the x-ray emission recorded by the time-integrated Johann spectrometer reflects the peak plasma temperature conditions. For neutral beam injection, the time-integrated record again is weighted to the high temperature conditions due to the increased line emission at the peak of this heating (see Figure 5.3).

### 5.5.3 He-like Ion Emission.

Figure 5.8 shows a typical high resolution n=2 He-like Al XII ion spectrum 7.75→7.9Å recorded during ~1MW of NBI heating 350msec into the shot lasting for ~100msec. This was an injected ion impurity produced by laser ablation during the neutral beam heating phase. The main spectral lines result from radiative decays from the first excited levels to the ground state, shown in the energy level diagram of Figure 5.9. The three intense lines are:

- The resonance line  $1s^2 \ ^1S_0 - 1s2p \ ^1P_1$  (w) is usually the most intense line in the spectrum whose decay probability scales as  $Z^4$ . This is an allowed electric dipole transition.
- The intercombination line  $1s^2 \ ^1S_0 - 1s2p \ ^3P_1$  (y) which is an electric dipole transition by the spin-orbit interaction where the decay rate scales as  $Z^9$ . The other intercombination line  $1s^2 \ ^1S_0 - 1s2p \ ^3P_2$  (x) has low emission for Aluminium, but is just visible for Silicon in Figure 5.11. (The improved resolution of the beam-foil measurement for Silicon in Chapter 7 shows the line clearly resolved). This line decays via a magnetic quadrupole transition at a probability scaling as  $Z^8$ . It occurs to the short wavelength side of the  $^3P_1$  line but is blended here. The separation and

emission increase with atomic number so that it can be resolved easily for He-like Chlorine ( $Z=17$ ).

- The forbidden line  $1s^2\ ^1S_0 - 1s2s\ ^3P_1$  ( $z$ ) decays by a relativistic magnetic dipole transition as  $Z^{10}$ .

The line between  $y$  and  $z$  is the He-like Mg XI  $1s3p\ ^1P_1$  transition which masks the Li-like Al XI inner-shell and dielectronic satellite lines. The low intensity lines to the long wavelength of the resonance line  $w$  are  $n \geq 3$  dielectronic satellites. (The line at  $7.77\text{\AA}$  is the  $d13$  transition, Table 7.1 Chapter 7).

The ion temperature  $T_i$  is extracted from a profile fit to the resonance line as shown in Figure 5.10. The line fit is stopped at the long wavelength side so as not to include satellite lines. This is a standard procedure for dealing with resonance lines from high  $Z$  with strong unresolved satellites, for example Fe ( $Z=26$ ) and Ni ( $Z=28$ ), see Bombarda et al<sup>96</sup>, but satellite contributions are not likely to be a serious problem here. The lines fitted with Voigt type functions are almost completely Gaussian in shape.

Further spectra from the intrinsic impurity He-like Silicon (Figures 5.11→5.14) recorded in subsequent days show changes in the line widths and intensity ratios. The intensity of the He-like Al XII  $1s^2\ ^1S_0 - 1s3p\ ^1P_1$  line at  $6.635\text{\AA}$  follows the changing injected Aluminium impurity concentration with plasma conditions. The ion temperatures observed on DITE are tabulated on Table 5.2.

It can be seen that there are differences in the intercombination line  $y$  and forbidden line  $z$  ratios for the two ions (Figure 5.8 and Figures 5.11, 5.13). These are long lived states which can have their populations depleted by collisional transitions to nearby states as the density increases. They are, therefore, useful density diagnostics in the corresponding intermediate density regime. As  $n_e$  increases from the low density limit, where lines are populated by electron impact excitation from the ground level, collisions deplete the forbidden line  $2\ ^3S_1 \rightarrow 2\ ^1P_1$  until  $z$  vanishes completely. Collisional transitions affect the longest lived levels with rising density, so that the forbidden line of low  $Z$  He-like ions is affected first. Thus, the He-like Oxygen ( $Z=8$ ) forbidden line is not observed on Tokamaks.

The R-ratio ( $=z/[x+y]$ ) is the defined parameter which is sensitive to density, with the R-ratios for Mg, Al and Si being the most useful for the DITE density range  $n_e=5 \times 10^{12} \rightarrow 10^{14}\text{cm}^{-3}$ . It may be noted that for Tokamak densities the G-ratio ( $= [x+y+z]/w$ ) is independent of density but is affected by electron temperature.

Both the R- and G-ratios have been measured on DITE and compared with theoretical calculations for Silicon<sup>97</sup> and Magnesium<sup>98</sup>. The ability to measure the density and temperature independently is essential here. Agreement for the measured and theoretical line ratios is within 10→15%. The main use of this diagnostic is its application to remote astrophysical plasmas for interpretation of density and temperature conditions.

$T_e$  Measurements from the Bragg Rotor Using Mg XII:  
Mg XI Line Ratios on DITE

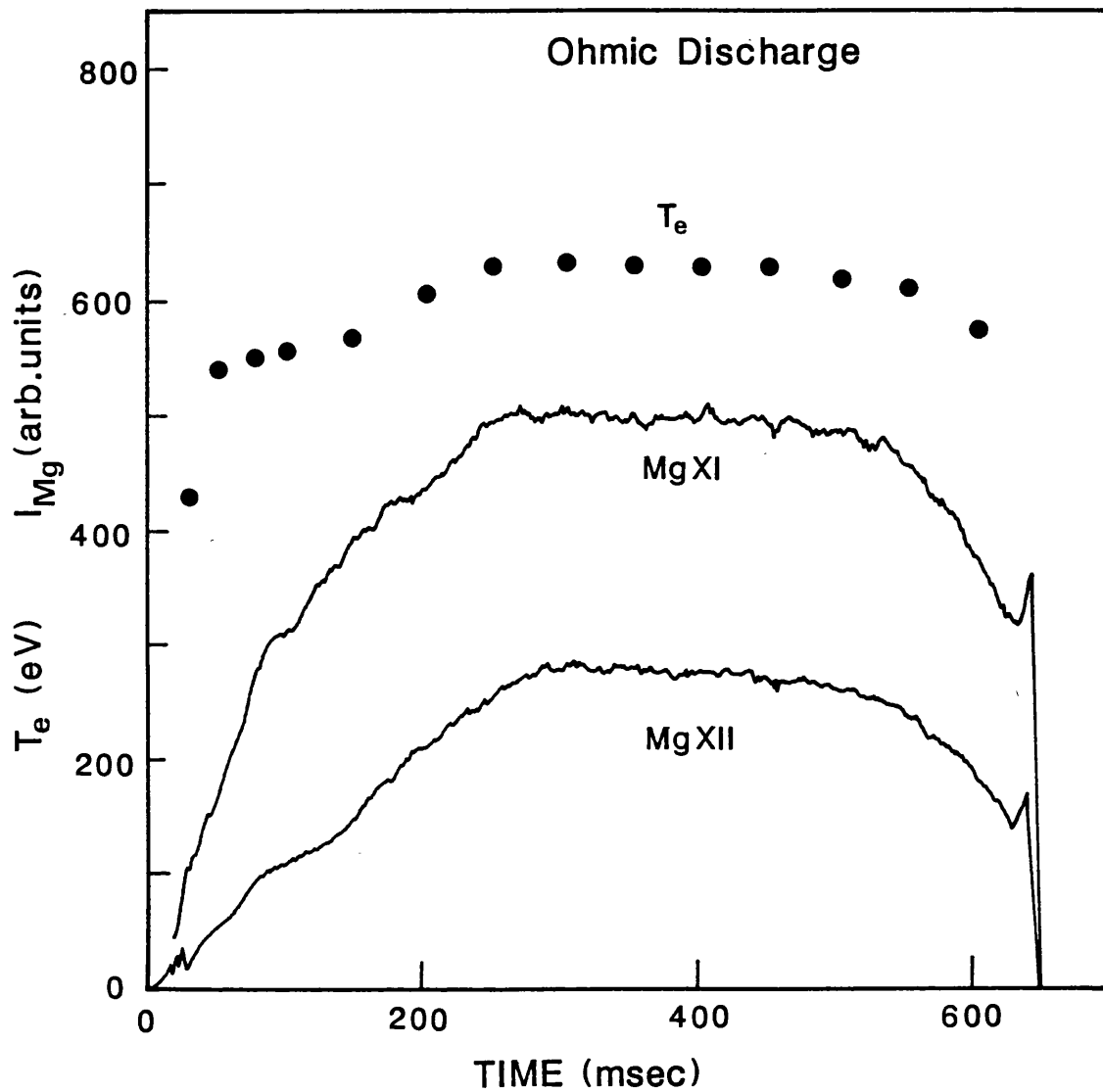


Figure 5.7 Bragg Rotor Measurement of the temporal emission of  $n=2$  Mg XII and Mg XI ion emission and calculated DITE electron temperature from line ratios.

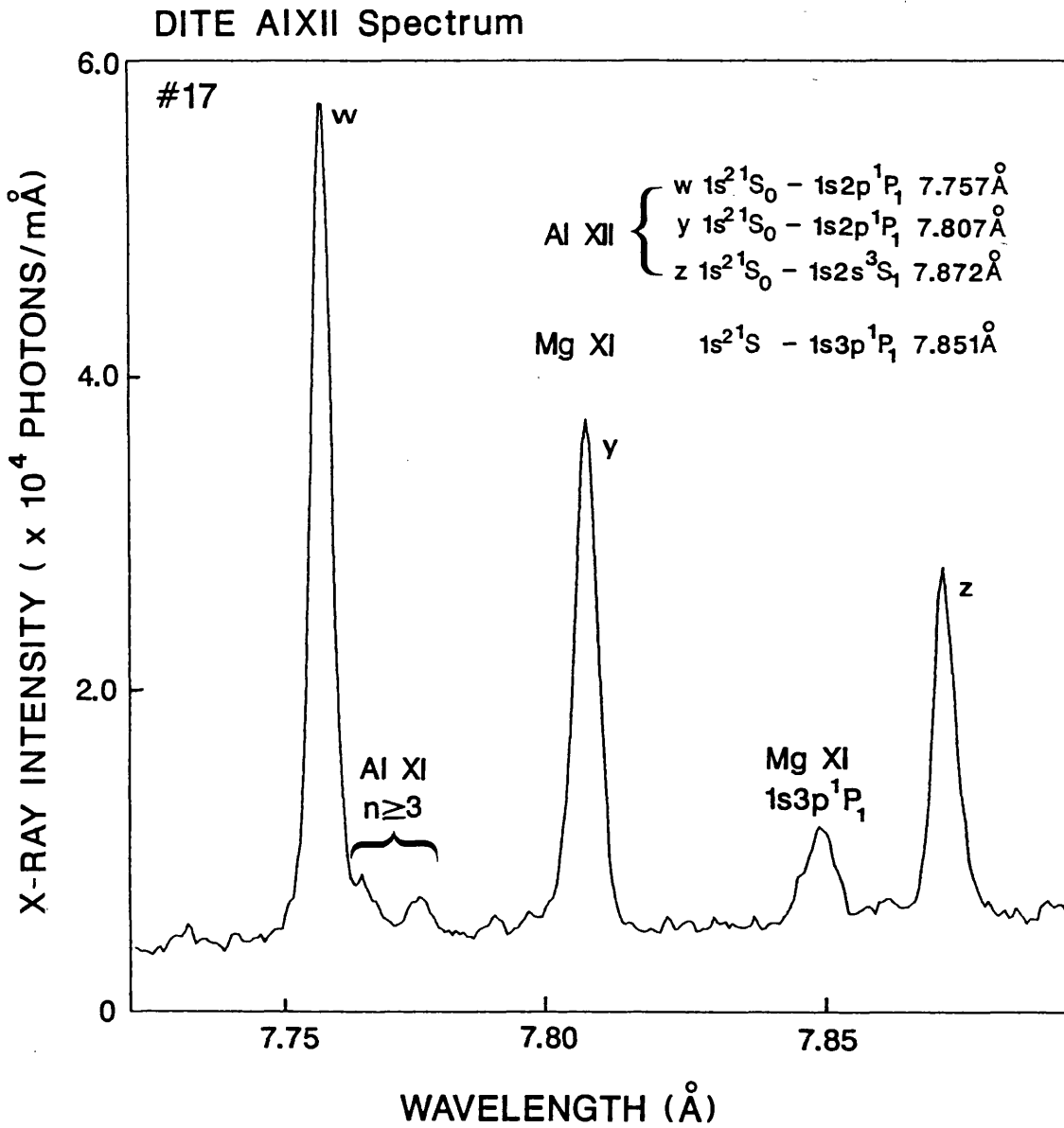


Figure 5.8 He-like Aluminium n=2 spectrum emitted during NBI.

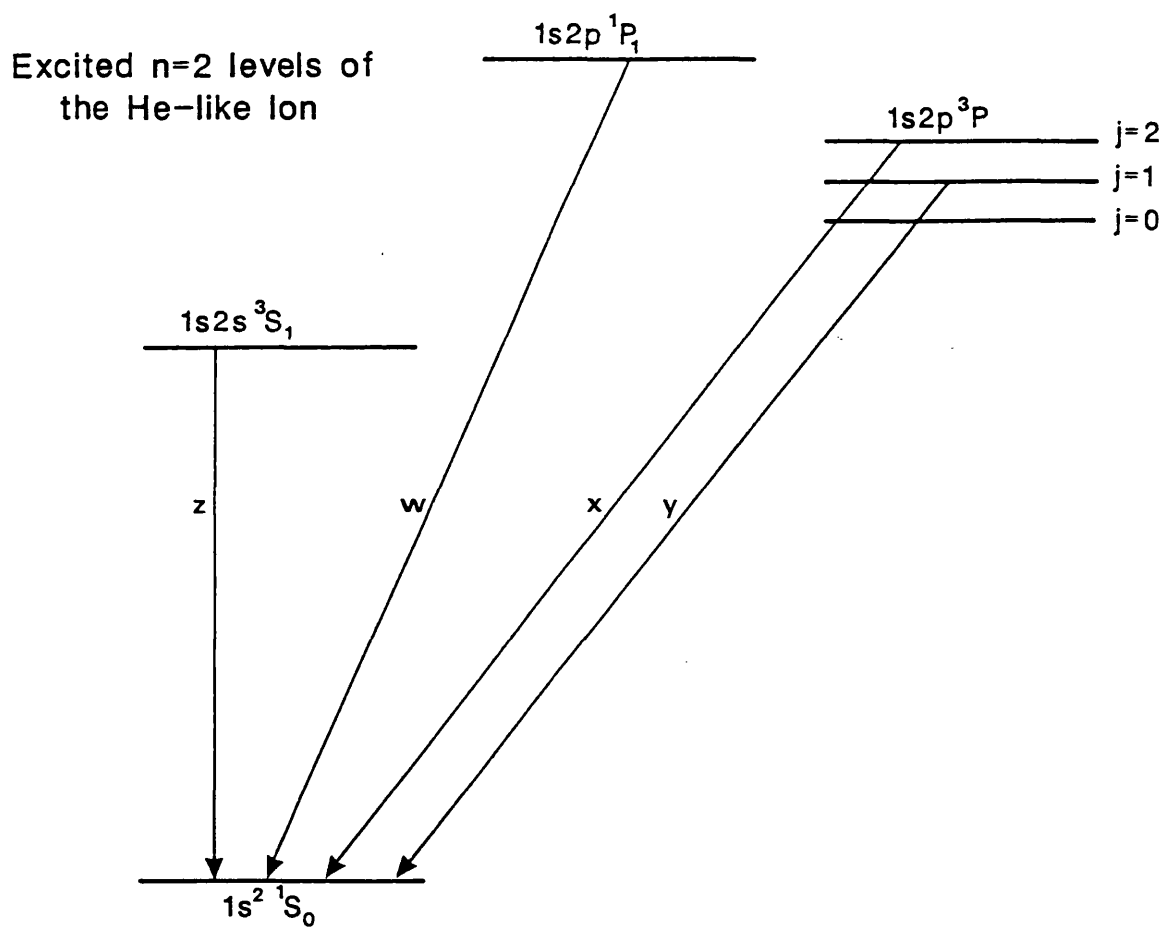


Figure 5.9 Energy level diagram of  $n=2$  excited states for He-like ion.

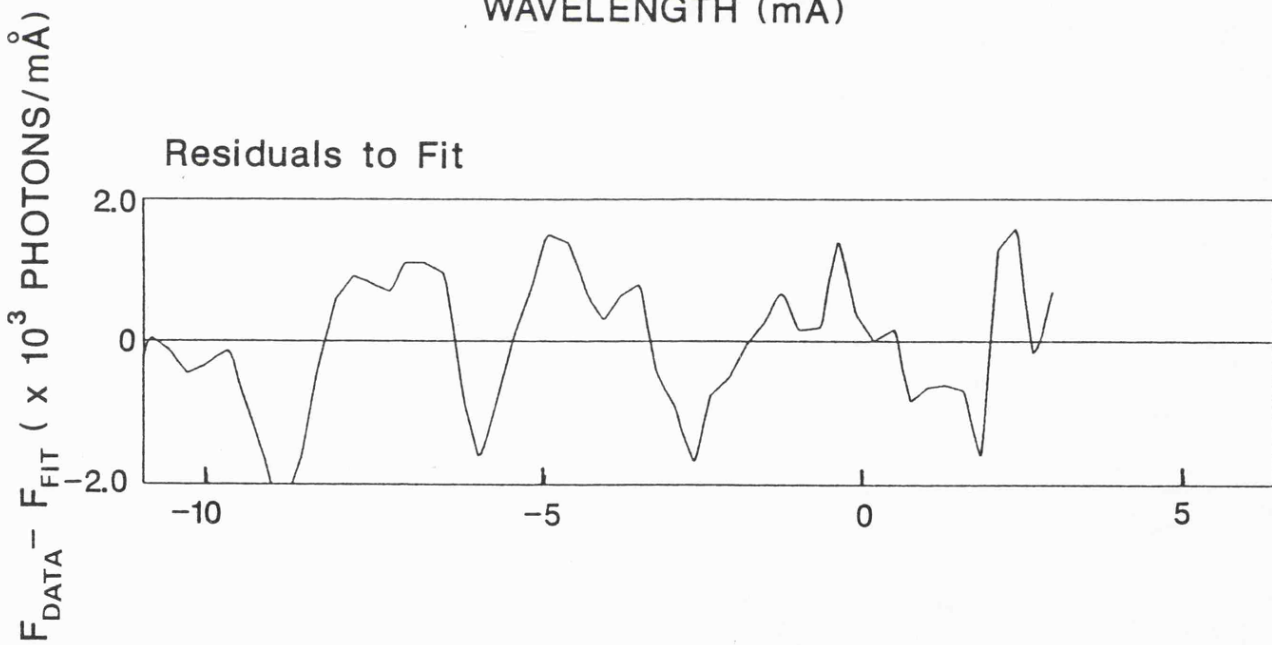
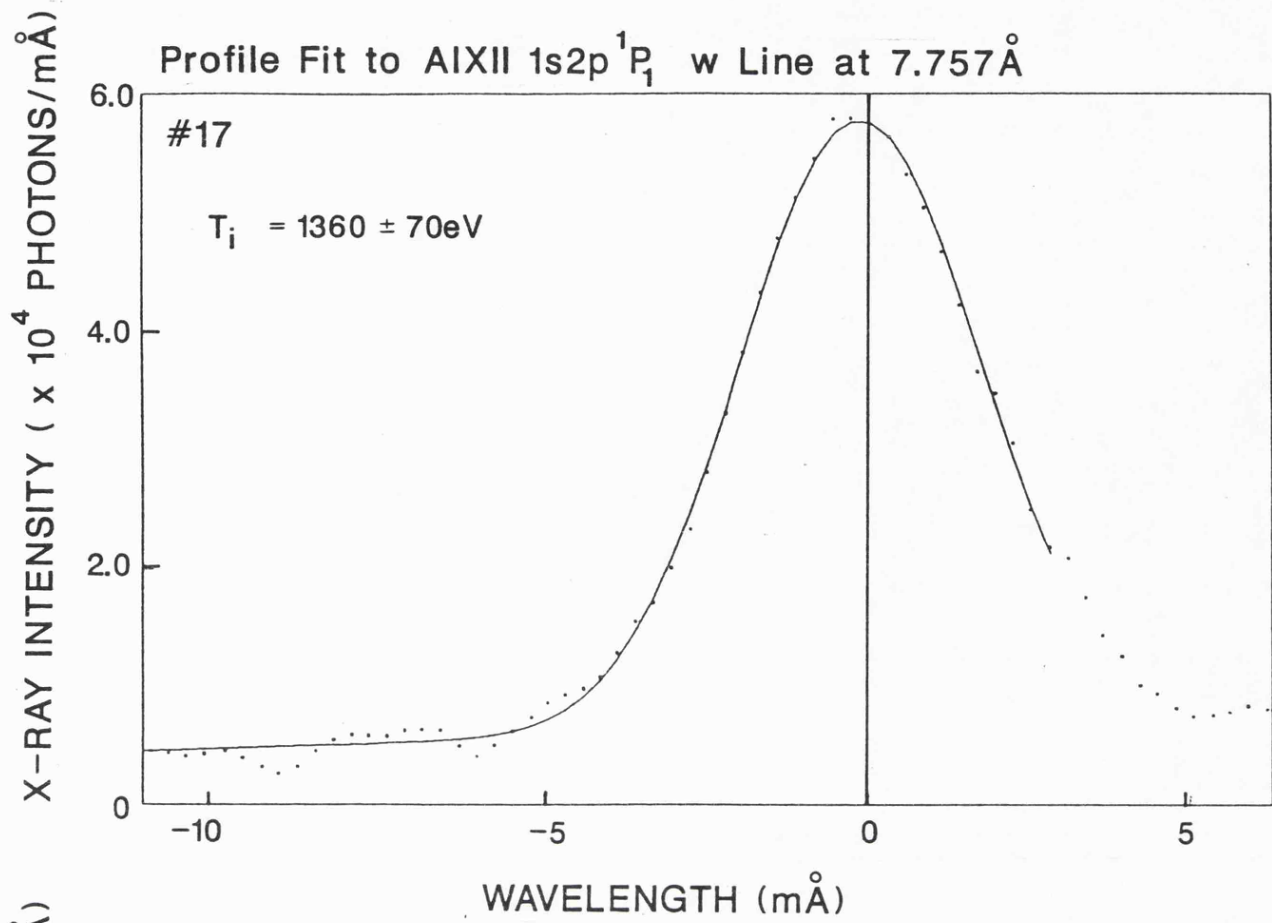


Figure 5.10 Profile fit to He-like Aluminium  $1s^2\ ^1S_0 - 1s2p\ ^1P_1$  (w) resonance line for DITE shot #17.

### DITE SiXIII Spectrum

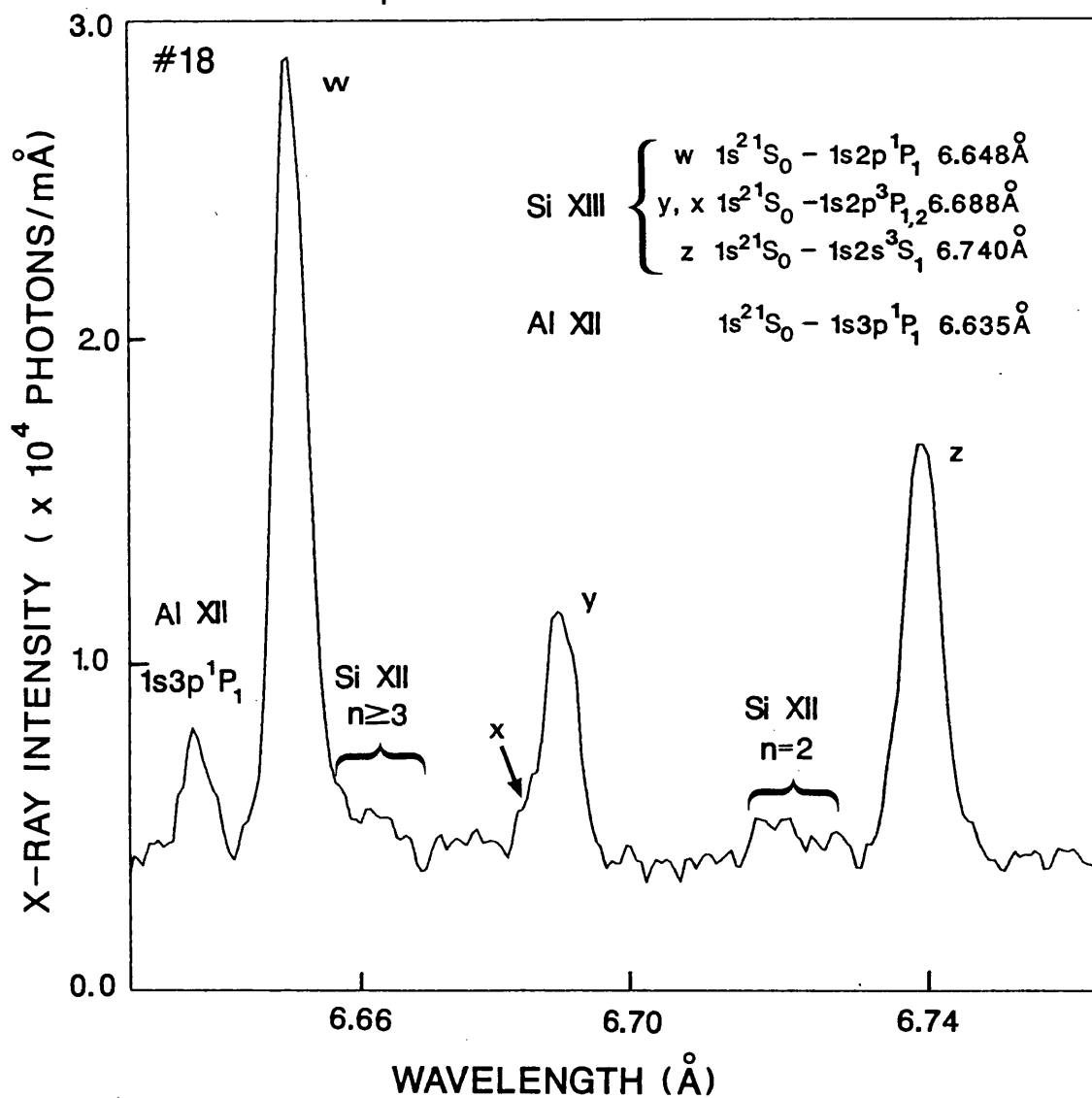


Figure 5.11 He-like Silicon n=2 spectrum emitted during NBI.

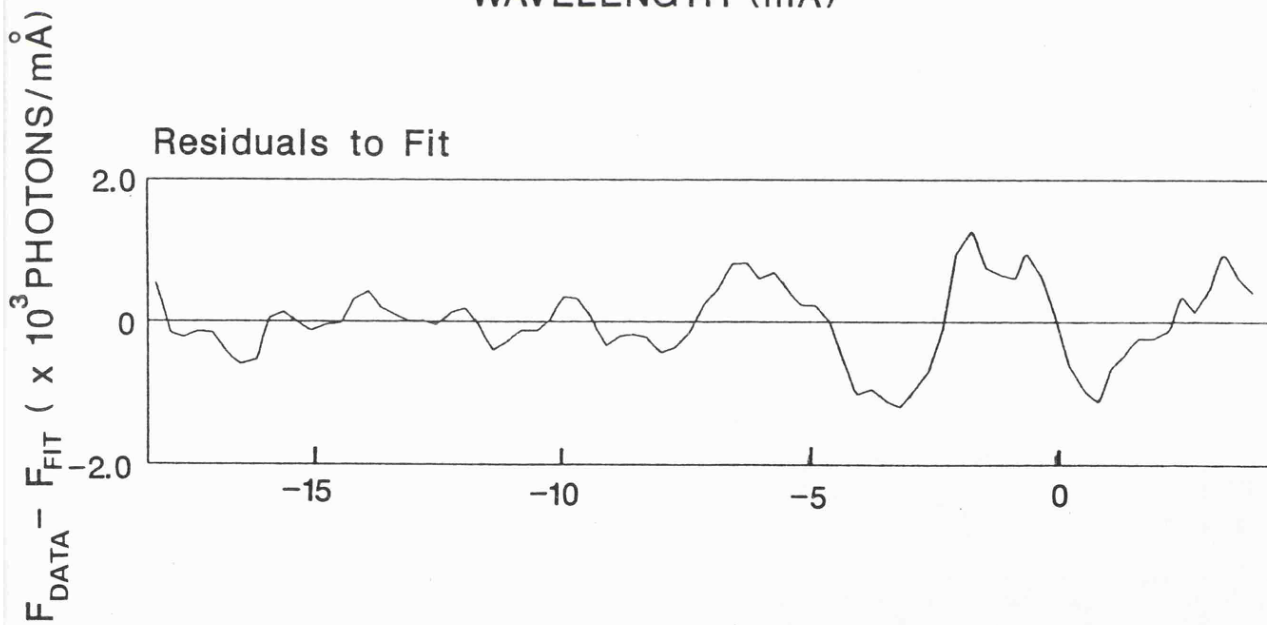
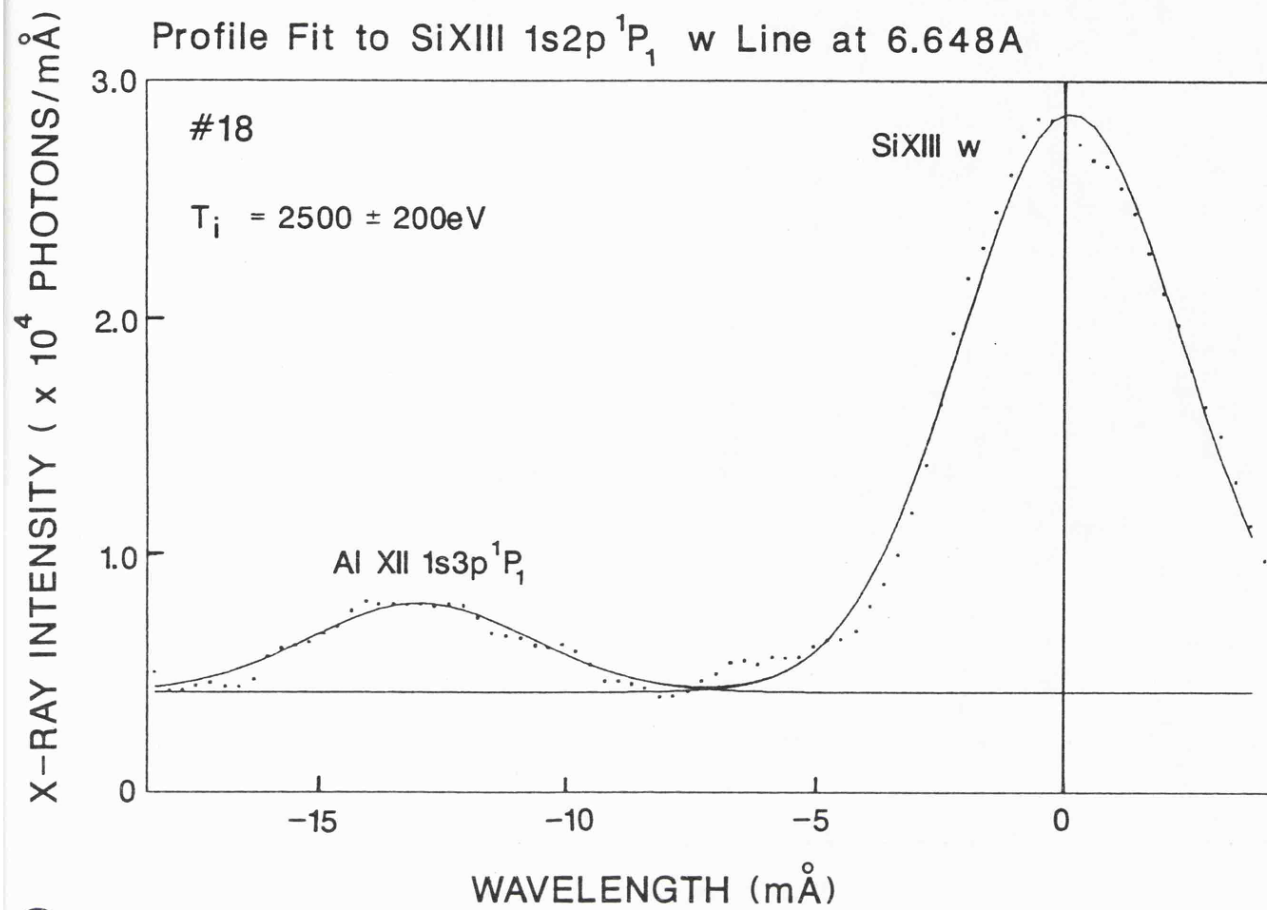


Figure 5.12 Profile fit to He-like Silicon  $1s^2\ ^1S_0 - 1s2p\ ^1P_1$  (w) resonance line for DITE shot #18.

### DITE SiXIII Spectrum

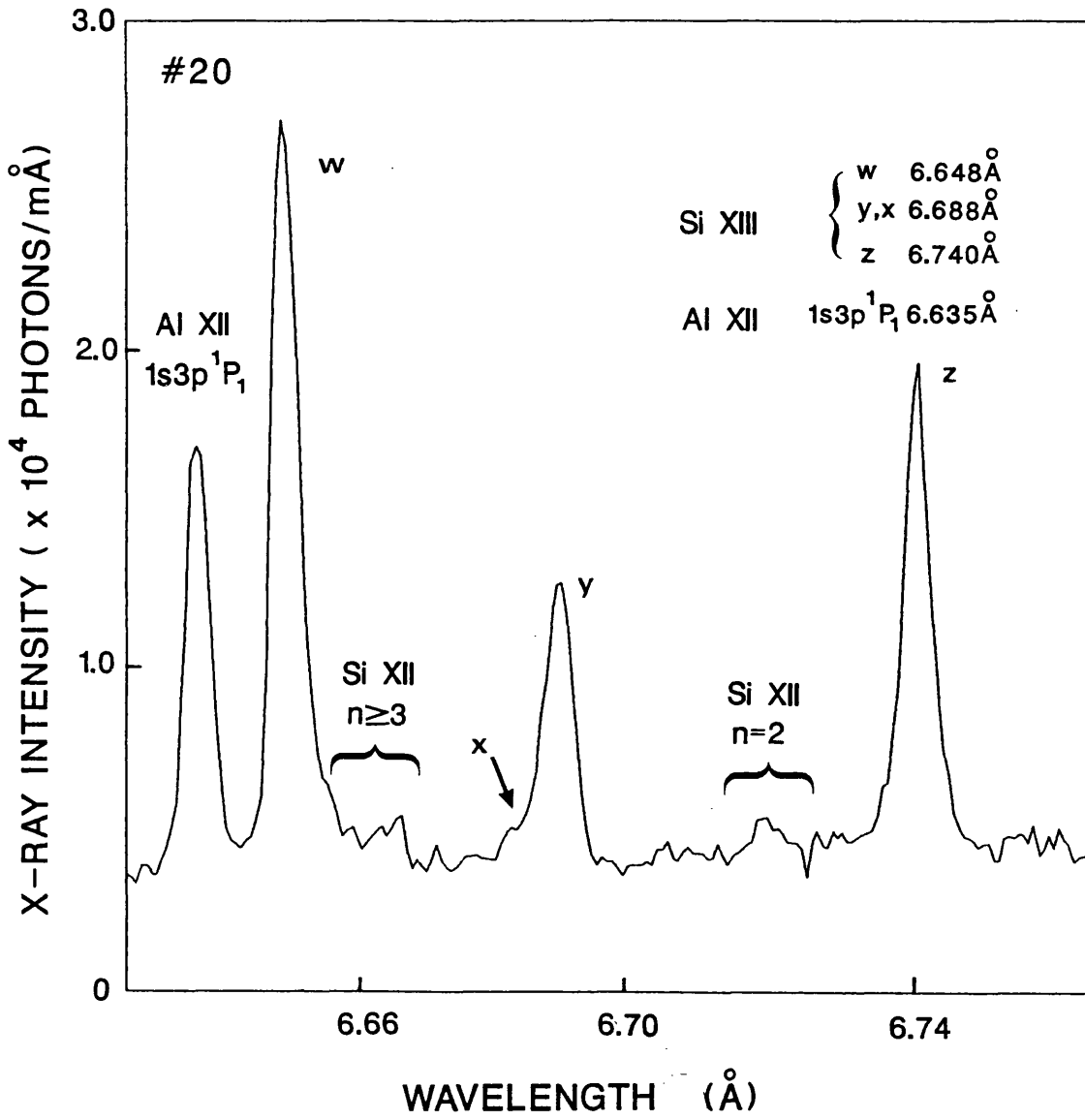


Figure 5.13 He-like Silicon n=2 spectrum emitted during NBI.

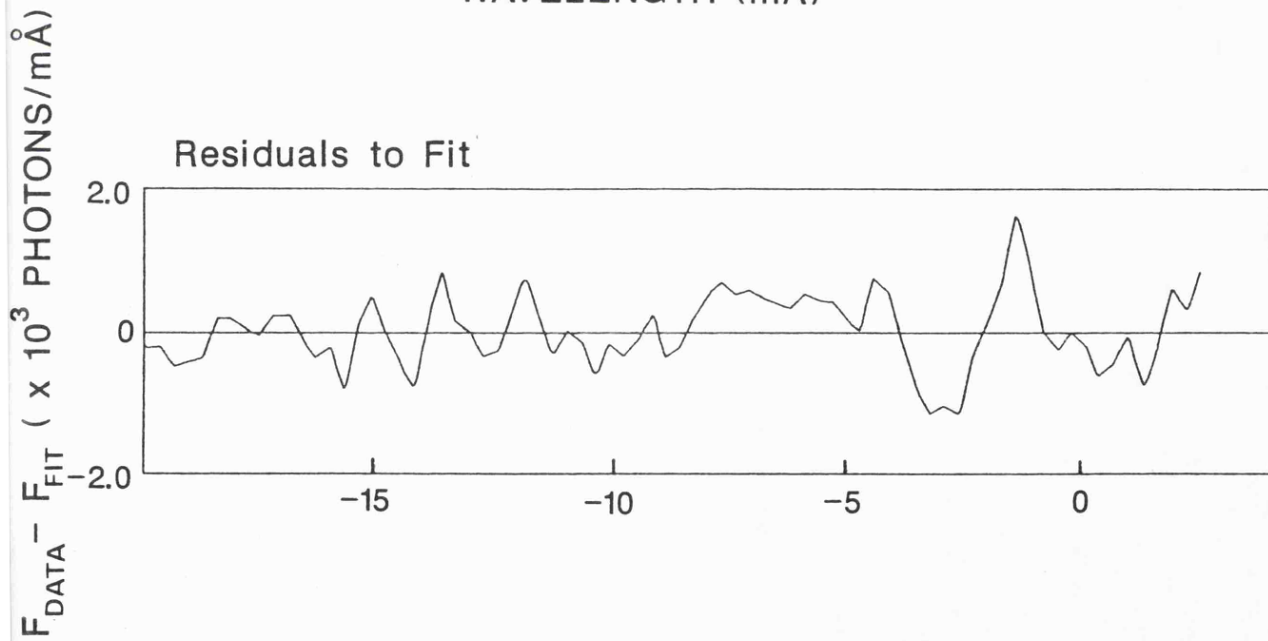
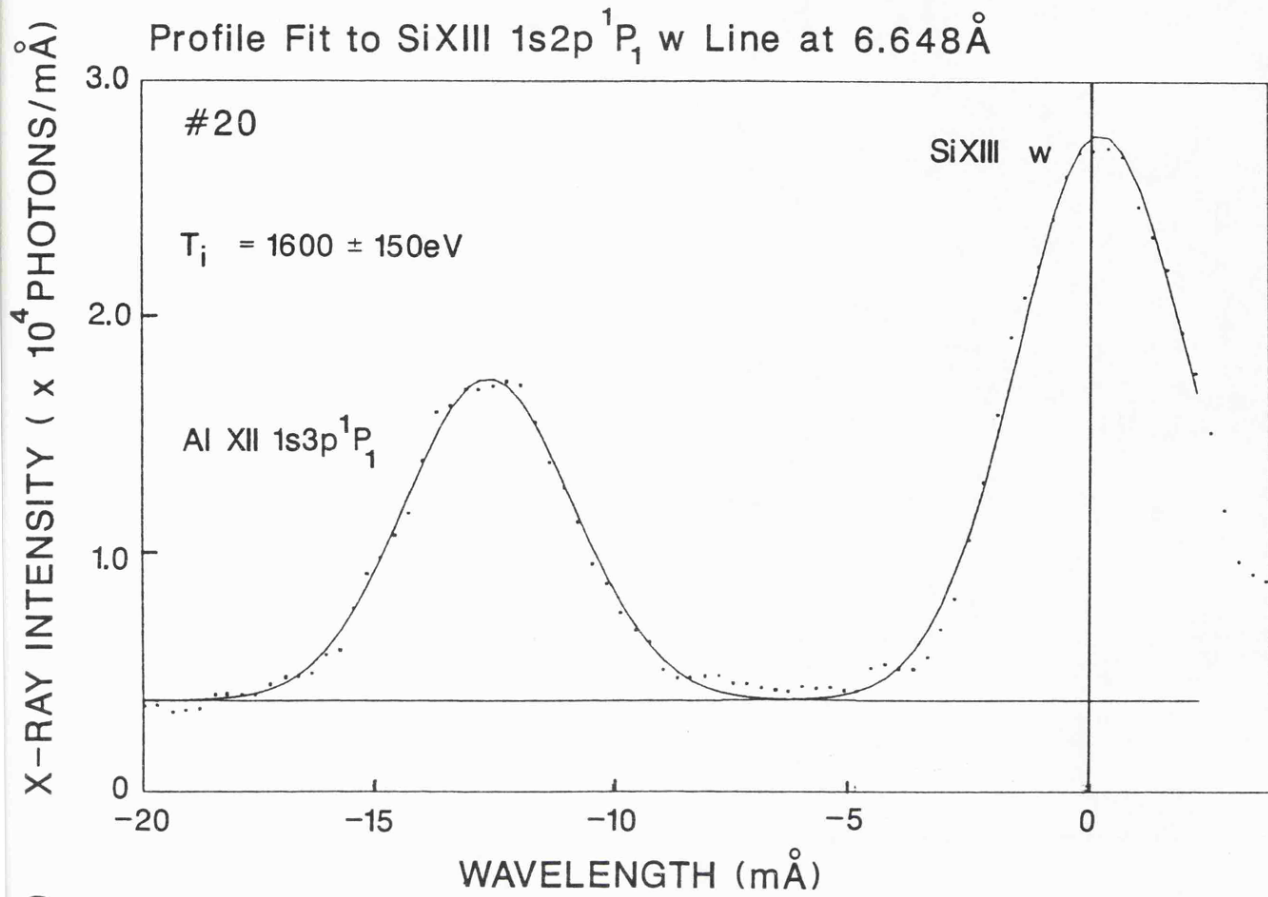


Figure 5.14 Profile fit to He-like Silicon  $1s^2\ ^1S_0 - 1s2p\ ^1P_1$  (w) resonance line for DITE shot #20.

Spatial Profiles of Electron Temperature  $T_e$  and Ion Temperature  $T_i$

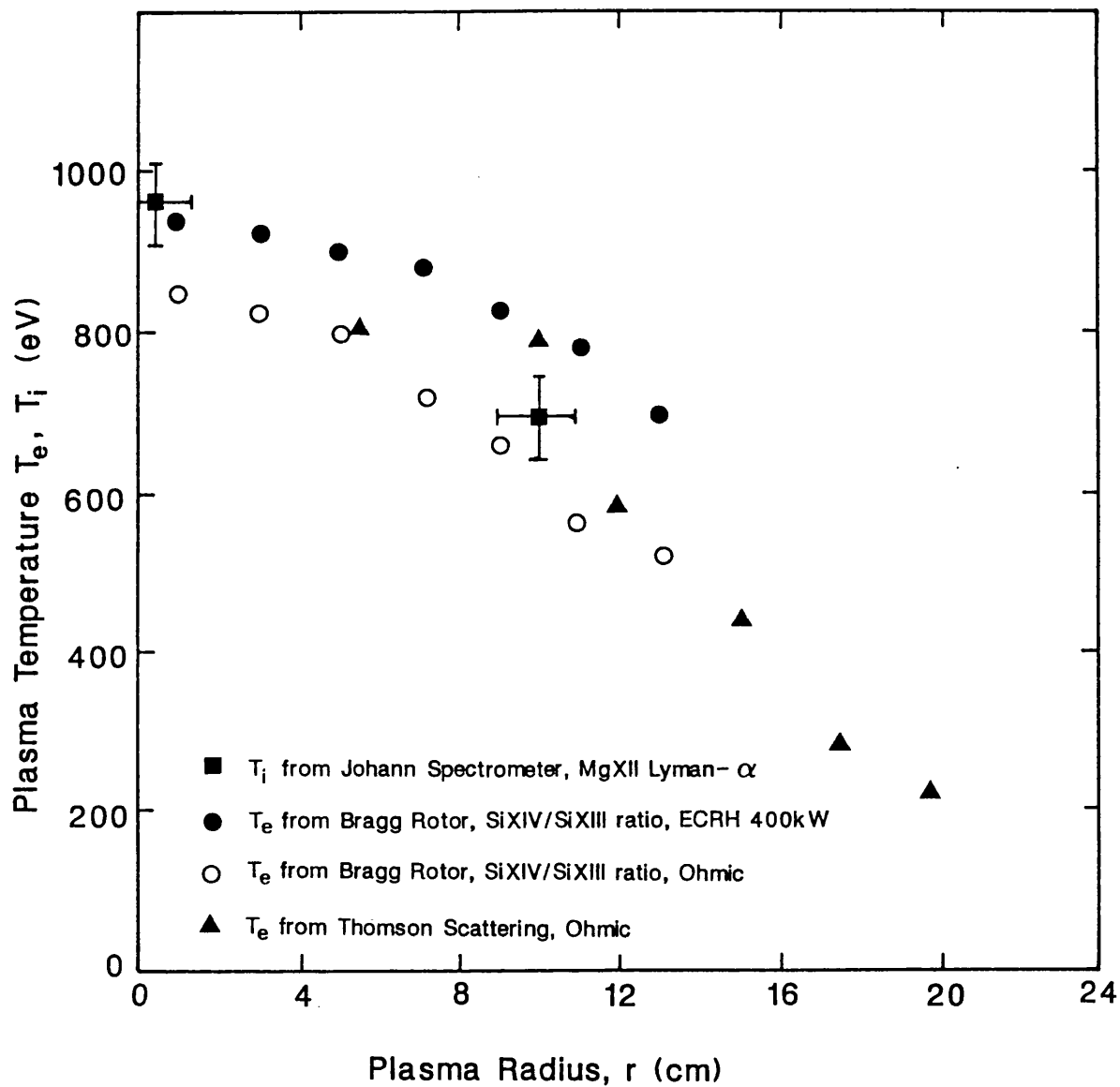


Figure 5.15 Radial scans of the plasma temperature from Thomson scattering, the Bragg Rotor and the Johann spectrometers.

**Table 5.2 Ion Temperature Measurements on DITE Tokamak.**

Spectrum Number	Position	X-ray lines §	No of shots	Measured T <sub>i</sub> (eV)	n <sub>e</sub> (x10 <sup>13</sup> cm <sup>-3</sup> )	T <sub>e</sub> (eV)	Additional Heating and Comments.
#16	A	AlXII 2p <sup>1</sup> P <sub>1</sub>	Inj	12	1290 ± 60	4.4	NBI: 3-Beams on, Beam line A on 7 shots. BDII on.
#17	A	AlXII 2p <sup>1</sup> P <sub>1</sub>	Inj	19	1360 ± 70	5.2	NBI: 12 shots 3-Beams on, 7 shots 2-Beams on, Beam line A on full time. BDII on.
#18	A	SiXIII 2p <sup>1</sup> P <sub>1</sub>	Int	24	2550 ± 180	4.0	NBI: 20 shots 3-Beams on, 3 shots 2-Beams on, Beam line A on full time. BDII off for 18shots. Neon puff at 350msecs.
#20	A	SiXIII 2p <sup>1</sup> P <sub>1</sub>	Int	28	1660 ± 130	5.8	NBI: 1 shot 3-Beams on, 14 shots 2-Beams on, 11 shots 1-Beam on. Beam line A on for 6 shots. BDII off for 6 shots.
		AlXII 3p <sup>1</sup> P	Inj		1540 ± 130		
		Al XIII Ly-α	Inj		1480 ± 80		
B		SiXIII 2p <sup>1</sup> P <sub>1</sub>	Inj		750 ± 50	3.0	Ohmic Heating.
B		SiXIV Ly-α	Inj		850 ± 70	3.0	Ohmic Heating.
B		SiXIV Ly-α	Inj		1050 ± 60	2.4	Ohmic Heating + 400kW ECRH.
B*		MgXII Ly-α	Inj		960 ± 50	2.7	High impurity concentration.
B*		MgXII Ly-α	Inj		690 ± 50	1.5	
# 32836	C†	MgXII Ly-α	Inj		925 ± 40	2.4	Ohmic Heating + 400kW ECRH.
# 32849	C†	MgXII Ly-α	Inj		1165 ± 40	2.4	High impurity concentration.

**Key:** \* Spatial scan § Int - Intrinsic impurity, Inj - Injected impurity.

† 2 crystal spectrometer

### **Spatial Scans on DITE.**

Spatial scan results of the plasma temperature from Thomson scattering, the Bragg Rotor and the Johann instruments are given in Figure 5.15. The data represents plasmas heated Ohmically and by electron cyclotron resonance heating (ECRH). There is good agreement between the  $T_i$  and the  $T_e$  radial profiles. The effect of ECRH on the electron temperature is apparent.

### **5.5.4 Toroidal Rotation during Neutral Beam Injection.**

Bulk toroidal motion of the plasma correlated with  $H^0$  beam injection has been reported on DITE Tokamak by Hawkes and Peacock<sup>99</sup>. Using a 1 metre normal-incidence grating-diffraction spectrometer viewing a fixed tangential chord almost parallel to the A-line injection beam, emission line profiles and shifts could be measured in the spectral range 250→6000Å. A multi-channel detection system with this instrument could read out a portion of the spectrum at 2.5msec intervals. Through study of emission lines from highly ionized intrinsic impurities in the plasma core, toroidal rotation velocities up to  $1.5 \times 10^7$  cm/s were observed during co-directional beam injection with the bundle divertor switched off. Lower rotational speeds of  $< 2 \times 10^6$  cm/s were reported with normal operation of the bundle divertor. In the case of no beam injection, toroidal rotation was reported to be zero.

An increase in the line width and asymmetry in the profile was noted<sup>99</sup> which could not be attributed purely to an ion temperature increase. Widths corresponding to  $T_i > 2.5$  keV could only be explained as rotational shear along the tangential line of sight.

A similar explanation can be given to the ion temperature results measured on consecutive days in position A during NBI (See Table 5.2), though the  $12^\circ$  angle of observation from the radial chord should reduce the observed toroidal velocities to  $v \sin 12^\circ$ . Since line emission is observed to rise strongly during NBI, the measured resonance line intensities come mainly from here. The Aluminium emission is only during NBI. Figure 5.10 for #17 exhibits a Gaussian profile corresponding to an ion temperature  $T_i \sim 1.3$  keV. The bundle divertor BD II was on throughout this exposure. Figures 5.11 and 5.12 show a dramatic increase in the line width ( $\sim 1:1200$ ) and a distorted non-Gaussian line shape. The  $T_i$  value increases to  $\sim 2.5$  keV even when broadening is included due to peak toroidal velocities of  $1.5 \times 10^7$  cm. Thus similar results to Hawkes and Peacock have been observed, consistent with the bundle divertor switched off during  $H^0$  injection. A repeat spectrum Figures 5.13, 5.14 the following day with lower power NBI and the bundle divertor on for all but 6 shots indicates that rotational shear in less than 25% of the shots is sufficient to increase the ion temperature measurement by a further 300eV.

## 5.6 The Bragg Rotor 2-Crystal Spectrometer.

A second high resolution spectrometer was used at a later date to make independent ion temperature measurements and verify the previous Johann data.

### 5.6.1 Instrument Description and Experiment.

The Bragg rotor spectrometer<sup>16</sup>, normally used as a single crystal, low resolution, time-resolved survey instrument, was modified<sup>54</sup> to give high spectral resolution on a few lines. The beam collimator, composed of Mylar slots FWHM of 0.002rad defining the instrumental resolving power ( $\lambda/\Delta\lambda=1100$  at  $\theta=65^\circ$ ), was removed and a second static crystal was added. The spectrometer geometry was used in the (1,+1) dispersive mode as shown in Figure 5.16, but with only the first crystal rotating. The MWPC detector recorded the x-ray photon beam from crystal 2 and the wavelength calibration came from the absolute angle encoder on crystal 1. A spectrum was obtained by turning crystal 1 during the shot, thus building the spectral coverage with time. This meant that the instrument line of sight was scanned at  $3\theta$  through the plasma, different parts of the plasma sequentially giving the spectrum.

Two identical PET (002) crystals, cleaved from the same block, were used to observe the Magnesium Ly- $\alpha$  doublet (8.42Å) at the Bragg angle of  $74.5^\circ$ . As observed earlier, this waveband was dominated by the strong Iron L-shell emission almost forming a continuum. The Magnesium ion impurity was introduced by a probe on the edge of the Helium plasma. The best results for ion temperature studies were achieved where the doublet was free from other contaminating lines.

### 5.6.2 Results and Analysis.

Figures 5.17 and 5.18 (DITE shots #32836 and #32849, respectively) were recorded on the same day under similar plasma conditions and represent the best data with this instrument. They show Mg Ly- $\alpha$  spectra emitted from the central plasma chord about 275 msec into the shot and integrated over 100msec. The peak signal count rates are high (several MHz), giving good S/N, with the detector showing no sign of saturation. Experimental data points are shown with the best profile fit (Gaussian in this case) for the doublet. The quality of the fit is excellent. There is no indication of Voigt-type wing features on the profile. This is consistent with the measurements of the Johann instrument. The measured line widths are also observed to vary on a shot to shot basis: the two results here differ by 10%, with 1:1975 and 1:1780, respectively.

## Schematic of 2-Crystal Spectrometer

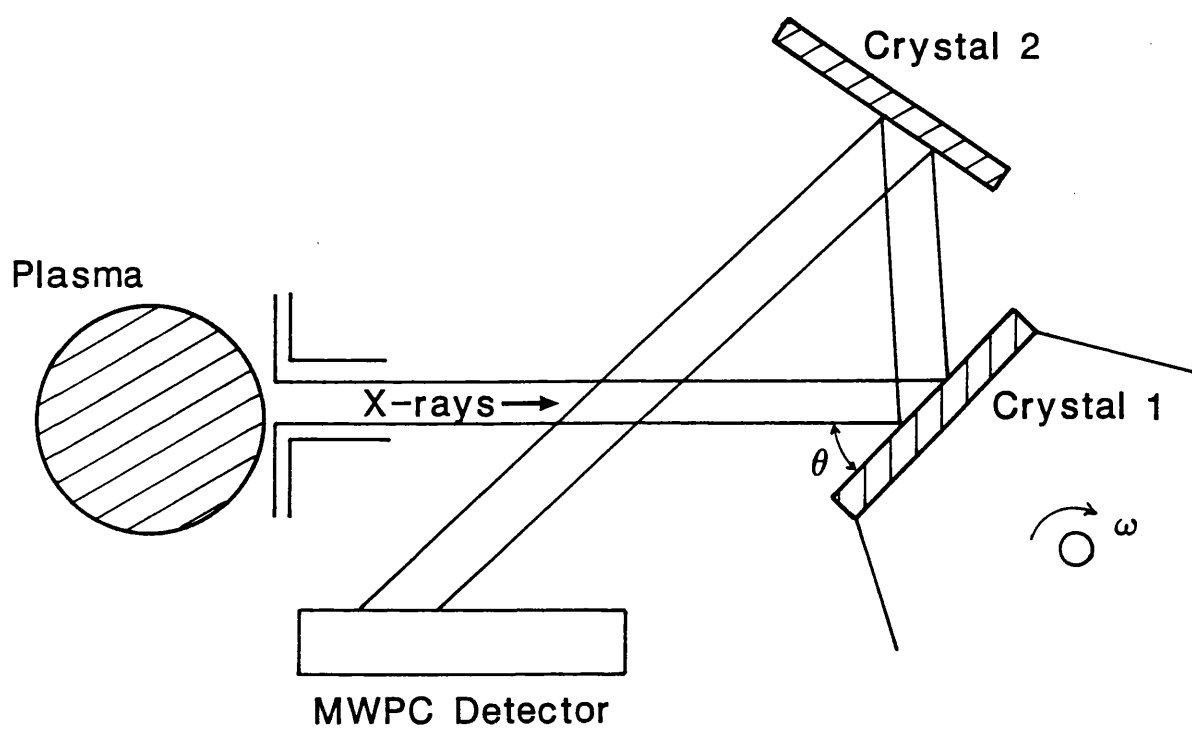


Figure 5.16 Schematic of Bragg Rotor spectrometer in 2 crystal configuration.

### MgXII Lyman- $\alpha$ Doublet at 8.42 $\text{\AA}$

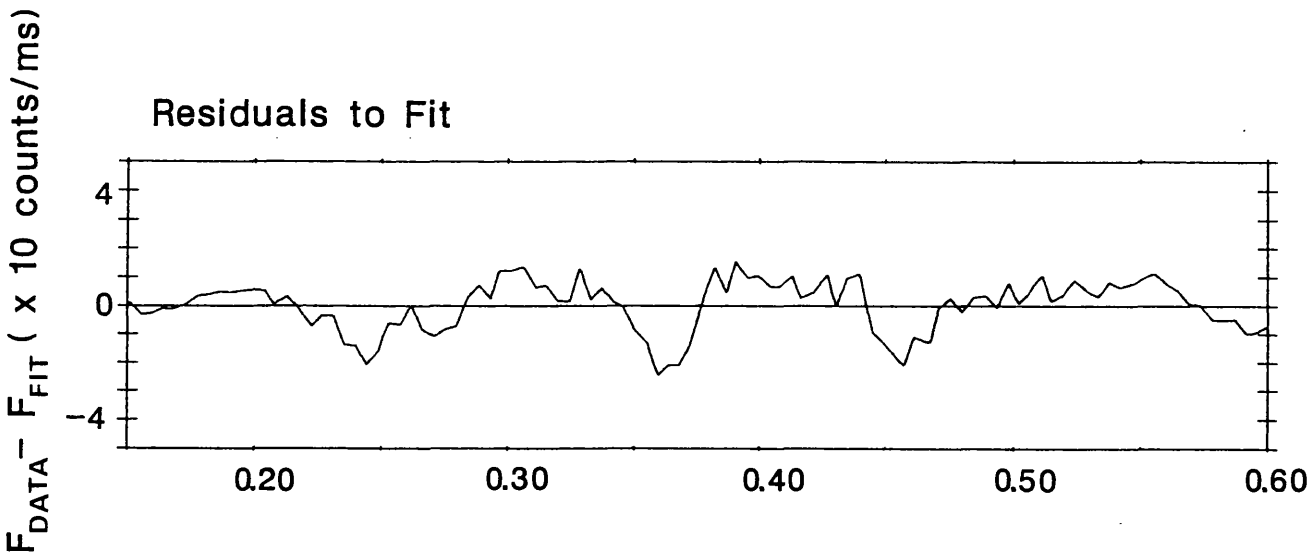
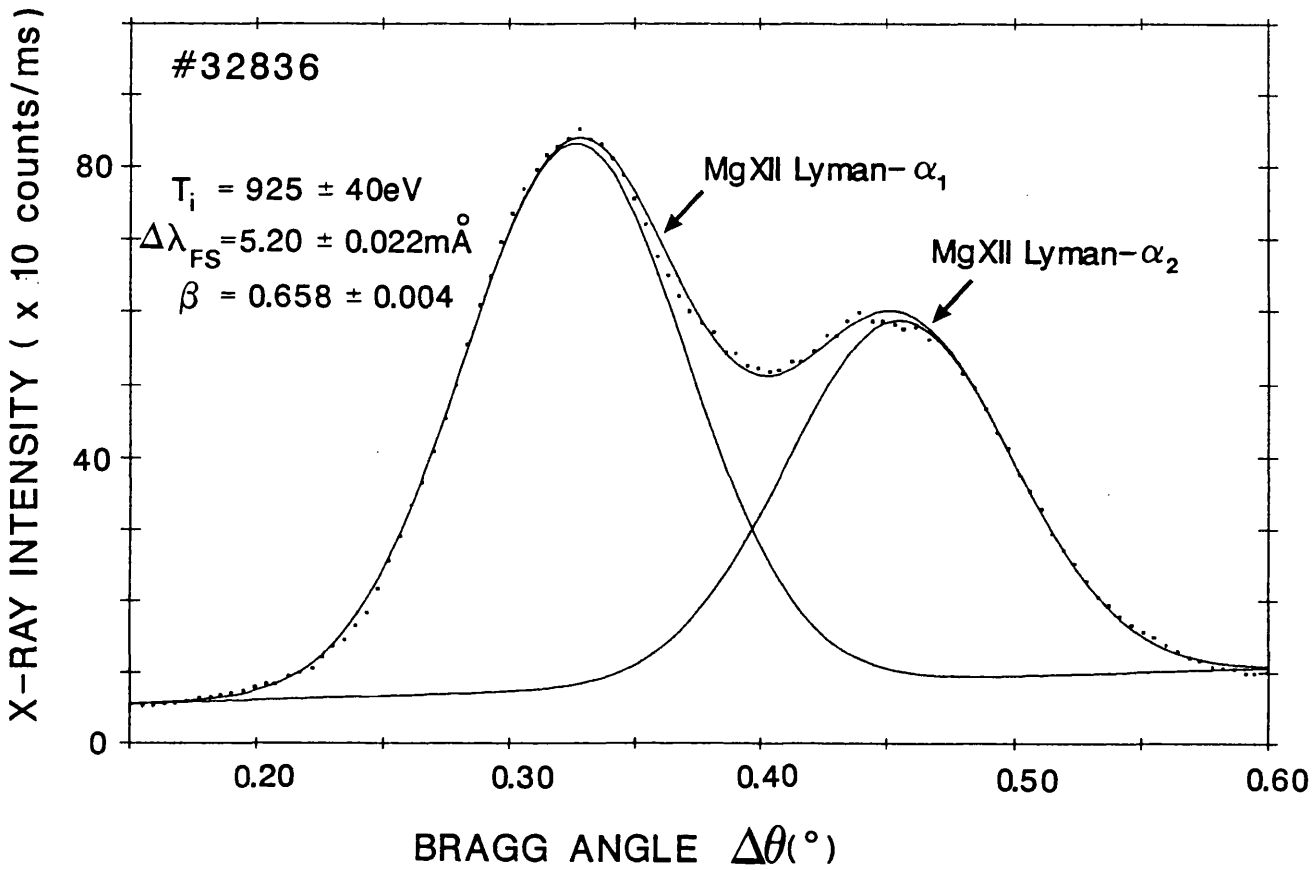


Figure 5.17 Mg XII Lyman- $\alpha$  spectrum recorded with Bragg Rotor 2-crystal spectrometer, shot #32836 on DITE Tokamak. Bottom window shows residuals to Gaussian line fit.

# MgXII Lyman- $\alpha$ Doublet at 8.42 $\text{\AA}$

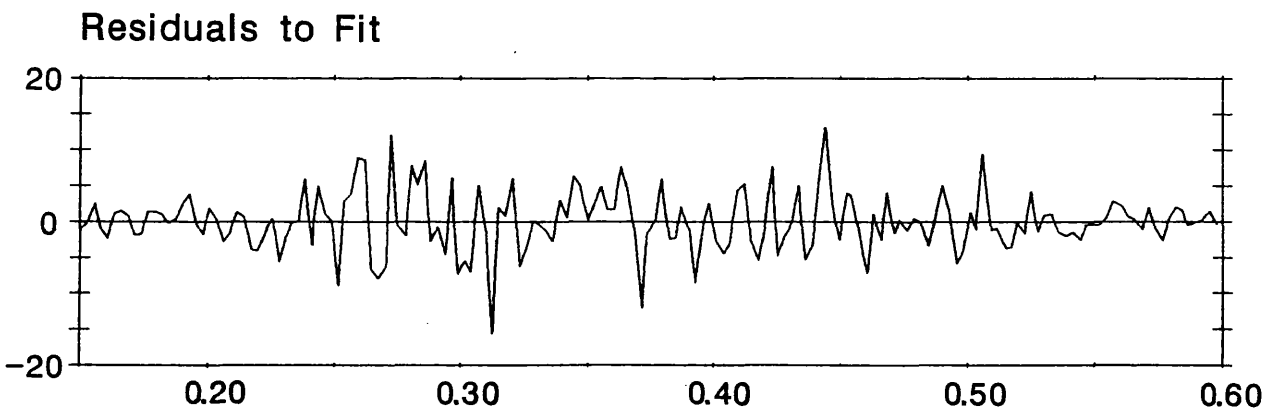
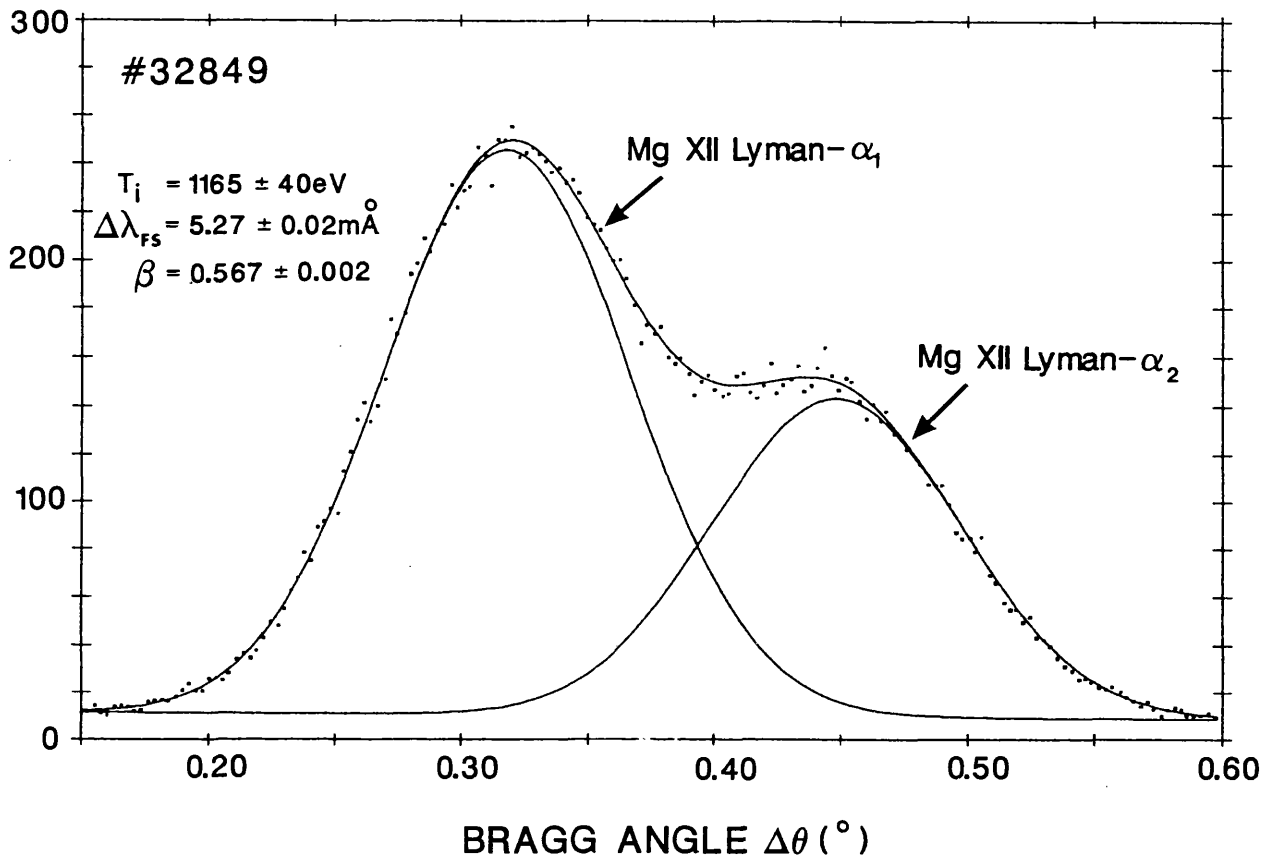


Figure 5.18 Mg XII Lyman- $\alpha$  spectrum recorded with Bragg Rotor 2-crystal spectrometer, shot #32849 on DITE Tokamak. Greater line broadening indicates higher ion temperature. Bottom window shows residuals to Gaussian line fit.

In order to measure the ion temperature  $T_i$ , the difference between the resolving power of a 1- and 2-crystal spectrometer must be considered. The resolving power of a 2-crystal spectrometer can be written as:

$$\frac{\lambda}{\Delta\lambda} = \frac{2\tan\theta_B}{\alpha w_c} \quad (5.48)$$

where  $w_c$  is the single crystal rocking curve width and  $\alpha$  depends upon the profile shape. Therefore, for  $\alpha < 2$  the 2-crystal instrument is superior. The PET (002) rocking curve profile tends to become more Gaussian as a result of increased absorption of the radiation within the crystal lattice with wavelength. This will give a value for  $\alpha$  closer to 1.4 than 2.0. A resolving power  $\lambda/\Delta\lambda \sim 5000 \rightarrow 7000$  can be assumed depending on the crystal condition.

The ion temperature is estimated to be  $T_i = 925\text{eV}$ ,  $1165\text{eV}$  with error bars  $\pm 40\text{eV}$  for #32836 and #32849, respectively. These values are in close agreement with the Johann instrument measurements with no NBI and in fact indicate a higher ion temperature for #32849. As shown by the high x-ray intensity, the plasma had a high Mg impurity.

The fine-structure separation  $\Delta\lambda_{FS}$  and intensity ratio  $\beta$  (see Chapter 8) have also been measured. Some differences with the Johann measurements are revealed which can be attributed to variation in the source function for the spectral lines as a result of the  $3\theta$  scan. The #32836 appears to be affected most with  $\Delta\lambda_{FS}$  4% smaller than the theoretical value. This result is well outside the estimated error bar of  $\pm 0.4\%$ . These are subtle effects which will not invalidate the ion temperature measurements but do highlight an instrumental characteristic. Rotation of both crystals simultaneously would give no movement of the line-of-sight through the plasma, while rotation of crystal 2 only would scan at  $\theta$  (Barnsley<sup>54</sup>).

## 5.7 Time-Resolved Spectra Using CCD Detector.

### 5.7.1 Description.

An opportunity presented itself to run the spectrometer with a standard TV format CCD detector<sup>100</sup>. The detector's active area measured  $8.5 \times 6.5\text{mm}^2$  (length  $\times$  height) with individual pixel sizes of  $22 \times 22\mu\text{m}^2$ . The detector readout was at standard video rates of 50Hz, corresponding to a frame every 20msec. The small detector size restricted the instrument waveband. The following parameters were given priority:

- High signal throughput was essential to utilise the 20msec time resolution.
- An injected silicon impurity was needed for strong x-ray emission.
- A waveband  $\Delta\lambda/\lambda = 0.15$  was needed to record the Si XIII ion resonance lines at  $6.648 \rightarrow 6.740\text{\AA}$  in each frame.

This led to the instrument specification:

- ADP (101) crystal radius  $R=657\text{mm}$  was chosen with active area  $28\times 22\text{mm}^2$  and set to a Bragg angle  $\theta=38.95^\circ$ .
- The CCD chip was mounted on the Rowland Circle, but perpendicular to the diffracted x-ray beam instead of the usual tangential geometry. A transparent  $0.5\mu\text{m}$  polypropylene window was placed over the CCD aperture to protect it from dust. A light tight  $2\mu\text{m}$  Mylar filter with  $1000\text{\AA}$  Al coating was used to pass the diffracted rays.
- Resolving power was reduced to  $\lambda/\Delta\lambda=2500$  due to the dominant Johann height error.

The CCD was also useful for focusing the crystal in visible light. An optical focus of  $60\mu\text{m}$  FWHM was easily achieved. The visible and x-ray light images were recorded onto video tape using a commercial video cassette recorder. Individual frames were analysed with a frame-store. The S/N ratio was improved by compressing the 2-dimensional height information into 1-dimension.

### 5.7.2 Results.

Figures 5.19(a) and (b) indicate the spectra taken on the same day by the Bragg Rotor and Johann CCD instruments for the Si XIII ion resonance lines. The Bragg Rotor PET (002) spectrum shows higher signal rates as a result of good sensitivity but has low spectral resolution, the  $^1P_1$  line resolved to 1:540. In contrast, Figure 5.19(b), a 20msec frame from the Johann spectrometer, exhibits higher spectral resolution by a factor of three but has low S/N ratio. The line intensity ratios are similar for the main transitions.

The observed spectral resolution may have been higher for the Johann instrument, had the crystal curvature not been disturbed during installation on the Tokamak. Figure 5.19(c) displays the optical focus quality in visible light; the usually narrow single line focus has multiple defocussed fringes featured to one side. These fringes are manifested on the x-ray spectrum of Figure 5.19(b), but as mentioned previously in Chapter 3, defects in the visible light focus are diminished in the corresponding x-ray image.

### Time Evolution of Spectral Emission.

Figure 5.20 indicates the time evolution of the He-like Si ion resonance line w during the shot. The top graph shows the integrated line intensity at 20msec intervals. The lower graph is the line width time history. This shot is not typical because the Si concentration is much higher than previous DITE plasmas. A consequence is a minor disruption at 220msec resulting in a sudden drop in the line emission.

The main features to be noted in the time history of shot #34150 are:

- A variation of a factor of six of the line intensity.
- A change in the observed line width of more than a factor two during the shot; observed spectral resolution  $\delta\lambda/\lambda$  lies between 1:950 and 1:2250.

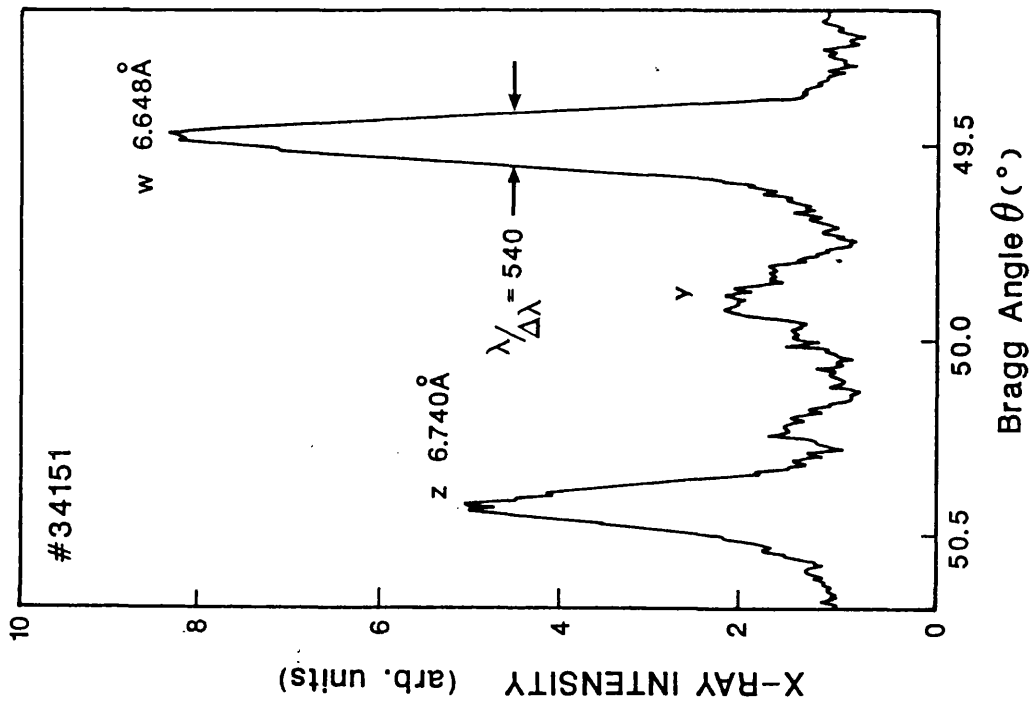
Figure 5.19 (a) (over the page) shows a typical slow scan Bragg Rotor PET (002) Si XIII n=2 spectrum at 6.65→6.74Å. Main line features are labelled according to Gabriel. The measured spectral resolution  $\delta\lambda/\lambda$  is 1:540.

(b) shows the same wavelength region recorded in a 20msec integration period 337msec into shot #34150 by the Johann spectrometer with a commercial TV format CCD chip. Spectral resolution on the resonance line w is a factor of three better. S/N ratio is lower than in (a) due to higher measured background noise on the detector.

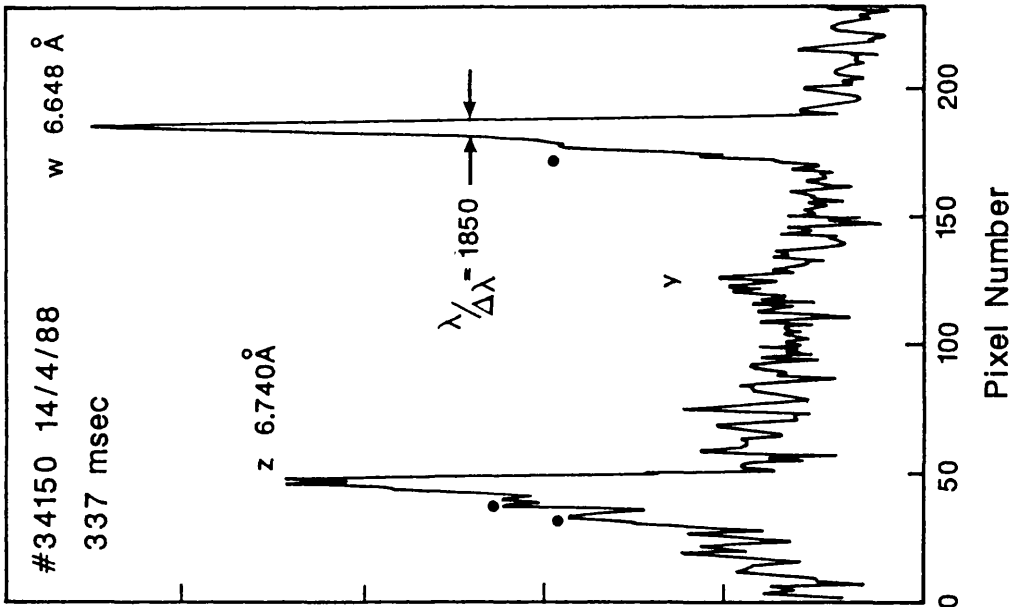
Features marked by • on the resonance line w and the forbidden line z indicate defocused fringing due to disturbed crystal during spectrometer installation.

(c) shows the optical focus quality of the crystal curvature recorded in visible light on the CCD detector. This image was recorded after the x-ray spectrum in (b). Defocused fringing to the left hand side of the main image is due to disturbed micrometer setting during the spectrometer installation on DITE Tokamak. Defocused fringing is visible on the x-ray spectrum but to a diminished extent. Normal focus quality should be single line feature with FWHM less than 60µm.

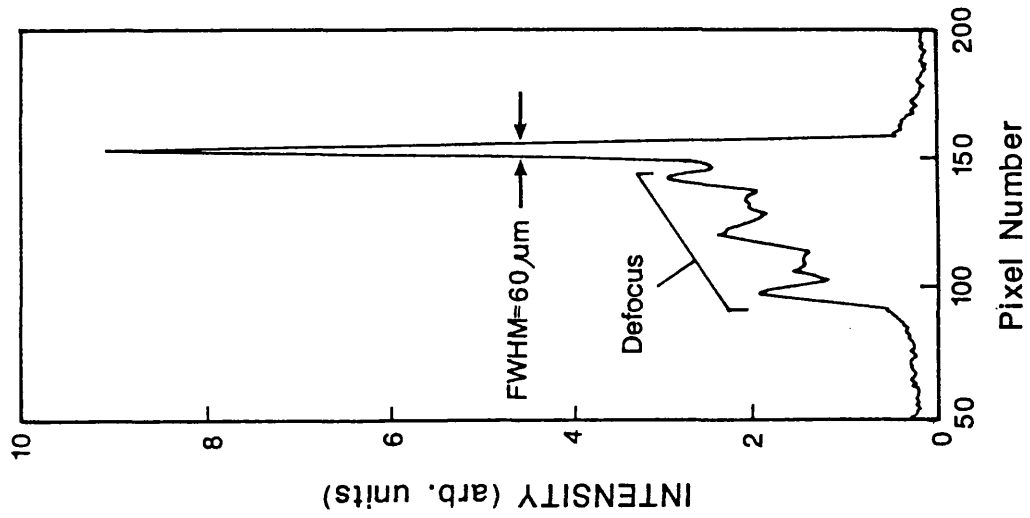
(a) Bragg Rotor, Si XIII Transitions



(b) Johann Instrument, 20 msec Integration of Si XIII



(c) Optical Focus Quality



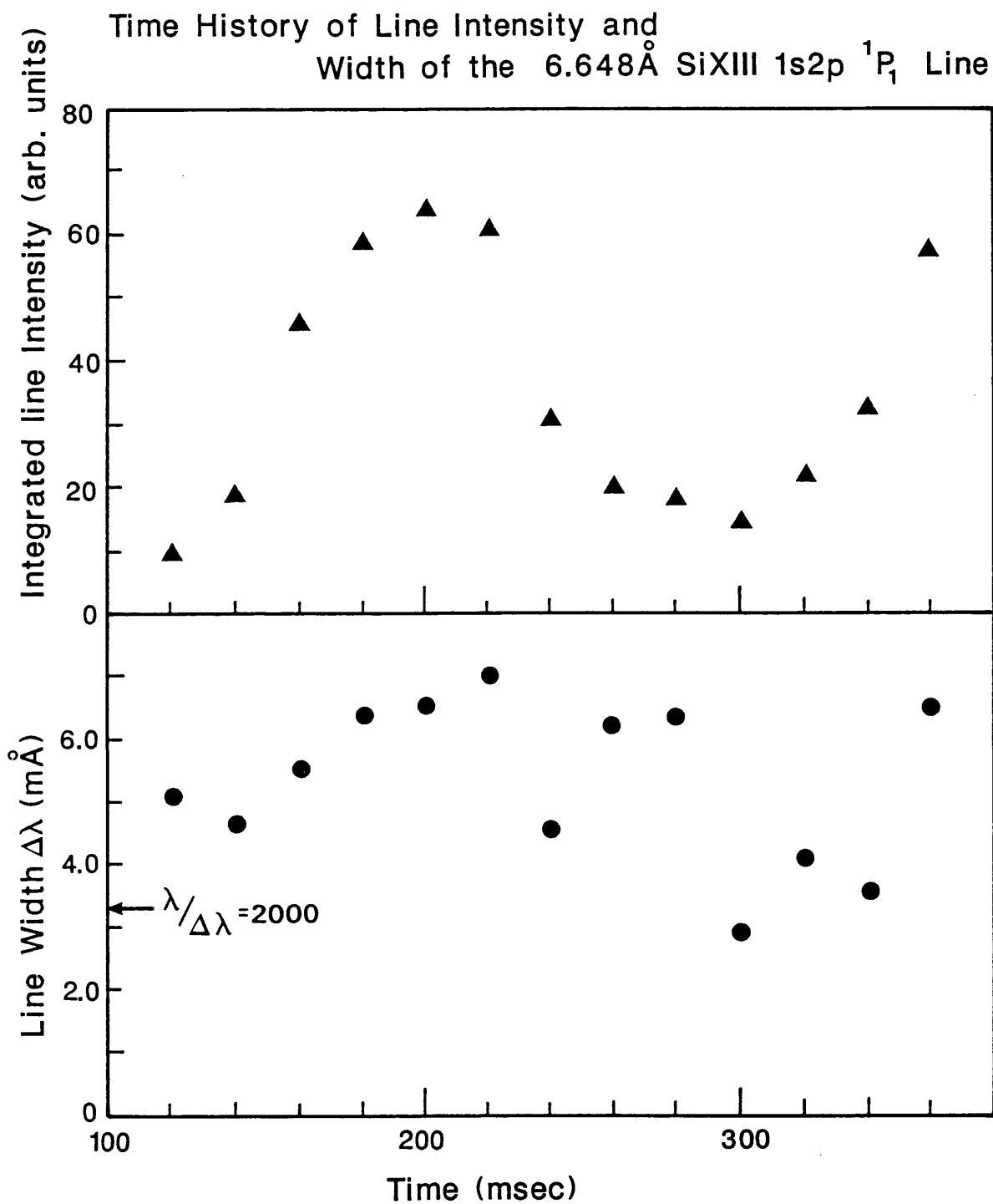


Figure 5.20 shows the time history of the 6.648Å Si XIII 1s2p <sup>1</sup>P<sub>1</sub> line for shot #34150 14/4/88 on DITE Tokamak. These results have been measured with the Johann CCD spectrometer at 20msec intervals. The top graph indicates the integrated line intensity. The bottom graph illustrates line width evolution.

The observed line width changes are very interesting and appear to correlate reasonably well with the line intensity. The best observed spectral resolution converges on the expected instrumental resolving power suggesting a minimum ion temperature of  $T_i=100\rightarrow 200\text{eV}$ . This is an acceptable result. However, the broader lines, corresponding to a peak ion temperature  $T_i\sim 4\text{keV}$ , are difficult to explain as genuine temperature results from only Ohmically heated plasmas. The gradual increase in the line width to the peak value at 220msec is consistent with the timescale for thermalisation amongst the ion species and follows a pattern observed on other Tokamaks ( see for example the review by Bartiromo<sup>101</sup>).

The low spectrometer resolving power and the fact that the crystal is not properly focused make this difficult to interpret. It is possible that the defocused crystal when combined with emission from a large spatial region of the plasma causes increased line broadening.

### **Background Noise.**

The cause of the high background noise on the CCD spectrum Figure 5.19(b) is not exactly clear but there are several areas that could be studied:

- Electrical noise from the high level of electro-magnetic activity in the Tokamak area is possible and would need investigation.
- Inherent detector electronic noise in the form of a dark current appears unlikely since the same CCD chip has been used subsequently as an x-ray pinhole camera in recent laser plasma experiments<sup>102</sup>. Extremely low background levels were recorded on later occasions. It can be noted that the dark current is halved with every 9°C of cooling<sup>81</sup>.
- Visible light from the Tokamak was filtered in the usual way. However, the increased sensitivity of the CCD to visible light and its closer position to the crystal chamber would increase the flux on the detector surface.

## **5.8 Conclusions.**

The following conclusions can be made from the Johann spectrometer for time-integrated operation on DITE Tokamak.

- Ion temperatures of  $T_i=750\rightarrow 1000\text{eV}$  have been observed for the central plasma chord during ohmic heating. This has been confirmed by the 2-crystal spectrometer for a 100msec time-resolved measurement during the middle of the plasma shot. Higher ion temperatures have been noted  $T_i=1165\text{eV}$  in conditions of high impurity concentration. Accuracy of 5→10% can be attained.
- A spatial scan reveals a 30% drop in the ion temperature ( $T_i=960\rightarrow 690\text{eV}$ ) for x-ray emission at 10cm from the plasma centre. This is in good agreement for spatial profiles of electron temperature  $T_e$  from other diagnostics.

- The use of H<sup>0</sup> beam injection (~1MW) at  $n_e=5 \times 10^{13} \text{ cm}^{-3}$  heats the observed impurity ions to an estimated  $T_i=1300 \rightarrow 1400 \text{ eV}$  for a central chord measurement. These values are repeatable and accurate for normal operation of the bundle divertor.
- NBI without the bundle divertor working, gives broadened non-Gaussian x-ray line profiles with apparent ion temperatures reaching  $T_i=1.6 \rightarrow 2.5 \text{ keV}$ . These high values are attributed to differential toroidal rotation across the plasma radial profile. The magnitude of the effect on time-integrated exposures is dependent on beam power and percentage operation of BDII. An increase in the ion temperature of 30% was observed with BDII switched off for 20% of DITE shots in exposure #20. Time-integrated ion temperature measurements are not as accurate under these conditions.

The measurements presented here are an average ion temperature for numerous shots. They do not, however, reflect the range of values within a DITE shot or from one shot to another. The operation of the CCD detector gave an insight to the time variation of the plasma emission for several strong spectral lines. Although not optimised for high resolution, sufficient sensitivity was achieved to read out the signal at 20msec intervals. Further improvement would be possible with an optimised CCD detector system as outlined in the previous chapter, giving highly resolved spectra with possibly 1msec time resolution.

#### **Choice of Impurity.**

It is evident from the results for Tokamak plasmas that dielectronic satellite lines are a low intensity feature of the spectral emission from medium Z ions. Satellite lines to the Si XIV Lyman- $\alpha$  were only a few percent of the parent line intensity at  $T_e \sim 1 \text{ keV}$ , barely observed above the background noise. Similarly, Li-like Si XII and Al XI satellites to the corresponding He-like ion  $n=2$  line, although stronger than the He-like satellites to the Lyman- $\alpha$ , were always interspersed with low level Iron L-shell lines. The factor of unresolved satellites affecting the measured line width of the resonance line, and therefore  $T_i$  measurements, was very low.

This advantage, however, was counter balanced by the inability to use the diagnostic potential of the dielectronic satellites for measuring the electron temperature and the ionization conditions. A higher Z impurity like Argon, Calcium or Titanium ( $Z=18 \rightarrow 22$ ) could still be observed in the He-like charge state for the central core temperatures of a small Tokamak like DITE or COMPASS. Sufficient theoretical data is available from Tokamak and solar corona plasmas to interpret the satellite line emission of these ions.

The study of this higher Z ion emission below  $4 \text{ \AA}$  conveniently allows the use of crystals with very high resolving power. A compact ( $R=1500 \rightarrow 2000 \text{ mm}$ ) spatially scanning Johann instrument covering the  $n=2$  resonance spectrum would produce very interesting plasma information.

# Chapter 6 Laser Produced Plasmas.

	Introduction.	157
6.1	Introduction to Laser Produced Plasmas.	157
	6.1.1 High Power Lasers: Brief History to the Present day.	157
	6.1.2 Plasma Production.	158
	6.1.3 X-Ray Emission and Comparison with Other Sources.	160
	6.1.4 Applications of Laser Plasmas.	160
6.2	Line Broadening Mechanisms.	161
6.3	Experimental Section.	163
	6.3.1 High Power Lasers at the Central Laser Facility.	163
	6.3.2 Description of Instrumentation.	163
	6.3.3 Optimisation of the Johann Spectrometer.	164
	6.3.4 Suprathermal Electron Transport Experiment.	166
6.4	Experimental Results from the Johann Spectrometer.	167
	6.4.1 He-like Aluminium Ion $1s^2$ - $1s2p$ Spectrum and Satellites.	167
	6.4.2 H-like Aluminium Ion $1s$ - $2p$ Spectrum and Satellites.	182
6.5	Opacity Calculations.	182
	6.5.1 Escape Factor Model.	183
	6.5.2 He-like Aluminium $1s^2$ - $1s2p$ Resonance Line.	184
	6.5.3 H-like Aluminium Lyman- $\alpha$ Resonance Line.	186
	6.5.4 He-like Dielectronic Satellite Lines.	192
6.6	Electron Density Measurements.	193
	6.6.1 H-like and He-like $n=2$ Resonance Lines.	193
	6.6.2 Density Sensitive Dielectronic Satellite Lines.	194
6.7	Discussion and Conclusions.	200
	6.7.1 Comparison of Density Measurements.	200
	6.7.2 Observed Anomalous Spectral Features.	201
	6.7.3 Instrumentation and Future Experiments.	204

## **Introduction.**

The following topics are discussed in this chapter:

- The production, applications and x-ray emission of laser produced plasmas.
- Additional line broadening mechanisms appropriate to high density plasmas.
- The optimisation of the Johann instrument to the laser plasma and description of the "Suprathermal Electron Transport" experiment.
- Experimental results of the He-like Al  $1s^2-1s2p$  and the H-like Al  $1s-2p$  spectra and associated satellite lines.
- An escape factor opacity model for estimation of the optical depth of resonance and satellite lines.
- Electron density measurements from the observed spectra.
- Conclusions about the interpretation of the spectra and improvements for future experiments.

The author has included significant reference material in this chapter since there is much information available on high density laser plasmas. De Michelis and Mattioli<sup>2,3</sup> are an excellent general starting point; more recent reviews in the "Laser Plasma Interactions series", St. Andrews University Summer Schools<sup>103</sup> cover trends in theory and experiment. Finally the "Annual Reports to the Laser Faculty Committee"<sup>104</sup> document the diverse, high power laser experiments performed at the Central Laser Facility, Rutherford Appleton Laboratory.

## **6.1 Introduction to Laser Produced Plasmas.**

### **6.1.1 High Power Lasers: Brief History to the Present Day.**

The laser was invented in 1958 by Schawlow and Townes<sup>105</sup>, and laser action was first demonstrated by Maiman<sup>106</sup>, two years later with a Ruby laser. The Neodymium:glass laser, still the main high power laser in use today, was first operated in 1961 by Snitzer<sup>107</sup>. It became clear almost immediately<sup>108</sup> that this device could heat small volumes of matter to high temperatures capable of initiating the nuclear fusion reaction. Other applications of the laser were realised where matter could be studied under the simultaneous conditions of high temperature, pressure and density in a laboratory environment. These could have been achieved previously only in chemical or nuclear explosions. The fusion application was to lead to the rapid development of high power pulsed glass lasers in the second half of the 1960's at many national laboratories, but principally at the Lawrence Livermore National Laboratory (LLNL), USA and at the Lebedev Institute in Moscow, USSR. This progression has continued with the establishment of high power laser laboratories in many other countries including Britain, Canada, France, Japan and Germany.

To date, the world's most powerful laser is Nova at LLNL which is capable of producing 20kJoules of  $0.35\mu\text{m}$  UV light. Energies greater than 50kJoules are likely in the next few

years<sup>109</sup>. For comparison, pulsed laser energies of 100kJoules are calculated to be needed to produce nuclear fusion by inertial confinement in spherical D-T microballoons.

### 6.1.2 Plasma Production.

Laser produced plasmas are generated when the focused beam of a high power laser interacts with the solid surface of the target and the energy deposited in that small volume exceeds the ionization threshold. This occurs typically when the laser irradiance or power density  $I$  of the focused beam is greater than  $10^{10}$ Watts/cm<sup>2</sup> in small  $\varnothing 10 \rightarrow 1000\mu\text{m}$  focal spots. (Much higher laser irradiances of up to  $10^{17}$ Watts/cm<sup>2</sup> are possible). Such high power laser pulses can only be achieved by short pulselengths of FWHM  $10^{-12} \rightarrow 10^{-9}$ secs, the plasma existing for approximately the same length of time after the laser has been switched off.

The time evolution of the laser produced plasma can be described as follows. Essentially, the electromagnetic field vector of the laser radiation, which can be as high as  $10^{12}$ Volts/m (Hughes<sup>110</sup>), interacts with the atoms on the target surface initially creating a cool dense plasma. This plasma absorbs further energy from the laser by the process of inverse bremsstrahlung where a laser photon is absorbed in the two-body interaction of a free electron with an ion. This absorbed energy increases the kinetic energy of the free electrons thus raising the electron temperature  $T_e$ . Further ionization is produced causing a rise in both the electron density and the rate of absorption.

This is an iterative process until  $n_e$  increases to the value of the critical density  $n_c$  at a surface in the plasma. At this density the electromagnetic wave propagation stops and the light is reflected. The plasma refractive index becomes zero because the resonant frequency of the plasma electrons in an oscillating electric field matches the laser frequency. The critical density  $n_c$  (cm<sup>-3</sup>) can be expressed in terms of the laser wavelength  $\lambda_1$  ( $\mu\text{m}$ ) by:

$$n_c = \frac{10^{21}}{\lambda_1^2} \quad (6.1)$$

Although the plasma is now opaque for densities greater than  $n_c$ , the heating and expansion of the plasma continue to the end of the laser pulse. Absorption of the laser energy no longer happens at the solid surface but is transferred to the layers immediately in front of the critical surface.

Figure 6.1 after Key<sup>111</sup> shows a schematic diagram of the spatial variation of the plasma density  $\rho$  and the electron temperature  $T_e$  after 100psecs when the plasma flow is in a steady state. It indicates the shock front travelling through the solid. Between the shock front and the thermal conduction front (at the initial solid surface) is a region of shock heated and compressed solid. As the ablation front is approached, the density remains approximately constant but is further heated by thermal conduction. There is a steady fall in the plasma density until the boundary of the critical surface is reached at density  $n_c$  at which the laser wave propagation stops.

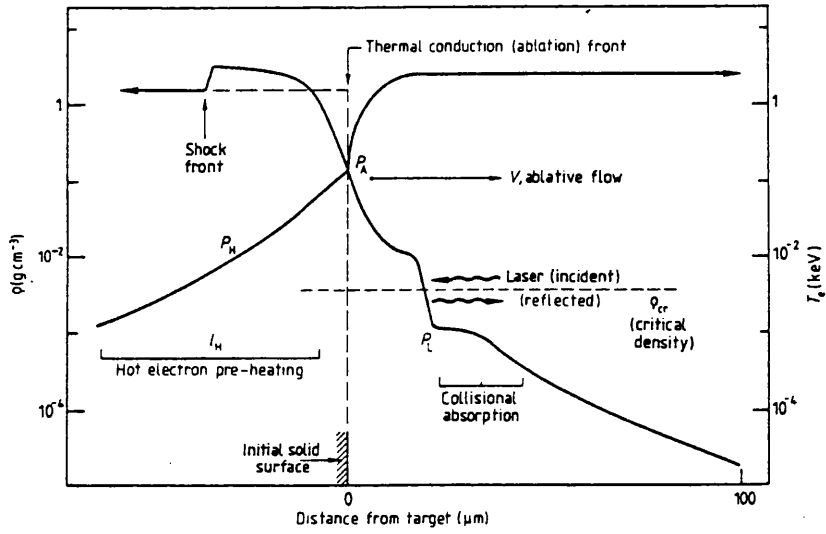


Figure 6.1 Schematic diagram after Key<sup>111</sup> showing spatial variation of the plasma for density and temperature parameters.

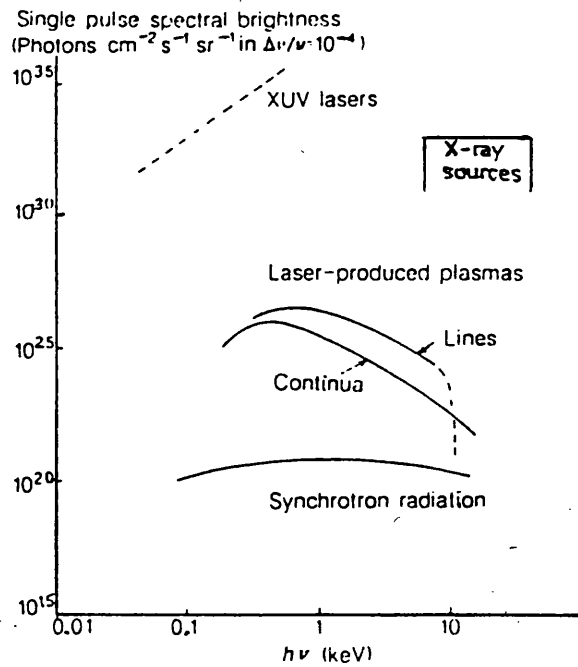


Figure 6.2 Comparison of absolute spectral brightness of a 1 Terawatt Nd:glass laser and synchrotron radiation source, after Key<sup>112</sup>.

Beyond this surface, is the laser light absorption zone and the electron density decreases as the plasma expands outwards into the vacuum.

The created plasma is dense,  $10^{19} < n_e < 10^{24} \text{ cm}^{-3}$ , many orders of magnitude greater than Tokamak densities (see Chapter 1, Figure 1.1). The fact that hot ( $T_e \sim 1 \text{ keV}$ ) matter can be observed at electron densities much greater than the critical density is discussed later in this chapter.

### **6.1.3 X-Ray Emission and Comparison with Other Sources.**

The rapid heating of matter near the surface of the target is sufficient to raise the electron temperature  $T_e$  locally to between 50eV and 5000eV. The resultant plasma consists of highly stripped H-like, He-like and Li-like ions of medium  $Z$  atomic number, typically less than  $Z=26$  (Iron). Targets with higher atomic numbers ( $Z < 40$ ) produce a dense Ne-like line spectrum for L-shell ionization while for  $Z > 40$  a quasi-continuous Ni-like spectrum is observed for M-shell ions. Intense line and continuum radiation are emitted in the XUV and x-ray energy band ( $0.1 < E < 10 \text{ KeV}$ ). (X-ray production occurs between the thermal conduction front and the critical density surface, see Figure 6.1).

Laser produced plasmas are the most intense pulsed laboratory sources of x-rays by several orders of magnitude. Figure 6.2 after Key<sup>12</sup>, compares the x-ray brightness of sources generated by synchrotron radiation and  $10^{12}$  Watt Neodymium:glass lasers. The extremely high brightness of XUV lasers is also illustrated.

Further evidence, of the x-ray brightness of laser plasma sources to Tokamaks and beam-foil interactions, is given when the integration time to achieve the same signal on the Johann spectrometer is considered. A single 20psec laser shot of 5J on an Aluminium ( $Z=13$ ) target generates H-like and He-like ion resonance lines of peak optical density  $D_{0,1} \geq 1$ . A minimum integration of 5secs, 10 shots of 500msec duration (see Chapter 5) would be needed to observe the same signal intensity for the ion impurity in a Tokamak plasma. Finally, an integration time of  $5 \times 10^4$  secs would be typical for a beam-foil source (see Chapter 7). The intense x-ray emission from laser produced plasmas is evident, although only a rough approximation has been made without provision for the different spectrometer optimisations for each source.

### **6.1.4 Applications of Laser Plasmas.**

There are four distinct areas for spectroscopic study of laser produced plasmas:

- (1) Hot, dense plasmas for nuclear fusion research.
  - (2) X-ray laser research.
  - (3) X-ray light source.
  - (4) Studies of atomic spectroscopy.
- (1) Inertial confinement fusion (ICF) research is another route to nuclear fusion (see Chapter 5.4). The action of multiple laser beams on spherical targets filled with

thermonuclear gas mixtures generates compressed, high temperature cores.

Spectroscopic investigation of these plasmas can measure temperature, density,  $\langle \rho R \rangle$  products, ablation pressures and other parameters necessary to characterise the imploded core. Research on energy transport from simpler planar target geometries is useful in this context.

The physics of hot dense matter can be studied as a topic in its own right. These conditions exist in astrophysics, for example in stellar interiors, neutron star atmospheres and in the vicinity of black holes.

- (2) X-ray laser research has developed extremely rapidly in the last ten years mainly with the advent of the multiterawatt laser system. Experiments use multiple high power lasers focused in a line to create a long (cm) cylindrical plasma of small diameter where amplification of spontaneous emission occurs in a single pass along the column. The spectral line intensity is observed to increase exponentially with length. Gain  $\times$  length products approaching  $g l \sim 14$  have been observed giving an amplification of  $10^6$  in a single pass for a collisionally excited Ne-like Se scheme at 207Å. (Laser action for Ni-like Eu has also been demonstrated at 71Å using a similar scheme).

Recombination schemes have also been shown to produce laser action for F IX at 81Å. The experiments discussed here and x-ray laser research in general are reviewed by Key<sup>113</sup>.

- (3) Laser plasmas have applications as a short wavelength light source, producing intense resonance line and continuum radiation, to absorption spectroscopy, time-dependent EXAFS studies and x-ray microscopy. They are used extensively in x-ray laser research. They are considerably cheaper than synchrotron sources and offer an alternative exposure programme for x-ray microscopy of biological samples.
- (4) Laser produced plasmas can be a source of very pure spectra from highly ionised elements. Line identification and intensity factors can be studied easily for a range of ionization stages. This is relevant to atomic physics and to high Z impurity identification in other sources, eg Tokamak plasmas where power loss through impurity ion radiation is significant. The laser plasma parameters are generally not important here, but may be tuned for conditions producing a particular ionization stage.

## 6.2 Line Broadening Mechanisms.

Additional line broadening mechanisms to those discussed in Chapter 4, occur in laser plasmas. The effect of the source function on instrumental line broadening may have to be considered for flat crystal spectrometers.

### Stark Broadening.

Stark broadening has been extensively studied as a density diagnostic for different plasma

sources. In laser plasmas the main interest has been in x-ray spectral lines of medium to high Z H-like and He-like ions. Hydrogenic line profiles have been studied theoretically by, amongst others, Griem<sup>114</sup>, Griem et al<sup>115</sup>, Lee<sup>116</sup> and Tighe and Hooper<sup>117</sup>; comparisons have been made with experiments (see Yaakobi et al<sup>118</sup>, Kilkenny et al<sup>117</sup>) for more than ten years. The theory is well understood and is the most reliable method for measuring high plasma densities.

The broadening process results from two processes:

- (a) Quasi-static Stark broadening due to interaction with the surrounding ion microfields.
- (b) Impact broadening due to the free electron gas.

For  $n_e$  greater than  $10^{21} \text{cm}^{-3}$ , Stark broadening usually exceeds Doppler broadening for higher series members of the Hydrogenic ion. The FWHM of spectral lines can be written as:

$$\Delta\lambda \approx C \lambda^2 (n_j^2 - n_i^2) n_e^\alpha Z^{-2/3} \quad (6.2)$$

where C is a constant, Z is the charge of the emitter,  $n_j$ ,  $n_i$  are the principal quantum numbers of the transition and  $2/3 < \alpha < 1$  represents the index of the electron density for a single species plasma. It can be seen that  $\Delta\lambda$  increases with density and the principal quantum number. Thus, the increased Stark broadening for high  $n_j$  is a more sensitive electron density diagnostic; also only one or two high  $n_j$  values may be intense enough and optically thin to be of use. Gases like Neon and Argon are often added in small traces to spherical target gas mixtures in order to measure the peak electron density of the compression core. He-like ion profiles, although requiring a more complicated theoretical treatment, can also be used (see Lee<sup>119</sup>).

### Doppler broadening

Doppler broadening can occur due to bulk motion in the ablation plasma. Where the viewing geometry is perpendicular to the plasma expansion, uniform Gaussian profiles can be observed. Ion streaming velocities  $v_s$  can often be several times greater than the thermal ion velocity  $v_i$ . The combination of Stark broadening and bulk plasma motion makes profile study less useful for ion temperature measurements. If the observed line widths are fairly constant along the series of a Hydrogenic ion then Doppler broadening is probably the dominant line broadening mechanism.

### Opacity Broadening

The effects of opacity are discussed later in this chapter. It may be noted that the preferential self-absorption of the line centre and smearing due to time-integration can increase the profile width, known as "opacity broadening". Thus, optically thick Stark broadened lines may give an overestimate of the plasma density. Peacock<sup>120</sup> reports the line wings are likely to remain optically thin and can still be fitted to measure density. The

effect of opacity on line profiles is treated by Irons<sup>121</sup>. McWhirter<sup>87</sup> has shown that the profile shape (for a Gaussian) can be written as:

$$I = S(1 - e^{-\tau_\lambda}) \quad (6.3)$$

$$\tau_\lambda = \tau_0 \exp \left[ - \left\{ \frac{\Delta\lambda}{\Delta\lambda_D} \right\}^2 \right] \quad (6.4)$$

where S is the source function assumed to be constant over the line profile,  $\Delta\lambda_D$  is the Doppler width,  $\tau_0$  and  $\tau_\lambda$  are the optical depths at line centre and  $\Delta\lambda$  from line centre, respectively.

## 6.3 Experimental Section.

### 6.3.1 High Power Lasers at the Central Laser Facility.

A short description is given of the high power lasers available at the CLF (Central Laser Facility), Rutherford Appleton Laboratory. More detailed information is available in recent RAL Annual Reports and references therein, see for example<sup>104</sup>. A review of the physics of high power lasers is presented by Holtzrichter<sup>122</sup>.

There are two high power laser systems at the CLF, each of which has its own target area(s) for a range of plasma studies. Most experiments are performed on the VULCAN laser, a Nd:glass design, which is capable of irradiating  $\varnothing 10 \rightarrow 1000\mu\text{m}$  targets with power densities of  $10^{16}\text{Watts/cm}^2$  with up to 12 beams. The output for this system is 2kJoules of  $1.06\mu\text{m}$  light in nsec pulses and 5TeraWatts ( $5 \times 10^{12}\text{Watts}$ ) in 20psec pulses. The laser light can be frequency converted to  $0.53\mu\text{m}$  green ( $2\omega$ ) light or  $0.35\mu\text{m}$  ( $3\omega$ ) blue light using KDP crystals. The conversion efficiency from the fundamental frequency is typically  $30 \rightarrow 50\%$ . The other high power laser is SPRITE, a Krypton Fluoride (KrF) gas excimer laser, which emits at  $0.248\mu\text{m}$  in the UV region. It is mainly a development facility for testing technology for the next generation multi-kJoule "SUPER-SPRITE" laser, destined to replace the Nd:glass as the main high power laser. It has a different output specification, ranging from two beams of 40Joules of UV light in 20nsecs to a single beam of 2.5Joules in 3.5psecs. The latter output when combined with small  $\varnothing 10\mu\text{m}$  focal spot diameters, gives the possibility of illuminating targets with a very high irradiance of  $10^{17}\text{Watts/cm}^2$ , short wavelength beam. A few experiments make use of the presently unique features of SPRITE. Most of the spectra presented in this chapter were recorded from targets irradiated with a single 20psec, 10Joule  $2\omega$  beam of the VULCAN laser.

### 6.3.2 Description of Instrumentation.

Two crystal spectrometers, a filtered pinhole camera and an x-ray diode array were used to monitor the x-ray emission from the plasma. A Johann type Pentaerythritol PET (002)

( $2d=8.74\text{\AA}$ ) crystal spectrometer<sup>123</sup> with high resolving power ( $\lambda/\Delta\lambda\sim 7000$ ) viewed the plasma at  $70^\circ$  from the laser beam axis and observed the  $n=2$  transitions of the He-like and H-like Al ion in the waveband  $7.0\rightarrow 7.9\text{\AA}$ . A  $2\mu\text{m}$  Mylar window coated with  $85\text{\AA}$  of Al was placed in front of the crystal to protect it from reflected laser light and target debris. A time integrated spectrum was recorded in a single laser shot on Kodak DEF 392 x-ray film, which was protected from scattered visible and UV light by a  $2\mu\text{m}$  Mylar filter coated with  $1000\text{\AA}$  of Al. The spectra of these resonance lines with satellite structure are presented below.

A miniature flat PET (002) crystal spectrometer<sup>17</sup> with moderate resolving power ( $\lambda/\Delta\lambda\sim 500$ ), was placed in front of the target angled at  $30^\circ$  from the laser beam axis. It recorded (on Kodak DEF film) the He-like and H-like resonance lines of Aluminium as well as the  $K\alpha$ -emission from the deeper Cl, K and Ca layers. This spectrometer provided electron density  $n_e$  information from the Stark width of the Al XII  $1s^2\ ^1S_0-1s3p\ ^1P_1$  line, monitored the  $K\alpha$ -emission and the electron temperature  $T_e$  (from the slope of the Al XIII recombination continuum).

### 6.3.3 Optimisation of the Johann Spectrometer.

The initial optimisation of the Johann spectrometer to miniature x-ray sources was to achieve the following goals simultaneously:

- To maximise instrumental resolving power in the selected waveband.
- To maintain high signal throughput.
- To study the most intense lines of the Al spectrum; the  $n=2$  transitions of the H-like and He-like ions at  $7.1\rightarrow 7.9\text{\AA}$ .

The following instrumental parameters were chosen accordingly.

#### Crystal Radius.

The crystal curvature could be set to any radius between  $R=150\rightarrow 5000\text{mm}$ . The following constraints had to be considered:

- (1) The minimum source/crystal separation without obstructing the view of the plasma of other diagnostics was  $\sim 90\text{mm}$ .
- (2) The instrument could be mounted within the laser target vacuum chamber if a crystal radius  $R \leq 500\text{mm}$  was chosen.
- (3) The DITE vacuum version could be bolted externally to the target chamber, but the crystal curvature would then be limited to  $R \geq 1000\text{mm}$ .

A  $500\text{mm}$  radius ADP (101) instrument was tried first and achieved an adequate x-ray line intensity for a long laser pulse length. However, the energy, and x-ray emission, dropped when the pulse length was reduced to  $20\text{psec}$ . The signal throughput was then increased by replacing the ADP (101) crystal with a smaller radius  $R=300\text{mm}$  PET (002) crystal. The smaller radius was preferred in order to keep the x-ray photon density high at the film plane. The observed spectral resolution was unaffected by the reduced crystal radius.

# Experimental Arrangement

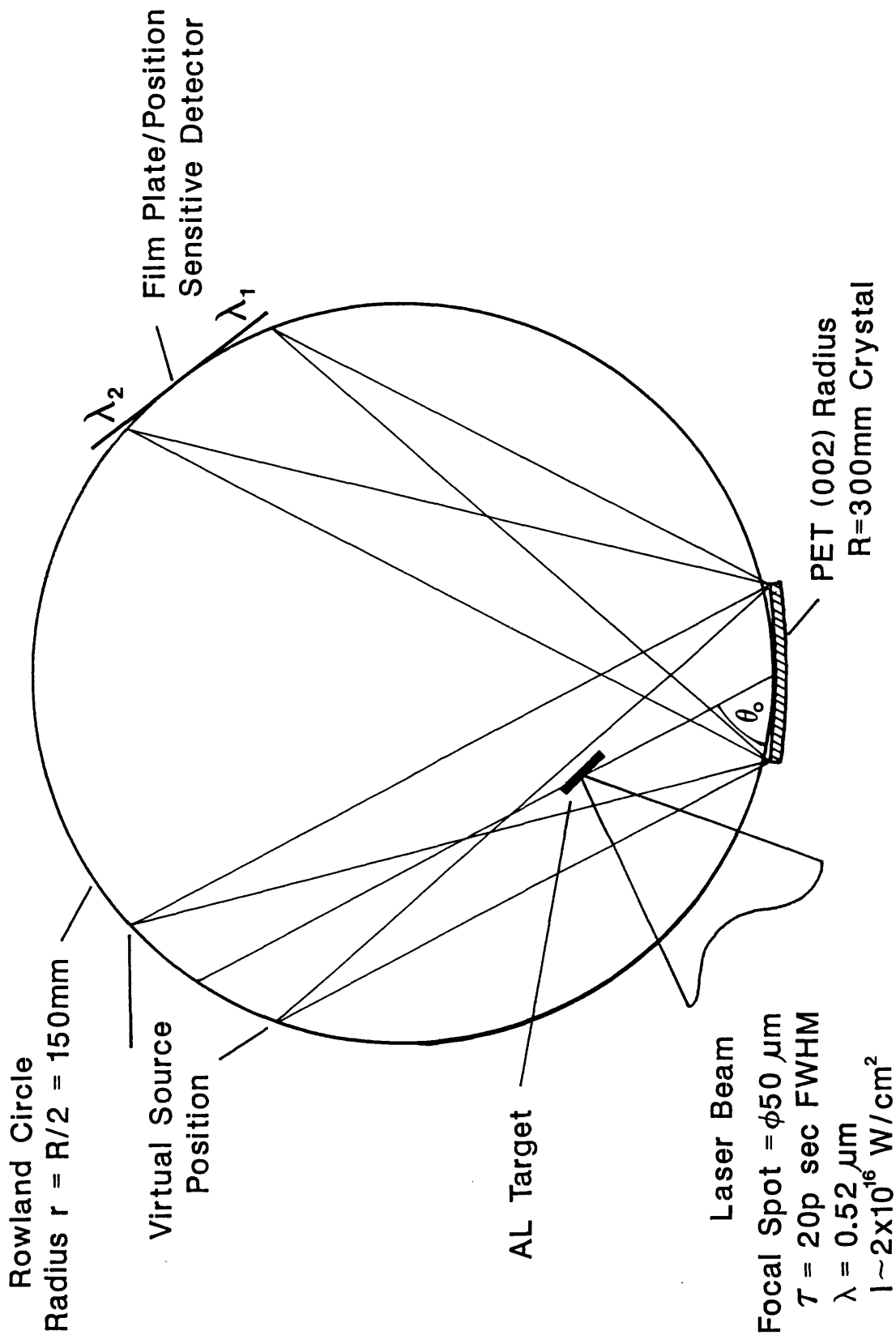


Figure 6.3 Schematic of Johann Geometry Relative to the Plasma Source.

**Waveband.**

To achieve a bandpass of  $\lambda/\Delta\lambda = 0.1$ , with an x-ray source of small ( $x < 100\mu\text{m}$ ) spatial dimensions, the Johann spectrometer was used in "defocused" mode. This required placing the target, about 90mm from the crystal (see Figure 6.3), inside the Rowland Circle as discussed in Chapter 2.3. The crystal area available for x-ray diffraction was  $20 \times 17\text{mm}^2$  (W x H); a larger crystal width or radius could have been chosen if the minimum crystal/source separation had been impractical.

**Sensitivity.**

When using the spectrometer in "defocused" mode, there is a compromise between the monochromatic sensitivity and the defined bandpass which is independent of the crystal radius. A laser target placed on the Rowland circle would allow a single spectral line (or part of a line) to be reflected from the full crystal width dimension. It may be noted that the conditions for Bragg reflection with the Johann geometry must be satisfied. By placing the source inside the Rowland circle to increase the bandpass, the monochromatic sensitivity is reduced and a spectral line is reflected from a fraction of the original crystal width. Thus, the monochromatic sensitivity falls off faster than the expected ratio of source/crystal separation to Rowland chord dimension. This sensitivity loss may be compensated by reducing the crystal radius. A positive consequence of this effect is the reduced Johann aberrations which allow high resolving power to be maintained with smaller crystal radii.

**Resolving Power.**

The instrumental resolving power, independent of the source dimensions, was determined by a number of factors; the convolution of the crystal line focus measured optically during the focusing procedure, the crystal diffraction width measured on the Leicester 2-crystal Spectrometer by Hall<sup>11</sup>, the Johann aberrations, see Chapter 2.3 for discussion, and the line defocus due to the spectral images being recorded on a flat film plate tangential to the Rowland circle. Due to the small spatial extent of the plasma and reduced monochromatic sensitivity, the Johann aberrations were negligible,  $\lambda/\Delta\lambda > 50000$ . The focus quality gave a broadening of  $\lambda/\Delta\lambda = 34000$  and the contribution from the line defocus was typically better than  $\lambda/\Delta\lambda = 23000$ . Therefore, the instrumental resolving power was mainly determined by the crystal diffraction width of 45 seconds of arc, corresponding to  $\lambda/\Delta\lambda = 7000$ .

**6.3.4 Suprathermal Electron Transport Experiment.**

The spectra were emitted from laser-irradiated solid  $\text{Ø}250 \rightarrow 1000\mu\text{m}$  Al wire and layered planar targets. The latter were  $\text{Ø}300\mu\text{m}$  discs with a thin Aluminium lamina of  $0.2\mu\text{m}$  buried under a plastic ablator top coat of variable  $0.1 \rightarrow 1.0\mu\text{m}$  thickness. A thin Aluminium layer was chosen to create a well ionized diagnostic plasma of small spatial extent and to minimise opacity effects on the higher series Lyman and Helium-like resonance lines. The plasma parameters, the electron density in particular, could be studied as a function of the depth of the buried layer.  $K\alpha$  fluorescence from the deeper layers of Cl, K and Ca buried in the planar targets were also used to indicate suprathermal electron production. A single

beam of 20psec FWHM pulselength from the VULCAN Nd:glass laser, frequency doubled to  $0.52\mu\text{m}$  and focused to a  $\varnothing 50\mu\text{m}$  spot size, illuminated the targets with a peak irradiance of  $2 \times 10^{16} \text{Watts/cm}^2$ . A typical shot had 7Joules of energy on target.

This was part of an energy transport study to show that in addition to thermal electron conduction heating matter at close to solid densities, there was increased suprathermal electron pre-heating due to the nature of the very short pulselength of short wavelength light at high intensity. Initial results from Brown et al<sup>124</sup> indicated that high temperature  $T_e \sim 500\text{eV}$  plasmas at  $n_e$  approaching  $10^{23}/\text{cm}^3$  were being generated in the buried layer targets. Detailed analysis of the data, Tallents et al<sup>125</sup> showed that the density range was  $n_e \sim 6 \rightarrow 8 \times 10^{22} \text{cm}^{-3}$  at temperatures of typically 1keV. In addition, it was shown that only 5% of the incident laser energy was converted into suprathermal electrons, having a temperature  $T_H$  less than 10keV. This suggested that the buried layer plasma was principally heated by thermal conduction.

## 6.4 Experimental Results from Johann Spectrometer.

### 6.4.1 He-like Aluminium $1s^2$ - $1s2p$ Spectrum and Satellites.

The  $n=2$  He-like Al ion spectrum is shown in Figure 6.4 for a  $0.2\mu\text{m}$  Al buried layer under  $0.5\mu\text{m}$  plastic overcoat. The spectral lines are labelled after Gabriel<sup>85</sup> and the transitions shown in Table 6.1. The strong He-like resonance line  $1s^2 \ ^1S_0 - 1s2p \ ^1P_1$  (w) and intercombination lines  $1s^2 \ ^1S_0 - 1s2p \ ^3P_{1,2}$  (x,y) are indicated at  $7.757\text{\AA}$  and  $7.807\text{\AA}$ , respectively. The metastable forbidden line  $1s^2 \ ^1S_0 - 1s2s \ ^3S_1$  (z) at  $7.87\text{\AA}$  normally seen in Tokamak spectra (Chapter 5, Figure 5.8), which coincides with the Li-like Al ion j,k,l dielectronic satellites, is not observed in laser plasmas due to collisional de-excitation (Peacock<sup>120</sup>).

The other lines are the Li-like dielectronic satellites of the type  $1s^2nl$ - $1s2pnl$  and  $1s^2nl$ - $1s2snl$ . The  $n \geq 3$  satellites appear as a continuous blend to the long wavelength side of the w line. (Since the flat crystal spectrometer did not observe resonance radiation beyond  $n=6$  for the H- and He-like ions, a similar cut-off should be expected with the merging of the higher order satellites with the resonance line). The  $n=2$  satellites fall into two groups; the weak  $n=2$  satellites are on either wing of the intercombination line while the strong  $n=2$  satellites fall into three resolved groups (q,r), (a-d) and (j,k,l) with increasing wavelengths. This spectrum should also be compared with the Si XIII spectrum of Chapter 7, Figure 7.5.

The upper level of the satellite lines can be populated either by dielectronic recombination through electron capture by the He-like ion or through direct inner-shell excitation of the Li-like ion. The relative intensities of these lines depend on the degree of ionization of the plasma and therefore the electron temperature  $T_e$ . For a recombining plasma, dielectronic recombination is usually the main excitation process though in conditions of rapid ionization where  $T_e < T_c$ , inner-shell excitation may be strong. Autoionization, where the uppermost excited electron is ejected from the ion leaving it in an unexcited state, is the

Al XII  $1s^2\ ^1S_0 - 1s2p\ ^1P_1$  Resonance Line and Satellite Structure

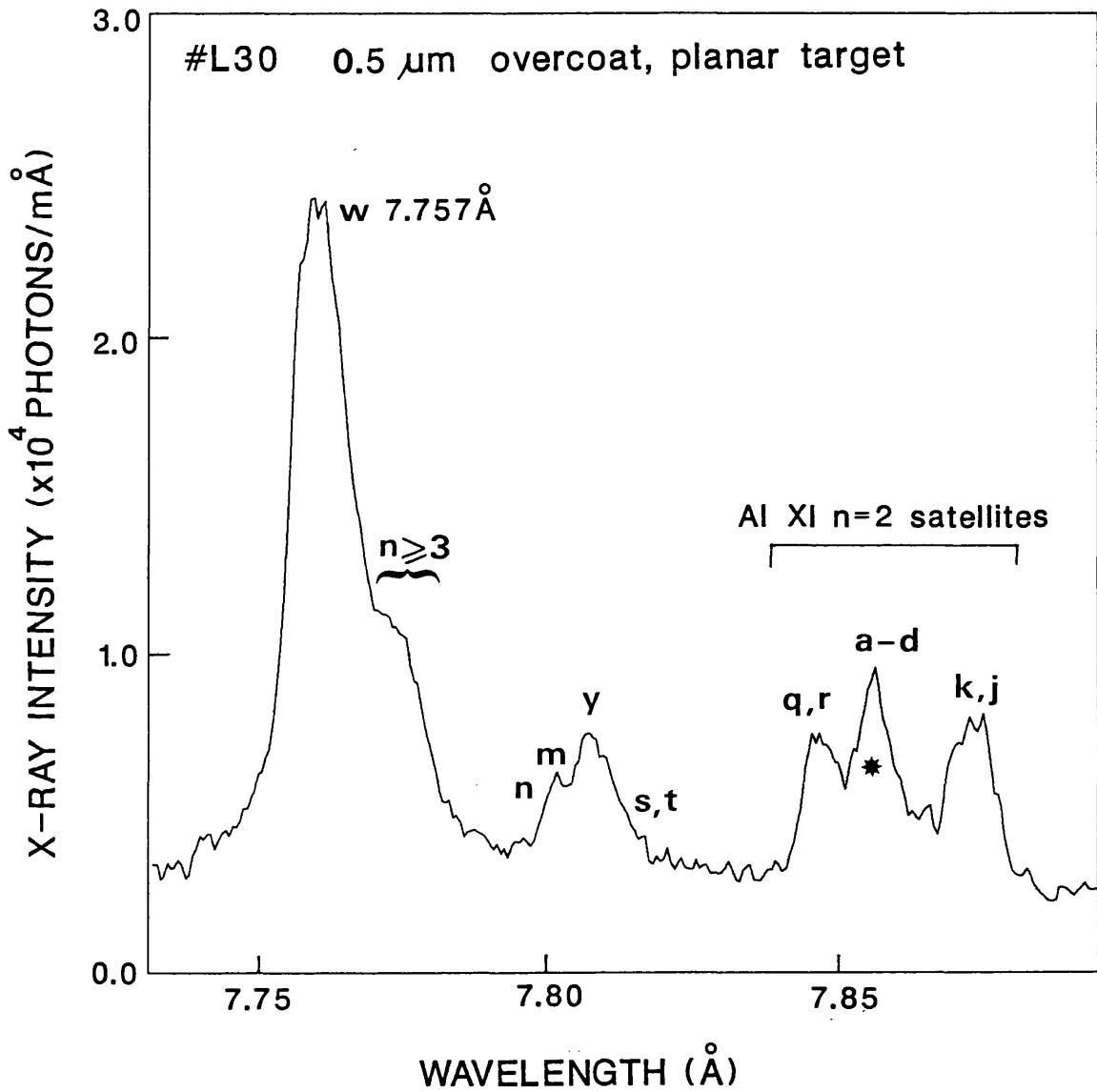


Figure 6.4 He-like Al  $n=2$  spectrum and satellites for 0.5  $\mu\text{m}$  plastic overcoated target.

Table 6.1 Theoretical and Experimental Wavelengths of Li-like Al XI Dielectronic Satellite Lines.

Key	Transition	$A_{ji}$ ( $s^{-1}$ )	$\Gamma_j$ ( $s^{-1}$ )	Satellite Wavelengths $\lambda(\text{\AA})$			This Expt
				Theory DRDB	Theory V+S (l)	Theory Gabriel	
n	$1s^2 2p \ 1P_{1/2} - 1s2p^2 \ 2S_{1/2}$	$3.47 \times 10^{12}$	$1.81 \times 10^{13}$	7.7987	7.7953	7.796	7.787
m	$1s^2 2p \ 2P_{3/2} - 1s2p^2 \ 2S_{1/2}$	$9.65 \times 10^{12}$	$1.81 \times 10^{13}$	7.8022	7.7989	7.799	-
s	$1s^2 2s \ 2S_{1/2} - 1s2s(\ ^3P)2p \ 2P_{3/2}$	$2.28 \times 10^{12}$	$7.64 \times 10^{13}$	7.8085	7.8081	7.7809	7.815
t	$1s^2 2s \ 2S_{1/2} - 1s2s(\ ^3P)2p \ 2P_{1/2}$	$3.68 \times 10^{12}$	$7.31 \times 10^{13}$	7.8097	7.8088	7.7810	-
q	$1s^2 2s \ 2S_{1/2} - 1s2s(\ ^1P)2p \ 2P_{3/2}$	$2.61 \times 10^{13}$	$4.37 \times 10^{12}$	7.8475	7.8460	7.846	7.848
r	$1s^2 2s \ 2S_{1/2} - 1s2s(\ ^1P)2p \ 2P_{1/2}$	$2.56 \times 10^{13}$	$7.72 \times 10^{12}$	7.8496	7.8479	7.848	7.850
b	$1s^2 2p \ 2P_{1/2} - 1s2s^2 \ 2P_{3/2}$	$4.61 \times 10^{13}$	$2.10 \times 10^{12}$	7.8538	7.8538	7.853	7.854
a	$1s^2 2p \ 2P_{3/2} - 1s2s^2 \ 2P_{3/2}$	$3.71 \times 10^{13}$	$2.10 \times 10^{12}$	7.8573	7.8574	7.856	7.859
d	$1s^2 2p \ 2P_{1/2} - 1s2p^2 \ 2P_{1/2}$	$2.90 \times 10^{13}$	$1.80 \times 10^{10}$	7.8574	7.8572	7.856	-
c	$1s^2 2p \ 2P_{3/2} - 1s2p^2 \ 2P_{1/2}$	$1.32 \times 10^{13}$	$1.80 \times 10^{10}$	7.8609	7.8606	7.860	7.863
k	$1s^2 2p \ 2P_{1/2} - 1s2p^2 \ 2D_{3/2}$	$1.37 \times 10^{13}$	$1.15 \times 10^{14}$	7.8683	7.8711	7.874	7.874
j	$1s^2 2p \ 2P_{3/2} - 1S2s^2 \ 2D_{5/2}$	$1.34 \times 10^{13}$	$1.17 \times 10^{14}$	7.8715	7.8754	7.877	7.878
l	$1s^2 2p \ 2P_{3/2} - 1s2p^2 \ 2D_{3/2}$	$3.96 \times 10^{11}$	$1.15 \times 10^{14}$	7.8719	7.8748	7.878	-

Lines labelled according to Gabriel<sup>185</sup>.

DRDB theoretical results from Duston et al<sup>126</sup>.

V+S (l) theoretical results for Al XI from Vainshtein and Safronova<sup>127</sup>.

PHG experimental results from Peacock et al<sup>128</sup>.

$A_{ji}$ ,  $\Gamma_j$  theoretical values for the radiative decay and autoionization probabilities.

N.B. All satellite lines in this work are measured relative to the He-like Al XII resonance line.

**Table 6.2 He-like Al XII Resonance Lines.**

Key	Transition	Theory Drake $\lambda$ (Å)	Theory V+S (II) $\lambda$ (Å)	Theory Gabriel $\lambda$ (Å)	Expt PHG $\lambda$ (Å)	This Expt $\lambda$ (Å)
w	$1s^2 \ ^1S_0 - 1s2p \ ^1P_1$	7.75730	7.75759	7.757	7.757	7.7573 calib.
x	$1s^2 \ ^1S_0 - 1s2p \ ^3P_2$	7.80388	7.80409	7.804	-	-
y	$1s^2 \ ^1S_0 - 1s2p \ ^3P_1$	7.80696	7.80719	7.807	7.806	7.807

Lines labelled according to Gabriel<sup>85</sup>.

Column 3 indicates theoretical calculations of Drake<sup>26</sup>.

Column 4. V+S (II), indicates theoretical calculations of Vainshtein and Safronova<sup>129</sup>.

Column 6, PHG, gives experimental results from Peacock et al<sup>128</sup>.

Column 7 gives experimental wavelengths for intercombination line y, assuming Drake's value for resonance line w. Agreement is within 0.001mÅ measurement error.

Al XI satellites in Table 6.1 measured relative to w.

Al XI Dielectronic Levels Showing Transitions

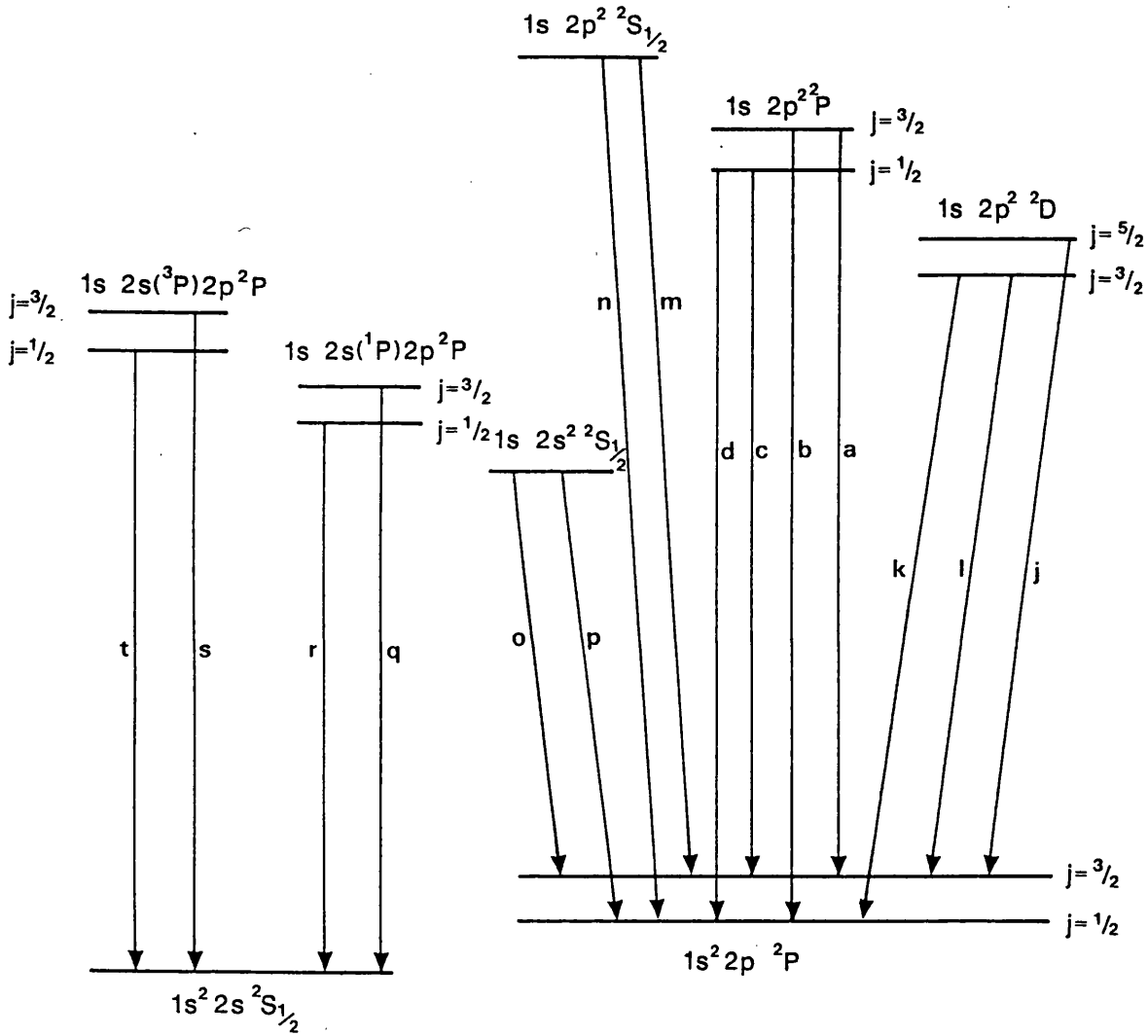


Figure 6.5 Energy level diagram for the Li-like Aluminium dielectronic satellites. Transitions are labelled according to Gabriel.

Al XII  $1s^2\ ^1S_0 - 1s2p\ ^1P_1$  Resonance Line and Satellite Structure

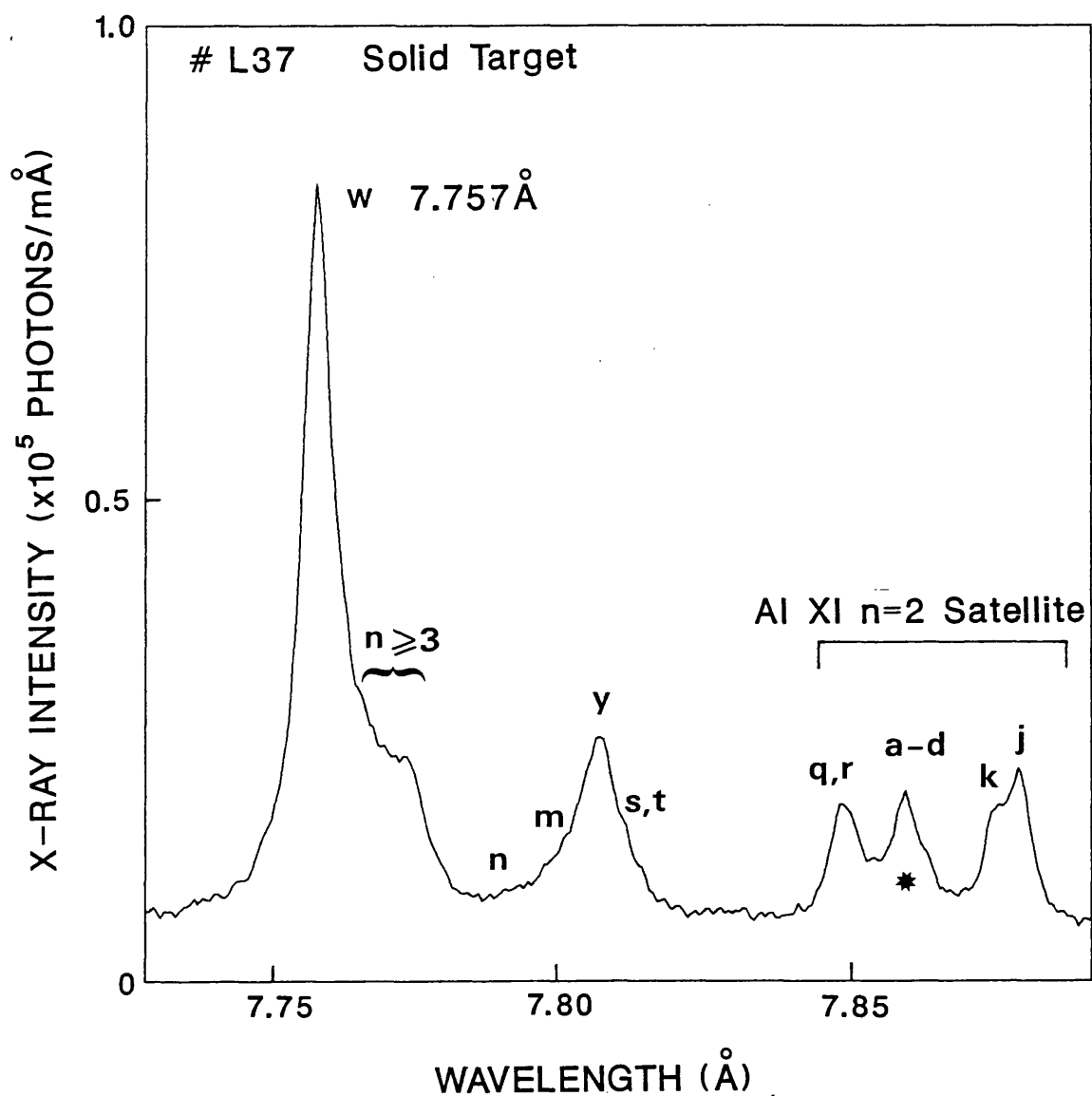
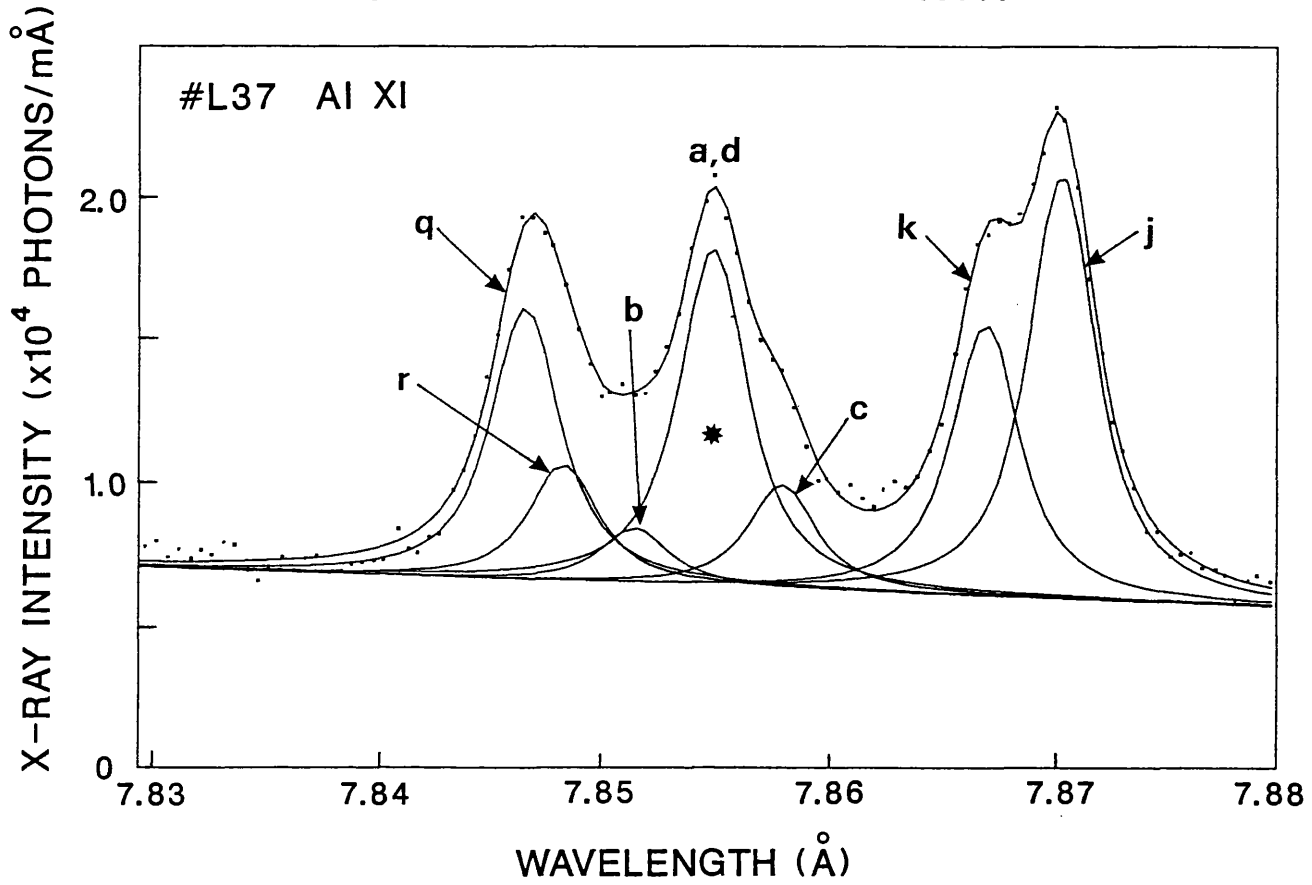


Figure 6.6 He-like Al n=2 spectrum and satellites for solid Ø1mm wire target.

Al XI n=2 Satellite Structure at 7.85→7.87Å



Residuals to Fit

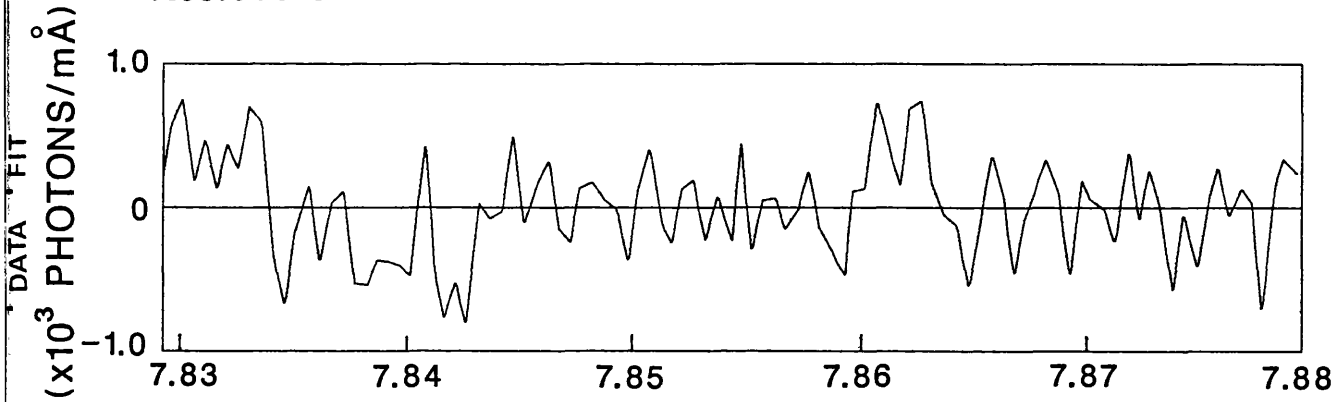


Figure 6.7 Profile fit to Li-like Aluminium dielectronic satellites 7.84→7.90Å of shot #L37.

inverse process to dielectronic capture and the competing process to radiative decay for stabilising the excited ion. The energy levels and transitions of the Al XI dielectronic satellites are shown in Figure 6.5. The main interest will be in the well-resolved satellites between 7.84→7.90Å.

### Satellite Profile and Widths.

Figure 6.6 shows the same spectrum for a laser irradiated Ø1mm Al wire. This was an atypical spectrum but was interesting for several reasons:

- The spectral resolution  $\lambda/\Delta\lambda=1770 \pm 70$  of the satellite lines was considerably higher than Figure 6.4 ( $\lambda/\Delta\lambda=1200$ ). There is a clear difference in the widths of the resonance and satellite lines. The w line is broader than the satellites, FWHM  $\Delta\lambda=6.6\text{mÅ}$  compared to  $4.5\text{mÅ}$ , probably due to opacity broadening or increased spatial and temporal emission.
- The line profiles were more Lorentzian. One explanation for this could be lower plasma expansion on this particular shot.

The improved spectral resolution has revealed more detail in the satellite groups at 7.84→7.90Å; the strong j,k lines are separately resolved and the blended lines in the other two groups are shown as asymmetries to the strong lines. The spectrum could be fitted with power law or Voigt profiles, starting first with the resolved j,k lines to find the line shape. A power law fit with  $n=2.2$  gave the best fit as shown in Figure 6.7.

### Satellite Transition Wavelengths.

The spectrometer dispersion relation (Chapter 2) and PET (002) crystal characteristics (Chapter 4) were used to calculate the wavelengths. The temperature was monitored throughout the experiment and remained constant at  $T=19.5\pm 0.2^\circ\text{C}$ . No systematic differences were noted between the inside and outside target chamber temperatures. The final precision of  $\pm 1\text{mÅ}$  was determined by the statistical fitting accuracy. The wavelengths are shown in Table 6.1 and compared with the theoretical results of Duston et al<sup>126</sup>, Vainshtein and Safronova<sup>127</sup> and the experimental results of Peacock et al<sup>128</sup>. There is good agreement with these results confirming the identification of the satellite lines.

Since the (j, k) dielectronic satellites at 7.878Å and 7.874Å, respectively, were well resolved, from the same multiplet, due to dielectronic recombination and the electron populations unaffected by collisional effects until  $n_e \sim 10^{24}\text{cm}^{-3}$ , they could be used to compare their relative intensity factors q with theory. The satellite intensity factor q is defined in chapter 5.2.3, equation (5.25), and depends on the radiative transition probability  $A_j$  and auto-ionization rate  $\Gamma_j$  (listed in Table 6.1 from Duston et al<sup>126</sup>) for a dielectronic line from the initial excited level j. Thus, the experimental value of the intensity ratio  $I(k)/[I(j)+I(l)]$  in Figure 6.7 was measured to be  $0.654\pm 0.006$  where the tolerance included the fitting, statistical and sensitivity errors. The ratio agreed extremely well (to within 1.5→3.5%) with the corresponding values 0.631 from Vainshtein and Safronova<sup>127</sup> and 0.664 from

# AlXIII Lyman- $\alpha$ and Satellite Structure

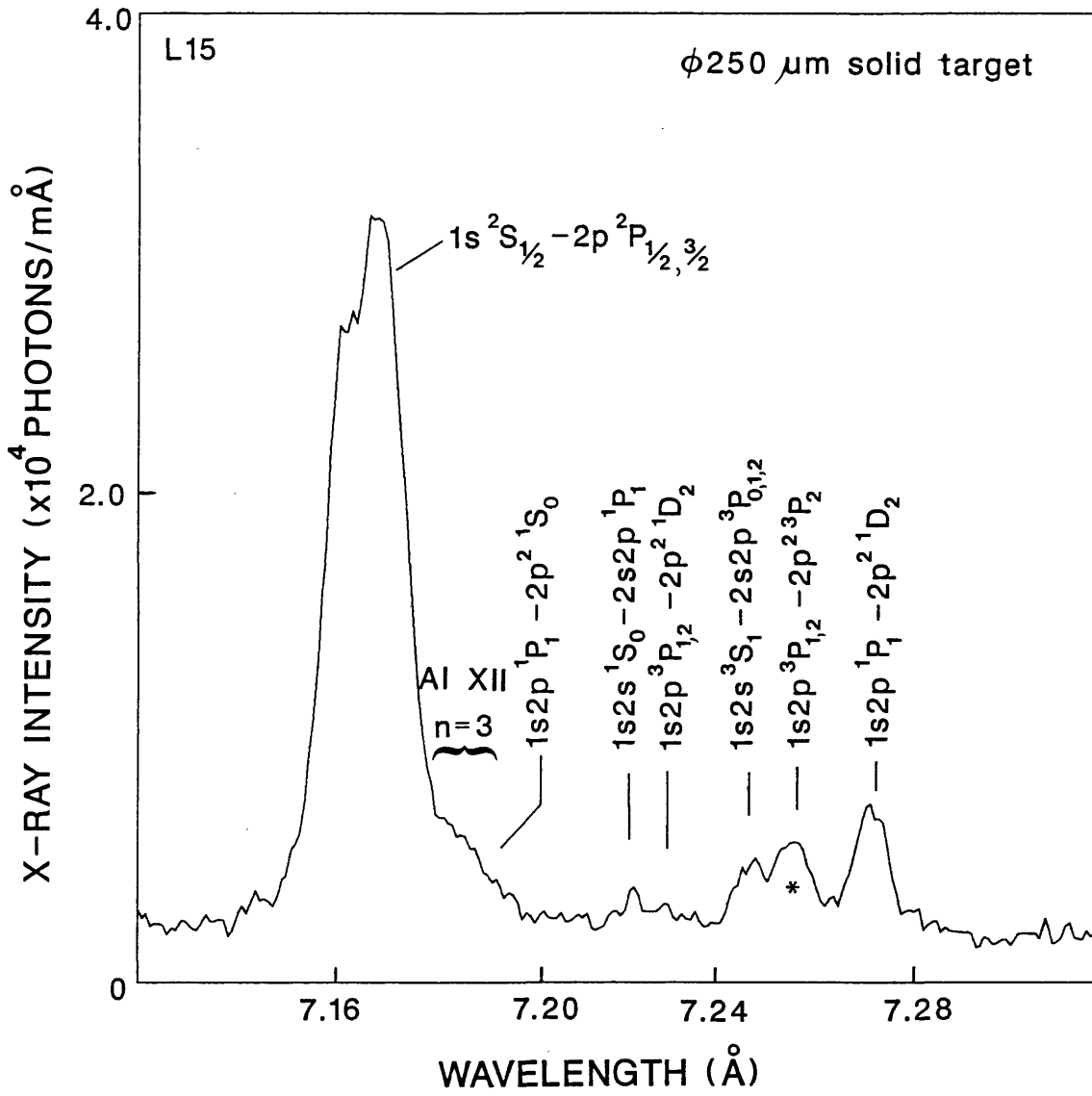


Figure 6.8 Al XIII Lyman- $\alpha$  and satellite structure for  $\phi 250\mu\text{m}$  solid target.

# Dielectronic Levels of n=2 AlXII Satellite Lines

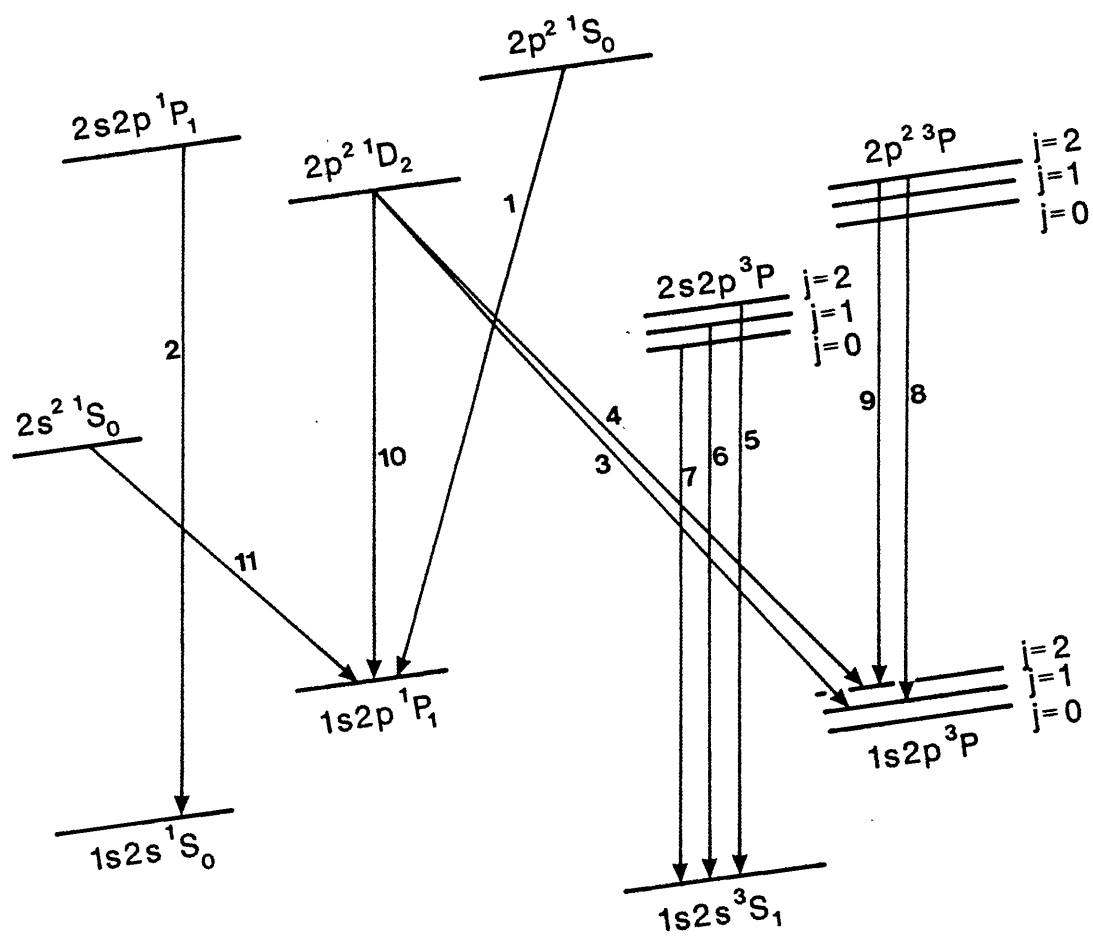


Figure 6.9 Dielectronic levels of Al XII satellite lines to the Lyman- $\alpha$ .

### AIXIII Lyman- $\alpha$ and Satellite Structure

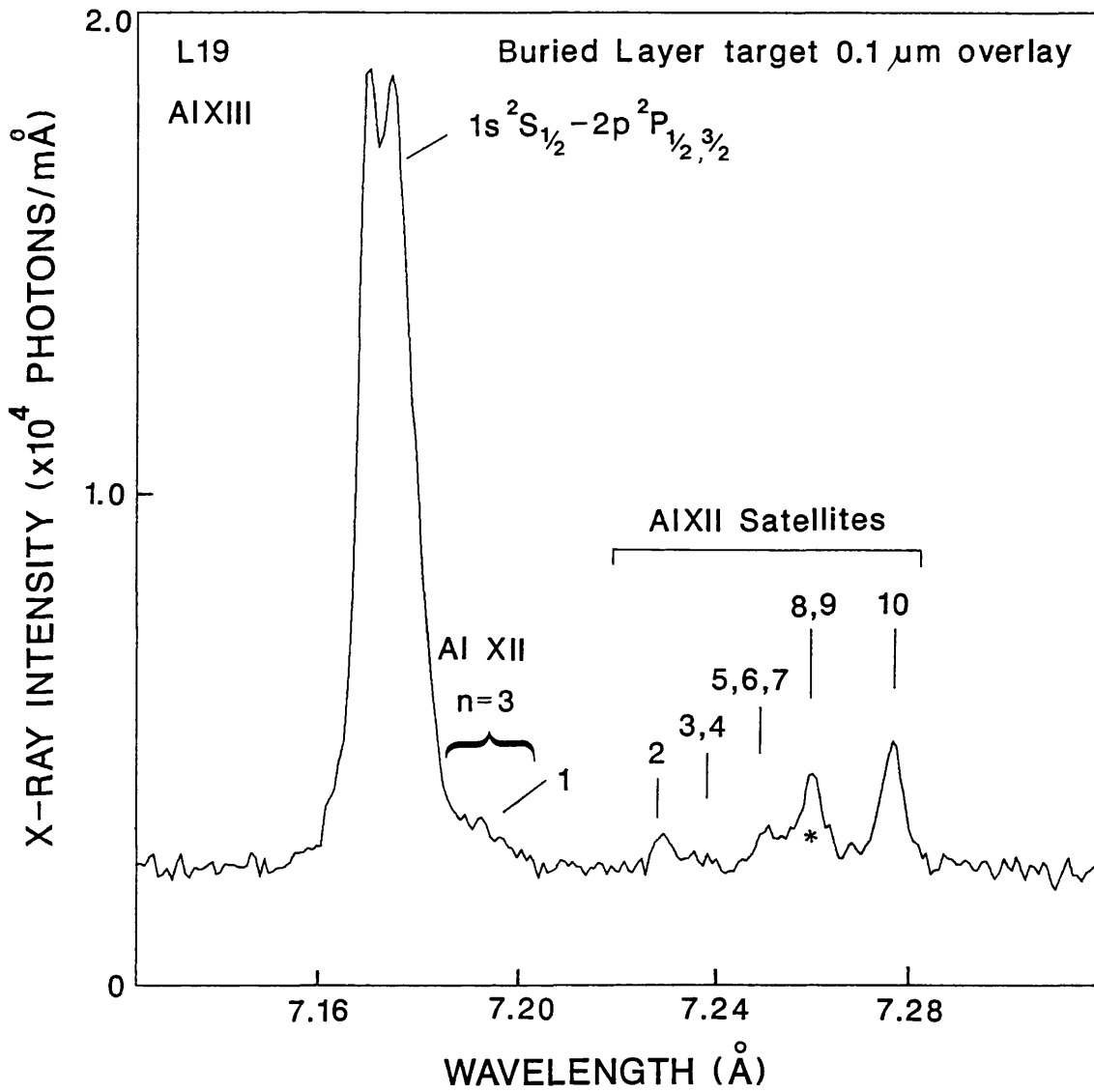
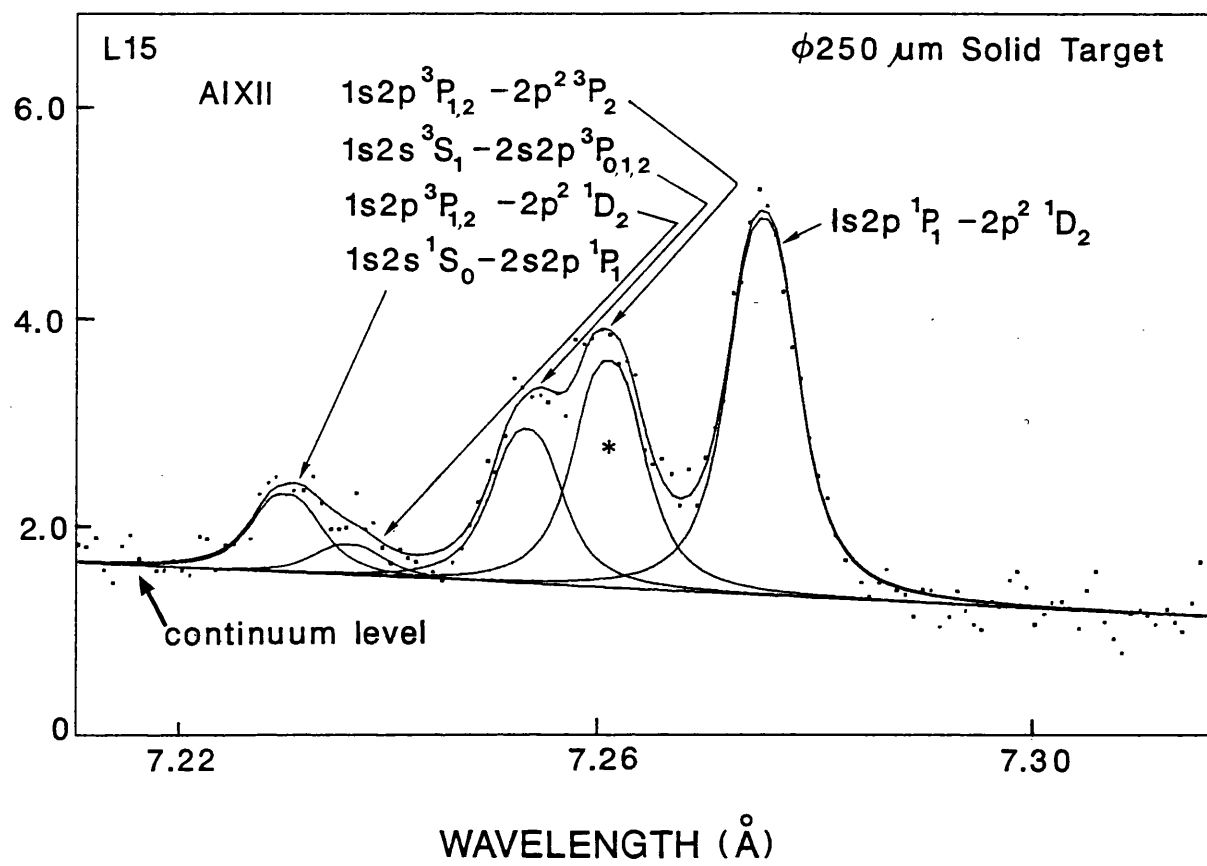


Figure 6.10 Al XIII Lyman- $\alpha$  and satellite structure for buried layer target with 0.1  $\mu\text{m}$  overcoat.

AIXII Satellite Structure 7.22→7.28Å showing Voigt Fit

X-RAY INTENSITY (x10<sup>3</sup> PHOTONS/mÅ)



Residuals to Fit

F<sub>FIT</sub> - F<sub>DATA</sub> (x10<sup>2</sup> PHOTONS/mÅ)

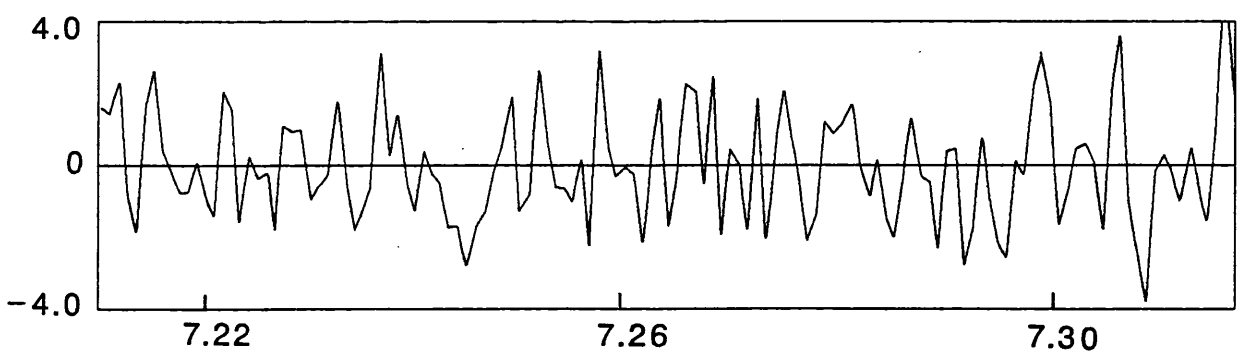


Figure 6.11 Voigt fit to Al Lyman-α dielectronic satellites of shot #L15.

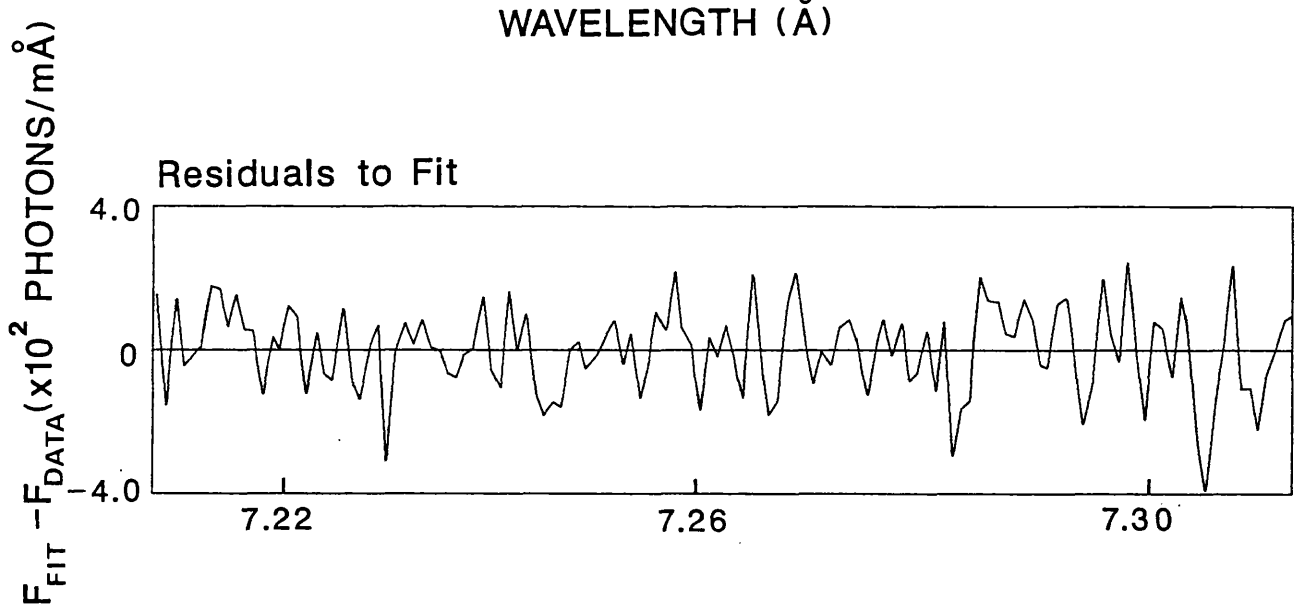
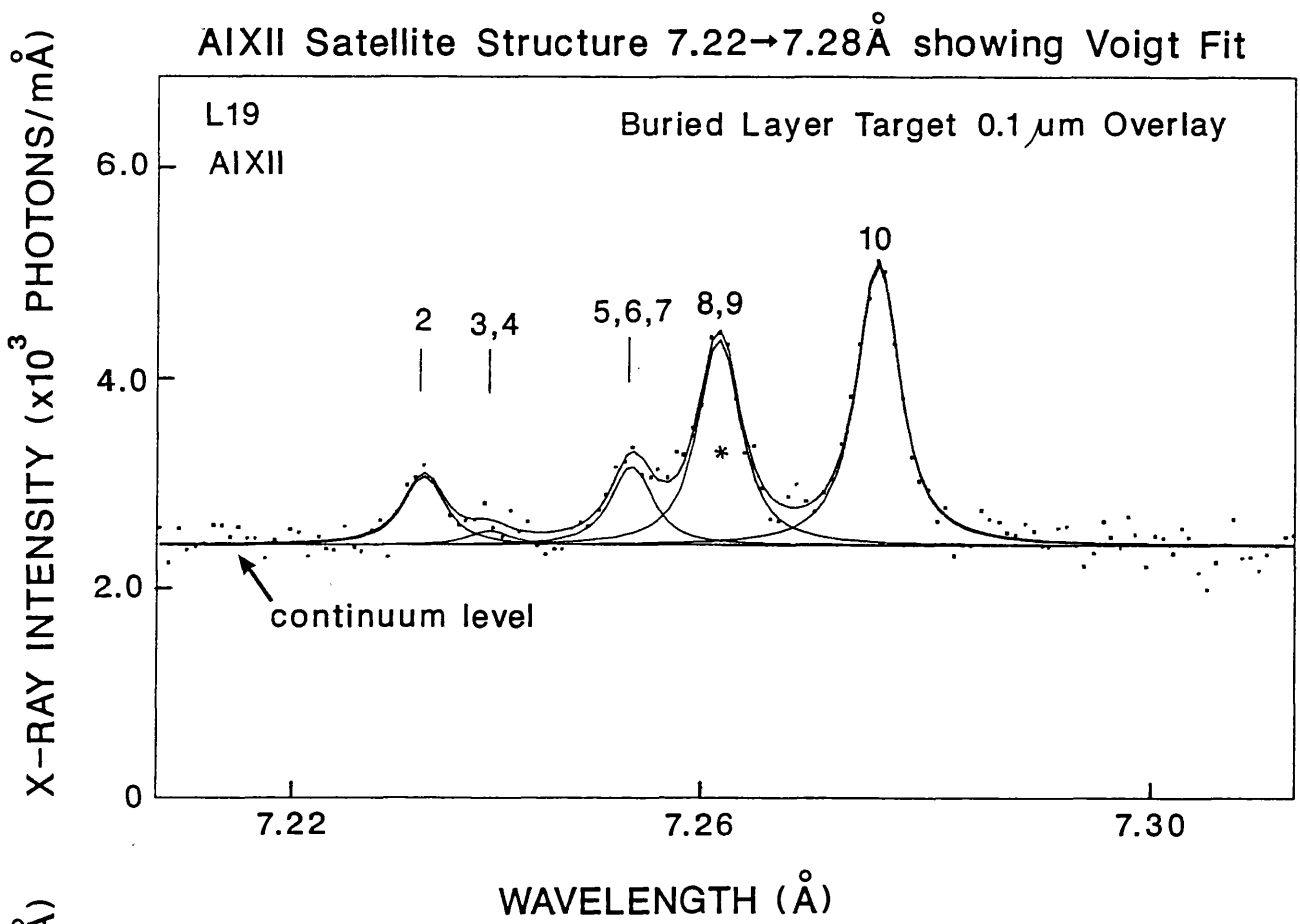


Figure 6.12 Voigt fit to Al Lyman- $\alpha$  dielectronic satellites of shot #L19.

### AlXIII Lyman- $\alpha$ and Satellite Structure

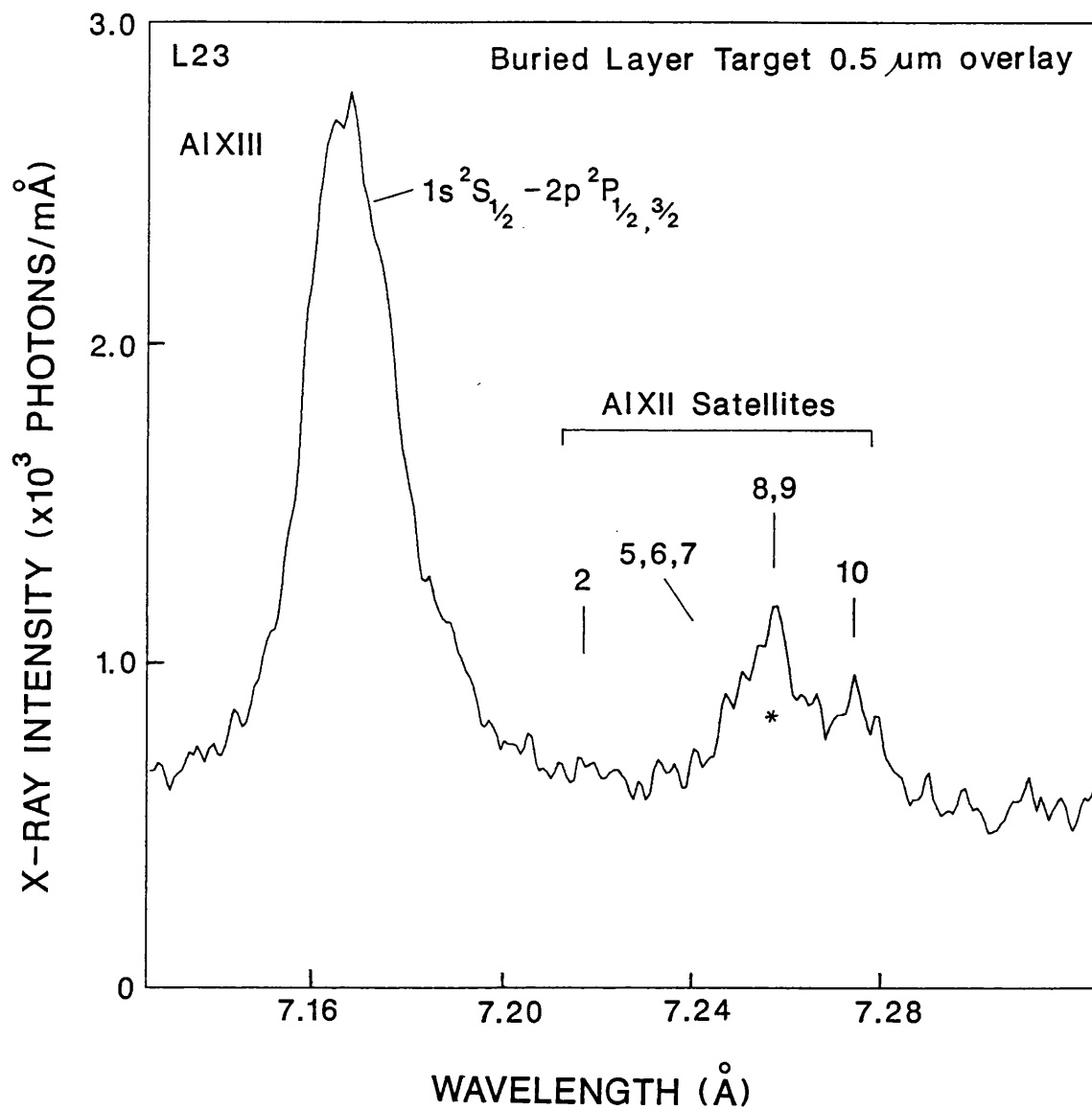


Figure 6.13 Al XIII Lyman- $\alpha$  and satellite structure for buried layer target with 0.5 $\mu\text{m}$  overcoat.

**Table 6.3 Theoretical and Experimental Wavelengths of the Al XII Dielectronic Satellite Lines to the Lyman- $\alpha$ .**

Key	Transition	$A_{ji}$ ( $s^{-1}$ )		$\Gamma_j$ ( $s^{-1}$ )		Satellite Wavelengths $\lambda(\text{\AA})$			
		DRDB		DRDB		Theory DRDB	Theory V+S (I)	Expt BFPS	This Expt
1	1s2p $^1P_1$ - 2p $^2$ $^1S_0$	2.77x10 <sup>13</sup>		1.26x10 <sup>13</sup>		7.1949	7.1912	7.1930	7.191
2	1s2s $^1S_0$ - 2s2p $^1P_1$	1.72x10 <sup>13</sup>		1.51x10 <sup>14</sup>		7.2284	7.2304	7.2300	7.227
3	1s2p $^3P_1$ - 2p $^2$ $^1D_2$	-		-		-	7.2316	-	-
4	1s2p $^3P_2$ - 2p $^2$ $^1D_2$	-		-		-	7.2343	-	7.233
5	1s2s $^3S_1$ - 2s2p $^3P_2$	1.72x10 <sup>12</sup>		1.19x10 <sup>13</sup>		7.2537	7.2495	7.2495	
6	1s2s $^3S_1$ - 2s2p $^3P_1$	1.72x10 <sup>12</sup>		1.20x10 <sup>13</sup>		7.2521	7.2533	7.2540	7.251
7	1s2s $^3S_1$ - 2s2p $^3P_0$	1.73x10 <sup>12</sup>		1.19x10 <sup>13</sup>		7.2487	7.2543		
8	1s2p $^3P_1$ - 2p $^2$ $^3P_2$	8.58x10 <sup>12</sup>		2.08x10 <sup>12</sup>		7.2558	7.2568		
9	1s2p $^3P_2$ - 2p $^2$ $^3P_2$	2.53x10 <sup>13</sup>		2.08x10 <sup>12</sup>		7.2588	7.2595	7.2590	7.259
10	1s2p $^1P_1$ - 2p $^2$ $^1D_2$	3.24x10 <sup>13</sup>		2.66x10 <sup>14</sup>		7.2710	7.2742	7.2745	7.2742 calibration
11	1s2p $^1P_1$ - 2s $^2$ $^1S_0$	7.66x10 <sup>12</sup>		2.59x10 <sup>14</sup>		7.3635	7.3690	-	7.368

DRDB Theoretical results from Duston et al<sup>126</sup>.

V+S (I) theoretical results for Al XI from Vainshtein and Safronova<sup>127</sup>.

BFPS Experimental results from Bolko et al<sup>130</sup>.

$A_{ji}$ ,  $\Gamma_j$  theoretical values for the radiative decay and autoionisation probabilities.

Duston et al<sup>126</sup>. The weak l-satellite was included in the theoretical intensity ratio because of the blend with the j-line. It only contributes 2% to the latter intensity because of its low radiative probability. This was further confirmation of the accuracy of the sensitivity calibration and fitting techniques to the data.

The He-like Al ion series emission was weak for overcoat thicknesses 0.7→1.0μm and this was only with the highest energy 10J on target.

#### **6.4.2 H-like Al 1s-2p Spectrum and Satellites**

The Al Lyman-α spectrum is shown in Figure 6.8 for laser irradiation of a solid Al Ø0.25mm wire target. The main observed differences to Tokamak spectra for medium Z ions (Chapter 8), are in the fine-structure intensity ratio and the strong satellite lines mostly to the long wavelength side of the Lyman-α. The former, discussed in section 6.5, can be largely attributed to opacity effects. The strongest He-like ion dielectronic lines fall in the 7.17→7.27Å waveband though a much weaker satellite is observed at 7.37Å. The satellites are due to dielectronic recombination and are in principle more simple to interpret. The line positions relative to the resonance line follow the same pattern as the Li-like satellites; n≥3 excited levels are observed as a blend to the resonance line while the stronger n=2 lines tend to be better separated and at a longer wavelengths. The most intense satellite is usually the 1s2p <sup>1</sup>P<sub>1</sub>-2p<sup>2</sup> <sup>1</sup>D<sub>2</sub> transition at 7.27Å. The n=2 dielectronic levels of Al XII are shown in Figure 6.9.

Improved spectral resolution, see Figure 6.10, is noted on all lines for the thin buried layer targets with 0.1μm plastic top coat, mainly because of lower expansion for the Aluminium plasma. The n=2 satellite lines are fitted with Voigt profiles as shown in Figures 6.11 and 6.12, in order to determine the wavelengths and intensities. The wavelengths are tabulated on Table 6.3 for comparison with other theoretical and experimental results.

It may be noted that as the overcoat thickness was increased, the emission of the Hydrogenic Al ion from the buried layer decreased rapidly until only the He-like series was observed at 0.7μm. This result was interpreted as a drop in the electron temperature T<sub>e</sub> due to reduced thermal conduction with buried layer depth. The use of density sensitive satellite lines to the Lyman-α could only be used for overcoat thicknesses up to 0.5μm for both the He- and Li-like satellites. Figure 6.13 shows the Al Lyman-α emission for buried layer targets buried under a 0.5μm overcoat layer. The line intensity is much lower than the previous spectra of Figures 6.8→6.12. This is discussed in section 6.6.

### **6.5 Opacity Calculations.**

An estimate is made of the optical thickness of the plasma for the strong n=2 resonance lines of the H-like and He-like ions. An escape factor approximation, as outlined by Keenan and Kingston<sup>131</sup>, is used. This has been adopted from Holstein<sup>132</sup> but does not include the full geometrical treatment of Irons<sup>121</sup>.

### 6.5.1 Escape Factor Model.

The escape factor  $g$  of any transition is the probability that a photon will escape from a plasma without being scattered from the observer's line of sight. Thus the intensity of the spectral line of interest is given by:

$$I_{ji} = \frac{1}{4\pi} A_{ji} g(\tau_{0,ij}) \int n_j dx \quad (6.5)$$

where  $n_j$  is the upper level population ( $\text{cm}^{-3}$ ),  $A_{ji}$  ( $\text{s}^{-1}$ ) is the radiative transition probability from level  $j$  to  $i$  and  $g(\tau_{0,ij})$  is the escape factor. This is a function of the optical depth  $\tau_0$  at the line centre. The intensity ratio of two lines originating from the same upper level  $j$  can be expressed as:

$$\frac{I_{ji}}{I_{jk}} = \frac{g(\tau_{0,ij})}{g(\tau_{0,kj})} \frac{A_{ji}}{A_{jk}} \quad (6.6)$$

For small  $\tau$ , McWhirter<sup>87</sup> writes the escape factor as:

$$g(\tau_0) = 1 + \sum_{n=1}^{\infty} \frac{(-1)^n (\tau_0)^n}{n! \sqrt{n+1}} \quad (6.7)$$

while for  $\tau_0 > 2.5$ , Holstein<sup>132</sup> uses the approximation:

$$g(\tau_0) = \frac{1}{\tau_0 \sqrt{\pi \ln \tau_0}} \quad (6.8)$$

A short Fortran code of 50 lines was written using equations (6.7) and (6.8) to calculate the escape factor as a function of optical depth  $\tau_0$ . The results are plotted in Figure 6.14.

Mitchell and Zemansky<sup>133</sup> have shown, assuming a uniform plasma, that the optical depth  $\tau_0$  for the line centre of a thermal Doppler broadened profile is:

$$\tau_{0,ij} = 1.16 \times 10^{-6} \sqrt{\frac{M}{T_i}} \lambda_{ji} n_i f_{ij} l \quad (6.9)$$

where  $T_i$  is in Kelvin,  $M$  is the ion atomic weight (in amu),  $\lambda_{ji}$  is the transition wavelength (cm),  $n_i$  is the lower level population density ( $\text{cm}^{-3}$ ),  $f_{ij}$  is the absorption oscillator strength and  $l$  is the line of sight plasma thickness (cm). The population density  $n_i$  can be written as:

$$n_i = \frac{n_i}{n_z} \frac{n_z}{n_{El}} \frac{n_{El}}{n_0} \frac{n_0}{n_e} n_e \quad (6.10)$$

where:

$n_i/n_z$  proportion of total population of charge state  $z$  in level  $n_i$ . For the ground state,  $n_i/n_z$  can be assumed to be unity.

$n_z/n_{El}$  proportion of element (Aluminium here) in the relevant charge state (Al XI, Al XII or Al XIII), strongly dependent on  $T_e$ .

$n_{El}/n_0$  fractional abundance of element to other plasma constituents.

$n_o/n_e$  ratio of plasma ion density to electron density  $n_e$  (also referred to the inverse of  $Z_{\text{eff}}$ , the effective ion charge of the plasma).

As a rough indication, optical depth (for  $\tau_o > 0.1$ ) should be calculated for the resonance line radiation if the population density of ions in the lower level of the  $n=2$  transition (in  $\text{cm}^{-3}$  units) x scale length product  $n_l l$  approaches  $2 \times 10^{15} \text{cm}^{-2}$ .

### 6.5.2 He-like Al $1s^2-1s2p$ Resonance Line

The optical depth of the He-like Al  $1s^2 \ ^1S_0 - 1s2p \ ^1P_1$  resonance line at  $7.76\text{\AA}$  was calculated for a solid Al and  $0.2\mu\text{m}$  Al layer buried under a  $0.1\mu\text{m}$  top coat. The proportion of Al in the Al XII charge state was estimated from the ionization abundance curves as a function of  $T_e$  from Duston et al<sup>126</sup>. The charge state population was assumed to be mainly in the ground state. The temperature  $T_e=T_i=500\text{eV}$  ( $5.8 \times 10^6\text{K}$ ) was adopted, with thermal electron conduction heating  $\sim 1.0\mu\text{m}$  layer in total.

The parameters for equations (6.9) and (6.10) are listed for the two targets in Table 6.4.

**Table 6.4 Parameters for Opacity Calculation of the He-like Al  $1s2p \ ^1P_1$  line.**

	Buried Layer	Solid Al
$n_e \ (\text{cm}^{-3})$	$7 \times 10^{22}$	$4 \times 10^{22}$
$T_i \ (\text{K})$	$5.8 \times 10^6$	
$n_1/n_{\text{Al XII}}$	0.66	0.66
$n_{\text{AlXII}}/n_o$	0.4	1.0
$n_o/n_e (=1/Z_e)$	1/7.1	1/11.3
$l \ (\text{cm})$	$0.24 \times 10^{-4}$	$1.0 \times 10^{-4}$
$n_1 l \ (\text{cm}^{-2})$	$5.2 \times 10^{16}$	$2.3 \times 10^{17}$

The density scale length product  $n_l l$  for both targets clearly indicates that the resonance line is optically thick. Table 6.5 shows the optical depth  $\tau_o$  for the Al XII  $n \geq 2$  lines.

**Table 6.5 Opacity  $\tau$  for He-like Al  $n \geq 2$  resonance lines.**

$n$	$\lambda(\text{\AA})$	$f_{ij}$	Buried layer	Solid Al
$n=2$	7.757	0.742	7.5	44.6
$n=3$	6.635	0.1506	1.3	5.8
$n=4$	6.311	0.0562	0.46	2.0
$n=5$	6.173	0.0272	0.22	1.0

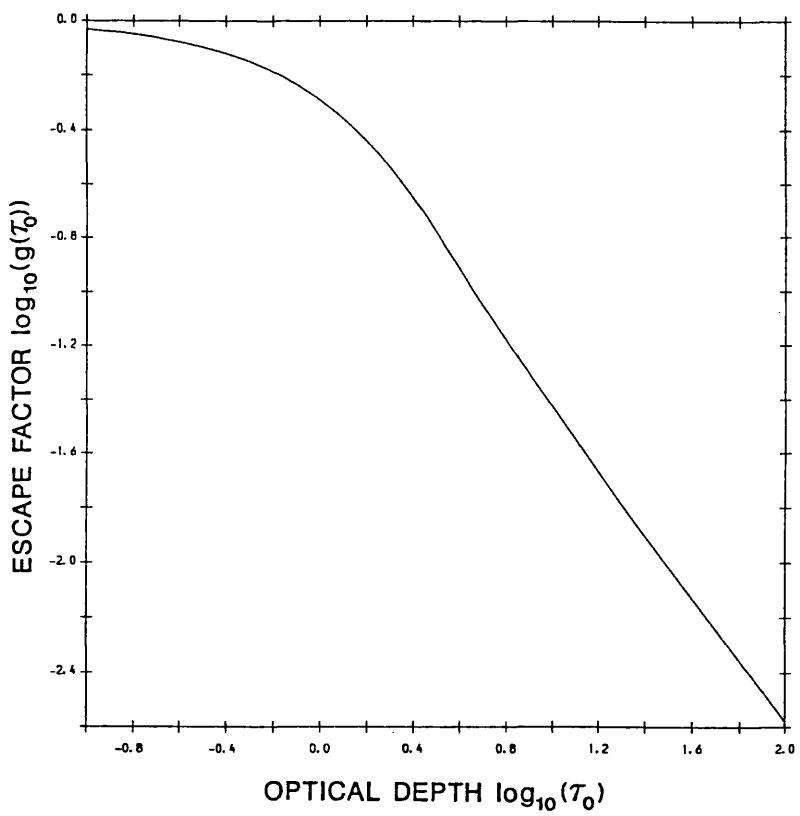
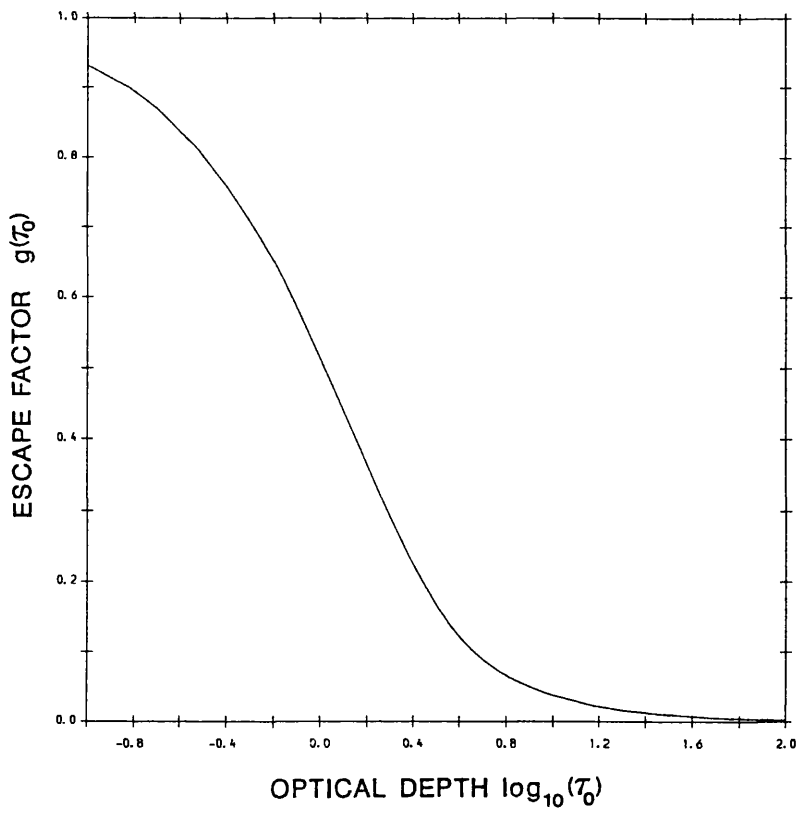


Figure 6.14 Escape factor  $g(\tau_0)$  as a function of the line centre optical thickness  $\tau_0$ . Both graphs show the same information except the ordinate of the lower graph is plotted as  $\log_{10} g$ .

Errors may arise as a result of the time integration and uncertainty in the exact values of  $n_i$  and  $l$ . The level population  $n_i$  may be considerably lower if the main emission is during the plasma recombination stage. Neglect of the plasma geometry is likely to contribute a small error in comparison with the above effects. Therefore, it can be concluded that the  $n=2$  resonance line is unsuitable for diagnostic purposes due to self-absorption.

### 6.5.3 H-like Al 1s-2p Lyman- $\alpha$ Resonance Line.

A similar calculation can be performed for the H-like Al 1s  $^1S_{1/2}$  - 2p  $^2P_{1/2,3/2}$  doublet at 7.171Å and 7.176Å. However, the experimental observation of the Lyman- $\alpha$  doublet intensity ratio can be used for comparison with the calculation. The principle works as follows. The optical depth for the  $^2P_{1/2}$  line is different from the usually more intense  $^2P_{3/2}$  line on account of the absorption oscillator strength being half of the  $^2P_{3/2}$  value. Thus in a uniform plasma, the Lyman- $\alpha$  radiation being emitted from the same spatial region, the  $^2P_{3/2}$  line will be preferentially absorbed and the intensity ratio will be different from the optically thin case.

The effect of opacity on the intensity ratio of the Lyman- $\alpha$  radiation for H-like ions has been treated comprehensively by Irons<sup>121,135</sup> for laser produced plasmas. He discusses the effect on the line profiles where differential plasma motion results in the overlapping of red- and blue-shifted components of the doublet. Differential motion becomes significant where  $\tau_o$  exceeds 10. Sylwester et al<sup>136</sup> discuss the effect of scattering of the Lyman- $\alpha$  radiation in relation to solar flare plasmas. The results here are compared to both these papers.

The optical depth  $\tau_o(3/2)$  for the  $^2P_{3/2}$  line is calculated in Table 6.6 using the parameters  $T_i = T_e = 500\text{eV}$ ,  $n_e = 7 \times 10^{22}\text{cm}^{-3}$  and  $n_e = 4 \times 10^{22}\text{cm}^{-3}$  for the thin buried Al layer and solid Al targets respectively as before. The absorption oscillator strength  $f=0.275$  for Al Ly- $\alpha$  calculated from equation (5.10) is in very close agreement with  $f=0.28$  for Mg Ly- $\alpha$  (Sylwester et al<sup>136</sup>).

The calculation shows that the optical depth is just above unity for the thin buried layer and  $\tau_o \sim 6$  for the solid target. On this basis Figure 6.14 shows that just over 40% of the Al Lyman- $\alpha$ , radiation is observed along the line of sight from the buried layer.

The opacities of the Al Lyman- $\alpha$  doublet can be defined as  $\tau_o(1/2)$  and  $\tau_o(3/2)$ , respectively, such that the observed intensity ratio  $\beta_{\text{Obs}}$  can be written as:

$$\beta_{\text{Obs}} = \beta \frac{g(\tau_o(1/2))}{g(\tau_o(3/2))} \quad (6.11)$$

where  $\beta$  is the intensity ratio for the optically thin case. Since the difference between the two optical depths occurs with the value of the oscillator strength  $f$ , then  $\tau_o(3/2) = 2 \tau_o(1/2)$  and the parameter  $\eta_{\text{opa}}$  representing the effect of opacity is defined as:

$$\eta_{\text{Opa}} = \frac{g(0.5 \times \tau_0(3/2))}{g(\tau_0(3/2))} \quad (6.12)$$

The opacity factor  $\eta_{\text{Opa}}$  is plotted as a function of  $\tau_0(3/2)$  in Figure 6.15 and tabulated for comparison with Sylwester et al<sup>136</sup> in Table 6.7. The table shows good agreement, except for the values of 0.6 and 0.8 for  $\tau_0(3/2)$  where there appears to be a typographical error in this paper.

From the optically thin case,  $\eta_{\text{Opa}}$  rises rapidly from 1.0 to a maximum of 2.56 occurring at  $\tau_0(3/2)=6.0$ . There is a slow decay with increasing opacity, reaching 2.17 at  $\tau_0(3/2)=100$ . It is clear that possible ambiguity may occur for  $\tau_0 > 6$  and so the method is only useful where  $\tau_0 \leq 6$ . It may be noted that the profile shapes would be readily opacity broadened for  $\tau_0 > 10$  and be distinguishable from optically thin radiation.

The  $\beta$ -ratio can also be affected by non-opacity mechanisms, see Chapter 8 and the next section, where collisional distribution of the electron population in the  $n=2$  levels is the most important effect. It can be estimated from the results of Boiko et al<sup>137</sup>, as shown in Figure 6.16, that at the densities here the Al XIII  $^2P_{1/2,3/2}$  levels are in LTE and  $\beta_{\text{col}}=0.51 \rightarrow 0.50$  for  $n_e=4 \times 10^{22} \rightarrow 10^{23} \text{ cm}^{-3}$ . Thus, a value of  $\beta=0.5$  can be adopted in equation (6.12) giving an observed ratio  $\beta_{\text{obs}}=0.5 \rightarrow 1.3$ , depending on opacity.

Table 6.8 shows the results of  $\beta_{\text{Obs}}$  from Figures 6.8 and 6.10. The equivalent  $\eta_{\text{Opa}}$  points are plotted on Figure 6.15. The agreement between the calculated and observed values of  $\tau_0(3/2)$  is reasonable, to within a factor of two, though fortuitously the best agreement is for the solid target.

### Ion Streaming Effects.

The mainly Gaussian profile of the Lyman- $\alpha$  doublet in Figure 6.8 is Doppler broadened by ion streaming effects. Other spectra recorded from irradiated solid targets under the same laser parameters, show a broadened single line with no observed fine-structure. Irons<sup>135</sup> points out that for conditions where  $\tau_0 \geq 10$  and the ion streaming velocity  $v_s > v_t$  (the thermal ion velocity), the plasma differential motion must be considered together with opacity. Figure 6.17, after Irons, shows the effect of differential plasma expansion on the Lyman- $\alpha$  profile for  $\tau_0=10$ . The parameter  $\eta$  in this paper is defined as  $2v_s/v_t$ . For solid targets here, assuming a minimum ion temperature  $T_i=300\text{eV}$ , can give values of  $\eta=3 \rightarrow 10$  and shows qualitative agreement with the observed profiles. Irons also reports that optically thick profiles can be distorted by differential expansion in such a way as to appear optically thin. In that situation, an increase in the fine-structure separation  $\lambda_{\text{FS}}$  of about 10% may be measured.

Finally, the use of optically thin targets together with spatially resolved spectral measurements with high resolution is the most effective way of determining opacity on the Lyman- $\alpha$  transitions.

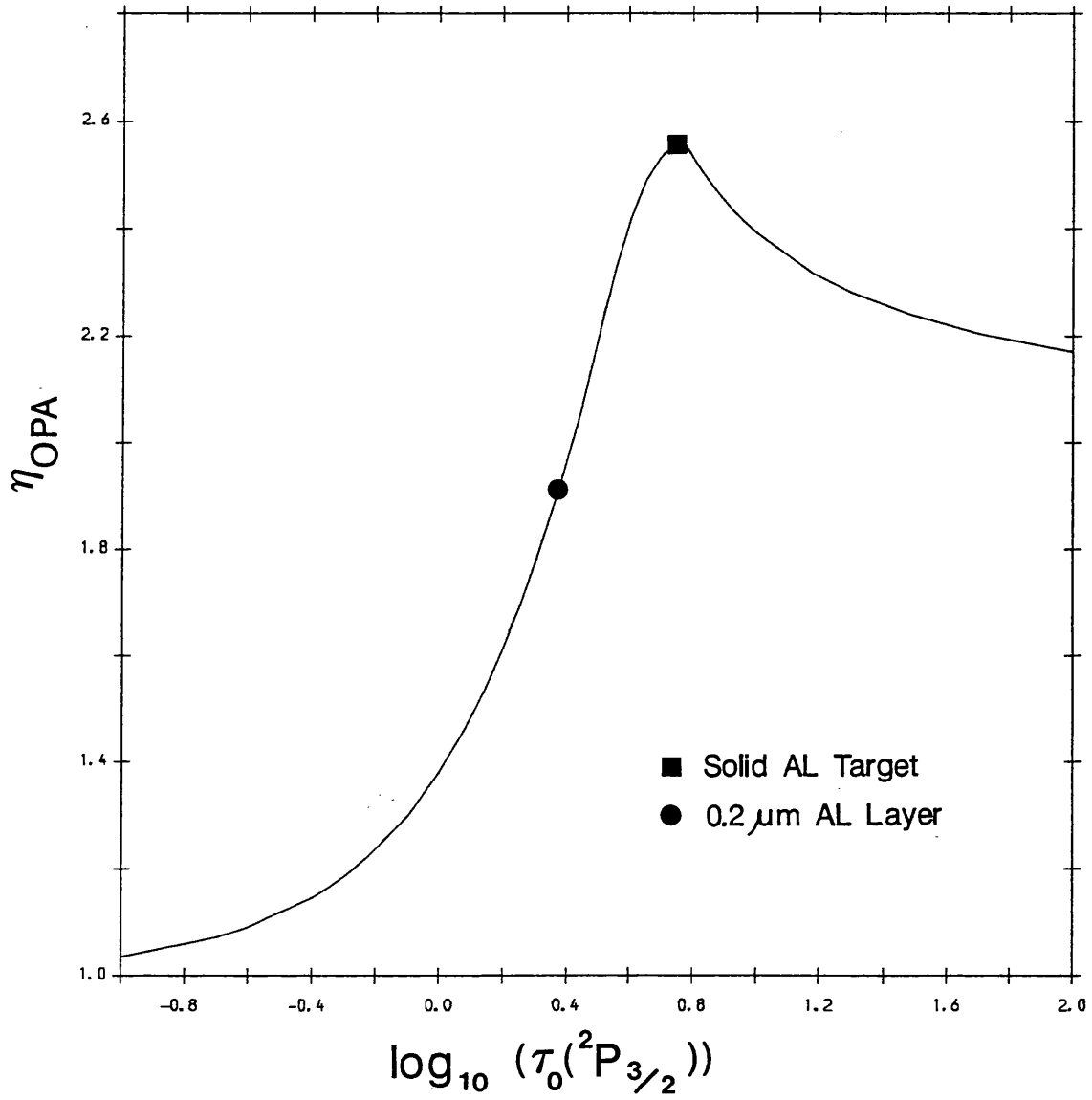


Figure 6.15 Variation of  $\eta_{opa}$  with optical depth  $\tau_0(3/2)$ .

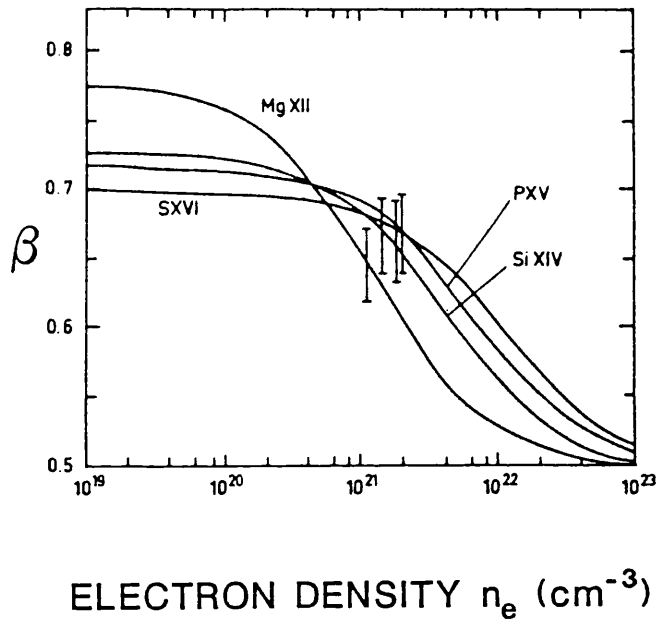


Figure 6.16 Optically thin Lyman- $\alpha$  intensity ratio as a function of electron density (after Boiko et al<sup>137</sup>).

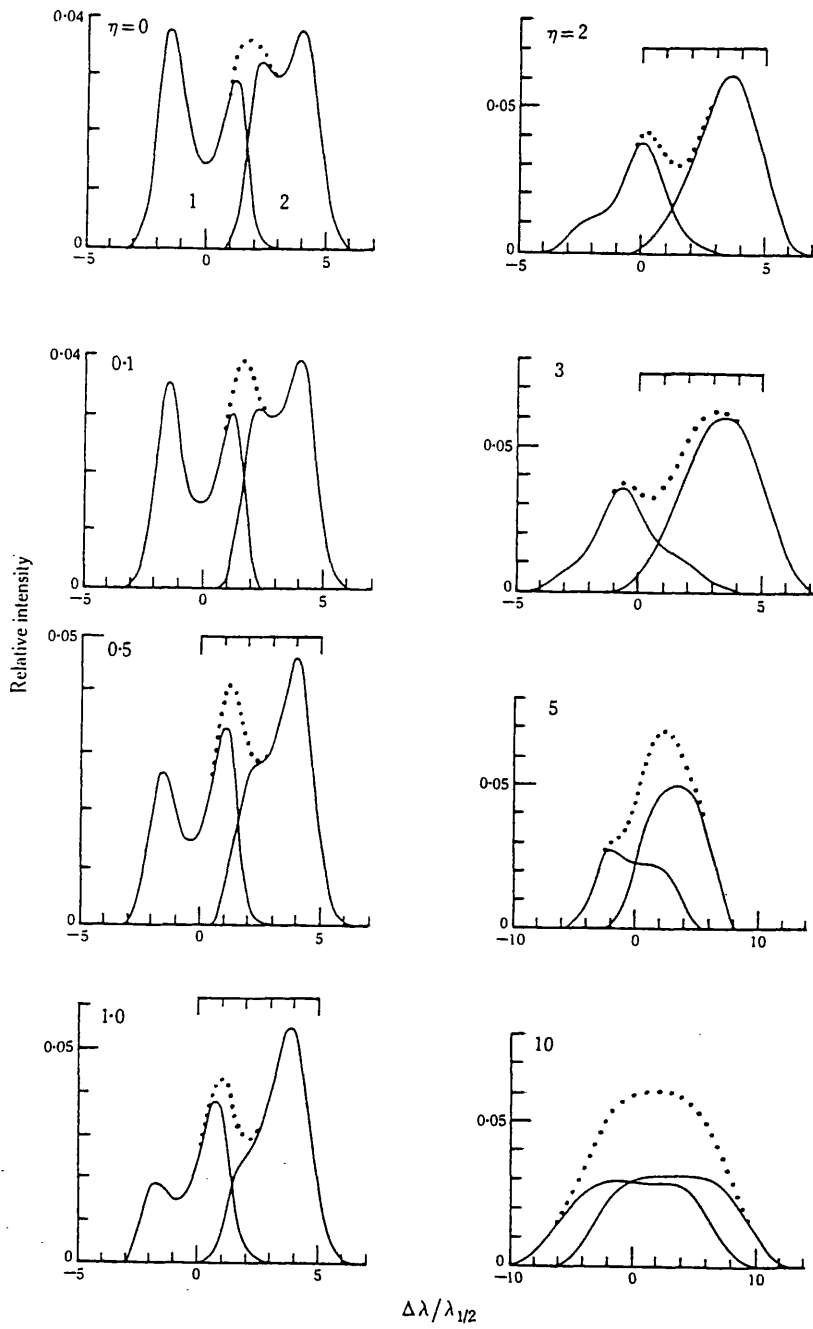


Figure 6.17 (after Irons<sup>135</sup>) shows the effect of varying the streaming velocity and opacity  $\tau_0=10$  (kept constant) on the Lyman- $\alpha$  doublet profile. The parameter  $\eta=2V_s/V_t$  refers to the ratio of the ion streaming velocity  $V_s$  to the thermal ion velocity  $V_t$  and should not be confused with the parameter  $\eta_{opa}$  of equation (6.12).

**Table 6.6 Parameters for opacity calculation of the H-like 2p  $^2P_{1/2}$  line.**

	Buried Layer	Solid Al
$n_e$ (cm $^{-3}$ )	$7 \times 10^{22}$	$4 \times 10^{22}$
$T_i$ (K)		$5.8 \times 10^6$
$n_1/n_{Al\ XIII}$	0.33	0.33
$n_{AlXIII}/n_o$	0.4	1.0
$n_o/n_e$	1/7.1	1/11.3
$l$ (cm)	$0.2 \times 10^{-4}$	$10^{-4}$
$n_{i1}$ (cm $^{-2}$ )	$2.6 \times 10^{16}$	$1.2 \times 10^{17}$
$f$		0.275
$\lambda$ (cm)		$7.17 \times 10^{-8}$
$\tau_o$ (3/2)	1.3	5.8

**Table 6.7 Values of  $\eta_{Opa}$  as a function of  $\tau_o(3/2) = 0.1 \rightarrow 1.0$ .**

$\tau_o(3/2)$	$\eta_{Opa}$ Sylwester et al <sup>136</sup>	$\eta_{Opa}$ This work
0.1	1.036	1.0357
0.2	1.072	1.0720
0.4	1.145	1.1464
0.6	1.185	1.2228
0.8	1.223	1.3009
1.0	1.379	1.3801

**Table 6.8 Observed Lyman- $\alpha$  Intensity Ratios.**

	0.2 $\mu$ m Al Buried Layer	Solid Al
$\beta_{Obs}$	0.95	1.28
$\eta_{Opa}$	1.90	2.56
$\tau_o(3/2)$	$2.4 \pm 0.3$	$6.0 \pm 0.3$

Errors represent 5 $\rightarrow$ 10% measurement accuracy in observed  $\beta$ -ratio.

### 6.5.4 Satellite Lines.

The main advantage of satellite lines as plasma diagnostics at high densities is that they usually are optically thin, on account of the lower state of the transition not being the ground state. This means that the lower level population  $n_i$  is considerably less than the ground state. Opacity, however, should not be neglected altogether for these transitions. Duston and Davis<sup>138</sup> have shown that the intensity ratio of the lines  $I(1s2p^3P \rightarrow 2p^2^3P)/I(1s2s^3S \rightarrow 2s2p^3P)$ , a group of He-like dielectronic satellites on the long wavelength side of the Lyman- $\alpha$  resonance line, can be modified by opacity effects and be misinterpreted as a density diagnostic. They calculate the ratio for Al to vary up to 2.0 for  $n_e > 10^{23} \text{cm}^{-3}$  in an optically thin plasma, while being reduced to 1.1 at a lower density of  $n_e \geq 4 \times 10^{22} \text{cm}^{-3}$  in the optically thick case. Different level populations and absorption oscillator strengths ( $f=0.2657, 0.3974$  for the  $2p^2^3P, 2s2p^3P$  lines, respectively<sup>138</sup>) produce this result as discussed in the previous section.

Audebert et al<sup>139</sup> and Lunney<sup>140</sup> point out that the intense He-like "singlet-D" satellite to the Lyman- $\alpha$ , labelled  $1s2p^1P_1 - 2p^2^1D_2$  at  $7.274 \text{\AA}$  for Al, is most likely to be affected by opacity. Therefore, a quick estimate can be made of the optical thickness of the satellite lines generally by comparing the relative intensity of the "singlet-D" line with other dielectronic lines.

A suitable line, not affected by collisional processes, is the  $1s2s^1S_0 - 2s2p^1P_1$  transition. The satellite line intensity factors  $q_{ji}$ , see Chapter 5.2, depend on the autoionization rate  $\Gamma_j$  ( $\text{s}^{-1}$ ), the radiative transition rate  $A_{ji}$  ( $\text{s}^{-1}$ ) and  $g_j$ , the statistical weight of level  $j$ . The observed line intensity ratios are compared directly with theory<sup>126,127</sup> by using the respective ratio  $q(1s2p^1P_1 - 2p^2^1D_2)/q(1s2s^1S_0 - 2s2p^1P_1)$ , tabulated for shots L15 and L19 in Table 6.9. The agreement is excellent to within 2% of theory when the following are considered:

- The intensity lost to forbidden lines from the  $2s2p^1P_1$  line due to Stark mixing at high densities as reported by Bañon et al<sup>141,142</sup> is added.
- The increase in sensitivity of the spectrometer ( $0.091\%/m\text{\AA}$  for  $7.0 \rightarrow 7.5 \text{\AA}$ ) is included.

The satellite lines are clearly optically thin. A similar argument may be presented for interpreting Li-like satellites to the He-like  $1s2p^1P_1$  line.

**Table 6.9 Al XII Satellite Intensity Ratios.**

	Intensity ratio $q(1s2p^1P_1 - 2p^2^1D_2)/q(1s2s^1S_0 - 2s2p^1P_1)$				
	Raw Data	Experimental Stark Mixing	Sens. Incl	Theory V+S	DRDB
Solid target L15	4.77	3.37	3.23	3.215	3.117
Buried layer L19	4.09	3.42	3.28	3.215	3.117

Note: There is a 3% difference between the two theoretical calculations. V+S refers to the results by Vainshtein and Safronova<sup>127</sup>. DRDB denotes Duston et al<sup>126</sup>.

## 6.6 Electron Density Measurements.

The measurement of electron density  $n_e$  is discussed for the Al XII and Al XIII  $n=2$  resonance and satellite line spectra. The different methods rely on the interpretation of the line intensity ratios. The suitability of  $n=2$  resonance and satellite line techniques is largely determined by opacity effects.

### 6.6.1 $n=2$ Resonance Lines.

#### (a) Relative Intensities of the He-like Al Ion Resonance and Intercombination Lines.

Various authors<sup>137,143,144</sup> have reported the use of the  $\alpha$ -ratio as a density sensitive diagnostic appropriate for  $n_e = 10^{18} \rightarrow 10^{24} \text{ cm}^{-3}$ . The ratio is defined as the relative intensity of the resonance to the intercombination lines ( $\alpha = I[1s^2 \ ^1S_0 - 1s2p \ ^1P_1] / I[1s^2 \ ^1S_0 - 1s2p \ ^3P_1]$ ), usually the strongest lines in the He-like  $n=2$  group. The ratio can be observed over a large range of electron temperature  $T_e$  conditions and is not affected by the degree of ionization of the plasma since both lines are from the He-like ion stage. The A-values of  $7.62 \times 10^{10} \text{ s}^{-1}$  ( $^3P_1$ ) and  $2.74 \times 10^{13} \text{ s}^{-1}$  ( $^1P_1$ ) from Lin et al<sup>145</sup> indicate that the "triplet" level is susceptible to collisional effects with increasing electron density. This is similar to collisional quenching of the forbidden line at Tokamak densities<sup>97</sup>. Thus, the "triplet" intensity is reduced and the  $\alpha$ -ratio increases with  $n_e$ . The  $\alpha$ -ratio is also modified, to a much lesser extent, by the electron temperature  $T_e$ , through the impact excitation rates determining the level populations.

#### Experimental Results Interpretation.

The observed  $\alpha$ -ratios are in the range  $4.5 \rightarrow 9.5$  for this experiment. Calculations by Keenan<sup>144,146</sup> for Si and Al, respectively, include inner shell ionisation of the Li-like Al XI ion as well as dielectronic and radiative recombination of the H-like Al XIII ion on the Al XII level populations. For  $T_e = 540 \text{ eV}$ , the ratio has the values  $\alpha = 40, 100, 195, 281$  for the density range  $n_e = 3 \times 10^{21}, 10^{22}, 3 \times 10^{22}, 10^{23} \text{ cm}^{-3}$ .

The measured ratio would appear to be low by a factor of  $5 \rightarrow 20$ . This anomaly may be explained when plasma opacity is considered once more. From the A-values or absorption oscillator strengths ( $f_{ij} = 2.08 \times 10^{-3}, 0.742$  ( $^3P_1, ^1P_1$ ) from Lin et al<sup>145</sup>), the optical depth of the "triplet" line is a factor  $3.55 \times 10^2$  lower than the "singlet" line. Therefore, in this experiment, the  $\alpha$ -ratio is considerably reduced by self-absorption of the  $^1P_1$  line.

Duston et al<sup>126</sup> note that the unresolved Li-like satellites denoted m,n and s,t on either wing of the  $^3P_1$  line, significantly increase the line intensity for  $n_e > 10^{21} \text{ cm}^{-3}$ . This may lead to a factor of 100 error in the measured plasma density.

It may be concluded that the  $\alpha$ -ratio, although only needing moderate resolving power  $\lambda/\Delta\lambda \sim 500$ , is not suitable for accurate determination of density under the experimental conditions encountered here.

### (b) Intensity Ratio $\beta$ of the H-like Al Ion Lyman- $\alpha$ Doublet.

This topic is discussed in detail in Chapter 8. Some comments pertinent to laser produced plasmas are added here.

The first investigation of the intensity ratio  $\beta$  for the Lyman- $\alpha$  fine-structure components of medium Z Hydrogenic ions was credited to Beigman et al<sup>147</sup>, where  $\beta = I(1s \ ^1S_{1/2} - 2p \ ^2P_{1/2}) / I(1s \ ^1S_{1/2} - 2p \ ^2P_{3/2})$ . They reported  $\beta$ -ratios reaching 1.7, at variance with the statistical value of 0.5. Vinogradov et al<sup>148</sup> concluded that for a plasma in ionization equilibrium, the states with  $n=2$  were populated by electron impact excitation from the ground state; the relative populations of the  $^2S_{1/2}$ ,  $^2P_{1/2}$  and  $^2P_{3/2}$  levels were determined by collisional transitions between the fine-structure states of the excited ions and other ionised plasma constituents. This would account for values of  $\beta = 0.5 \rightarrow 0.8$ , see Figure 6.16 from Boiko et al<sup>137</sup>. Ratios as high as 1.7 can only be explained by the inclusion of plasma opacity<sup>9</sup>.

The advantages of the  $\beta$ -ratio as a density diagnostic may be summarised as:

- the emission comes from the hottest and densest part of the plasma and for the results reviewed by Boiko<sup>137</sup>, it appears to give accurate densities in the regime below  $10^{22} \text{cm}^{-3}$ .
- Low impurity traces of various elements can then be used to spatially map the plasma.
- It also has the strength of being relatively simple to extract the ratio accurately and occurring within a small waveband.

There are several disadvantages to this technique:

- Optically thin plasmas are absolutely essential, achieved by reducing the ion concentration to the level where  $\tau_0 < 0.1$ .
- X-ray spectrometers with high signal throughput and resolving power  $\lambda/\Delta\lambda \sim 5 \times 10^3$  are needed for good definition of the fine-structure components; increasing the target atomic number Z is important.
- Even if the first two are satisfied, the  $\beta$ -ratio has a low dynamic range of 0.6 ( $\beta = 0.5 \rightarrow 0.8$ ) for density spanning 3 orders of magnitude ( $n_e = 10^{20} \rightarrow 10^{23} \text{cm}^{-3}$  for Al XIII).

### 6.6.2 Density Sensitive Satellite Lines.

The use of satellite lines to interpret electron density for laser produced plasmas has been discussed by various authors, for example Bayanov et al<sup>150</sup>, Seely<sup>151</sup>, Boiko et al<sup>137</sup>, in the last 15 years. These are present in the satellite groups to the  $n=2$  H-like and He-like ion resonance lines, where the upper level populations are determined by collisional transitions.

The experimental results presented here for an Aluminium plasma are primarily compared with the theoretical model calculations of Jacobs and Blaha<sup>149</sup>, Duston and Davis<sup>138</sup> and co-

workers<sup>126</sup>. The strongest density sensitive lines are indicated by (\*) in the spectra. A collisional radiative equilibrium CRE model (Bates, Kingston and McWhirter<sup>88</sup>) is used by Duston et al<sup>126</sup>, where the rate equations:

$$\frac{dn_i}{dt} = \sum_j W_{ji} n_j - \sum_i W_{ij} n_i \quad (6.13)$$

are solved for each energy level in the model where  $n_i$  is the population density for level  $i$  and  $W_{ji}$  is the transition rate from level  $j$  to  $i$ . The latter coefficients are defined by the plasma temperature, density and opacity. The left-hand side of equation 6.13 is zero for an equilibrium plasma. The ground states and the  $n=2 \rightarrow 4$  levels for the H-like, ion and selected levels for  $n=2 \rightarrow 5$  states of the He-like and Li-like ions. (It may be noted that at these densities Duston et al<sup>126</sup> report that ion-ion collisions should populate the individual  $j$ -values of a single  $nl$  level into statistical equilibrium with each other, thus only  $nl$  levels need to be treated for collisional coupling).

#### (a) Al XII Satellite lines.

The principle of density sensitive lines can be explained by considering the 2i2i' doubly excited levels of AlXII. At electron densities below  $10^{19} \text{cm}^{-3}$ , these levels are mainly populated by dielectronic recombination where a free electron is captured by the Hydrogenic ion while simultaneously exciting the bound electron. The doubly excited levels are above the ionization limit for the He-like ion. The ion stabilises either by radiative decay giving rise to these spectral lines or through autoionization; the reverse process of dielectronic recombination where an electron is ejected leaving an unexcited Hydrogenic ion.

However, as the electron density increases, levels with small autoionization rates and therefore long lived (see Table 6.3), particularly the  $2p^2 \ ^3P$  states which have a low dielectronic recombination rate compared to adjacent levels, become populated by electron collisional transitions from the  $2s2p \ ^3P$  and  $2s2p \ ^1P$  states. Thus, in an optically thin plasma at  $T_e=500\text{eV}$ , the  $2s2p \ ^3P-2p^2 \ ^3P$  to  $1s2s \ ^3S-2s2p \ ^3P$  line intensity ratio rises from  $0.24 \rightarrow 1.95$  for  $n_e=10^{20} \rightarrow 10^{23} \text{cm}^{-3}$  using the CRE model predictions of Duston and Davis<sup>138</sup>.

Figure 6.18 shows the predicted ratio as a function of density with observed data indicated as points. This line ratio is weakly dependent on electron temperature  $T_e$  and readily gives an indication of the electron density. It can be seen that the highest observed values are marginally greater than the maximum calculated LTE ratio. The ratio is saturated above  $n_e=10^{23} \text{cm}^{-3}$ . The overall intensity ratio  $I(1s2p \ ^3P-2p^2 \ ^3P+1s2s \ ^3S-2s2p \ ^3P)/I(1s2p \ ^1P_1-2p^2 \ ^1D_2)$  referred to as the "triplet to singlet-D" ratio can still be used for higher densities. This may be shown in Figure 6.19 where the "triplet to singlet-D" ratio steadily increases with overcoat thickness. This is strong evidence of high densities  $n_e > 10^{23} \text{cm}^{-3}$  being produced in the Aluminium layer for the  $0.5\mu\text{m}$  plastic top coat layered targets.

### Al XII Satellite Line Intensity Ratios vs Electron Density

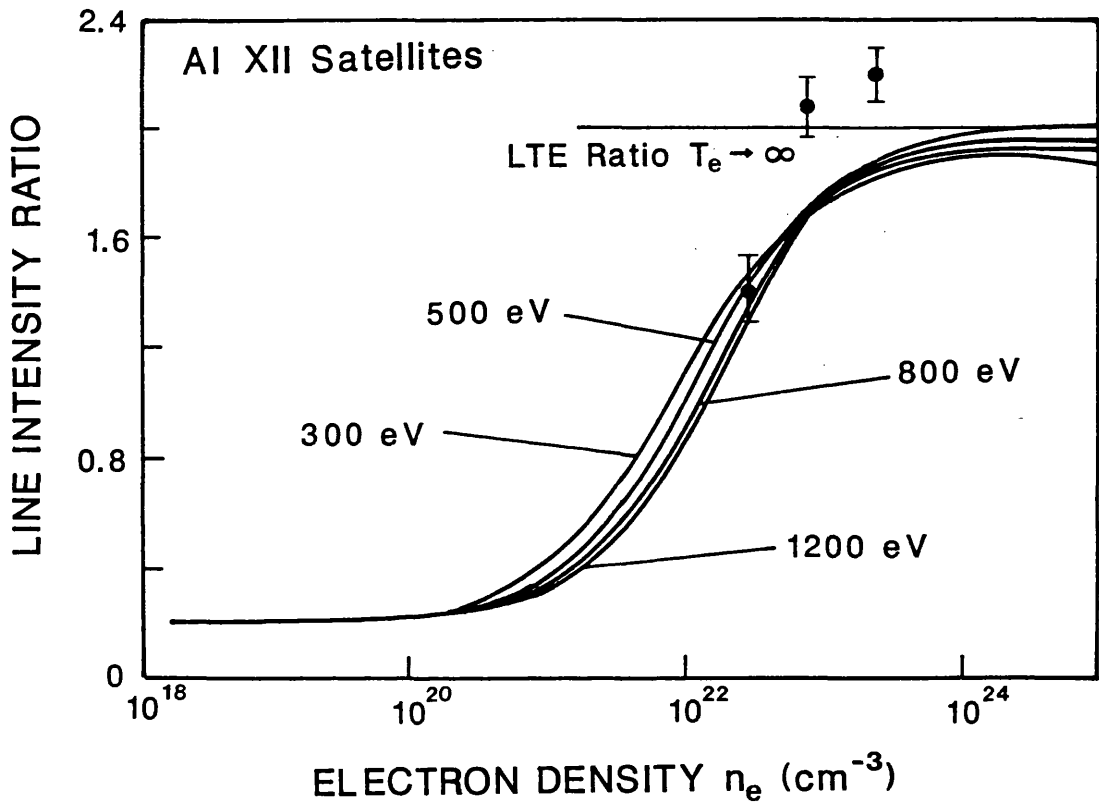


Figure 6.18 Al XII satellite line intensity ratio as a function of electron density. Solid curves are theoretical predictions of Duston and Davis<sup>138</sup>.

"Triplet" to "Singlet-D" Intensity Ratio  
vs Electron Density

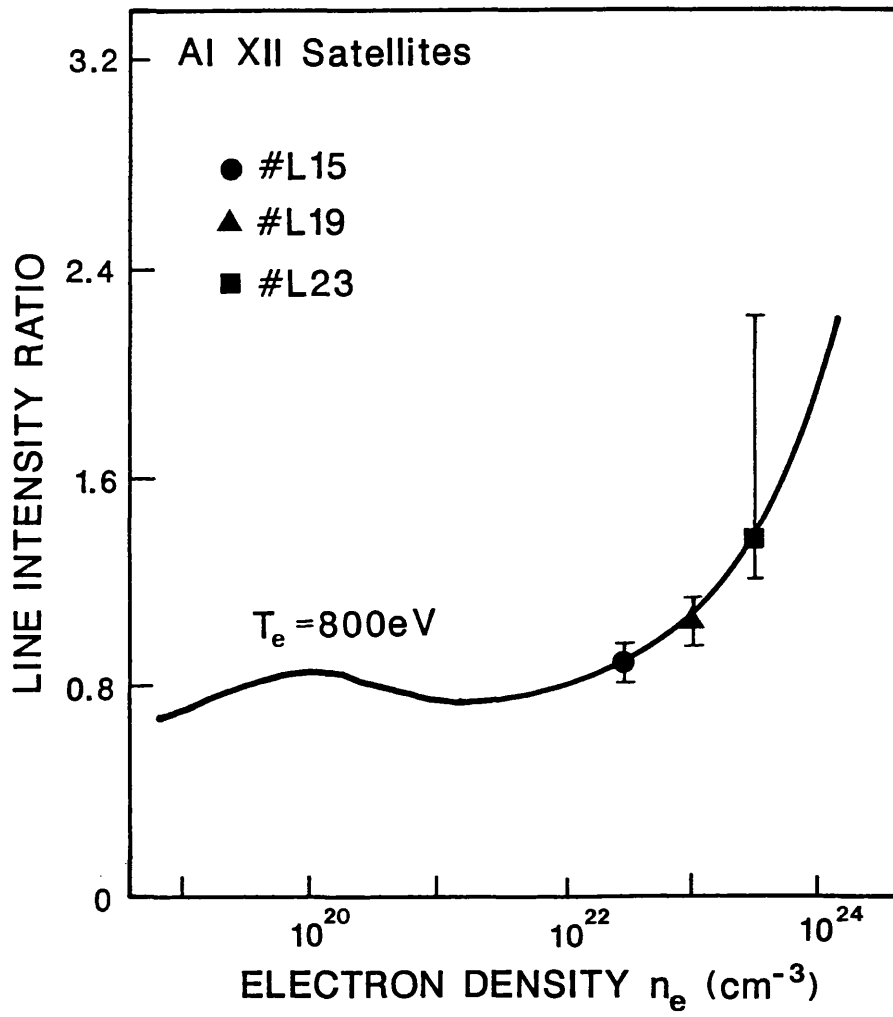


Figure 6.19 "Triplet to singlet-D" intensity ratio as a function of electron density.

Al XII Satellite Line Intensities  
(normalised to the Ly- $\alpha$ )  
vs Electron Temperature

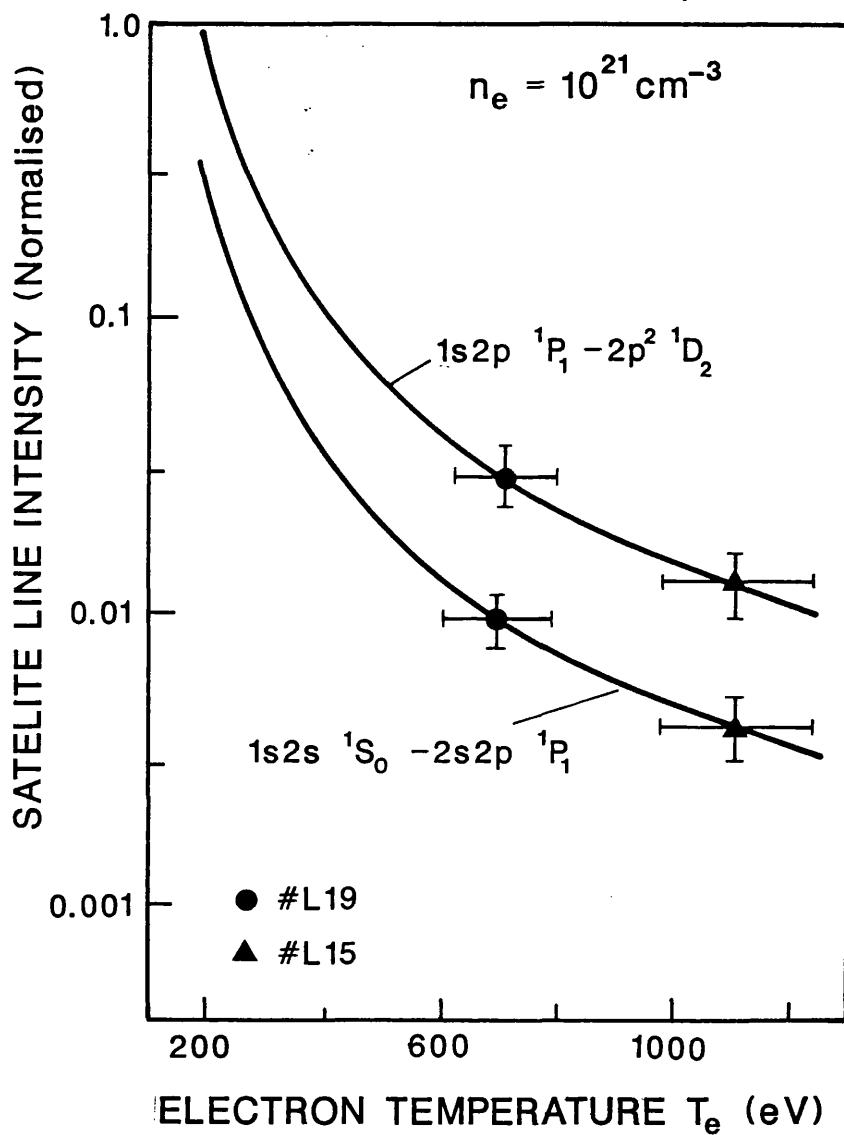


Figure 6.20 Electron temperature dependence of the 1s2p  $^1P_1$ -2p $^2$   $^1D_2$  and 1s2s  $^1S_0$ -2s2p  $^1P_1$  satellite lines to the Al Lyman- $\alpha$ .

## Density Sensitive Al XI Satellite Line Ratios

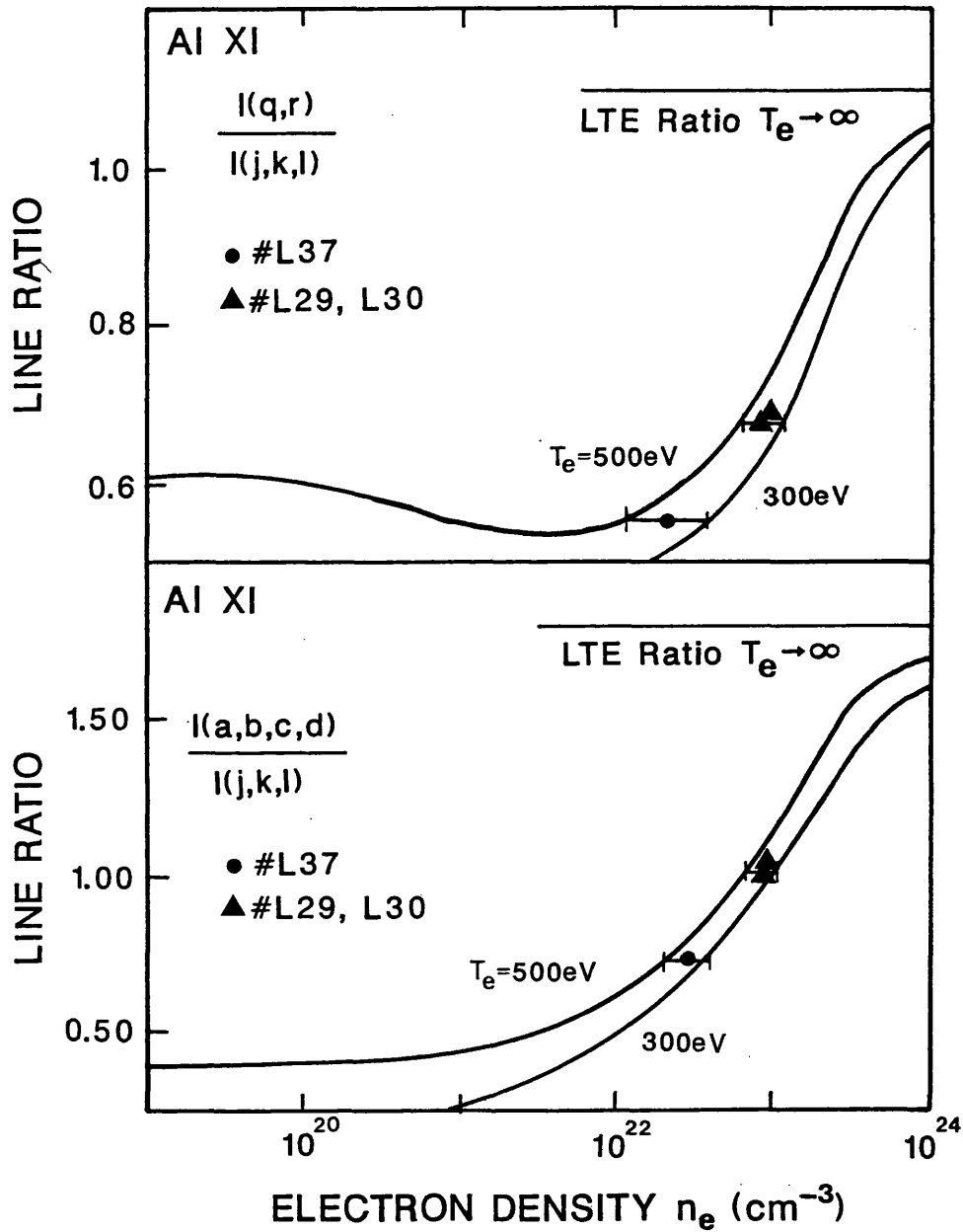


Figure 6.21 Density sensitive Al XI satellite line ratios. Solid curves are theoretical calculations of Jacobs and Blaha<sup>149</sup>, experimental data shown as points. Top graph is  $I(q, r)/I(j, k, l)$  ratio while bottom graph shows  $I(a, b, c, d)/I(j, k, l)$  ratio.

### Electron Temperature $T_e$ .

The  $2p^2\ ^1D_2$  transition is not affected by electron collisions until  $n_e=10^{24}\text{cm}^{-3}$  and can still be used as a temperature diagnostic if the Al XIII Lyman- $\alpha$  resonance line is optically thin. An estimate of  $T_e$  using the opacity calculations of Chapter 6.5 for the Lyman- $\alpha$  line is shown for the different target configurations in Figure 6.20. The electron temperature is estimated to vary between 600eV and 1100eV with error bars of  $\pm 100\text{eV}$ . A drop in the temperature is associated with increasing overcoat thickness and reduced thermal conduction.

### (b) Al XI Satellite lines.

Much of the previous section applies to the Al XI satellite lines, though inner-shell excitation is equal to electron capture in populating the  $1s2s(^1P)2p$  (q, r) levels, and dominant in the  $1s2p^2\ ^2S$  (m, n),  $1s2p^2\ ^2P$  (a-d) levels. At low electron densities these levels are collisionally uncoupled and inner-shell excitation populates the upper levels. This process becomes greatly diminished as the density (and collisional coupling) increases and the levels are populated by electron collisions from the autoionizing states. Study of the autoionization rates  $\Gamma_j$  in Table 6.1, show that the levels with low values will be populated mostly by electron collisions. Thus, the (a-d) lines will be affected most followed by (q, r) and (m, n). The (m, n) lines are less useful here because they are unresolved from the  $^3P_1$  intercombination line.

Figure 6.21 has the Li-like Al XI satellites groups (q, r) and (a-d), respectively, plotted against the (j, k, l) group as a function of density after Jacobs and Blaha<sup>149</sup>. The levels (j, k, l) and (s, t) have the highest autoionization rates and are unaffected by electron collisions until  $n_e=10^{24}\text{cm}^{-3}$ . The experimental data confirm the rise in density of the buried Aluminium layer with increasing top coat thickness. The measured peak density  $n_e=7\rightarrow 8\times 10^{22}\text{cm}^{-3}$  appears to be slightly lower than the Lyman- $\alpha$  satellite observations.

## 6.7 Discussion and Conclusions.

### 6.7.1 Comparison of Density Measurements.

It is interesting to compare the density measurements (Figure 6.22) from the satellite line intensities with those from the Stark broadened  $1s^2\ ^1S_0-1s3p\ ^1P_1$  line<sup>125</sup>. This data was recorded simultaneously with the flat miniature spectrometer. Fairly good agreement is achieved showing the general trend of increasing density, well above the critical density  $n_c$ , with overcoat thickness. The electron density values of the satellite intensity ratios are generally higher, the Lyman- $\alpha$  exhibiting the highest overall density. The shaded area shows the theoretical predictions of the 1-dimensional MEDUSA hydrodynamic code for the layered target geometry and laser irradiation conditions; the top and bottom surfaces of the shading represent the inside and outside surfaces, respectively, of the buried Aluminium layer.

Higher density measurements from the Lyman- $\alpha$  satellites is not unexpected. They are generated through dielectronic recombination with the Hydrogenic ion, which is noted by Boiko et al<sup>137</sup> to be produced in hotter, denser plasma conditions than the Helium like ion stage. Audebert et al<sup>139</sup> have studied the same lines with a space resolving flat spectrometer. They observed the Aluminium Lyman-  $\alpha$  satellites to be emitted closer to the target surface than the He-like resonance lines. They found lower density measurements inferred from the Stark broadening of the He-like  $1s^2$ - $1s4p$  line.

The conclusion that can be drawn from this, in the absence of space-resolved measurements, is that the the satellite lines are being emitted from a dense plasma region spatially different from the He-like ions. It is worth noting that switching to shorter  $3\omega$   $0.35\mu\text{m}$  laser light target irradiation generates higher densities than the  $2\omega$   $0.52\mu\text{m}$  wavelength for similar overcoat thicknesses. This indicates better coupling of the laser energy to the target, which is well known. This also has been observed by Audebert et al<sup>139</sup>, who note an increase in the density sensitive satellite line ratios when the laser light is reduced from  $1.06\mu\text{m}$  to  $0.27\mu\text{m}$ . Further information of the spatial profile and evolution of the satellite lines is needed during the laser pulse.

### 6.7.2 Observed Anomalous Spectral Features.

Additional lines were observed adjacent to the  $1s2p$   $^1P_1$ - $2p^2$   $^1D_2$  and the  $1s2s$   $^1S_0$  -  $2s2p$   $^1P_1$  satellite lines to the Lyman- $\alpha$  which could not be interpreted from the papers of Boiko et al<sup>130</sup> or Vainshtein and Safronova<sup>127</sup>. These lines were similar to features observed by Audebert et al<sup>139</sup>, except the lines here were broader and more intense.

Very recent work by Bañon et al<sup>141,142</sup> (1989) interprets the anomalous results of Audebert as due to Stark mixing of the states resulting in the de-population of the allowed dielectronic upper levels and the appearance of forbidden Stark lines (Figure 6.23). These effects become strong above  $n_e=10^{22}\text{cm}^{-3}$  and are readily observed on the spectra of Figures 6.11 and 6.12 in several ways:

- $1s2p$   $^1P_1$ - $2p^2$   $^1D_2$  and the  $1s2s$   $^1S_0$  -  $2s2p$   $^1P_1$  satellite lines become depopulated and have reduced intensity due to Stark mixing. Table 6.9 shows that this strongly decreases the  $1s2s$   $^1S_0$  -  $2s2p$   $^1P_1$  line intensity.
- Low intensity spectral lines are observed to the long wavelength side of the transition  $1s2s$   $^1S_0$  -  $2s2p$   $^1P_1$  and the short wavelength side of  $1s2p$   $^1P_1$ - $2p^2$   $^1D_2$ . The latter although not individually fitted in the analysis can be seen in Figure 6.12.
- Stark mixing induces centroid shifts in the wavelength separation  $\Delta\lambda$  of the above two lines such that  $\Delta\lambda$  increases with density. Thus the discrepancy in Table 6.3,  $\Delta\lambda=47.2\text{m}\text{\AA}$ , may be interpreted as due to density  $n_e\sim 3\times 10^{22}\text{cm}^{-3}$ .

Bañon et al report that Stark mixing effects are likely to be observed for atomic number  $Z<17$  and for Li-like satellite lines.

## Electron Density Measurements from Satellite Line Intensities and Stark Broadening

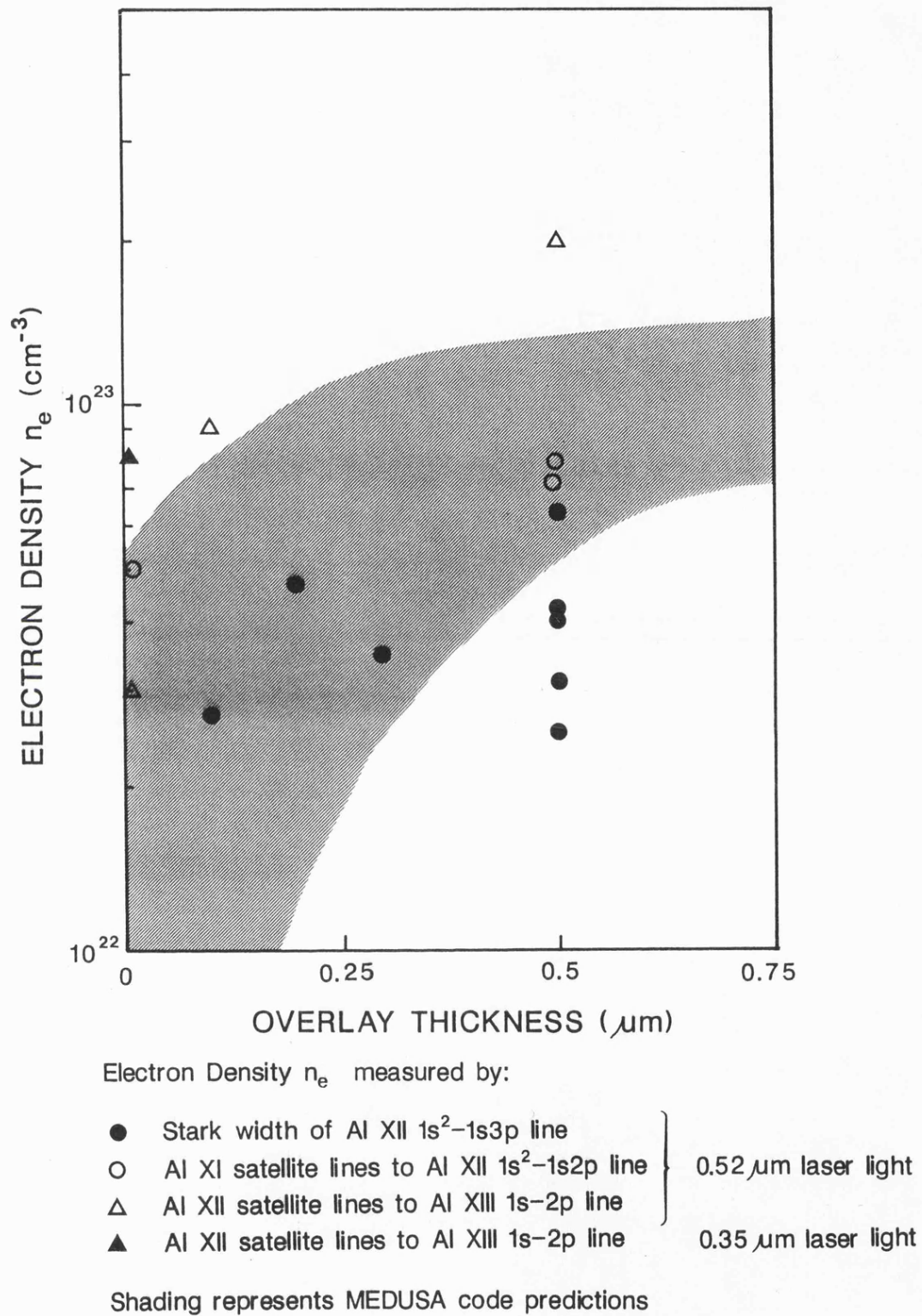


Figure 6.22 Density measurements from Al XI and Al XII satellite line intensities compared with the Stark broadened line widths of the He-like  $1s^2\ ^1S_0-1s3p\ ^1P_1$  resonance line.

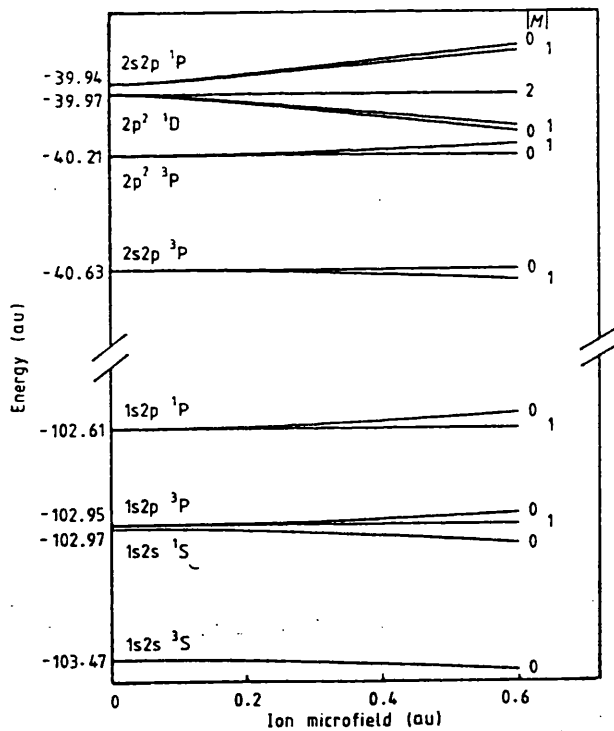
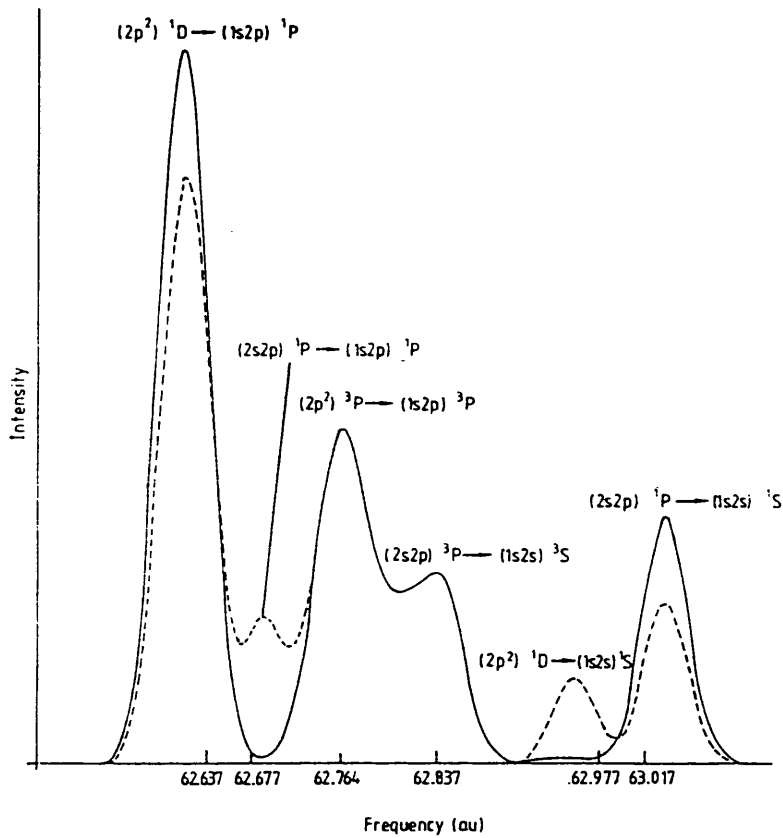


Figure 6.23 Predicted satellite spectrum (top) of the Al XIII Lyman- $\alpha$   $n=2$  dielectronic satellites at an electron density of  $2.5 \times 10^{22} \text{ cm}^{-3}$  and electron temperature  $T_e = 600 \text{ eV}$  (after Bañon et al<sup>141,142</sup>). Broken curve indicates oscillator strength mixing effect; full curve is without Stark mixing. Note that the wavelength scale is increasing from right to left.

Stark splitting of doubly excited  $2l2l'$  and singly excited  $1s2l$  energy levels of the Aluminium He-like ion (bottom).

Finally, the density sensitive satellite lines observed in this work are much higher than the observed or calculated spectra of Audebert et al or Bañon et al, indicating much higher densities ( $n_e > 3 \times 10^{22} \text{cm}^{-3}$ ). The line widths are also considerably broader. Bañon et al<sup>141</sup> report that the relative widths due to ion, electron and Doppler broadening for the conditions  $n_e = 3 \times 10^{22} \text{cm}^{-3}$  and  $T_e = 600 \text{eV}$  are 30%: 15%: 55%, respectively. Assuming that they mean  $T_e = T_i = 600 \text{eV}$ , then the same ratio for the  $1s2p \ ^1P_1 - 2p^2 \ ^1D_2$  line is 1.44: 0.72: 2.65 mÅ. The lines observed in the buried layer target Figure 6.12 have a more Lorentzian shape which reflects the lower ion temperatures  $T_i < 350 \text{eV}$  (2.0 mÅ) and greater Stark broadening. The measured width of shot #L19 is in fact 4.7 mÅ, giving an estimated Stark component of 2.7 mÅ after the instrumental width is subtracted.

### 6.7.3 Instrumentation and Future Experiments.

#### Target Design.

Some changes can be made to the planar target design to confirm the opacity calculations. By varying the thickness of the Al diagnostic layer, one in principle should be able to measure variations in the Lyman- $\alpha$  intensity ratio. In addition, the use of micro-dot spectroscopy would simplify the geometrical treatment of opacity.

#### Spectrometer Optimisation.

The spectrometer worked extremely well and was able to show changes in the observed spectral features from shot to shot. This was primarily due to the combination of high instrumental resolving power, signal throughput and optimisation of the S/N ratio. Some of the advantages this geometry offers cannot be matched by the flat miniature spectrometer design and may be summarised as follows:

- High resolving power which is independent of the plasma geometry. Large micro-balloon targets  $\sim \text{Ø}500 \rightarrow 1000 \mu\text{m}$  could be observed with the Johann spectrometer with no reduction in the instrumental resolving power.
- Absolute wavelength calibration of  $\lambda/\delta\lambda \sim 2000$  from absolute angle measurements. Complicated high Z L-shell spectra could be studied and identified as possible line coincidences for resonant photo-pumped laser schemes.
- Multiple exposures can be time-integrated with no loss in spectral resolution. Very weak line features could be studied by this method.
- High instrument dispersion, for example the plate factor is  $16 \text{mÅ/mm}$  for  $7.17 \rightarrow 7.27 \text{Å}$  with  $R=300 \text{mm}$ , may be varied without changing the waveband and resolving power. The crystal radius is a free parameter which can be chosen to match the instrument dispersion to a streak camera (for time-resolved spectra) or a CCD detector<sup>102</sup>.
- Spatial resolution of the plasma can be achieved in the direction perpendicular to the plane of dispersion by placing a slit ( $\sim 10 \rightarrow 20 \mu\text{m}$  wide) between the crystal and the plasma. The magnification can be adjusted to suit the target geometry.

### **Future Experiments.**

It is clear that the instrument is limited by the use of film emulsion to record the spectra. A priority would be to convert the spectrometer to work with a linear, digital electronic system, eg an optimised CCD detector system.

Secondly, the lack of time-resolved data gives an average record of the plasma conditions. Observation of appropriate emission lines, coincident with the peak plasma density and temperature, may give a picture weighted towards the peak plasma conditions but is not a substitute for direct time resolution with a streak camera. A repeat experiment with time-resolved density measurements would be extremely useful.

The Johann spectrometer would be ideal for studying the line widths of the H-like  $1s-np$  and He-like  $1s^2-1snp$  resonance lines where  $n \geq 3$ . In fact, with a waveband  $\Delta\lambda/\lambda \sim 0.1$ , coverage of the He-like Al  $1s^2-1s3p$  line and satellites and the H-like Al Al  $1s2p$  line plus satellites ( $6.635 \rightarrow 7.27\text{\AA}$ ) would allow simultaneous measurements of density by the same instrument.

# Chapter 7 Fast Ion Beam Spectroscopy.

	Introduction.	207
7.1	Introduction to Fast Ion Beam Spectroscopy.	207
	7.1.1 General Description.	207
	7.1.2 Beam Ionization and Excitation.	208
	7.1.3 Ion Charge State Distribution.	209
7.2	Lamb Shift in the 1s Ground State of Hydrogenic Ions.	209
7.3	Axial Observation.	213
7.4	Experimental Description and Method.	213
	7.4.1 Instrumentation.	214
	7.4.2 Instrument Alignment to Source.	214
	7.4.3 MWPC Detector for Experiment.	215
7.5	Silicon XIII Axial Observation.	217
	7.5.1 Experimental Details.	217
	7.5.2 Results.	218
7.6	Neon X Axial Observation.	224
	7.6.1 Experimental Details.	224
	7.6.2 Results.	224
7.7	Conclusions and Future Experiments.	225
	7.7.1 Discussion on Present Experiment.	225
	7.7.2 Application to Different Beam-Target Interactions.	228
	7.7.3 Instrumentation and Techniques for Future Experiments.	229

## Introduction.

This final experimental chapter describes the work to measure the intrinsic line-broadening mechanism of the Oxford Folded Tandem accelerator by recording high resolution spectra of the fast ion beam. The areas discussed are:

- Brief introduction to fast ion beam spectroscopy.
- The use of this x-ray source to test Quantum Electrodynamics (QED), specifically the Lamb shift in the 1s ground state of Hydrogenic ions.
- The technique of axial observation of the source.
- A description of the experiment and method.
- The Silicon XIII observation.
- The Neon X observation.
- Conclusions and future experiments.

For a more complete introduction, the reader is guided to a recent review by Martinson<sup>152</sup> and the references therein. Other useful references are "Fast Ion Beam Spectroscopy" edited by Knystautas and Drouin<sup>153</sup>, "The Physics of Highly Ionised Atoms" edited by Silver and Peacock<sup>154</sup> and "Atomic Spectroscopy and Highly Ionised Atoms" edited by Berry, Dunford and Young<sup>155</sup>. These give a good overview of current research in experiment and theory.

## 7.1 Introduction to Fast Ion Beam Spectroscopy.

### 7.1.1 General Description.

Fast ion beams and their interaction with matter result in the emission of electro-magnetic radiation from the visible to the x-ray band, this being of great importance in the field of atomic spectroscopy. The fast ion beam accelerator can produce virtually any element, accelerate it to a chosen energy in a particular state of ionization. The ion velocity is usually known to better than 0.1% and the generated mono-energetic ions are of high spectral purity, both chemically and isotopically. This gives the experimental spectroscopist the opportunity to study a chosen transition from a particular element which is free from various effects normally attributed to the source. For example in laser produced plasmas, the plasma properties such as opacity, high thermal temperature, Stark broadening (at high density) as well as the steep gradients in space and time associated with each of these, can have a dominant effect on the line radiation. Similarly with Tokamaks, where there can be high thermal temperature and plasma rotation effects, the plasma can also contain varying degrees of impurity.

The ion beam particle densities are typically  $10^6\text{cm}^{-3}$ , considerably lower than in Tokamak discharges where  $n_e \sim 10^{13} \rightarrow 10^{14}\text{cm}^{-3}$ . As a result, the photo-emission from beam-foil sources is considerably lower than other sources, but has the advantage of being a continuous source as opposed to pulses lasting seconds for Tokamaks and nanoseconds or shorter for laser produced plasmas.

### 7.1.2 Beam Ionization and Excitation.

The ionization of the beam is produced by the interaction of the fast moving beam ions with the stationary target material, usually by passing the particle beam through a thin foil made of Carbon or Beryllium. The process of collisional ionization is dependent on the ion beam energy; generally, increasing the ion beam energy results in higher stages of ionization. The Oxford Folded Tandem accelerator for example, where the spectra in this chapter were measured, works by the following principle.

A sputtering source produces negative ions which are accelerated across a potential difference (up to 10MVolts), stripped in a foil to become positive and are subsequently re-accelerated back across the potential difference. The ion beam can be stripped to higher ionization stages by passing through further foils using this process of collisional ionization. The kinetic energy of the ions then depends on the potential difference and the ion charge. A pure ion beam of the preferred kinetic energy is selected by means of mass-analysis, generally in a bending magnet. The ion beam is finally excited at the point of observation by passing through a foil or gas target.

Inner-shell excitation, charge-exchange recombination and radiative recombination are the main excitation processes. Dielectronic recombination, which results in satellite lines observed in both astrophysical and laboratory plasmas, is not a strong excitation mechanism here. For medium  $Z \geq 8$  (Oxygen) in a H-, He- or Li-like ion stage, if the excited ion stabilises by radiative decays to the ground state this results in photo-emission in the soft x-ray band below 25Å. The x-radiation is Doppler shifted, depending on the viewing geometry, since the beam velocity can be  $0.05 \rightarrow 0.2c$  (the speed of light). The first order Doppler effects disappear if the radiation is observed perpendicularly to the ion beam direction. However, second order Doppler broadening of the spectral lines is present due to the spread in ion velocities and the angular divergence of the ion beam. (This is described in more detail in section 7.3).

#### Excited State Lifetime Measurements.

A standard technique for measuring the lifetime of some excited states has been developed because the regions of the beam excitation and decay are spatially separated. Since the ions are moving at a fraction of the speed of light, by viewing perpendicularly the intensity of long-lived states, for example  $1s^2 \ ^1S_0 - 1s2p \ ^3P_2$  which is a magnetic quadrupole decay, is observed to reduce exponentially as a function of distance downstream from the foil position. This can therefore give the lifetime to a high degree of accuracy and allow comparison with theory. The experiments have to be performed carefully and problems like cascade re-population of the upper level and line-blending can cause difficulties in interpretation, see Pinnington<sup>156</sup>.

### 7.1.3 Ion Charge State Distribution.

It is important when deciding upon the programme of observation to know the equilibrium charge state distribution after foil excitation. The calculations at the Nuclear Physics Department, Oxford University, were based on the Betz formula and the semi-empirical formula by Ziegler, extrapolated to the energies of interest. They relied on the assumption that the beam charge states settle into equilibrium during passage through the foil. This condition depends primarily on the beam energy, but also on the foil thickness. Although the accuracy of the method is uncertain, it can be used as a rough guide for the ion state distribution<sup>157</sup>. The equilibrium charge state distribution has also been calculated and measured by various authors. A simple formula, given by To and Drouin<sup>158</sup>, can quickly determine the average charge  $q$  of the beam after foil excitation. It can be written as:

$$q = Z \left[ 1 - \exp\left\{\frac{-v Z - 0.45}{v'}\right\} \right] \quad (7.1)$$

where  $Z$  is the atomic number of the ion beam,  $v$  is the ion beam velocity and  $v' = 3.6 \times 10^8$  cm/s. The dependence of the final state of ionization of the beam with energy and atomic number is clearly shown.

This has been demonstrated in the emitted spectra, see Stöckli and Richard<sup>159</sup> for example, where the He-like satellite structure to the main H-like resonance lines is reduced with increasing ion beam energy. The two methods for determining the charge state distribution outlined above, give broadly similar results for the experiments. The ionization of the beam may also be decreased depending on the conditions. This can happen when a fully stripped ion beam gains one or more electrons by a process of electron capture as the beam exits the foil surface.

### 7.2 Lamb Shifts in the 1s Ground State of Hydrogenic Ions.

The first experimental measurements of the "Lamb shift" were performed by Lamb and Retherford<sup>160,162</sup> in 1947 on the  $^2S_{1/2} - ^2P_{1/2}$  interval in Hydrogen. Dirac theory predicts that the levels are degenerate because they have the same  $j=1/2$  value. However, the subtle effects of QED break this degeneracy. The experiment indicated that the  $^2S_{1/2}$  level is displaced higher than the  $^2P_{1/2}$  level (see Figure 8.1, Chapter 8), thus an electron transition between them produces a radiative decay in the radio-frequency region at 1058MHz.

Since we are dealing with the simplest atomic system consisting of a nucleus and a single bound electron, the energy levels can be calculated extremely accurately. They are determined from the sum of the Dirac energy, the correction for the reduced mass of the nucleus and the Lamb shift. The latter is the collection of various smaller effects, namely the finite size of the nucleus, relativistic and QED effects. Consequently, by measuring the transition energies accurately, the theoretical electron energy levels can be verified experimentally.

This effect is present in all Hydrogenic ions and its magnitude scales rapidly with nuclear charge, approximately as  $Z^4/n^3$ ,  $n$  being the principal quantum number. Thus, the Lamb shift associated with the  $n=1$  level is eight times greater than the  $n=2$  level, and so the ground state measurement is a more sensitive indication of QED effects. The Lamb shift scaling with  $Z$  can be demonstrated by taking it as a fraction of the  $1s\ ^1S_{1/2} - 2p\ ^2P_{1/2}$  transition energy. Using the results tabulated by Mohr<sup>27</sup>, the fraction for Ne ( $Z=10$ ), Cl ( $Z=17$ ) and Zr ( $Z=40$ ) is 146ppm, 318ppm and 1015ppm, respectively. The trend is therefore to make experimental measurements at a higher nuclear charge in order to test the theories more precisely. This is particularly important since the calculations by Mohr, above, when compared with Erickson<sup>162</sup> show a small divergence with increasing  $Z$  which is typically at the 1% level for Argon.

Similar contributions to the electron energies are present in He-like ions, but these are more complicated to determine due to electron correlation effects. Recent results have been presented for various theoretical models by Drake<sup>163</sup> and Indelicato<sup>164</sup>, and references therein.

### **Experiments.**

To date, most  $1s$  ground state Lamb shift experiments in beam-foil spectroscopy have viewed the source perpendicularly to the ion beam direction. This technique has been used extensively to make precise wavelength measurements for the  $1s-2p$  Hydrogenic resonance lines, as well as the  $1s^2-1s2p$  He-like ion resonance lines, from medium to high  $Z$  atomic numbers. The most recent state of the art experiments have been measurements of Cl XVII  $1s-2p$  transitions by Richard et al<sup>78</sup> using a Chlorine beam with Carbon foil excitation. Deslattes et al<sup>165</sup> have made  $1s$  measurements at the 15% tolerance for the same ion by reducing the satellite lines caused by the presence of spectator electrons. This method uses electron capture of the bare Chlorine beam in a Helium gas target. Similar experiments have been performed in a gas "recoil-ion" target, discussed in detail in section 7.7, for  $1s$  measurements at the 1.5% tolerance of ArXVIII  $1s-2p$  levels by Beyer et al<sup>166</sup>. Precision wavelength measurements at the 12ppm level, corresponding to 3.3% accuracy for the  $1s$  Lamb shift, have been reported for the He-like Ar XVII  $1s^2\ ^1S_0 - 2s2p\ ^3P_{1,2},\ ^1P_1$  transitions by Deslattes et al<sup>167</sup>.

Generally, these measurements have been achieved using high resolution Johann spectrometers to measure the line radiation relative to  $Z+1$   $K\alpha$  secondary reference standards. New methods for improving the quality of the spectra are extremely relevant to measurements of Lamb shift in high  $Z$  ions.

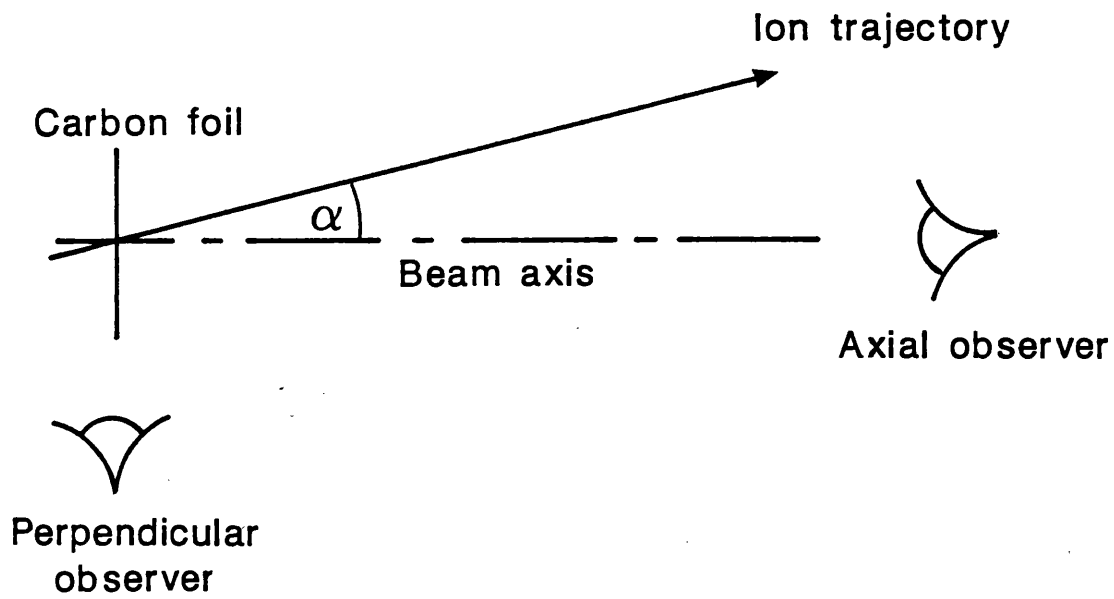


Figure 7.1 Schematic showing beam-foil geometry.

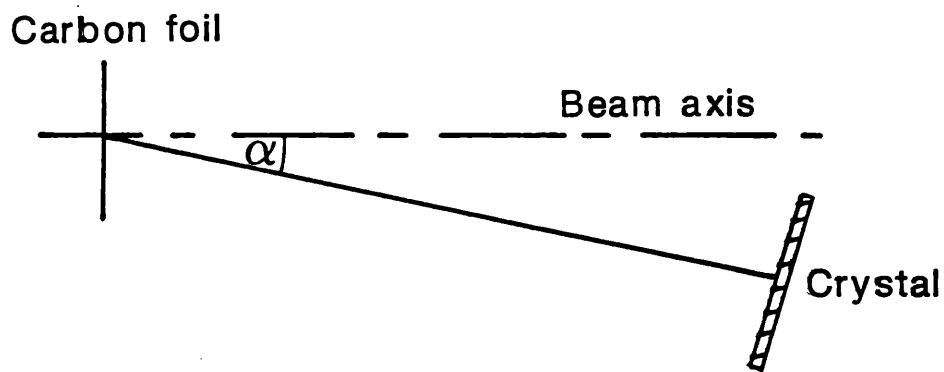
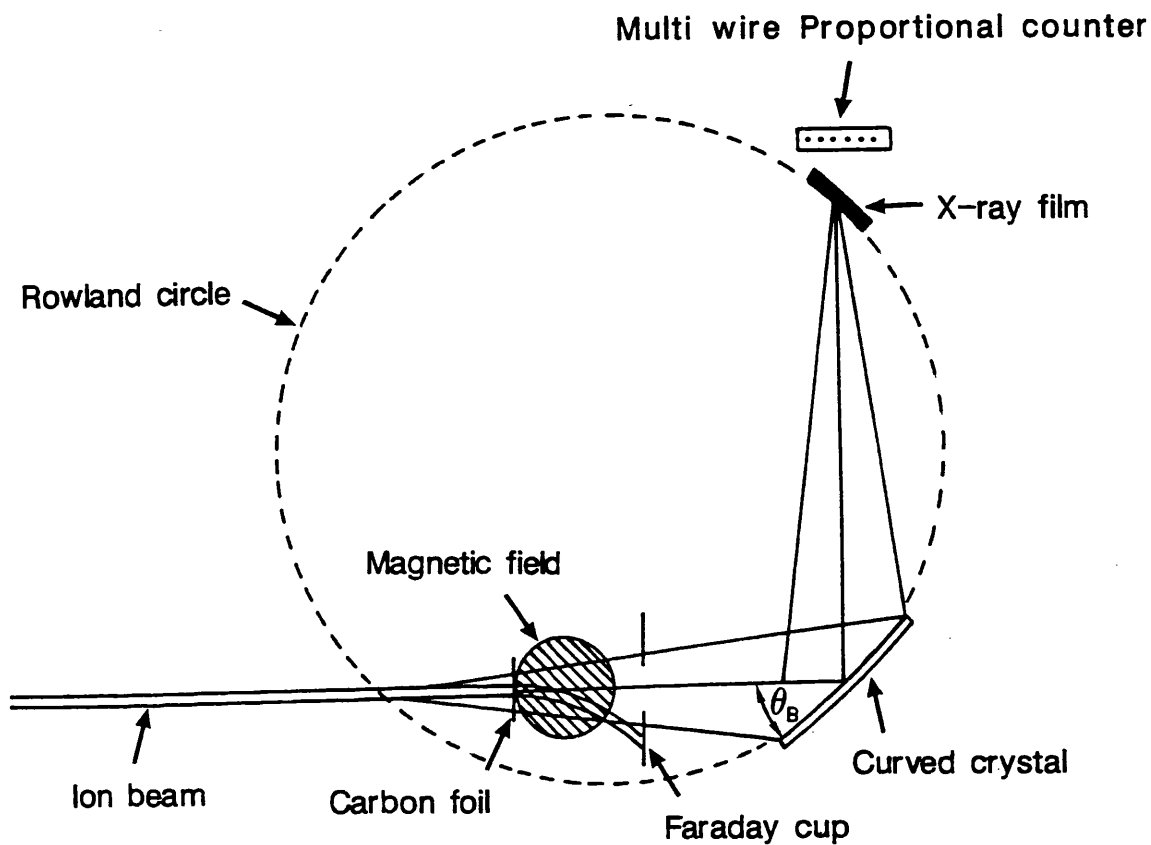


Figure 7.2 Side view showing instrument small angle,  $\alpha=1.9^\circ$ , departure from purely axial viewing.



Schematic diagram of experimental apparatus.

Figure 7.3 The curved crystal spectrometer is shown relative to the ion beam/Carbon foil. The foil is placed within the Rowland circle to increase the waveband. The ion beam is deflected onto a Faraday cup after foil excitation. A MWPC detector records the diffracted x-ray beam to check the spectrometer alignment and signal count rate before replacement with the film holder.

### 7.3 Axial Observation.

It was first suggested by various authors including Désevelles<sup>168</sup>, that for observation along the ion beam axis, the Doppler broadening of spectral lines was mainly due to the spread in the ion beam velocity, while viewing perpendicularly the spectral resolution was due to the ion beam divergence. Figure 7.1 shows the beam-foil geometry.

If an ion moving with velocity  $\beta c$ , where  $c$  is the speed of light, along the beam axis emits electro-magnetic radiation of wavelength  $\lambda_0$ , then Special Relativity predicts that the doppler shifted wavelength seen by an observer at an angle  $\alpha$  to the beam direction can be written as:

$$\lambda' = \gamma \lambda_0 (1 - \beta \cos \alpha) \quad (7.2)$$

where  $\gamma = (1 - \beta^2)^{-1/2}$ . The line width due to the spread in ion velocity  $\Delta\beta c$  and the ion beam divergence  $\Delta\alpha$  is:

$$\Delta\lambda = \left[ \frac{\delta\lambda'}{\delta\beta} \right] \Delta\beta + \left[ \frac{\delta\lambda'}{\delta\alpha} \right] \Delta\alpha \quad (7.3)$$

Then, for typical conditions on the Oxford Folded Tandem accelerator with  $\Delta\beta \sim 10^{-4}$ ,  $\beta \sim 0.06$ ,  $\Delta\alpha \sim 5 \times 10^{-3}$ , the predicted spectral resolution from the two observation positions is calculated to be:

$$\frac{\Delta\lambda}{\lambda_0} = 3.0 \times 10^{-4} \quad (\text{Perpendicular, } \alpha = 90^\circ) \quad (7.4)$$

$$\frac{\Delta\lambda}{\lambda_0} = 1.0 \times 10^{-4} \quad (\text{Axial, } \alpha = 0^\circ) \quad (7.5)$$

and clearly shows an improvement of a factor of three for axial observation. The value for  $\Delta\beta$  depends mainly on fluctuations of the Tandem terminal voltage as well as beam collimation through the  $90^\circ$  bending magnets immediately after acceleration. The beam divergence  $\Delta\alpha$  can be measured from the beam guide upstream from the foil target and the burn spot size on the foil. Additional contributions, referred to as straggling, due to the stripping process in the foil are negligible in comparison with the accelerator characteristics.

The result of (7.5) above is independent of the precise value of  $\alpha$ , provided  $\alpha$  remains small. (If  $\alpha = 5^\circ$ , the spectral resolution is reduced by about 20%). For experimental reasons, the minimum viewing angle possible was  $1.9^\circ$  to the beam axis. Figure 7.2 shows the side view of the experimental layout.

### 7.4 Experimental Description and Method.

The experiments were carried out on the Oxford Folded Tandem accelerator in late 1986, early 1987, and could equally well have been tried on other suitable particle accelerators.

Two experiments using a Silicon ( $Z=14$ ) and Neon ( $Z=10$ ) beam, successfully demonstrated the technique of axial observation:

- (a) The He-like resonance and intercombination lines of  $\text{Si}^{12+}$  were observed together with many satellite transitions from Li-like and Be-like charge states using a PET (002) crystal.
- (b) The  $\text{Ne}^{9+}$  Lyman- $\alpha$  doublet was observed with the best resolution to date, from any source, using a KAP (002) crystal.

The results of (a) and (b) are discussed in sections 7.5 and 7.6, respectively.

#### **7.4.1 Instrumentation.**

The experimental setup, see Figure 7.3, indicates that the ion beam, having passed through the Carbon foil target, was deflected by bending magnets onto the Faraday cup to avoid damage to the crystal. Vertical slits formed an aperture to pass only the x-radiation, emitted isotropically after the foil. This also reduced the background noise and x-ray fluorescence from the beam dump. Most of the transitions from the short-lived states occur within the first few millimeters after the foil. The instrument was set below the horizontal axis of the beam to allow undeflected lower charge states to pass above.

Waveband and resolving power were the main criteria which dictated the choice of the instrument parameters. The beam diameter of  $\text{\O}4\text{mm}$  indicated that the source, the Carbon foil, would have to be placed inside the Rowland circle to maximise the wavelength region. The crystal to source separation however, was limited to 600mm due to the mechanical restriction of the instrument vacuum chamber and the bending magnets. The crystal radius of curvature  $R$ , therefore, was chosen at between 1100mm and 1300mm to give adequate bandpass, see Chapter 2, while still retaining high instrumental resolving power. The generated optical focus in the active crystal aperture of  $20 \times 25 \text{mm}^2$  was better than  $\lambda/\Delta\lambda \sim 60000$ . The Rowland width and height aberrations were  $\lambda/\Delta\lambda \sim 30000$  and  $\lambda/\Delta\lambda \sim 14000$  respectively. The dominant instrumental broadening was therefore the rocking curve of the crystal used;  $\lambda/\Delta\lambda = 6000$  for PET (002)<sup>11</sup> at  $6.2\text{\AA}$ ,  $\lambda/\Delta\lambda = 9000$  for KAP (002), (Burek<sup>12</sup>) at  $11.4\text{\AA}$ .

#### **7.4.2 Instrument Alignment to Source.**

The crystal was focused and the Bragg angles set, as described in Chapter 3, taking account of the blue Doppler shifted wavelengths from equation (7.1). This was performed on a flat metrological surface in the beam hall a few meters from the experimental site. This ensured that temperature variations, monitored at all times, between aligning and running the instrument were minimised.

The instrument was installed on the beam line and the following optical procedures performed:

- A telescope looking axially along the beam was used to align the crystal pole onto the beam axis.
- A second alignment was needed to place the source at the correct position in relation to the crystal. This was achieved by shining a light down the beam guide, towards the crystal, from outside the Rowland circle. The instrument bellows, used for fine-tuning the source to the correct Bragg angle, were then adjusted while observing the reflected light from the crystal surface through the aperture on the film back. The correct bellows angle was found when the bright reflected vertical image was obscured by the vertical cross-wire of the film back.
- Using the same optical technique, the vacuum tube was rotated so that the crystal pole was inclined at the angle  $\alpha$  from the vertical axis. This could be observed visibly when the reflected light was in the mid-plane of the crystal and the horizontal cross-wire of the film back.

The measured spectra demonstrated that the optical alignment procedures were very accurate, setting the source to the correct angular position to better than 1 minute of arc. An additional method, described in the next paragraph, was employed to verify the alignment.

#### **7.4.3 MWPC Detector for Experiment.**

It was decided that useful information about the source, in particular the signal intensity and background noise, could be measured by using a 1-dimensional position sensitive MWPC detector to look at the diffracted radiation. The detector was designed at the Brookhaven Laboratory (Gordon<sup>169</sup>) and had active region dimensions of 19x10x1.8mm<sup>3</sup> (WxHxD). It was a through-flow design, running at atmospheric pressure, and used either P10 (Argon/Methane, 10% Methane) or a Xenon/Carbon Dioxide (10% CO<sub>2</sub>) gas mixture. The latter was preferred for its higher absorption characteristic, but its use was expensive in this detector type.

The detector window was unsupported 6 $\mu$ m Mylar coated with a conducting graphite layer. The detector was bolted externally to the vacuum chamber via an apertured bulkhead. The vacuum chamber pressure was maintained by 2 $\mu$ m Mylar supported from atmospheric pressure on a stainless steel mesh, with 50% optical transmission. The air gap, between the vacuum and detector windows, was flushed with Helium gas. A Co<sup>57</sup> source producing Fe K-shell x-rays was placed here to calibrate the energy scale of the detector.

The detector was run at a high voltage in the region of 1050→1150 Volts. Figure 7.3 shows the detector perpendicular to the diffracted x-ray beam, just outside the Rowland circle. The spatial resolution of the detector  $\Delta x \sim 500\mu\text{m}$  was insufficient to realise the high resolving power of the spectrometer and was further reduced by the defocusing errors due to the detector not lying tangentially to the Rowland circle. However, it was adequate to distinguish line features. Figure 7.4 shows the detector output where the Silicon XIII

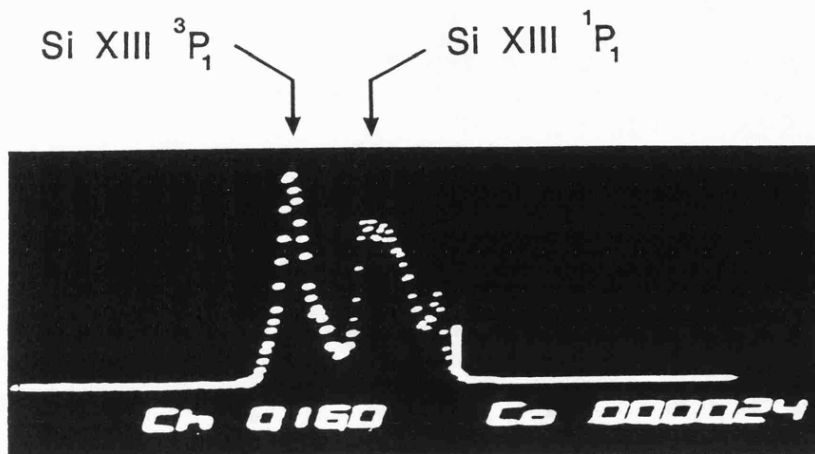


Figure 7.4(a) Position readout of MWPC detector for Si XIII experiment. Indicated lines are the Si XIII resonance and intercombination transitions. This should be compared with the final spectrum of Figure 7.5.

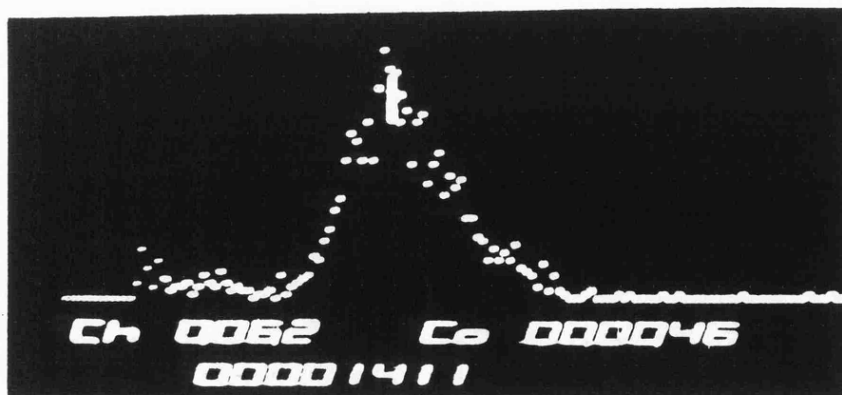


Figure 7.4(b) Pulse height spectrum of Si XIII  $1s^2-1s2p$  transitions. The spectrum is calibrated against a  $\text{Co}^{57}$  source producing Fe K-shell x-rays at  $\sim 1.94\text{\AA}$ , mean channel position 203. Mean position of observed x-rays at channel 62 indicates radiation at  $\sim 6.4\text{\AA}$ .

resonance and intercombination lines are resolved. This diagram should be compared with the final result of Figure 7.5 in the next section. Figure 7.4(b) is a pulse height spectrum for the Si XIII experiment.

The bellows, aligning the spectrometer to the source, were adjusted in small incremental steps and the x-ray signal rate was measured in each position. The spectrometer alignment was then set at the position giving the maximum signal rate. This confirmed the previous alignment procedures. It also provided further invaluable data using the detector energy resolution  $\Delta E/E \sim 0.35$ . The signal strength could be measured, sometimes as low as 0.2 counts/sec for the Neon X experiment, and other background noise sources determined. This technique diagnosed on one occasion that the strong x-radiation at 8.3Å was caused by Al K-shell fluorescence produced when the ion beam hit the crystal bending jig body during the failure of the power supply to the deflecting magnets.

When the experiment was determined to be working properly, the absolute signal intensity was calculated, taking account of the detector efficiency from the mesh, filters and gas absorption characteristics. The integration time for the x-ray film was estimated and the film holder substituted for the detector.

## 7.5 Silicon XIII Axial Observation

The axial viewing technique was first demonstrated with  $\text{Si}^{12+}$  where the strong  $1s^2 \ ^1S_0 - 1s2p \ ^1P_1$  and  $1s^2 \ ^1S_0 - 1s2p \ ^3P_{1,2}$  resonance and intercombination lines of the He-like ion were observed together with numerous satellite transitions in the immediate wavelength region.

### 7.5.1 Experimental Details.

The Folded Tandem operation used a Middleton sputterer with SiO to generate negatively charged Si ions which were then accelerated up to the anode. There it was foil- or gas-stripped to produce  $\text{Si}^{7+}$  or  $\text{Si}^{8+}$  and accelerated down the other side to a final energy of 63MeV. The Silicon beam was further ionised and excited in a  $10\mu\text{g}/\text{cm}^2$  Carbon foil. The observed x-radiation was produced as a result of the stabilisation of the ion by radiative decay, mostly a few millimetres after the foil. Since the ion beam was travelling towards the spectrometer, the radiation was Doppler shifted,  $\beta=0.0692$  after energy loss in the foil, to 6.2Å.

A PET (002) crystal ( $2d_{18}=8.7358\pm 0.0006\text{Å}$ ) was used at a radius  $R=1291\text{mm}$  and was estimated to give an instrumental resolving power of  $\lambda/\Delta\lambda=6000$ , limited by the crystal diffraction width. The Bragg angle  $\theta_0=45.22^\circ$  was set after correcting the lattice spacing for temperature; this remained fairly constant throughout the experiment at  $T=25.0\pm 0.5^\circ\text{C}$  and the lattice spacing was adjusted using the thermal expansion coefficient of  $(110\pm 10)\times 10^{-6}/\text{K}$  and refractive index value for the crystal material of  $\delta/\lambda^2=1.98\times 10^{-6}\text{Å}^{-2}$ . These PET crystal

parameters were either measured directly on the Leicester 2-crystal spectrometer by Hall<sup>11</sup> or calculated from this data by the present author.

### Signal Intensity.

The proportion of the Silicon beam in the charge state of interest after foil excitation, namely the He-like ion, was estimated from the equilibrium charge state distribution. For a 63MeV Si<sup>7+</sup> beam, the distribution of charge states Si<sup>8+</sup>: Si<sup>9+</sup>: Si<sup>10+</sup>: Si<sup>11+</sup>: Si<sup>12+</sup>: Si<sup>13+</sup>: Si<sup>14+</sup> was in the ratio 0.1%: 1.9%: 13.2%: 36.6%: 36.1%: 11.1%: 0.9%<sup>5</sup>. This agreed with a value of  $q=11.6$  for the mean charge using equation (7.1). The He-like ion stage was slightly more than a third of the beam, with the  $n=2$  quantum number states being the most intense in the series. The total signal intensity rate, through the instrument as measured by the gas detector, from the 400nA Silicon beam was about 320counts/sec and could be easily detected above the background noise. The exposure time for the film was 15 hours, giving a total integrated beam charge of 21.6mC.

### 7.5.2 Results.

The film was developed, the back emulsion removed, the data digitised and the film response calculated to convert the image optical density into x-ray photon density, in accordance with Chapter 4. Figure 7.5 shows the resultant spectrum of the two intense He-like resonance and intercombination lines. The spectrum can be looked at in two groups:

- The continuous blend of lines to the long wavelength side of the <sup>1</sup>P<sub>1</sub> resonance line is mainly due to  $n \geq 3$  Li-like, and to a lesser extent Be-like, satellite transitions.
- The better resolved lines around the <sup>3</sup>P<sub>1</sub> intercombination line are only due to  $n=2$  Li-like satellite transitions.

The observed resolving power was measured as  $\lambda/\Delta\lambda=4000 \pm 200$ , where the error results from the spread in the linewidth values from the two groups and uncertainty in unresolved satellites under the strongest lines. This group of lines have been studied previously from various x-ray sources including laboratory beam-foil experiments using perpendicular observation geometry<sup>170,171</sup>, beam-foil observations<sup>172</sup> at  $\alpha=45^\circ$ , solar coronal plasmas<sup>173,174</sup> and Tokamak plasmas as mentioned in Dunn et al<sup>175</sup> and Chapter 5. However, the combination of the high instrumental resolving power and the inherent reduced line broadening of the axial observation technique have given the best resolved line measurements to date.

### Wavelength Calibration.

Theoretical wavelengths were chosen for the resonance and intercombination lines from Drake<sup>26</sup> and were used to calibrate the spectrum. The quoted uncertainty for these wavelengths is  $\pm 2\mu\text{\AA}$  and although no measurements have been made for Silicon, good agreement has been reported for these transitions in Ar<sup>16+</sup> by Deslattes et al<sup>167</sup>. The

### Silicon XIII n=2 Spectrum

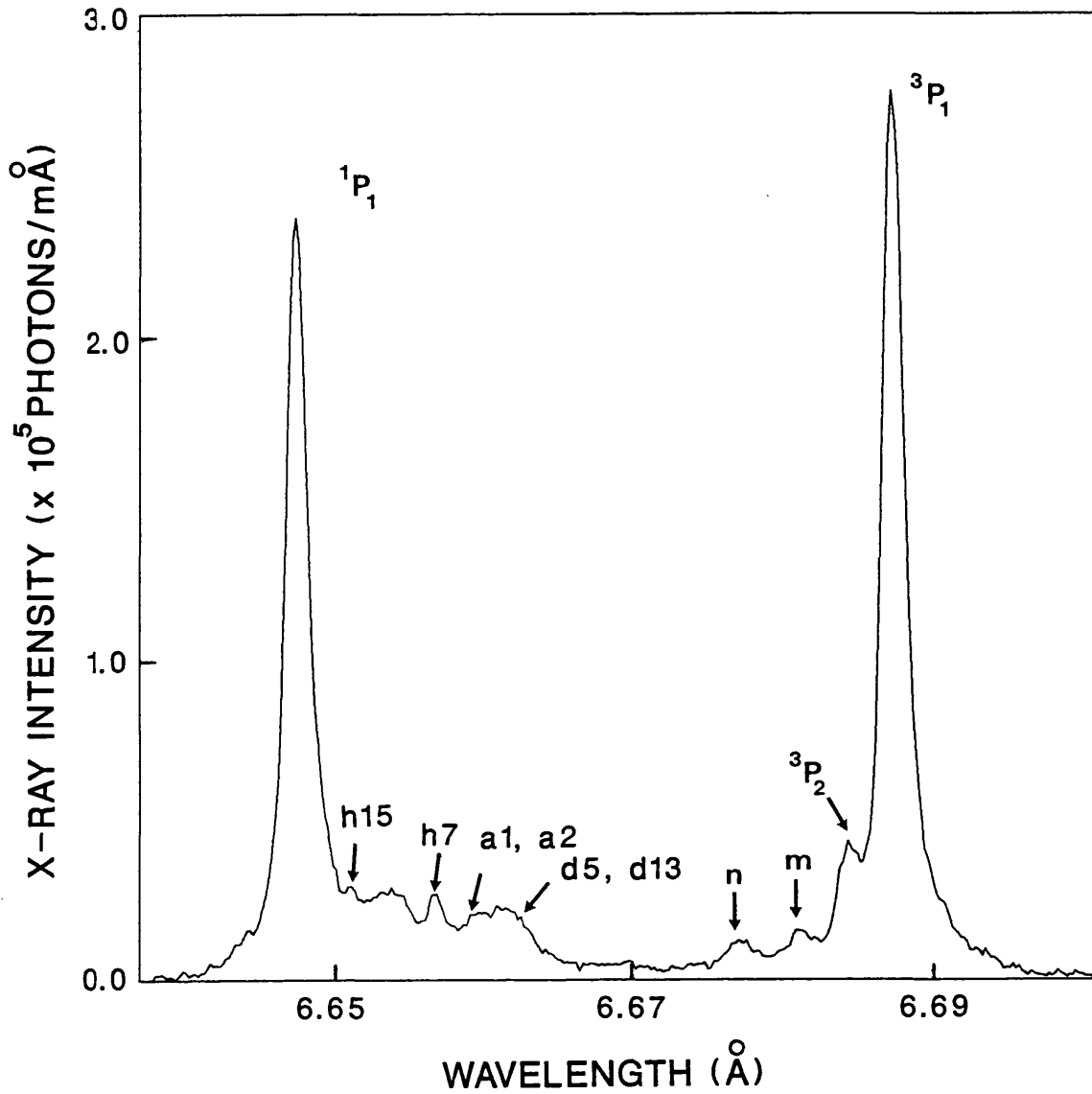


Figure 7.5 High resolution Si XIII n=2 spectrum reveals intense <sup>1</sup>P<sub>1</sub>, <sup>3</sup>P<sub>1</sub> transitions with adjacent Si XII and Si XI satellite structure. A tentative identification of the Si XIII <sup>3</sup>P<sub>2</sub> quadrupole transition is made for the next strongest line, to the short wavelength side of the <sup>3</sup>P<sub>1</sub> line. Lines are resolved to  $\lambda/\Delta\lambda=4000$ .  
 NB: Wavelengths have been corrected to the ion beam rest frame.

Table 7.1 Satellite Wavelengths and Identifications for the Silicon Spectrum

Label	Ion Stage	Identification	Observed Wavelength (This Work) Å	Observed Wavelength (Other Work) (Other Work) Å	Theoretical Wavelength Å
<sup>1</sup> P <sub>1</sub>	Si XIII	1s <sup>2</sup> 1S <sub>0</sub> - 1s2p <sup>1</sup> P <sub>1</sub>	6.6480 Calibration	6.647±0.001 [172] 6.648±0.0025 [170]	6.6480 [26] 6.6478 [172]
h15	Si XII Si XII	1s <sup>2</sup> 3d <sup>2</sup> D <sub>5/2</sub> - 1s2p3d <sup>2</sup> F <sub>7/2</sub> 1s <sup>2</sup> 3d <sup>2</sup> D <sub>5/2</sub> - 1s2p3d <sup>2</sup> F <sub>5/2</sub>	6.653 Blend		6.650→6.656 [172]
h7	Si XII Si XII	1s <sup>2</sup> 3d <sup>2</sup> D <sub>5/2</sub> - 1s2p3d <sup>2</sup> D <sub>5/2</sub> 1s <sup>2</sup> 3d <sup>2</sup> D <sub>3/2</sub> - 1s2p3d <sup>2</sup> D <sub>3/2</sub>	6.657 Blend	6.657±0.005 [170]	6.58→6.66 [171]
d5, d13 a1, a2	Si XII Si XII	1s <sup>2</sup> 3p <sup>2</sup> P <sub>3/2</sub> - 1s2p3p <sup>2</sup> P <sub>3/2</sub> , <sup>2</sup> D <sub>5/2</sub> 1s <sup>2</sup> 3s <sup>2</sup> S <sub>1/2</sub> - 1s2p3s <sup>2</sup> F <sub>3/2</sub> , <sup>1</sup> / <sub>2</sub>	6.661 Blend		6.658→6.664 [172]
n	Si XII	1s <sup>2</sup> 2p <sup>2</sup> P <sub>1/2</sub> - 1s2p <sup>2</sup> <sup>2</sup> S <sub>1/2</sub>	6.6781	6.677±0.001 [172]	6.677 [172]
m	Si XII	1s <sup>2</sup> 2p <sup>2</sup> P <sub>3/2</sub> - 1s2p <sup>2</sup> <sup>2</sup> S <sub>1/2</sub>	6.6821	6.681±0.001 [172]	6.681 [172]
<sup>3</sup> P <sub>2</sub>	Si XIII Si XII	1s <sup>2</sup> 1S <sub>0</sub> - 1s2p <sup>3</sup> P <sub>2</sub> 1s <sup>2</sup> 3d <sup>2</sup> D <sub>5/2</sub> - 1s2p( <sup>3</sup> P <sub>1</sub> ) 3d <sup>2</sup> F <sub>7/2</sub>	6.6852	6.685±0.001 [172]	6.6850 [26]
<sup>3</sup> P <sub>1</sub>	Si XIII	1s <sup>2</sup> 1S <sub>0</sub> - 1s2p <sup>3</sup> P <sub>1</sub>	6.6882 Calibration	6.687±0.001 [172]	6.6882 [26], 6.6879 [172]
s	Si XII Si XII	1s <sup>2</sup> 2s <sup>2</sup> S <sub>1/2</sub> - 1s2p( <sup>3</sup> P) 2s <sup>2</sup> P <sub>3/2</sub> 1s <sup>2</sup> 3d <sup>2</sup> D <sub>3/2</sub> - 1s2p( <sup>3</sup> P) 3d <sup>2</sup> F <sub>5/2</sub>	6.6894	6.688±0.001 [172]	6.688 [172]
t	Si XII Si XII	1s <sup>2</sup> 2s <sup>2</sup> S <sub>1/2</sub> - 1s2p( <sup>3</sup> P) 2s <sup>2</sup> P <sub>1/2</sub> 1s <sup>2</sup> 3d <sup>2</sup> D <sub>5/2</sub> - 1s2p( <sup>3</sup> P) 3d <sup>2</sup> F <sub>5/2</sub>	6.6914	6.689±0.001 [172]	6.689 [172]

Observed wavelengths, where quoted to four decimal places, are accurate to ±0.0002Å.  
Observed blended wavelengths are quoted to three decimal places for mean wavelength, and are accurate to ±0.001Å.  
Numbers in square brackets [ ] indicate references.

measured wavelengths are shown in Table 7.1 with likely identifications. The better resolved lines mainly adjacent to the  $^3P_1$  line (shown to four decimal places) are quoted to  $\pm 0.0002\text{\AA}$  accuracy while the blended lines (to three decimal places) are quoted to  $\pm 0.001\text{\AA}$ .

#### Satellite Structure Identification.

The satellite structure is very similar to the measured and theoretical results of Mosnier et al<sup>172</sup>, with the difference that the spectrum here is about a factor of two better resolved. The spectral resolution of the other Si beam-foil data is too low to warrant comparison, and therefore discussion is limited to Mosnier et al.

The continuous band of satellites to the long wavelength side of the  $^1P_1$  Si XIII ion originate from  $1s2p3s, -3p, -3d$  configuration of the Si XII ion where the 2p electron makes the transition. The feature labelled h7 in Figure 7.5, seen by Träbert et al<sup>170</sup> and calculated by Träbert and Fawcett<sup>171</sup>, has been labelled tentatively as one of the  $1s^22s^22p - 1s2p^4$  transitions in B-like Si X ion by Laming et al<sup>176</sup>. This is unlikely to be the case considering the low abundance of the Si X charge state at this beam energy.

Figure 7.6 shows the  $^3P_1$  Si XIII line in more detail together with line fitting to the adjacent line structure. In spite of a high S/N ratio, the fitting of the  $^3P_1$  line using different power law and Voigt profiles is not exact. This can be explained by unresolved satellites or more likely, the observed line has a shape determined mainly by the crystal diffraction width (see Figure 2.3, Chapter 2). The lines marked n,m according to Gabriel's notation<sup>85</sup>, belong to the Si XII  $1s^22p^2P_{1/2,3/2} - 1s2p^2^2S_{1/2}$  transitions and are in good agreement with the calculations of Mosnier et al. The transition at  $6.6852\pm 0.0002\text{\AA}$  is very close to the  $1s^2^1S_0 - 1s2p^3P_2$  line predicted to be at  $6.6850\text{\AA}$ <sup>26</sup>. This is coincident, however, with a strong satellite line Si XII  $1s^23d^2D_{5/2} - 1s2p(^3P)3d^2F_{7/2}$  and is verified to some extent by the pair of lines appearing to the long wavelength side of the  $^3P_1$  Si XIII line. These lines agree with the other transitions  $^2D_{3/2} - ^2F_{5/2}$  and the  $^2D_{5/2} - ^2F_{5/2}$  of this multiplet, but also happen to be coincident with the Si XII decays  $1s^22s^2S_{1/2} - 1s2p(^3P)2s^2P_{3/2,1/2}$  labelled s,t respectively.

There does not appear to be a way of identifying these lines unambiguously, without repeating this experiment at different beam energies, thus changing the charge state distribution. The line identified as the  $^3P_2$  should then remain in the same intensity ratio to the  $^3P_1$  Si XIII line, independently of beam energy. Mosnier et al<sup>172</sup> do not observe the  $^3P_2$  line because it is a long-lived state with  $\tau=4.4\text{ns}$ <sup>177,178</sup>. This is to be expected, as suggested by Laming et al<sup>176</sup>, since their spectrometer views a 0.5cm region after the foil observing very little of the 7.6cm decay length for the 44MeV beam. In contrast, the axial observation will be able to measure this and other long-lived decays.

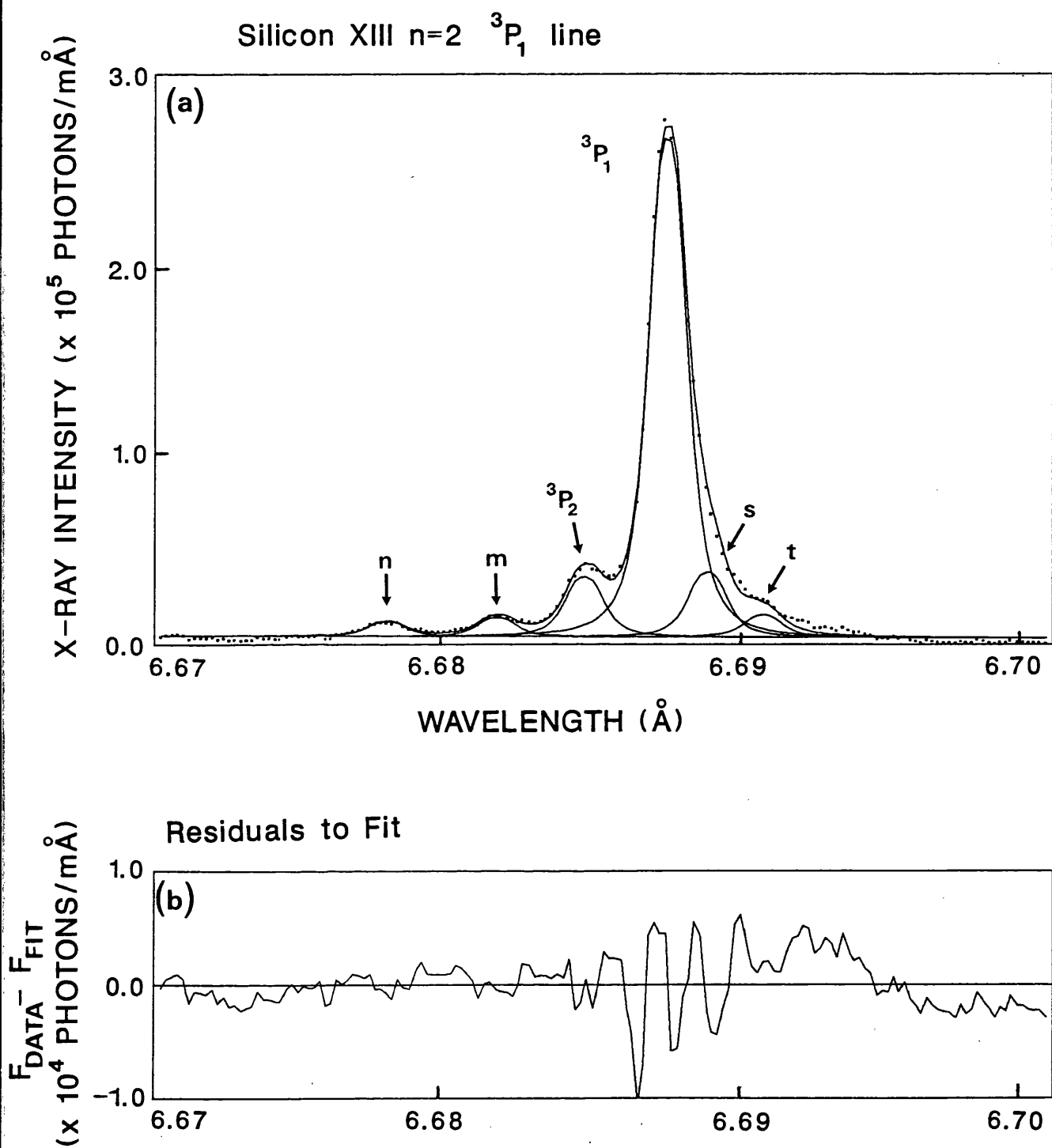
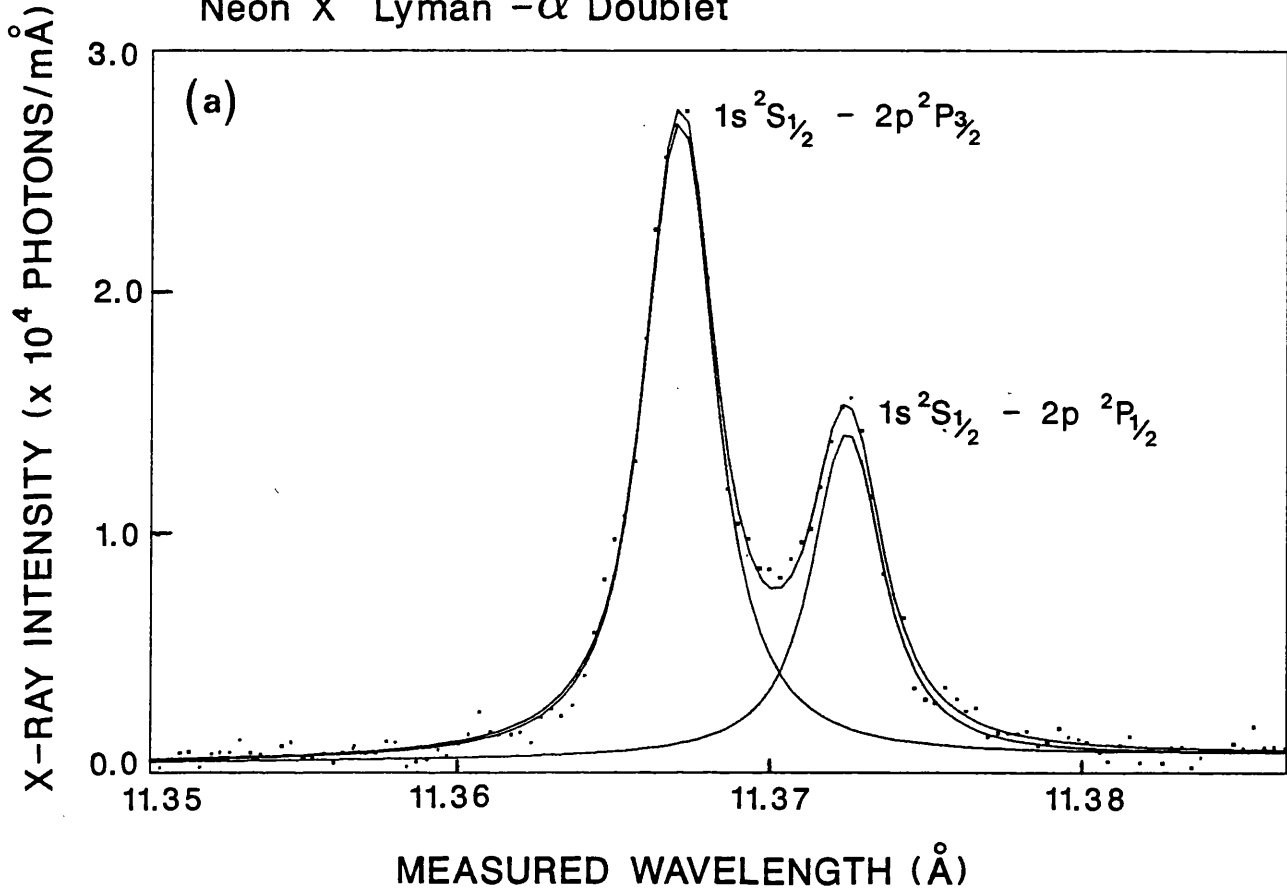


Figure 7.6 illustrates profile fitting to the Si XIII  $1s^2\ ^1S_0-1s2p\ ^3P_1$  resonance line and adjacent satellite structure. On the short wavelength side is the the magnetic quadrupole decay transition of Si XIII  $1s^2\ ^1S_0-1s2p\ ^3P_2$ . The other lines n, m, s and t are labelled according to Gabriel and are Li-like Si XII satellites.

Neon X Lyman - $\alpha$  Doublet



Residuals to Fit

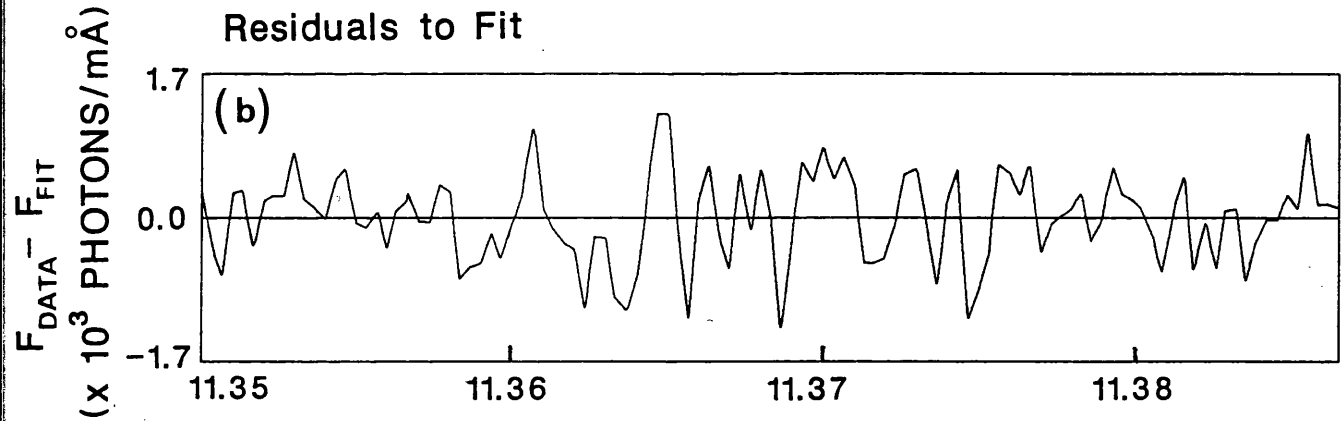


Figure 7.7 Neon X Lyman- $\alpha$  spectrum from a continuous exposure of 31 hours with the high resolution KAP (002) spectrometer. The measured wavelengths at 11.37 $\text{\AA}$  have been Doppler shifted from 12.13 $\text{\AA}$ . The spectrum has extremely low x-ray continuum, with the doublet essentially sitting on the background film noise for a single unexposed emulsion layer. Residuals to fit are shown in window below spectrum.

## 7.6 Neon X Axial Observation.

### 7.6.1 Experimental Details.

The experiment was repeated using a beam current of 100nA of  $\text{Ne}^{8+}$  ions at 39MeV energy. The positive Neon ions were generated by a radio-frequency source and accelerated by the Oxford Folded Tandem in "single-ended" operation. It was decided to observe the Neon X Lyman- $\alpha$  doublet and if possible resolve the  $1s\ ^2S_{1/2}$ - $2p\ ^2P_{1/2}$  fine structure component at 12.137Å, requiring an instrumental resolving power of considerably better than  $\lambda/\Delta\lambda\sim 2300$ . A KAP (002),  $2d=13.3164\text{Å}^{57}$ , crystal used at a radius of  $R=1073\text{mm}$  gave an estimated instrumental resolving power of  $\lambda/\Delta\lambda=9000$  limited by the crystal diffraction width<sup>12</sup>. The Doppler shift  $\beta=0.0642$  was calculated after energy loss in the foil, thus shifting the Neon Ly- $\alpha$  to the blue from 12.1Å to 11.4Å as indicated by equation (7.1). The Bragg angle  $\theta=58.64^\circ$  was set after the lattice spacing was corrected for temperature ( $T=25.0\pm 0.5^\circ\text{C}$ ,  $\alpha=(40.5\pm 2.0)\times 10^{-6}/\text{K}$  and refractive index effects ( $\delta/\lambda^2=(2.30\pm 0.05)\times 10^{-6}\text{Å}^{-2}$ ) from Table 4.1.

#### Signal Intensity.

The signal intensity was expected to be lower than the Si XIII for a number of reasons. The ion beam was about 25% of the previous experiment though the charge state of interest Ne X was proportionally similar to Si XIII. The equilibrium charge state distribution<sup>157</sup> of the Neon beam after foil excitation for  $\text{Ne}^{6+}$ :  $\text{Ne}^{7+}$ :  $\text{Ne}^{8+}$ :  $\text{Ne}^{9+}$ :  $\text{Ne}^{10+}$  was in the ratio of 0.8%: 11.4%: 43.8%: 37.8%: 6.2%. This was in good agreement with  $q=8.5$  for the mean ion beam charge calculated from equation (7.1). The integrated reflectivity  $R_c$  of KAP (002) was  $5.0\times 10^{-6}\text{rad}$  at  $11.4\text{Å}^{55}$ , compared with  $8.5\times 10^{-5}\text{rad}$  for PET (002) at  $6.2\text{Å}^{11}$ . Finally, Kodak DEF x-ray film has twice the sensitivity to radiation at 6Å than at 11Å<sup>70</sup>. Therefore, even with 31 hours exposure the final integrated Neon signal on film was expected to be about one order of magnitude smaller than the Silicon experiment.

### 7.6.2 Results.

Figure 7.7 shows the spectrum of the  $1s\ ^2S_{1/2}$ - $2p\ ^2P_{1/2,3/2}$  transitions in  $\text{Ne}^{9+}$ . The Lyman- $\alpha$  doublet is clearly resolved,  $\lambda/\Delta\lambda=4400$ . As expected the signal was low; the Lyman- $\alpha_1$  peak intensity on film of 0.13 photons/ $\mu\text{m}^2$  corresponds to roughly  $2.8\times 10^4$  photons/mÅ for the 1.4mm high densitometer scan. The experimental data (points) are fitted using a power law and Voigt type functions. The residuals to the fit, Figure 7.7(b), are low and predominantly film grain noise. The line profiles are mainly Lorentzian ( $n=2.0$ ) although a marginally better least squares fit gave  $n=2.2$ . The apparent discrepancy in the power  $n$  could be explained by either the crystal diffraction profile not being purely Lorentzian or a contribution from the convolution of the source broadened profile. The Voigt fit confirmed this with a value of  $\eta=0.67$ , corresponding to a Lorentzian:Gaussian ratio of 1.8:1.0. This did not warrant further investigation without first trying to improve the statistics. The background x-ray continuum was extremely low with the lines sitting on the single

emulsion unexposed fog level. It was also noted that 2-electron satellites to the Lyman- $\alpha$  lines, normally a strong feature of a beam-foil spectrum, were either absent or too low to be registered.

### **Neon X Fine-Structure.**

The fine-structure, see Chapter 8, was measured as  $5.59 \pm 0.04 \text{ m\AA}$  after the Doppler shift was corrected. The main source of error came from the uncertainty in the beam velocity and spectrometer alignment, though the possibility of unresolved satellite lines was not completely discounted. The Lyman- $\alpha$  intensity ratio  $I(\alpha_2)/I(\alpha_1)$  was  $0.513 \pm 0.006$ , with error contributions coming equally from statistics and the accuracy of the film response function. This compared very well with the expected theoretical statistical weighting of 0.5, but shows the difference between results achieved for the Lyman- $\alpha$  intensity ratio of Magnesium, Aluminium and Silicon emitted from denser sources. This latter group which includes laser produced and Tokamak plasmas can be affected by electron and ion collisional excitation, discussed in Chapter 8, transferring the electron population preferentially from the  $2s \ ^2S_{1/2}$  state to the near-lying  $2p \ ^2P_{1/2}$  state resulting in the observed intensity ratio.

## **7.7 Conclusions and Future Experiments.**

This section is divided into three parts and summarises the main conclusions of this chapter under the following titles:

- Discussion on present experiment.
- Application to different beam/target interactions.
- Instrumentation and techniques for future experiments.

### **7.7.1 Discussion on Present Experiment.**

#### **High Spectral Resolution.**

The main conclusion is that the axial observation technique when combined with the use of a high resolution spectrometer produced the best resolved spectra measured from any beam-foil source. These results also represent the best resolved Neon Lyman- $\alpha$  spectrum and Si XIII resonance lines recorded from any source. For comparison, the best resolved spectrum by observing beam-foil targets perpendicularly, was recorded by Richard et al<sup>78</sup> for a measurement of the 1s Lamb shift in Hydrogenic Chlorine. The Chlorine Lyman- $\alpha$  resonance lines at  $4.2 \text{ \AA}$  were resolved to  $\lambda/\Delta\lambda=2900$  using a Johann spectrometer with a Si(111) crystal,  $2d=6.248 \text{ \AA}$ , of radius  $R \sim 2.0 \text{ m}$  and a position sensitive backgammon proportional counter. Since the horizontal divergence of the ion beam was defined using a pair of slits upstream  $\Delta\alpha=7 \times 10^{-4} \text{ rad}$  and was considerably smaller than the same figure for the Oxford Tandem, the line broadening would appear to be mainly instrumental, probably as a result of the detector spatial resolution. This is confirmed by the measured profile

shapes being predominantly Gaussian though a contribution from the Doppler broadening of the extended source is also possible.

### Spectral Line Profiles.

Apart from putting the present results into perspective, comparing data from different accelerators under different operating conditions is not useful for verifying the predictions of section 7.3. The experiment must clearly apply to one accelerator for the same ion at the same beam energy, but using the two observation geometries. Perpendicular observation experiments<sup>170</sup> were performed on the Oxford Tandem for Si XIII as mentioned in section 7.5, but the low resolution survey spectra  $\lambda/\Delta\lambda=660$  were not of sufficient quality to show the difference. However, since the axial observation has been performed here for two different ions it may be possible to draw some conclusions from the technique.

There are a few points to be considered:

- The effect of the source broadening on the line profile is not known accurately. Discussions in section 7.3 indicated that the spread in the beam energy was the main cause, with small Doppler broadening due to the small angle deviation from the purely axial geometry. A Gaussian shape can be suggested for the source function, but there seems to be a lack of hard evidence to support this assertion.
- No tolerances were available for the Folded Tandem parameters.

**Table 7.2 Doppler Contribution Estimate using Voigt Profile Analysis**

Ion	Instrumental $\lambda/\Delta\lambda$	Measured $\lambda/\Delta\lambda$	Gaussian§ $\lambda/\Delta\lambda$	Lorentzian $\lambda/\Delta\lambda$	Voigt1 $\lambda/\Delta\lambda$	Voigt2 $\lambda/\Delta\lambda$
Ne X	9000	4400	5000	8600	6300	10000
Ne X	7000	4400	5700	11900	7300	
Si XIII	6000	4000	5400	1200	7200	

N.B. The instrumental resolving power is determined by the crystal diffraction width.

§ This is not a good assumption since a Gaussian shape is not observed for the measured line profile.

Table 7.2 shows estimates of the source broadened contribution to the measured line profile by assuming Gaussian, Lorentzian and Voigt shapes throughout for the instrument and source function. Other contributions, for example from the natural line widths, are negligible. The three rows of data represent two estimates for the crystal diffraction width for the Neon X and the Silicon XIII results. The first and second columns give the measured line width and crystal diffraction widths respectively, expressed as a resolving power. The

next column gives the calculated source broadening by assuming that all profiles are Gaussian and can be added quadratically. It can be noted that this is not a good assumption since neither the observed spectrum nor the crystal profile is a strong Gaussian function, but does give a lower limit estimate for the source broadening. The fourth column repeats the process for Lorentzian profiles, where the widths can be added linearly. Again, this should be treated as an upper limit estimate. The fifth column simply assumes a Voigt profile for the measured line and takes the crystal diffraction as a Lorentzian. The Voigt parameter  $\eta$  is then calculated using the Lorentzian as a fraction of the measured line width. The final column is the result achieved by doing the converse. It uses a Voigt fit to the measured line profiles to estimate the Gaussian content just from the line shape information only. The last two columns give a self-consistent check about the various assumptions about the line profiles up to this point.

One would expect the Voigt estimates to be somewhere between the Gaussian and Lorentzian calculations. This can be seen to be generally true except for the case of  $\lambda/\Delta\lambda=9000$  for the Neon X spectrum. This theoretical value for the crystal diffraction width appears to be optimistic. If a slightly lower value of  $\lambda/\Delta\lambda=7000$  is substituted, then a consistent trend for the source broadening of  $\lambda/\Delta\lambda=7 \times 10^4 \rightarrow 10^4$  becomes apparent. The tolerance,  $\lambda/\Delta\lambda=8500 \pm 1500$ , reflects the uncertainty in the various assumptions, partly for example that the crystal profile is purely Lorentzian. Specifically, the spread in the value for source broadening arises from differences between the numbers derived from the profile shape and line width of the measured line. (Measured diffraction profiles, particularly for PET (002), have a more complicated shape and cannot be described in terms of simple functions).

It is clear from column four, that if the instrumental resolving power is over estimated then the deconvolved source broadening contribution rapidly decreases. It then becomes almost impossible to quote a value for the source broadening with any accuracy. This reinforces the following points regarding the measurement and interpretation of line profiles:

- (1) The instrumental line profile must be accurately known.
- (2) The instrumental line width should also be several times smaller than the emission line to be measured. Any uncertainties in the instrumental line width then have a minimal effect on the deconvolved line.
- (3) The emission line profile should be accurately known, particularly if the emission line width is smaller than or equal to the instrumental width.

It is clear that all three points apply to the results presented in this chapter. However, sufficient information is available to give broad agreement with the predictions of section 7.3. The major improvement to this experiment would be to repeat it using considerably higher instrumental resolving power. Changes in the source broadening could be observed by varying the beam collimation and energy spread.

### 7.7.2 Application to Different Beam-Target Interactions.

There are two fundamental limitations to beam-foil experiments:

- Large Doppler shifts for axial observation.
- The observed line widths are determined by the accelerator parameters.

The improvements in x-ray spectroscopic techniques can be applied to other types of heavy ion beam target interaction. There is some interest in using beam-solid spectroscopy, where highly charged particles of the target material are generated producing  $K\alpha$  multiple-vacancy spectra, to study plasma-surface interactions. Some recent results have been presented by Chantler and Silver<sup>179</sup>.

#### Beam-Gas Target Interactions.

Perhaps more importantly for testing relativistic and quantum electrodynamical effects is the use of beam-gas target spectroscopy. The heavy ions in the beam, preferably a high  $Z$  element like Bromine ( $Z=35$ ) for medium sized accelerators or often Uranium ( $Z=92$ ) for high energy accelerators, collide with the atoms in the gas target, usually a noble gas, leaving the latter in a highly ionised and excited state. A small amount of energy, about  $5 \rightarrow 20$  eV, is given to the target ions which almost completely recoil in the perpendicular direction to the ion beam<sup>180</sup>. The surrounding electrons, however, may have energies of the order of keV. Thus the gas "recoil-ions", are highly ionised and have low Doppler velocities in the perpendicular direction to the beam.

#### Axial Beam-Gas Target Measurements.

If one views the gas target axially<sup>181</sup> then this recoil Doppler effect disappears leaving the x-ray emission line width largely determined by room temperature thermal effects and the natural decay time of the excited state. The advantages of this method are clear:

- The absence of large Doppler shifts, present for example in axial beam-foil spectroscopy, allows precise wavelength measurements to be made while looking axially.
- X-ray emission lines below  $4\text{\AA}$  with spectral resolution of  $\delta\lambda/\lambda \sim 10^{-5}$  should then be possible for H- and He-like Argon ( $Z=18$ ) ions.

The precision measurements should then be limited by the accuracy of the reference lines, crystal refractive index effects and instrumental dispersion. The nature of satellite lines, particularly those from high  $n$  quantum states occurring close to the main resonance line, could also be revealed. This is of considerable importance since the accuracy of recent "recoil-ion" gas target experiments at the 1.5% level<sup>186</sup> has been restricted by satellite line contamination.

#### Measurement of Short-lived Levels of High $Z$ Ions.

Following the trend of studying higher  $Z$  elements to improve the accuracy of the ground state Lamb shift measurements, the natural line width of the transition should become

significantly larger than room temperature Doppler motion. One can envisage an axial observation of a Krypton ( $Z=36$ ) "recoil-ion" gas target experiment performed on the GSI (Gesellschaft für Schwerionenforschung) accelerator at Darmstadt. In addition to measuring the wavelengths at the 1ppm level, it should be possible to measure the natural line widths of the Kr Lyman- $\alpha$  doublet at 0.92Å. The A-values for these allowed resonance lines generally scale as  $Z^4$  and are expected to be  $\sim 10^{15}\text{s}^{-1}$  for this level. The spectral resolution of the radiative decay will be  $\delta\lambda/\lambda \sim 5 \times 10^{-5}$ , a potentially measurable quantity. This may be a valuable technique for measuring short lived states which otherwise cannot be detected by the standard beam-foil method, Chapter 7.1.

The prospects are interesting because the instrumentation and accelerator technology for this experiment have now become available in recent years.

### **7.7.3 Instrumentation and Techniques for Future Experiments.**

These improvements in accelerator technology have refined the accuracy of possible Lamb shift experiments to the point where it now places greater demands on the instrumentation and techniques. These demands primarily require simultaneously, high resolution and high precision from the x-ray spectrometer, but also high sensitivity because of the low emission from accelerator based experiments. The Johann spectrometer has been used almost exclusively for this purpose to date.

However, the problems calibrating the recorded spectrum with the appropriate x-ray standards to sufficient precision, as perceived by one key experimentalist (Deslattes<sup>182</sup>), has led to the proposed use of a high resolution  $\lambda/\Delta\lambda=40000$  two crystal spectrometer for the 1Å region. This is undoubtedly the most precise method for absolute wavelength measurements, but the question of adequate bandpass and sensitivity still remain. Nevertheless, this appears to be the direction for future research. As discussed in Chapter 4.6, the Johann type spectrometer can be improved to the same high standards and has an important role in these experiments in spite of this trend.

#### **Calibration by Two-Channel Spectroscopy.**

The main disadvantage of the axial observation technique for beam-foil interactions, lies in the calibration of the Doppler shifted x-ray lines relative to rest frame x-ray standard lines. The use of a pair of Johann spectrometers to correct for Doppler shifts is a well documented technique, for example Dietrich et al<sup>183</sup> for beam-foil sources and Aglitsky et al<sup>184</sup> for vacuum spark sources. Both spectrometers view the source separated by 180° so that the Doppler shift is cancelled by the two channel measurement against the same reference line.

This method is most effective when the total shift is small  $\beta \sim 10^{-3} \rightarrow 10^{-2}$  and the x-ray lines occur within a similarly small waveband. Although it would be possible to have two

spectrometers looking axially, one viewing upstream while the second views downstream, a large waveband with different x-ray reference lines would be necessary to cover the total shift of at least  $\beta \sim 0.14$  for the present experiments. Despite these shortcomings, the two channel method has some merit for the calibration of these large Doppler shifts and should be attempted.

#### **"In-Beam" Calibration.**

A novel and simpler method proposed by Silver and co-workers<sup>185</sup> uses "in-beam" calibration lines which are insensitive to the Doppler shifts. The technique, demonstrated by perpendicular observation, uses the 4:1 ratio of the wavelengths of the Balmer- $\beta$  and Lyman- $\alpha$  transitions to compare the Lyman- $\alpha$  lines diffracted in fourth order with the Balmer- $\beta$  lines diffracted in first order. It has the advantage of the lines occurring in a small waveband, for example  $\lambda/\Delta\lambda \sim 0.01$  for Iron transitions. Theoretical values<sup>162</sup> are assigned to the Balmer- $\beta$  lines to calibrate the spectrum. Initial results<sup>185</sup> for Iron ( $Z=26$ ) have measured the Lyman- $\alpha$  transitions with an accuracy of 107ppm, thus giving the ground-state Lamb shift to 17% and the  $^2P_{1/2,3/2}$  fine-structure splitting to 3%. The measurement has been repeated for Germanium ( $Z=32$ ) Lyman- $\alpha$  transitions with an accuracy of 75ppm<sup>63</sup>.

Some problems have been encountered with this method, mainly due to unexplained shifts in the line positions, which the present author believes is principally due to the instrumentation. The dual arm Johann spectrometers  $R=300\text{mm}$  recording the spectra can really only be used as low resolution survey instruments with this type of x-ray source. Firstly, Johann aberrations are considerable, scaling as  $R^{-2}$ , at this small crystal curvature. These mainly effect the instrumental resolving power.

The x-ray images along the film height will be curved due to the geometrical effect described in Chapter 2. Therefore, the dispersion at various heights on the film will vary. This is further complicated by the Doppler effect when viewing perpendicularly. A slope is introduced to the x-ray lines along the height dimension because of the Doppler effect from radiation slightly upstream and downstream. Thus analysis of the line positions becomes complicated by various interacting effects.

A larger Rowland circle instrument viewing axially, when combined with several x-ray reference lines to calibrate both the gross Doppler shift relative to the Balmer- $\beta$  lines and the dispersion accurately, should increase the accuracy of these Lamb shift measurements to the level predicted by Deslattes<sup>186</sup>.

# Chapter 8 Fine-Structure Measurement.

	Introduction.	232
8.1	Interest in Fine-Structure Measurements.	232
8.2	Theory for Fine-Structure Splitting.	234
8.3	Experiments and Dispersion Calibration.	235
	8.3.1 Experimental Details.	235
	8.3.2 Spectrometer Wavelength Calibration.	236
	8.3.3 Results.	238
8.4	Fine-Structure Intensity Ratio.	243
	8.4.1 Collisional Mixing of the $n=2$ Levels.	243
	8.4.2 Non-collisional Effects.	244
	8.4.3 Experimental Data.	246
8.5	Review of Fine-Structure Splitting Measurements.	248
	8.5.1 Discussion of Measurements from Other Sources.	248
	8.5.2 Satellite Lines.	252
	8.5.3 Satellite-Free Spectra.	254
8.6	Conclusions.	254

## Introduction.

In this final chapter, the Lyman- $\alpha$  doublet from various Hydrogenic ions is analysed. Tokamak and beam-foil measurements are used, but the laser plasma results from Aluminium (Chapter 6) are not suitable due to strong self-absorption effects. The main topics covered in this chapter are:

- Scientific interest in measuring the fine-structure interval.
- Brief definition of the fine-structure splitting in Hydrogenic ions, its magnitude and dependence on the atomic number  $Z$  and principal quantum number  $n$ .
- Description of different experiments and limiting factors to the overall precision of the measurement.
- Interpretation of anomalous  $\beta$ -ratios observed for Mg XII, Al XIII and Si XIV ions on DITE Tokamak and discussion of the contributing factors. The Ne X result is included.
- Review and comparison of fine-structure splitting measurements with other x-ray sources.
- Conclusions about measurements presented in this work.

## 8.1 Interest in Fine-Structure Measurements.

Spectra of Hydrogenic ions have been observed from a number of high temperature plasma sources like laser-produced plasmas<sup>130</sup>, Tokamaks<sup>187</sup>, and solar flares<sup>188</sup>. Other non-plasma sources, including fast ion beam target interactions (Martinson<sup>189</sup>), have allowed the observation of the H-like charge state from much higher atomic numbers<sup>190</sup>.

Growing interest in the effects of quantum electrodynamics (QED) on the energy levels of high  $Z$  Hydrogenic ions has produced precision laboratory experiments (for example<sup>78,185,191</sup>) to test theoretical calculations. Accurate absolute x-ray wavelength measurements are needed in these experiments in order to determine the magnitude of QED effects and the scaling with atomic number  $Z$ . The relativistic Dirac theory is assumed to be correct when the small corrections of QED are neglected.

In principal, by looking at the spin-orbit interaction splitting in the energy levels of the excited states, for the same principal quantum number  $n$  but with different  $j$ -values, this assumption can be tested very easily. The  $j=1/2,3/2$  splitting, shown in the energy level diagram of Figure 8.1, is most readily observed in the first member of the Lyman series by resonance transition; the splitting in the energy levels scales as  $n^{-3}$ . For the resolved doublet, a relative wavelength or energy measurement can be made and the separation determined.

In practice, few experiments have been able to confirm theoretical calculations to better than 0.5% and many more show considerable deviations.

Excited  $n=2$  levels of the H-like Ion

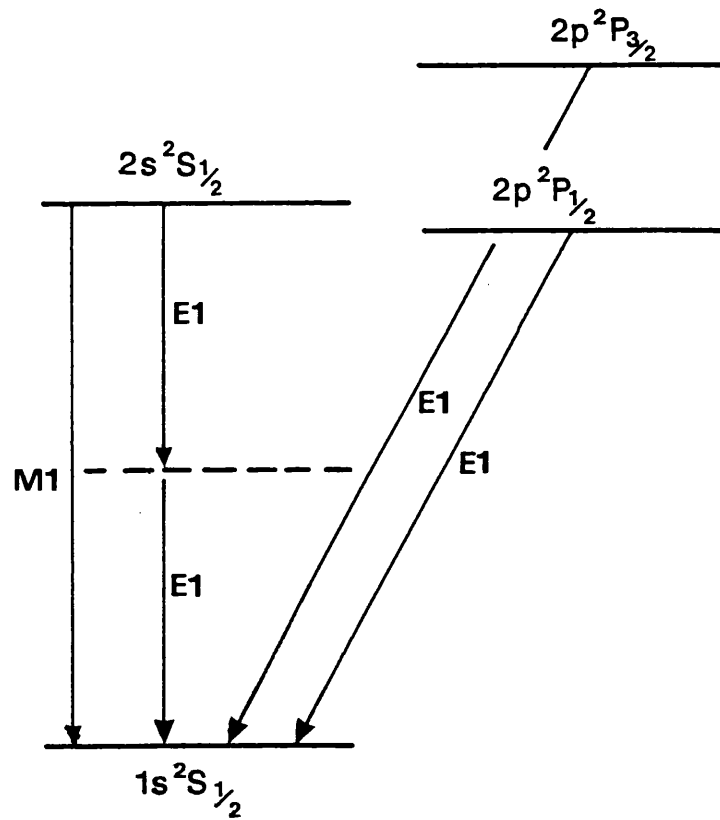


Figure 8.1 Energy level diagram for  $n=2$  transitions of Hydrogenic ions.

The main objective of this chapter is to present new measurements of the 2p spin-orbit interaction for medium Z elements. There are very few measurements of the Lyman- $\alpha$  doublet separation for this Z region of the periodic table, mainly because the splitting is small and the lines are blended by Doppler broadening. High resolving power  $\lambda/\Delta\lambda=5000$  is essential, limiting the choice of available crystals for Bragg diffraction techniques to observing  $Z \geq 10$  (Neon) in the waveband below 13 Å.

Spectra of Hydrogenic Neon ( $Z=10$ , blue-shifted to 11.4Å) emitted on a foil-excited ion beam accelerated on the Oxford Folded Tandem (see Chapter 7) and Hydrogenic Magnesium, Aluminium and Silicon ( $Z=12 \rightarrow 14$  at 8.42Å, 7.17Å and 6.18Å respectively) emitted from DITE Tokamak (Chapter 5) were observed with high resolution. The fine-structure component is resolved in each case and the spectra are generally free of satellite lines, allowing the fine-structure interval to be measured to better than 0.5% for the Magnesium spectra. This is an improvement on the previous measurements<sup>215</sup> where the Magnesium spectrum was affected by intense Iron L-shell transitions.

The Neon beam-foil experiment was discussed in Chapter 7 (see Laming et al<sup>176</sup>) principally as evidence of improved spectral resolution by axial observation of the source. It is included here for comparison with the Tokamak measurements.

The intensity of the individual components of the doublet have also been accurately measured. The Lyman- $\alpha$  intensity ratio  $\beta$  is different from the expected statistical value of 0.5 and shows some variation with atomic number Z and plasma conditions. The observed  $\beta$ -ratios here have been successfully interpreted as a result of different effects and are discussed in section 8.4.

A comparison of the fine-structure interval is made with the full quantum electrodynamical calculations of Mohr<sup>27</sup>, together with a review of fine-structure measurements by x-ray wavelength dispersive methods in section 8.5.

## 8.2 Theory for Fine-Structure Splitting.

The energy level structure of Hydrogenic ions has been calculated to high accuracy by various authors<sup>27,28,162,192</sup> where the absolute wavelengths are sensitive to the exact QED treatment, but generally the pure Dirac results are in close agreement with those which include QED. The binding energy  $E_n$  ( $\text{cm}^{-1}$ ) of an electron in neutral Hydrogen or H-like ion can be described by the Schrödinger equation and written as:

$$E_n = - R_\infty \frac{Z^2}{n^2} \quad (8.1)$$

where the Rydberg constant  $R_\infty$  equals  $109737.31 \text{cm}^{-1}$ . By including corrections introduced by Sommerfeld, to account for the relativistic mass increase of the electron, the Darwin term (affecting the S electron only) and the spin-orbit interaction, the first term in the relativistic Dirac equation is:

$$E_r = E_n \left\{ \frac{Z\alpha}{n} \right\}^2 \left[ \frac{n}{j + 1/2} - 3/4 \right] \quad (8.2)$$

where  $\alpha$  is the Sommerfeld fine-structure constant and equals  $1/137.036$ . Substituting in turn,  $j=1/2$  and  $3/2$  for  $n \geq 2$  into equation (8.2) and noting that both excited levels decay to the  $1s \ ^2S_{1/2}$  ground state, then the fine-structure interval  $\Delta E_{FS}$  ( $\text{cm}^{-1}$ ) can be expressed to first order as:

$$\Delta E_{FS} = \frac{R_\infty Z^4 \alpha^2}{2n^3} \quad (8.3)$$

If the next higher terms are added, equation (8.3) from Schleinkofer et al<sup>183</sup> becomes:

$$\Delta E_{FS} = \frac{R_\infty Z^4 \alpha^2}{2n^3} \left[ 1 + \frac{5}{8}(Z\alpha)^2 + \frac{53}{128}(Z\alpha)^4 + \frac{303}{1024}(Z\alpha)^6 + \dots \right] \quad (8.4)$$

Further small corrections to equation (8.4) are needed to include the effect of reduced mass. The most significant though, are the addition of QED effects which increase  $\Delta E_{FS}$  by 0.2%, as calculated by Mohr<sup>27</sup> for the range  $Z=10 \rightarrow 40$ .

It is evident from equation (8.4) that the fine-structure interval scales as  $Z^4$  and  $n^{-3}$ , where  $n$  is the principal quantum number. The transition energy scales as  $Z^2$ , therefore  $\Delta E_{FS}/E$  is proportional to  $Z^2$ . This implies that the fine-structure splitting becomes better resolved with increasing atomic number: for comparison,  $\Delta E_{FS}/E$  equals  $\sim 4.4 \times 10^{-6}$  and  $\sim 4.4 \times 10^{-4}$  for Hydrogen ( $Z=1$ ) and Neon ( $Z=10$ ) respectively.

Measurements can be easily compared for different  $Z$  if the interval  $\Delta E_{FS}$  is expressed as a wavelength difference  $\Delta \lambda_{FS}$ . Then  $\Delta \lambda_{FS}$  remains virtually constant and independent of  $Z$ , see column 4 of Table 8.3. This is a direct consequence of the inverse relationship between transition energy  $E$  and wavelength  $\lambda$ . For example, the 2p, 3p and 4p spin-orbit interactions give rise to  $\Delta \lambda_{FS}$  splittings of  $\sim 5.4 \text{m}\text{\AA}$ ,  $\sim 1.14 \text{m}\text{\AA}$  and  $\sim 0.43 \text{m}\text{\AA}$  respectively. The 2p splitting can be resolved by x-ray spectroscopic techniques for  $Z \geq 10$  (Laming et al<sup>176</sup>) while the 3p splitting should become easily resolved for  $Z \geq 26$ . Therefore, most results are available for the 2p splitting and is the main interest of this study. Finally, for the remainder of this chapter,  $\Delta \lambda_{FS}$  will refer to the 2p spin-orbit effect.

## 8.3 Experiments and Dispersion Calibration.

### 8.3.1 Experimental Details.

#### I Tokamak Experiments.

The experiment was performed on the UKAEA Divertor Injection Tokamak Experiment (DITE). On different occasions using a Helium plasma, a Magnesium and Silicon probe were used to introduce small amounts of these elements into the Tokamak via the edge of the plasma. The primary motivation was to measure the central ion temperature. The temporal and spatial variation of the elements are determined by the particle transport and the

relevant atomic collision rates. The H- and He-like ions are observed dominantly in the high temperature core where near coronal balance conditions are obtained. The background x-ray emission generally lasted from the beginning to the end of the shot<sup>194</sup>, about 600msec. The Aluminium was injected into the plasma by laser ablation 375msec after the start; the duration of the x-ray emission (related to the ion confinement) was shorter, lasting for 100msec. The electron density was in the range  $n_e=5 \times 10^{12} \rightarrow 10^{14} \text{cm}^{-3}$  and a core temperature of  $T_e=T_i=700 \rightarrow 1000 \text{eV}$  was routinely achieved. Spectral line widths were largely due to thermal Doppler broadening, typically  $\lambda/\Delta\lambda \sim 2000$ . The spectrometer, (see Chapter 5 for details of source/spectrometer geometry), viewed the plasma radially through the central chord. The exception was for Magnesium data where the line of sight was scanned through the minor radius towards the plasma edge. This gave a better resolved spectrum from the cooler plasma ion temperature  $T_i \sim 690 \text{eV}$ .

The Lyman- $\alpha$  lines were observed using the high resolution ( $\lambda/\Delta\lambda \sim 9000$ ) Johann ADP (101) crystal x-ray spectrometer, with a crystal radius of  $R=1100 \rightarrow 1300 \text{mm}$ . The x-ray lines in a waveband  $\Delta\lambda/\lambda \sim 0.1$  were recorded with Kodak DEF392 x-ray film in a flat cassette mounted tangentially to the Rowland Circle. A minimum of 10 DITE shots were integrated to increase the optical image density on film and gave a peak signal/noise ratio of  $\sim 50$ .

## **II Beam-Foil Experiment.**

This experiment was performed on the Oxford Folded Tandem accelerator as discussed in the previous chapter. A 39MeV  $\text{Ne}^{6+}$  ion beam was stripped and excited in a  $10 \mu\text{g}/\text{cm}^2$  Carbon foil and observed axially using a high resolution ( $\Delta\lambda/\lambda \sim 7000$ ) Johann KAP (002) x-ray spectrometer, with a crystal radius of  $R=1073 \text{mm}$ . An exposure time of 30 hours was needed as a result of the the low x-ray emission. The ambient temperature remained constant during the exposure at  $25.0 \pm 0.5^\circ\text{C}$ . The spectrum was Doppler-shifted ( $v/c=0.0642$ ). The observed lines were highly resolved ( $\Delta\lambda/\lambda \sim 5000$ ) and were essentially broadened by second order Doppler effects due to the spread of ion velocities in the beam. The fine-structure was clearly visible and could be accurately determined.

### **8.3.2 Spectrometer Wavelength Calibration and Errors.**

For measurement of small wavelength intervals, absolute wavelengths are less important than the dispersion characteristics. A relative wavelength measurement can be made and the doublet separation determined to good precision if the dispersion function is accurately known. This can be based on knowledge of the spectrometer alignment at the 1 minute of arc level. Bragg's law and the instrumental dispersion characteristics have been described in Chapter 2. The main interest here is to determine the contributing errors from all sources which define the final accuracy of the measurement.

#### **Calibration Errors.**

Table 8.1 exhibits the magnitude and sources of error which can arise from the relative wavelength measurement of  $5.4 \text{m}\text{\AA}$ . The most significant, in experiment I, is the large uncertainty in the crystal 2d spacing, discussed below. For experiment II, the crystal lattice

spacing is known accurately but an additional error for the Doppler shifted ion beam must be included.

**Table 8.1 Error contributions to the fine-structure measurement resulting from the crystal, instrument setting, refractive index and temperature effects.**

Error Contribution	$\Delta\lambda$ (mÅ)
Difference in crystal 2d spacing for ADP (see text):	0.021
Statistical accuracy of centroid fitting , film base stability & digitisation process:	0.012
Crystal radius error of $\pm 1$ mm:	0.005
Angle setting error $\pm 0.03^\circ$ :	0.003
Refractive index error $\pm 10\%$ :	0.001
Temperature variations $\pm 2^\circ\text{C}$ :	0.001
<b>Total error (added in quadrature):</b>	<b>0.025mÅ</b>

### Crystal Lattice Spacing and Characteristics.

#### Experiment I: Mg XII, Al XIII and Si XIV

Ammonium Di-hydrogen Phosphate (ADP,  $\text{NH}_4\text{H}_2\text{PO}_4$ ) is an inorganic crystal grown from solution. A literature search for the lattice spacing of ADP (101) reveals the following values:

- $2d_{10} = 10.6402 \pm 0.0012 \text{Å}$ , (Deslattes et al<sup>29</sup>).
- $2d_{20} = 10.6425 \pm 0.0005 \text{Å}$  and  $\alpha = (18.1 \pm 0.6) \times 10^{-6} / ^\circ\text{C}$ , (Barrus et al<sup>30</sup>).
- $2d = 10.658 \text{Å}$ , (Wyckoff<sup>31</sup>).

The first two results agree to within the quoted errors when their temperatures are normalised, but the third lattice spacing is considerably different. Barrus et al<sup>30</sup> point out that there can be variation in the inter-planar spacing depending on individual sample purity and source of origin. It can be shown that by accepting this level of uncertainty in the lattice spacing (the difference between the upper and lower values), contributes the major error to the total budget (see Table 8.1), but is generally small ( $\leq 0.4\%$  of the fine-structure interval).

The refractive index can be calculated for each wavelength from Compton and Allison<sup>10</sup>, see Chapter 2.1.4, taking into account the Phosphorus K-edge at  $5.79 \text{Å}$ , and expressed as  $\delta/\lambda^2$ . The results are:

- $\delta/\lambda^2 = 2.34 \times 10^{-6} \text{Å}^{-2}$  for Si Lyman- $\alpha$  at  $6.18 \text{Å}$ .
- $\delta/\lambda^2 = 2.40 \times 10^{-6} \text{Å}^{-2}$  for Al Lyman- $\alpha$  at  $7.17 \text{Å}$ .
- $\delta/\lambda^2 = 2.42 \times 10^{-6} \text{Å}^{-2}$  for Mg Lyman- $\alpha$  at  $8.42 \text{Å}$ .

Adopting a  $\pm 10\%$  error bar on the refractive index correction, which in fact covers the spread in the calculations, makes a negligible contribution to the error budget. Similarly, temperature effects on the lattice spacing produce a negligible error.

## Experiment II Ne X

Measured values of the KAP (001) crystal lattice spacing are in good agreement:

- $2d_{26}=26.6328 \pm 0.0001\text{\AA}$  reported by Bearden and Huffman<sup>57</sup>.
- $2d_{18}=26.6347 \pm 0.0012\text{\AA}$  and  $\alpha=(40.5 \pm 2.0) \times 10^{-6}/^{\circ}\text{C}$ , (Barrus et al<sup>30</sup>).

The refractive index can be similarly calculated from Compton and Allison<sup>10</sup>, taking into account the Potassium K-edge at  $3.437\text{\AA}$ , and expressed as  $\delta/\lambda^2$ . This compares well with the present author's calculations based on the data of other work:

- $\delta/\lambda^2=2.21 \times 10^{-6}\text{\AA}^{-2}$ , from Chapter 2.1.4.
- $\delta/\lambda^2=(2.30 \pm 0.05) \times 10^{-6}\text{\AA}^{-2}$ , calculations based on data from Bearden and Huffman<sup>57</sup> for Cu  $K\alpha$  radiation reflected in multiple orders.
- $\delta/\lambda^2=2.30 \times 10^{-6}\text{\AA}^{-2}$ , calculations based on data from Barrus et al<sup>30</sup>.

Error bars of  $\pm 10\%$  again have a negligible effect on the total error budget.

The next largest error arises from a combination of several effects which are difficult to separate individually. These include the statistical accuracy of the centroid location process (dependent on the S/N ratio), the digitisation process, unresolved satellite lines at the  $1 \rightarrow 2\%$  level (see 8.6) and the film stability. In the latter case, the overall film stability can be assumed to be as good as the base stability. This depends on film handling and processing, as well as the effect of temperature and humidity changes. The net result can either be an increase or decrease in the film dimensions from the initial recording of the x-ray image. For Kodak DEF film, a  $180\mu\text{m}$  polyester base is used and an upper limit of  $\pm 0.02\%$  can be estimated for the dimensional stability<sup>195</sup>.

The crystal bending jig and the film holder are mounted on high precision rotary stages (calibrated to 1 minute of arc =  $0.017^{\circ}$ ) at opposite ends of a rigid steel tube, which also forms part of the vacuum vessel. The instrument alignment process is potentially better than the arcminute level, but for the results here the absolute Bragg angle and wavelength setting is determined by the rotary stage calibration. Allowing an angle setting error of  $\pm 0.03^{\circ}$ , introduces a small change of  $0.003\text{m\AA}$  in the dispersion function of equation (2.38) and (2.39) for the interval measurement. Likewise, the instrument dispersion is immune to fairly large tolerances in the crystal radius R; an uncertainty of 1mm in R introduces a  $0.005\text{m\AA}$  error in Table 8.1.

### 8.3.3 Results.

Figures 8.2, 8.3 and 8.4 show the spectra for Magnesium, Aluminium and Silicon, respectively. The experimental data are labelled as points while the fitted functions are represented by solid lines. Differences between the experimental data and the fitted functions are shown in the window below labelled "Residuals to Fit". The fit is extremely good in all cases. Background film grain noise is the main contribution to the residuals and satellite line intensity is very low. The Magnesium and Aluminium spectra have the best S/N, mainly because of the higher recorded signal. The Aluminium data was also recorded

DITE Mg XII Lyman - $\alpha$  Doublet at 8.42 $\text{\AA}$

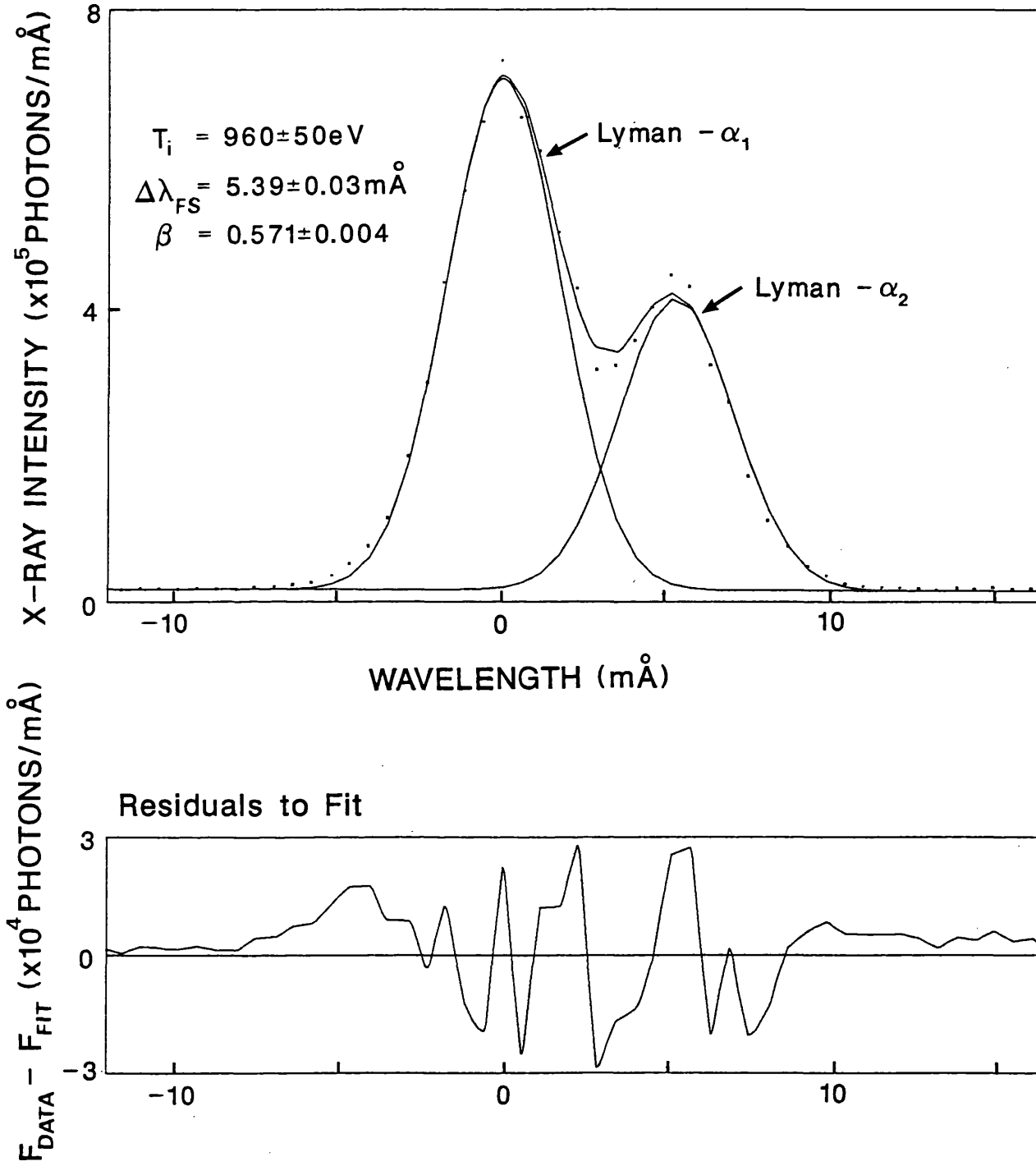


Figure 8.2 DITE Mg XII Lyman- $\alpha$  Spectrum at 8.42 $\text{\AA}$ .

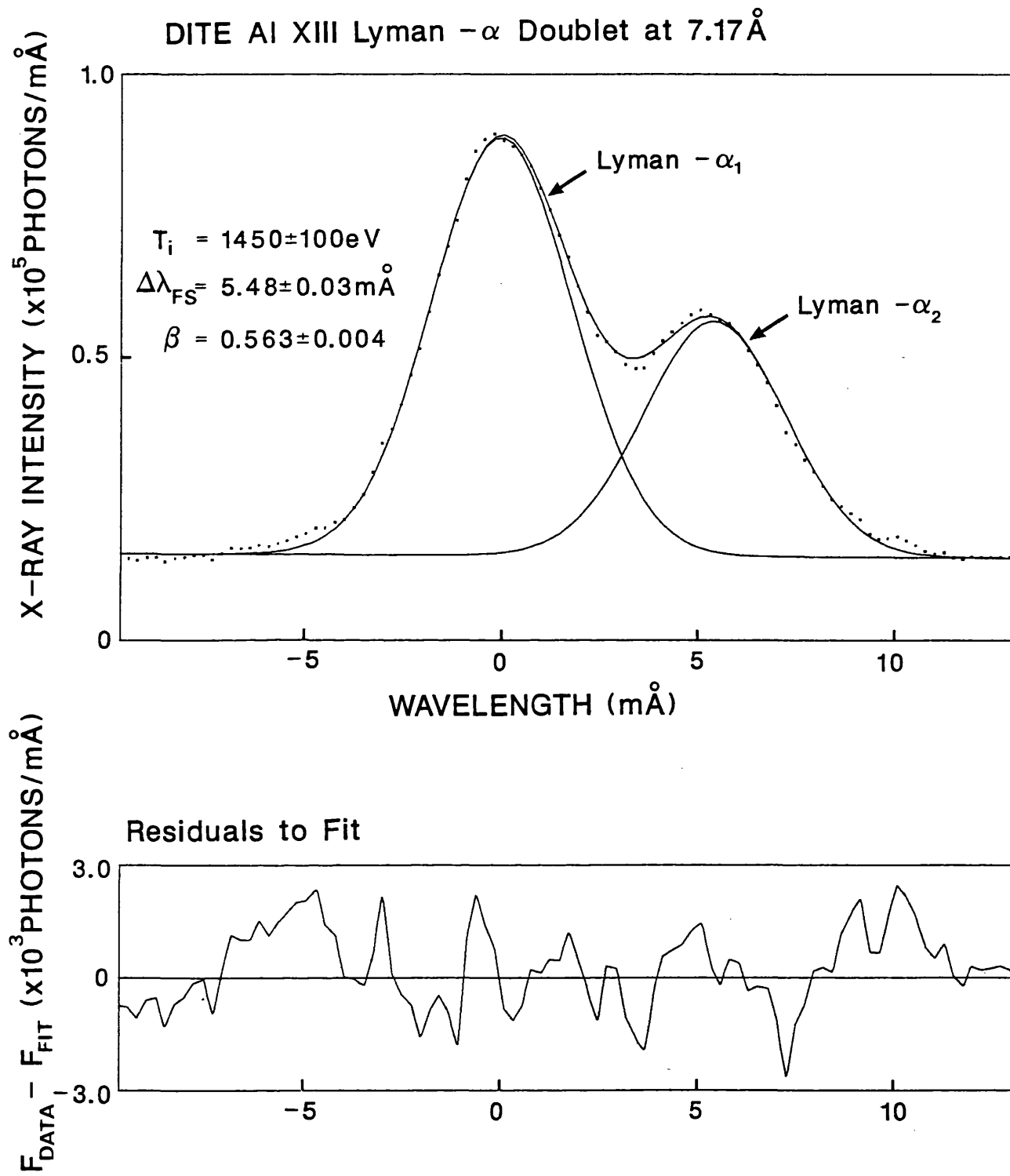


Figure 8.3 DITE Al XIII Lyman- $\alpha$  Spectrum at 7.17 $\text{\AA}$ .

### DITE SiXIV Lyman - $\alpha$ Doublet at 6.18 $\text{\AA}$

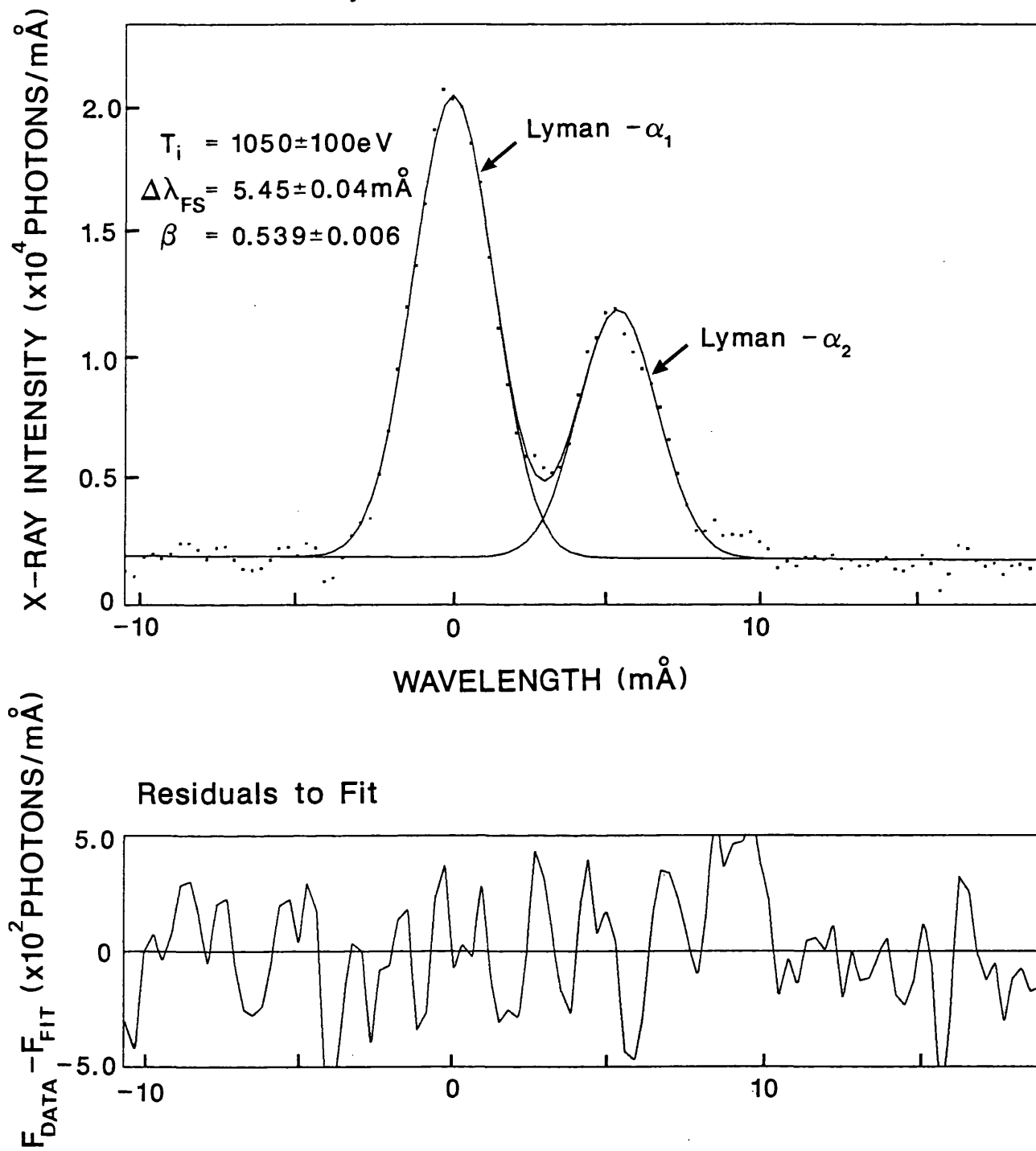


Figure 8.4 DITE Si XIV Lyman- $\alpha$  Spectrum at 6.18 $\text{\AA}$ .

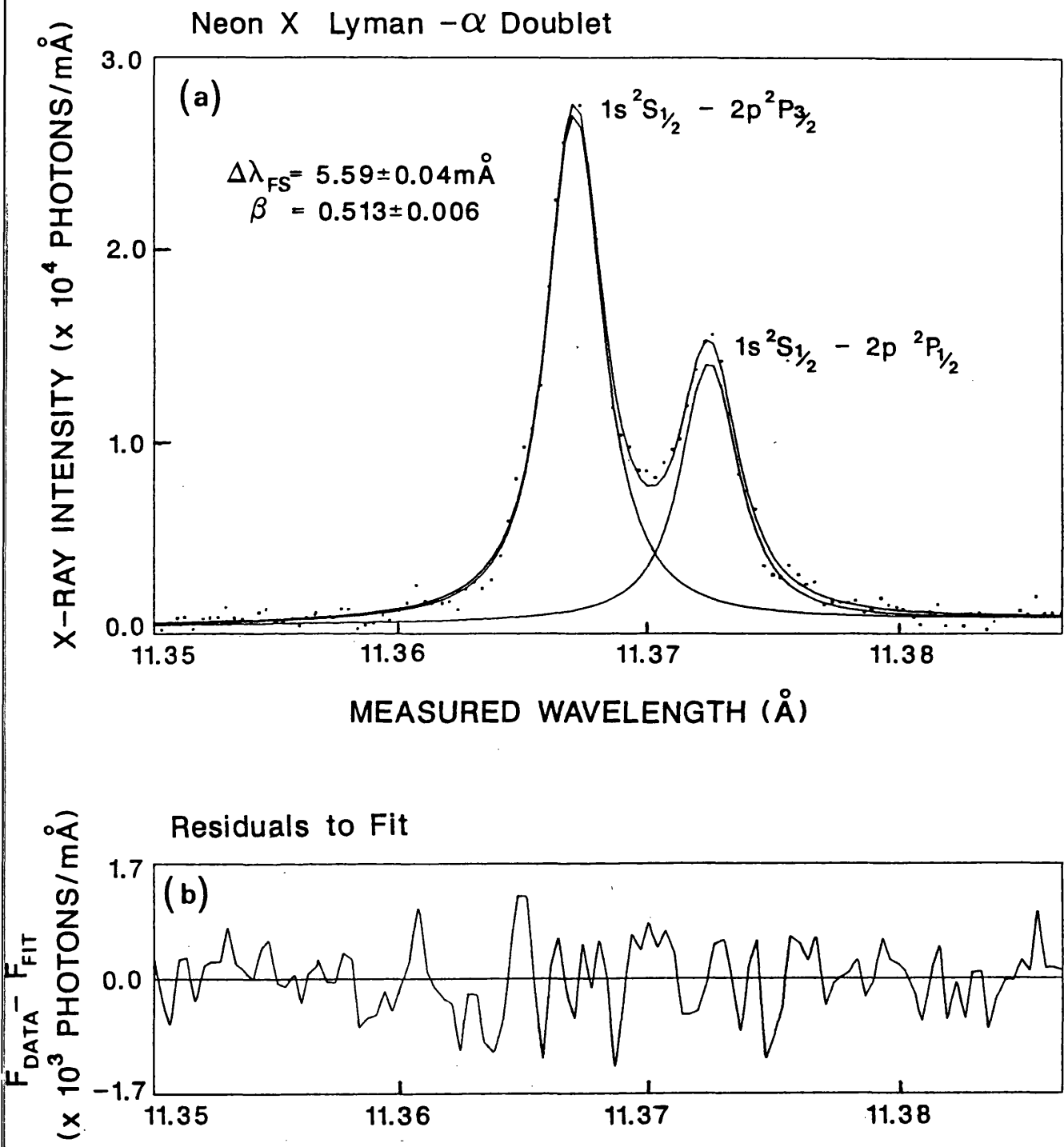


Figure 8.5 Blue-shifted beam-foil Ne X Lyman- $\alpha$  spectrum at 11.4 $\text{\AA}$ .

during neutral beam injection heating of the Tokamak which heats the ions directly and therefore has the greatest Doppler broadening. It can be noted that the doublet becomes better resolved with increasing atomic number  $Z$ . Figure 8.5 shows the Neon spectrum with the fine-structure clearly resolved.

## 8.4 Fine-Structure Intensity Ratio.

### 8.4.1 Collisional Mixing of the $n=2$ Levels.

Early observation of the Mg Lyman- $\alpha$  emission from solar flares by Grineva et al<sup>188</sup>, with the fine-structure resolved, gave an intensity ratio of  $\beta \sim 0.6$  where:

$$\beta = \frac{I(1s\ 2S_{1/2} - 2p\ 2P_{1/2})}{I(1s\ 2S_{1/2} - 2p\ 2P_{3/2})} \quad (8.5)$$

at variance with the expected statistical value of 0.5. This result for Magnesium was also confirmed by Phillips et al<sup>58</sup> who measured  $\beta=0.64$  from Solar Maximum Mission data. These results were not confined to solar flare plasmas and similar effects were observed for low concentration H-like Sulphur ions in the Alcator Tokamak<sup>196</sup> and various H-like ions in dense laser produced plasmas<sup>147</sup>. Vinogradov et al<sup>197</sup> produced calculations of  $\beta$  for optically thin laser produced plasmas which indicated the effect was due to collisional redistribution of the electron population from the  $2s\ 2S_{1/2}$  metastable level to the  $2p\ 2P_{1/2,3/2}$  levels. The effect was dependent on the plasma particles, density and temperature.

At low densities and coronal equilibrium, the  $2P_{1/2}$  and  $2P_{3/2}$  levels can be populated by direct excitation from the ground state, by recombination and cascades from higher levels. The observed line intensity by radiative decay to the ground state, is dependent on the level population, statistical weight and emission oscillator strength. The emission oscillator strength (proportional to the absorption oscillator strength) is in a ratio of 2:1 for the  $2P_{3/2} : 2P_{1/2}$  giving a  $\beta$ -ratio of 0.5. The  $2s\ 2S_{1/2}$  is similarly populated here, but makes a transition to the ground state by two-photon ( $2E1$ ) decay, Figure 8.1, and has no effect on the  $2P$  populations.

At high density, where the probability of collisional de-excitation between the  $n=2$  levels becomes of the same order or greater than the lifetime of the  $2P$  sublevels, the individual  $j$ -states are determined by a Boltzmann distribution and populated according to their statistical weights; the  $\beta$ -ratio returns to 0.5. Tallents<sup>198</sup> identifies the low and high density regimes as  $Z$  dependent by the relation:

$$\begin{aligned} \text{Low Density, } \beta=0.5 \text{ if } n_e \leq 10^2 Z^{10} \text{ cm}^{-3} \\ \text{High Density, } \beta=0.5 \text{ if } n_e \geq 3 \times 10^{14} Z^8 \text{ cm}^{-3} \end{aligned} \quad (8.6)$$

However, if the density is steadily increased from the low density regime, the probability of collisional de-excitation (by plasma particles) of the  $2S_{1/2}$  electron population becomes larger than the transition probability for radiative decay by two-photon emission. The  $2s$

$^2S_{1/2}$  level is very close to the  $2p\ ^2P_{1/2}$  level, the degeneracy of the states is removed by QED effects where the difference is known as the Lamb shift, and therefore particle collisions preferentially populate this state. The  $\beta$ -ratio is observed to increase from 0.5. Thus in this intermediate density regime the  $\beta$ -ratio can be used as a possible density diagnostic.

Equation (8.6) gives the start of the intermediate density regime for  $Z=12 \rightarrow 14$  as

$n_e \sim 6 \times 10^{12} \rightarrow 3 \times 10^{13} \text{ cm}^{-3}$  which is within the density conditions of DITE Tokamak.

Collisional effects are expected to be important. For a Hydrogen (or Helium) plasma with a small content of the H-like ion of interest, ion collisions are more important than electron collisions for close-lying levels and so proton (or  $\text{He}^{2+}$ ) impact excitation is the main collisional mechanism. The maximum value of  $\beta$  depends on the collision excitation rates and is changed by the plasma electron and ion temperature. Tallents<sup>198</sup> reports that an uncertainty in plasma temperature of a factor of two can lead, using this technique, to an order of magnitude error in the interpretation of electron density.

#### 8.4.2 Non-collisional Effects.

The  $\beta$ -ratio can be increased by other non-collisional effects depending on the plasma conditions and atomic number of the observed ion. The observed ratio  $\beta_{\text{obs}}$  can be described according to Ljepojevic et al<sup>199,200</sup>, who include unresolved satellites and the  $1s\ ^2S_{1/2} - 2s\ ^2S_{1/2}$  Magnetic Dipole (M1) transition contribution in a detailed study, as:

$$\beta_{\text{Obs}} = \eta_{\text{Sat}} \eta_{\text{M1}} \eta_{\text{Opa}} \beta_{\text{Col}} \quad (8.7)$$

The parameter  $\beta_{\text{Col}}$  is due to collisional effects,  $\eta_{\text{Sat}}$  represents the contribution from satellite lines in a small waveband around each fine-structure component,  $\eta_{\text{M1}}$  is from the M1 transition while  $\eta_{\text{Opa}}$  covers variations for optically thick plasmas. Although Tokamak plasmas are optically thin, the latter parameter is included for completeness (see Sylwester et al<sup>136</sup>). The  $\eta$  factors are usually greater than or equal to 1.0. Unresolved satellite lines are probably the most significant at low density and low electron temperature but are overtaken by collisional effects at intermediate densities.

#### Unresolved Satellite Contribution.

A contribution to the observed  $\beta$ -ratio can be produced by the presence of unresolved satellite lines caused by an additional spectator electron in a higher quantum level. The He-like satellite lines are of the form  $1snl-2pnl$  with  $n \geq 2$ . The  $n=2$  satellites are easily resolved to the long wavelength side of the doublet<sup>130</sup>. The  $n \geq 3$  satellites, however, are blended with the Lyman- $\alpha$  resonance lines, forming two series which approach each line with a separation scaling as  $n^{-3}$  (Dubau et al<sup>201</sup>).

In Tokamak plasmas, the upper level is populated by dielectronic recombination of the Hydrogenic ion. This occurs where an electron is captured from the continuum while simultaneously exciting the ground state electron. The resultant doubly excited states are above the ionization limit for the He-like ion. The ion stabilises either by autoionization,

where the excited electron is ejected leaving the H-like ion in the ground state, or by a radiative transition. The latter are then observed as satellite lines. The satellite line intensity  $I_s$  is dependent on the dielectronic capture rate  $C_d(T_e)$  while the main 1s-2p resonance line intensity  $I_r$  is determined by the collisional excitation rate  $C_r(T_e)$  from the ground state. The intensity ratio  $I_s/I_r$ , assuming a Maxwellian distribution for the electron energy, can be determined, as discussed in Chapter 5.2. The ratio is independent of electron density and ionization balance at low Tokamak densities and varies only with the electron temperature (Dubau and Volonté<sup>86</sup>).

At low Z, the unresolved satellite contribution can be small at high electron temperatures since the dielectronic rate coefficient decreases with increasing electron temperature  $T_e$ . For example, at  $T_e=0.5 \rightarrow 1$  keV the higher quantum satellites in a 5.4mÅ waveband centred on each Lyman- $\alpha$  component are calculated<sup>200</sup> to contribute 3.6 $\rightarrow$ 1.7% to the observed  $\beta$ -ratio for Silicon Lyman- $\alpha$ . This is confirmed by the very low intensity of the well resolved n=2 satellites ( $1s2s\ ^1S_0-2s2p\ ^1P_1$ ,  $1s2p\ ^1P_1-2p^2\ ^1D_2$ ) which are just visible above the background noise. Satellite intensity relative to the resonance line becomes significant for  $Z \geq 20$  because the radiative transition probability scales according to  $Z^4$  while the auto-ionization probability varies slowly with Z.

#### **Optical Depth Effects.**

Opacity effects must also be considered since the absorption oscillator strength for the  $2p\ ^2P_{3/2}$  line is twice that of the  $2p\ ^2P_{1/2}$  line as discussed in some detail in Chapter 6. This gives increased absorption of the  $^2P_{3/2}$  line with modest optical depths ( $\tau_o \geq 0.1$ ) and an observed increase in the  $\beta$ -ratio ( $\eta_{opa} \geq 1.04$ ). Some plasma geometries may reduce the ratio. Sylwester et al<sup>136</sup> have investigated solar flare spectra, from the Intercosmos 7 satellite, of the Mg Lyman- $\alpha$  doublet in some detail. Their analysis shows that the ratio falls within the interval  $\beta=0.38 \rightarrow 0.66$  but cannot be explained by satellites or collisional effects alone. (Solar flare density of  $n_e \sim 10^{11} \text{cm}^{-3}$  in this instance is too low). They conclude that absorption of resonance lines in a non-spherical plasma volume can be the only explanation for all observed values.

As a rough indication, optical depth should be calculated for the resonance line radiation if the population density of ions in the lower level of the Lyman- $\alpha$  transition, the ground state here, (in units of  $\text{cm}^{-3}$ ) x scalelength product  $n_l l$ , where  $l$  is the length of plasma along the line of sight, approaches  $2 \times 10^{15} \text{cm}^{-2}$ . In the case of DITE,  $n_l l \sim 10^{10} \text{cm}^{-2}$  will be the upper limit for the ions studied here and therefore  $\eta_{opa}$  can be set at unity.

#### **The Magnetic Dipole Transition.**

The  $2s\ ^2S_{1/2}$  excited state can stabilise by an allowed two-photon process (2E1) to the ground state. However, there is a competing forbidden process by magnetic dipole decay (M1) which becomes relevant at high Z. This (M1) line cannot be resolved from the  $2p\ ^2P_{1/2}$  line and therefore will increase the  $\beta$ -ratio in proportion to its intensity. The radiative transition

probabilities  $A_{M1}$ ,  $A_{2E1}$  corresponding to the M1 and 2E1 decays have been derived by Drake<sup>202</sup> and Breit and Teller<sup>203</sup> as:

$$\begin{aligned} A_{M1} &= 2.496 \times 10^{-6} Z^{10} \text{ (s}^{-1}\text{)} \\ A_{2E1} &= 8.228 Z^6 \text{ (s}^{-1}\text{)} \end{aligned} \quad (8.8)$$

The  $Z^{10}$  dependence of the magnetic dipole transition rapidly increases the radiative probability of this process for high  $Z \geq 20$  ions. The intensity ratio of the M1 line to the Lyman- $\alpha_2$  line can be written as:

$$\frac{I(M1)}{I(Ly-\alpha_2)} = c \frac{A_{M1}}{A_{M1} + A_{2E1}} \quad (8.9)$$

where  $c$  refers to the ratio of the excitation rates of the  $2s \ ^2S_{1/2}$  and  $2p \ ^2P_{1/2}$  levels from the ground state  $1s \ ^2S_{1/2}$ , and depends on  $T_e$ . Bitter et al<sup>187</sup> quote  $c=0.63$  for  $T_e=2\text{keV}$  for Ti XXII; assuming a value of  $c \sim 0.5$  can give a good approximation for the magnetic dipole intensity here. For  $Z=10 \rightarrow 14$  in equations (8.8) and (8.9),  $I(M1)/I(Ly-\alpha_2)$  has values in the range  $0.0015 \rightarrow 0.0058$  and is clearly a very small contribution to the observed  $\beta$  value.

#### 8.4.3 Experimental Data.

The experimental Tokamak values of  $\beta$  are in the range  $0.54 \rightarrow 0.57$  for the different  $Z$  and are listed in Table 8.2 below. Average central chord integrated electron density is determined with a microwave interferometer<sup>204</sup> and the electron temperature is measured from Thomson scattering<sup>205</sup> data. Additional  $n_e$  and  $T_e$  information come from the R- and G-ratios for He-like Si described by Keenan et al<sup>97</sup>, which is observed simultaneously with the Lyman- $\alpha$  emission for Al and Si. These different measurements show some variation giving  $\sim 15\%$  error bars for  $T_e$  and  $\sim 20\%$  error bars for  $n_e$ . The general trend of the observed  $\beta$ -ratio from DITE Tokamak is to decrease with increasing  $Z$  because of the expected higher density threshold for collisional mixing. The experimental points are compared with the calculations of  $\beta_{obs}$  of Sylwester et al<sup>136</sup> for Mg and Ljepojevic et al<sup>200</sup> for Si. The results for Mg are plotted on Figure 8.6. The theoretical satellite contribution is chosen for the waveband  $5.4\text{m}\text{\AA}$  centred on each Ly- $\alpha$  component. All calculations are corrected for the small contribution from the Magnetic Dipole transition. The Al and Si data points are scaled for density using the  $n_e/Z^7$  interpolation<sup>200</sup> and plotted on Fig 8.6.

It can be seen from the theoretical curves that collisional mixing becomes dominant causing the  $\beta$ -ratio to increase rapidly with electron density. The experimental points show good agreement with the predicted curves, though tend to be slightly high. This could be explained as an overestimate of  $T_e$  for the measurements or more likely as a result of collisional effects from other light plasma impurities like Carbon or Oxygen which are more abundant, at the level of  $\sim 1 \rightarrow 2\% n_e$ . The injected element ion density is typically  $\sim 0.01\% n_e$ .

Comparison Between Observed  $\beta$ -ratios and Theoretical Calculations

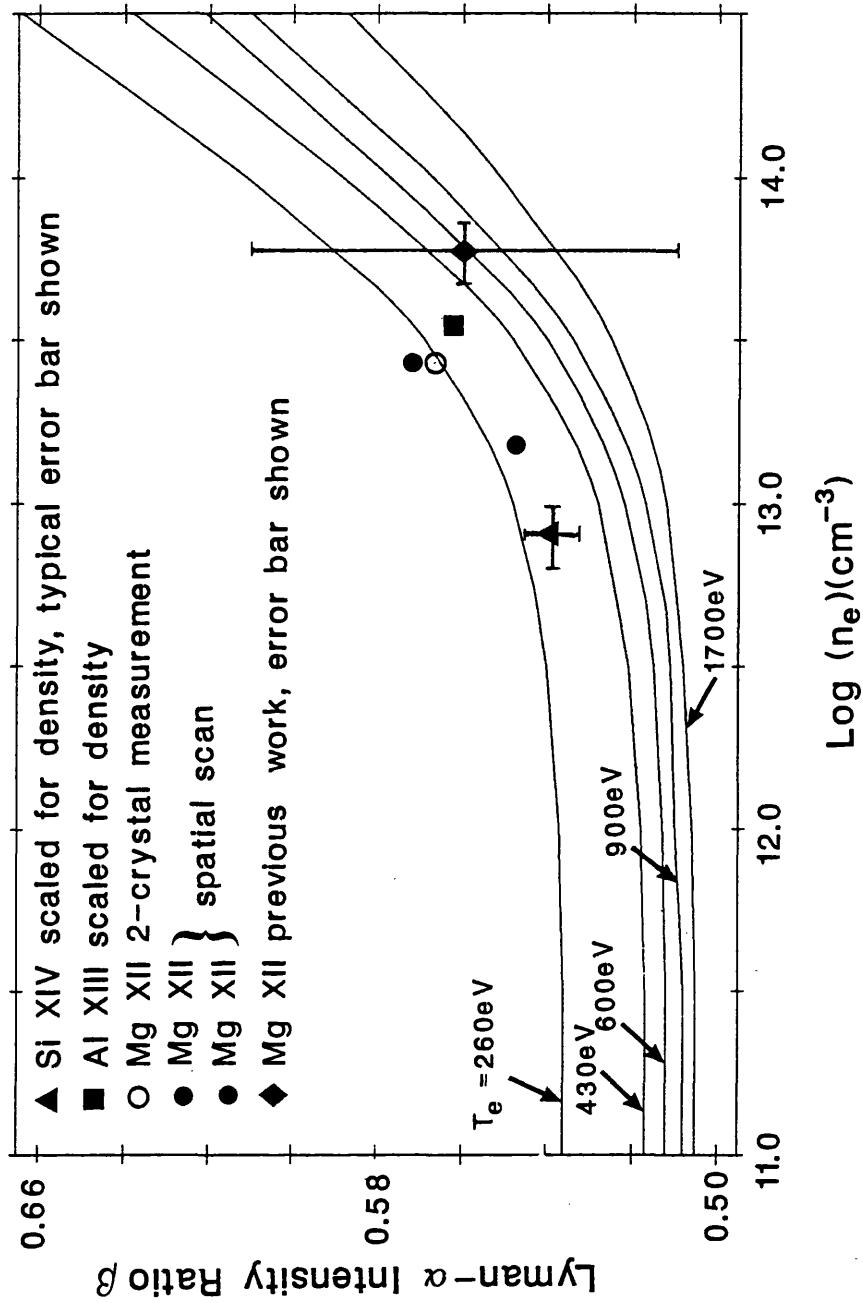


Figure 8.6 Measured  $\beta$ -ratios for Mg XII, Al XIII and Si XIV ions (points) are compared with Mg XII theoretical predictions (solid curves) for different electron temperatures. The Al and Si points are scaled for density, see text. Error bars on Si point show typical tolerances for all other points, except previous Mg XII result with larger error bars due to Fe L-shell contamination. Mg points which exhibit highest  $\beta$ -ratios  $\sim 0.57$  also happen to be plasmas with highest impurity concentrations. This correlation is likely to be verified with further investigation.

**Table 8.2 Experimental  $\beta$  values.**

Z	Element	$N_e$ ( $\times 10^{13} \text{cm}^{-3}$ )	$T_e$ (eV)	$\beta_{\text{Obs}}$
10	Neon	N/A	N/A	$0.513 \pm 0.006$
12	Magnesium	2.7	900	$0.571 \pm 0.004$
		2.7	1000	$0.567 \pm 0.002^\dagger$
		1.5	500	$0.547 \pm 0.006$
13	Aluminium	4.7→6.0	700	$0.563 \pm 0.004$
14	Silicon	2.4→3.0	800	$0.539 \pm 0.004$

$^\dagger$  2-crystal spectrometer measurement.

For comparison the Neon Lyman- $\alpha$  beam-foil observation has a value of  $\beta=0.513\pm 0.006$ , with an equal error from statistics and the film calibration. The M1 transition is likely to be negligible here since its maximum intensity will be  $\sim 0.2\%$  of the  $^2P_{1/2}$  over a decay length of  $\sim 10^5 \text{cm}$ , assuming direct excitation from the ground state. The likely contribution is from satellite lines though the strongest  $n=2$  satellites were not observed.

## 8.5 Review of Fine-Structure Splitting Measurements.

### 8.5.1 Discussion of Measurements from Other Sources

Table 8.3 and Figure 8.7 allow a comparison between the fine-structure interval measurements and theory for different atomic numbers  $Z=10\rightarrow 36$ . As stated earlier, there are very small differences between the calculations; the theoretical results of Mohr<sup>27</sup> for the absolute wavelength of the Ly- $\alpha_1$  and fine-structure interval are indicated in columns 3 and 4. The absolute wavelength calculations are accurate to the last significant figure. The fine-structure interval expressed as a wavelength difference  $\Delta\lambda_{\text{FS}}$ , as discussed in section 8.2, varies very slowly with atomic number.

The spectra are observed from various x-ray sources; Tokamak plasmas and beam-foil are the most common, but a few results also come from beam-gas target and solar flares. These are shown in column 5 and have been converted to a wavelength difference. Most of the experiments are specific attempts to determine QED effects, the fine-structure itself or adjacent satellite structure; they should therefore represent the best available measurements.

After an initial study of Table 8.3, it is surprising that better accuracy has not been achieved for the fine-structure interval  $\Delta\lambda_{\text{FS}}$ . This is particularly true for  $Z\geq 17$  (Chlorine) where the doublet becomes clearly resolved,  $\lambda/\Delta\lambda_{\text{FS}}\leq 800$ . The results are graded from **A**→**D** in column 6 according to their quoted accuracy: **A** is for 0.5% or better, **B** is for 0.5%→1%, **C** is for 1→2% and **D** signifies results with errors greater than 2%. Less than half of the results are quoted to 1% or better.

**Table 8.3 Comparison of  $n=2$   $2P_{3/2}-2P_{1/2}$  fine-structure interval  $\Delta\lambda_{FS}$  measurements with theory for different  $Z=10\rightarrow 36$ .**

Z	Element	Ly- $\alpha_1$ $\lambda^{\S}$ (Å)	Theory $^{\S}$ (mÅ)	Experiment (mÅ)	$\gamma$ #	X-ray Source $^{\dagger}$ and Reference
10	Neon	12.13208	5.4081	5.59 ± 0.04	B	BF This Work
12	Magnesium	8.419200	5.4096	5.7 ± 0.6 5.39 ± 0.03	D A	Tok Dunn et al [215] Tok This Work
13	Aluminium	7.176317	5.4104	5.4 ± 0.1 5.48 ± 0.03	C A	Tok Dunn et al [215] Tok This Work
14	Silicon	6.180426	5.4112	5.5 ± 0.1 5.45 ± 0.04	C B	Tok Dunn et al [215] Tok This Work
16	Sulphur	4.727351	5.4131	5.40 ± 0.04 5.3	B	BF Schleinkofer et al [193] Tok Källne et al [196]
17	Chlorine	4.185329	5.4141	5.43 ± 0.04 5.50 ± 0.04 5.38 ± 0.28	B B D	Tok Källne et al [206] BF Richard et al [78] BGT Deslattes et al [165]
18	Argon	3.731101	5.4152	5.3 ± 0.2 5.7 ± 0.5 5.37 ± 0.04 5.42 ± 0.03 5.30 ± 0.05 5.5 ± 0.8	D D B A B D	Tok Bartiromo et al [207] BF Briand et al [208] Tok Marmar et al [191] BGT Beyer et al [166] Tok Beiersdorfer et al [68] BGT Beyer et al [209]
20	Calcium	3.018480	5.4175	5.35 ± 0.11	C	SFl Seely and Feldman [210]
22	Titanium	2.491198	5.4200	5.4 ± 0.1 5.4	C	Tok Bitter et al [187] BF Dohmann et al [211]
26	Iron	1.778016	5.4257	5.40 ± 0.05 5.5 ± 0.1 5.6 ± 0.1 5.40 ± 0.05 5.49 ± 0.17	B C C B D	Tok Beiersdorfer et al [68] BF Hailey et al [212] BF Briand et al [213] BF Briand et al [190] BF Silver et al [185]
28	Nickel	1.530340	5.4288	5.38 ± 0.08	C	Tok Bombarda et al [214]
30	Zinc	1.330516	5.4322	5.48 ± 0.11	C	BF Hailey et al [212]
32	Germanium	1.166963	5.4358	5.44 ± 0.02	A	BF Laming et al [63]
36	Krypton	0.917794	5.4435	5.52 ± 0.10	C	BF Briand et al [190]

**Key:**

References are indicated in square brackets: [ ].

$^{\S}$ Theoretical results from Mohr <sup>27</sup>.

$\#$ Grading of experiment accuracy,  $\gamma$ -

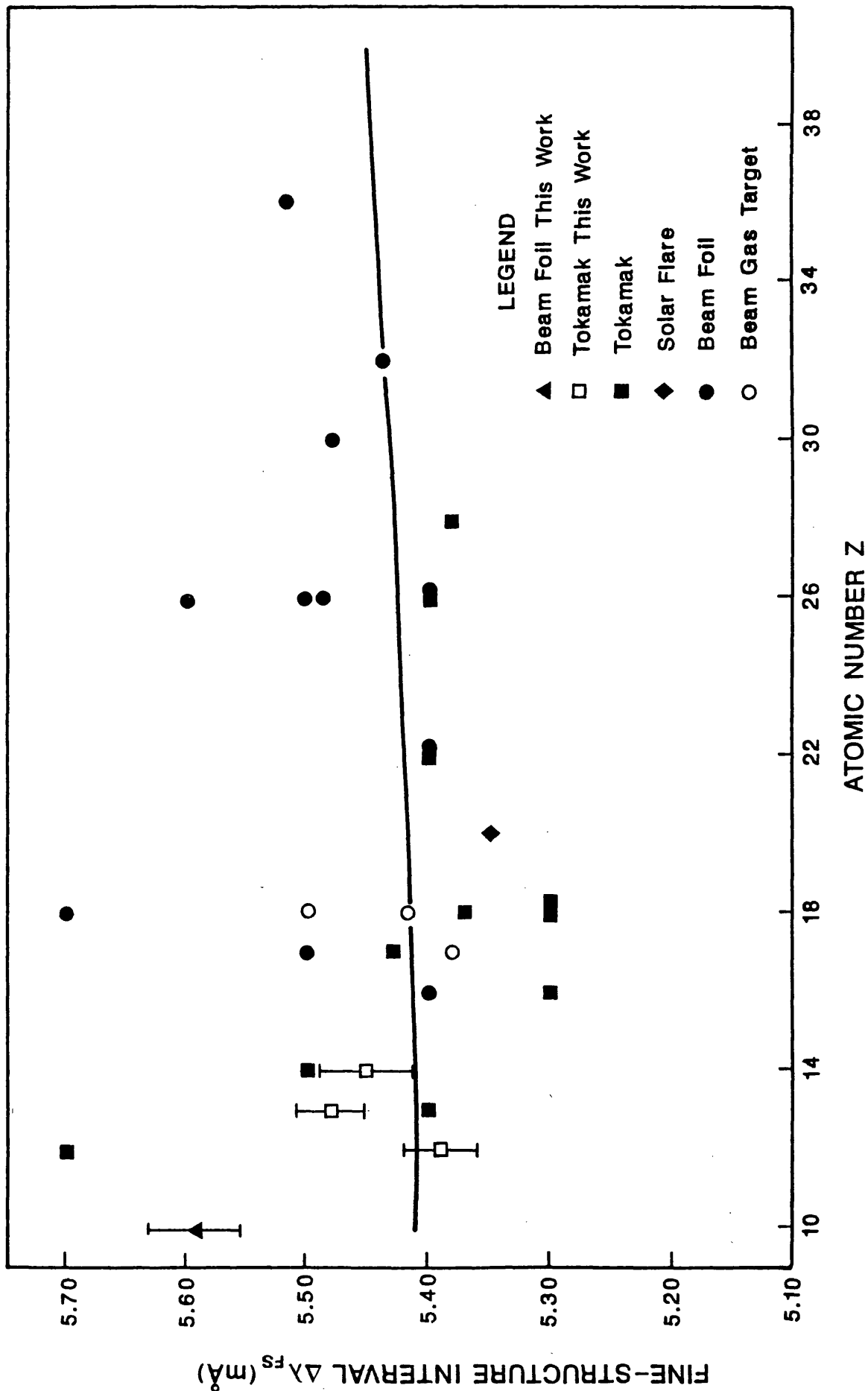
- A:  $\gamma \leq 0.03\text{mÅ}$ , better than 0.5%
- B:  $0.03 < \gamma \leq 0.06\text{mÅ}$ , between 0.5% and 1%.
- C:  $0.06 < \gamma \leq 0.12\text{mÅ}$ , between 1% and 2%.
- D:  $0.12\text{mÅ} < \gamma$ , less than 2%.

$^{\dagger}$ X-ray Sources:

- BF Beam-foil.
- BGT Beam Gas Target.
- SFl Solar Flare.
- Tok Tokamak

Figure 8.7 (Over the page) is a comparison between theoretical calculations, by Mohr<sup>27</sup>, and experimental measurements of the Lyman- $\alpha$  fine-structure wavelength interval  $\Delta\lambda_{\text{FS}}$  for various atomic numbers. For clarity, error bars are only indicated for the medium  $Z$  data of this work; all results are tabulated on Table 8.3 with references. The experimental data is mostly from Tokamak plasmas and beam-foil interactions. Other results are available from solar flares and beam-gas target x-ray sources. Few experimental results are available for low  $Z \leq 16$  or high  $Z \geq 30$  elements. Considerable spread in the experimental data points is apparent. Very few measurements, however, are accurate enough to test the theory, though there may be some evidence of higher values for beam-foil sources.

# Comparison of n=2 Fine-Structure Interval Measurements with Theory Against Z



There also appear to be systematic trends which are source dependent. If the measurements with error bars greater than 10% are neglected, then:

- (1) Beam-foil measurements, although within experimental error of calculated values, are mainly high. The 11 measurements, ignoring the fact that they come from different Z, give a mean value  $\Delta\lambda_{FS}$  of 5.4840mÅ with a standard deviation of  $\sigma=0.070\text{mÅ}$ .
- (2) Tokamak results show a more even spread around theory, but tend to be lower. The 13 measurements give a mean value of  $\Delta\lambda_{FS}$  of 5.392mÅ with a standard deviation of  $\sigma=0.065\text{mÅ}$ .
- (3) The remaining three measurements are very close to the Tokamak results with  $\Delta\lambda_{FS}$  of 5.383mÅ and a standard deviation of  $\sigma=0.035\text{mÅ}$ .
- (4) For comparison, a mean value of the theoretical results is  $\Delta\lambda_{FS}=5.425\text{mÅ}$  and  $\sigma=0.013\text{mÅ}$  for all  $Z=10\rightarrow 40$ .

These results have been determined independently by different experimental groups using different spectrometers: the instruments use single crystal reflection techniques, either collimated flat crystals scanned through the waveband sequentially or static curved crystal Johann spectrometers which observe the complete band simultaneously. Therefore, it can be concluded that there should be no systematic errors in the whole data set. Although there is an overlap in the error bars ( $\pm 1.2\%$ ) for the mean values of the Tokamak and beam-foil experiments, the two means are separated by 1.7% of the interval. The Tokamak mean is closer ( $-0.033\text{mÅ}$ ) to the theoretical calculation than the beam-foil mean ( $+0.059\text{mÅ}$ ). This is reinforced by the smaller data set of other measurements (3) exhibiting close agreement with the Tokamak data but showing no overlap with beam-foil measurements. There is sufficient evidence to suggest that the systematic difference between these measurements, is source dependent and may be due to a physical effect not considered up to now. Stark shifts and charge exchange in beam-foil interactions may contribute here.

### 8.5.2 Satellite Lines

The presence of satellite lines or other contaminating lines, blended with the doublet, can often be observed as an asymmetry to the line shape or as a variation in the Lyman- $\alpha$  intensity ratio  $\beta$ . They may introduce shifts to the centroid positions depending on their wavelength and intensity. Fast beam experiments have some advantage here since they are chemically and isotopically pure. Tokamak plasmas tend to contain various impurities, often having elements with spectral lines superimposed on the waveband of interest.

However, satellite lines in fast beam experiments are usually more intense than in Tokamaks and pose more of a problem. (Compare the results for Titanium from Dohmann et al<sup>211</sup> with those from Bitter et al<sup>187</sup> in Figure 8.8). In low density Tokamak plasmas, satellite structure results from dielectronic recombination of the H-like ion and is fairly well understood. Charge exchange processes which occur in beam-foil stripping, preferentially populate high n' and are state selective processes. Fast beam spectra also

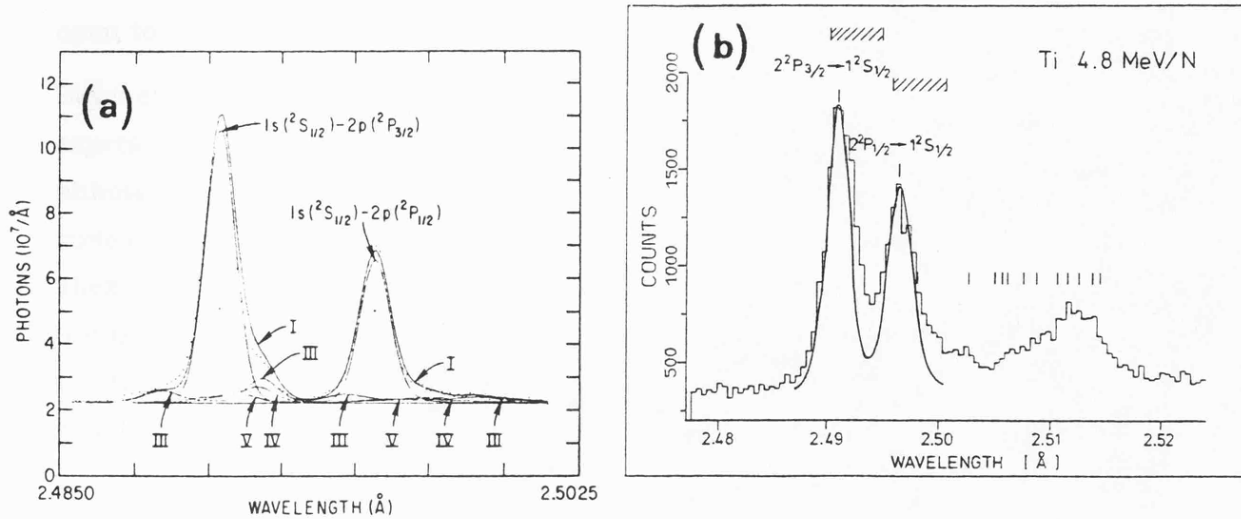


Figure 8.8 Compares the Ti XXII Lyman- $\alpha$  from a Tokamak plasma (a), with beam-foil sources (b). The spectral resolution is clearly better in (a). Reduced satellite contributions in (a) would be expected to produce a more accurate determination of the fine-structure splitting

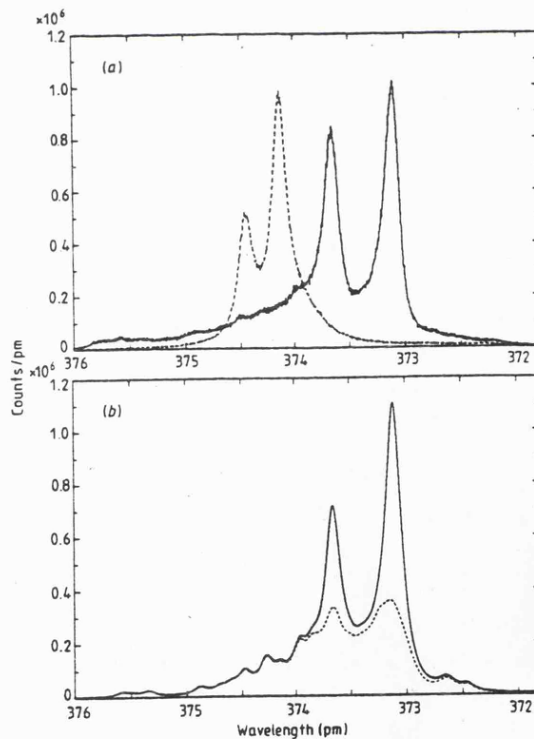


Figure 8.9 Top frame shows Argon XVIII Lyman- $\alpha$  spectrum (full curve) from beam-gas target source (after Beyer et al<sup>166</sup>), and Potassium K $\alpha$  calibration spectrum (broken curve). Bottom frame indicates theoretical spectrum with satellite contributions as broken curve. The Ar XVIII Lyman- $\alpha$  measurements will be affected by the satellite lines.

exhibit a greater spread of charge states. The error in the fine-structure measurement, where the two resonance lines sit on a continuum of satellites, is then model dependent and open to interpretation.

Beyer et al<sup>166</sup> have used this treatment to analyse the data, from a beam-gas target experiment, to determine the Lamb shift for H-like Argon recoil ions. The Lyman- $\alpha$  lines although clearly resolved, sit on a continuum of  $n \geq 3$  satellite lines, see Figure 8.9. This is in spite of minimising satellite production by using a heavy  $U^{66+}$  5.9MeV/nucleon ion beam. Their fine-structure measurement agrees to good precision with theory at the  $\sim 0.5\%$  level, but is finally dependent on the satellite line interpretation. They approach this problem on two fronts, based on a theoretically calculated satellite spectrum, and separately from a simple empirical viewpoint. The two methods, when applied to different subsets of data, give very good agreement for the mean  $\Delta\lambda_{FS}$  to  $0.001m\text{\AA}$ , but with a stated preference for the empirical fitting procedure. However, it is interesting to note that no comment is made about the different Lyman- $\alpha$  intensity  $\beta$ -ratios of  $\sim 0.5$  and  $\sim 0.75$  for the respective theoretical and empirical procedures. This is a significant point which appears to have been overlooked and weakens the argument for the quoted high precision.

### 8.5.3 Satellite-Free Spectra

The best way of overcoming the satellite problem is either by creating satellite-free spectra or by improving the observed spectral resolution as proposed by Laming et al<sup>176</sup>. Some experiments have produced one-electron spectra largely free of satellite contamination:

- (1) A beam of fully stripped Cl nuclei capture a single electron in a He gas target (Deslattes et al<sup>165</sup>). Two electron capture is very low.
- (2) Varying the energy of a Cl beam affects the degree of satellite production in foil-excitation experiments (Richard et al<sup>76</sup>). Higher beam energies result in less intense satellite structure. This is observed to reduce the high fine-structure value slightly but is still within the quoted experimental error.
- (3) Laming et al<sup>63</sup> use a beam of bare Ge nuclei which capture a single electron and are excited in a thin foil target. He-like and Li-like charge states are observed to be very low, but an increase in the fine-structure interval of  $0.04m\text{\AA}$  is noted with thickness of the final exciting foil.

Satellite contamination still has to be treated carefully in fast heavy ion beams and to a lesser extent for medium  $Z$  elements in Tokamak plasmas.

## 8.6 Conclusions

Precision measurements of the 2p fine-structure interval at the 0.5% level are given for medium  $Z$  ions. The accuracy of the results is comparable to the best fine-structure measurements that have been made to date. It is remarkable to be able to determine this difficult region of the periodic table accurately, where previously there have been few measurements. The use of a Johann spectrometer giving high spectral resolution, good

sensitivity and simultaneous coverage of the waveband (thus cancelling time variations in the source emission) is essential in this respect. It may be commented that while the agreement with theory is very close for the Tokamak data, it is not sufficient to resolve the apparent discrepancy between different x-ray sources exhibited in Table 8.3.

The beam-foil Neon fine-structure measurement, while being better resolved, free from satellite lines and determined with a similar precision, is perplexing due to the fairly large difference with theory. No other precise experimental values are available for comparison and so it may be interesting to repeat the measurement for various atomic numbers on Tokamak, beam-foil and beam-gas target sources with the same crystal and instrument.

Tokamak plasmas have some advantages for use in precision spectroscopy when compared to beam-foil sources; for example they are an intense x-ray light source and do not suffer from large Doppler shifts. Plasma poloidal and toroidal rotation may be considerable under some conditions but in principle the viewing geometry can be chosen to minimise these effects. Beam-foil sources, however, are more commonly used for precision spectroscopy on account of better intrinsic spectral resolution.

The Lyman- $\alpha$  intensity ratio has been accurately measured and successfully interpreted for Tokamak plasma conditions and beam-foil interactions. The results described for DITE suggest that collisional and satellite effects contribute equally to the departure of  $\beta$  from 0.5 for Silicon. However, collisional mixing dominates by a factor of 3 for Magnesium. It may be possible to use the  $\beta$ -ratio of medium Z Hydrogenic ions as a density diagnostic (up to  $n_e = 10^{15} \text{ cm}^{-3}$ ) for Tokamak or other similar low density plasmas. An accurate interpretation of this diagnostic requires a priori knowledge of the electron temperature and satellite contributions.

Finally, the  $\beta$ -ratio is a useful guide to the presence of satellite lines in all precision experiments but particularly for beam-foil and beam-gas target sources. Proper interpretation of this ratio is crucial for accurate measurement of the spin-orbit effect and should not be ignored.

## Final Conclusions.

In summary, this Johann spectrometer has been used to good effect on a number of disparate laboratory x-ray sources. The versatility of the design has been clearly shown when optimised to the different experiments. However, the common feature in each case has been the need for high resolving power. The instrument has been more than capable in every experiment: ion temperature measurements from Doppler broadened emission lines on DITE Tokamak, electron density from satellite line intensity ratios in laser produced plasmas and axial observation of foil-excited fast ion beams. In the latter experiments the full potential of the spectrometer was realised. The transitions of the He-like Silicon and H-like Neon ions were the best resolved spectral lines in this wavelength region to date.

High spectral resolution has allowed the study of the Lyman- $\alpha$  fine-structure in some detail: the measurement of non-statistical intensity  $\beta$ -ratios on DITE has been interpreted as a combination of collisional and unresolved satellite line effects. The measured  $\beta$ -ratios have also been useful for estimating resonance line opacity in dense laser produced plasmas. Measurements of the fine-structure separation  $\Delta\lambda_{FS}$  are of continued interest in the field of atomic spectroscopy.

This work can be concluded with a number of suggestions for the improvement of the spectrometer specification outlined in Part I. These should be combined with proposed future experiments that are a natural progression of this research. These can be found in the conclusions of the chapters in Part II.

## **Appendices**

# Appendix I.

## Film Handling and Development Procedures.

The procedure, below, from Henke et al<sup>70</sup>, was followed in the development of Kodak DEF 392 x-ray film:

### Kodak Type DEF (DEF-392)

The Kodak DEF or DEF-392 (the difference being the sheet-film or 35-mm format) should be handled under Kodak Safelight Filter no. GBX-2 with a 15-W bulb, no closer than 1 m from the film. This practice should be followed during processing as well. Special care should be taken not to bend the film too sharply, since doing so will result in many minute cracks in the emulsion. Fresh processing solutions should be used whenever possible; this is especially true for the developer because it will deteriorate when in an open tray or processing tank. The processing of the film is as follows, with all solutions, including the wash water, at 68°F in either a developing tank for roll film or a tray for sheet film:

1. Development: 5 min in Kodak GBX developer with gentle but continuous agitation.
2. Rinse: 30 sec in Kodak Indicator stop bath with gentle but constant agitation.
3. Fixing: 6 min in Kodak Rapid Fixer or GBX fixer with constant agitation.
4. Wash: 30 min in running water then 30 sec in Kodak Photo-Flo 200 working solution.
5. Drying: At room temperature in still air, or at elevated temperatures not over 100°F in moving air.

In drying the film at elevated temperatures, care should be taken not to allow the relative humidity at the film to drop below 50%, as this can cause excessive shrinkage of the emulsion and a possible distortion of the image. The use of Photo-Flo wetting agent will help promote uniform drying of the film by either method, with a minimum of drying artifacts and water spots.

### Kodak Type SB-5 (SB-392)

Recommended film handling and development procedure is that described above for Kodak DEF.

Kodak D-19 developer was used regularly instead of GBX, keeping temperature and developing time constant, and it was found to give satisfactory results. Ilford Hypam fixer for ordinary black and white film was often used and no deterioration in the film quality was noticed.

## Appendix II.

### Voigt Profile Synthesis.

The following Fortran code will synthesise the Voigt line parameters of the table by Tudor Davies and Vaughan<sup>79</sup>. The fast operation of the code relies on the NAG routine DO1ARF to evaluate the integral in equation (4.26) Chapter 4, for each point on the Voigt profile. The Voigt parameter  $\eta$  (ETA in code) is chosen; the intensity position on the profile, as a fraction of the peak intensity, is also requested.

The half width value is expressed in absolute units and as a fraction of the half width at half maximum (HWHM). Peak intensity for chosen  $\eta$  is also given. The integral is evaluated in Function F1. Most of the code is needed to express the half width/HWHM for a given intensity position. This can be easily modified to be run as a subroutine in a line profile analysis programme.

PROGRAM VOIGT

C  
 C J DUNN 10/8/88  
 C  
 C  
 C Voigt profile routine using the NAG routine D01ARF to evaluate the  
 C integral. The Voigt code is accurate to 5 ppm; use of the D01ARF  
 C routine is much faster (typically by a factor of 100) than other  
 C integrating routines.  
 C  
 C Program asks for ETA value then will calculate the line width as  
 C a fraction of the HWHM at the requested intensity.  
 C

IMPLICIT DOUBLE PRECISION(A-H,O-Z)

REAL\*8 ALPHA(390),BV(10000),C(10000)  
 INTEGER IFAIL,IPARM,N

EXTERNAL F1  
 COMMON /VAR/ X,ETA,PI

C  
 C ETA is the ratio of the Lorentzian width to the Gaussian width  
 C

PRINT \*, 'ENTER ETA COEFFICIENT VALUE'  
 READ \*, ETA  
 PI=3.141592654  
 IF (ETA.LE.0.1) THEN

    B=17.0  
     ELSEIF ((ETA.GT.(0.1)).AND.(ETA.LT.(0.8))) THEN  
         B=17.0-(10.0\*(ETA-0.1))  
     ELSE  
         B=8.0/ETA  
     ENDIF

35 CONTINUE  
 IF (NOGO.EQ.0) THEN  
   AY=0.5  
   ELSE  
     PRINT \*, 'ENTER INTENSITY'  
     READ \*, AY  
   ENDIF

IPARM=0  
 DATA ABSACC,RELACC/0.0,5.0E-6/  
 DATA A/0.0/

RINC=1.0  
 IL=0  
 IU=1000  
 J=0

40 CONTINUE

DO 1 I=IL,IU  
 X=DBLE(I)/RINC  
 J=J+1  
 IFAIL=1  
 MAXRUL=9

```

CALL DO1ARF(A,B,F1,RELACC,ABSACC,MAXRUL,IPARM,
+ACC,ANS,N,ALPHA,IFAIL)
IF (IFAIL.EQ.0) THEN
*   WRITE (2,*) X,ANS
*   PRINT *,'X=',X,'FUNCTION=',ANS

ELSE
PRINT *,'IFAIL=',IFAIL
PRINT *,I/RINC,C(J)/C(1)-AY
ENDIF
BV(J)=X
C(J)=ANS

      IF ((C(J)/C(1))-AY.LT.(0.0)) THEN
      GOTO 50
      ELSEIF (DABS((C(J)/C(1))-AY).LE.(RELACC)*AY) THEN
      GOTO 100
      ENDIF
1    CONTINUE

50   RINC=RINC*10
*   PRINT *,1,IL,IU

      IL=1+(I-1)*10
      IU=IL+10
      IFLAG=IFLAG+1
      GOTO 40

100  IF (DABS((C(J)/C(1))-0.5).LE.(5.0E-6)) THEN
      SIG2=BV(J)
      ELSE
      ENDIF
      NOGO=1

      PRINT *,'HALF WIDTH=',BV(J),'AT INTENSITY=',C(J)
      PRINT *,'HWHM=',SIG2,'HALF WIDTH/HWHM=',BV(J)/SIG2
      PRINT *,'PEAK INTENSITY=',C(1)
      GOTO 35
      END

REAL FUNCTION F1(Y)
IMPLICIT DOUBLE PRECISION(A-H,O-Z)
COMMON /VAR/ X,ETA,PI

VAL=(ETA*ETA*Y*Y)/4.0
F1=COS(X*Y)*EXP(-Y-VAL)
*   PRINT *,' '
*   PRINT *,'COS(X*Y)=' ,COS(X*Y)
*   PRINT *,'Y=' ,Y,'VAL=' ,VAL
*   PRINT *,'F1=' ,F1
*   PRINT *,' '
RETURN
END

```

## List of Publications.

### 1987

1. R Barnsley, K D Evans, N J Peacock, J Dunn and N C Hawkes,  
"Time Resolved Radial Profiles of Tokamak Core Impurity Ions Using a Bragg Rotor Spectrometer". In Proc of "Basic and Advanced Diagnostic Techniques for Fusion Plasmas", Varenna, Italy, September 1986. Publ by Int School of Plasma Physics, Piero Caldirola, Milano (1986).

### 1988

2. J Dunn, R Barnsley, K D Evans and N J Peacock,  
"High Resolution Spectroscopy of DITE Tokamak in the 10Å Region". Jn de Phys (Paris), 49, 91-94 (1988).
3. J M Laming, J D Silver, R Barnsley, J Dunn, K D Evans and N J Peacock,  
"Axial Observation of a Beam-Foil Source", Jn de Phys (Paris), 49, 339-342 (1988).
4. J M Laming, J D Silver, R Barnsley, J Dunn, K D Evans and N J Peacock,  
"Axial Observation of a Beam-Foil Source", Phys Lett A, 126(4), 253-257 (1988).
5. J Dunn, R Barnsley, K D Evans and N J Peacock,  
"High Resolution X-Ray Spectroscopy Using a Johann Spectrometer", Annual Report to LFC, SERC Rutherford Appleton Laboratory, RAL-88-042, A7.3, 146-149 (1988).
6. D Brown, P A Norreys, E Wooding, J Dunn, R Barnsley, M H Key, G J Tallents and H A Baldis,  
"Short Pulse Energy Transport by Thermal and Superthermal Electrons", Annual Report to LFC, SERC Rutherford Appleton Laboratory, RAL-88-042, A2.3, 58-62 (1988).

### 1989

7. J Dunn, R Barnsley, K D Evans, N J Peacock, G J Tallents, P A Norreys and M H Key,  
"Experimental Measurement of Dielectronic Satellites to the He-like Al  $1s^2-1s2p\ ^1P_1$  Resonance Line From Laser Produced Plasmas", Jn de Phys (Paris), 50, 551-7 (1989).
8. F P Keenan, R Barnsley, J Dunn, K D Evans, S M McCann and N J Peacock,  
"Theoretical Electron Density and Temperature Sensitive Emission Line Ratios for Helium-like Si XIII Compared to DITE Tokamak Observations", Jn de Phys (Paris), 50, 559-564 (1989).
9. F P Keenan, S M McCann, R Barnsley, J Dunn, K D Evans and N J Peacock,  
"Electron Density and Temperature Sensitive X-Ray Emission Line Ratios for Helium-Like Si XIII in the DITE Tokamak". Phys Rev A, 39, 4092 (1989); Culham Laboratory Report No. CLM-P854 (1989).
10. G J Tallents, M H Key, P A Norreys, D Brown, J Dunn and H A Baldis,  
"Production of Hot Near-Solid-Density Plasma by Electron Energy Transport in a Laser-Produced Plasma", Phys Rev A, 40(5), 2857-9 (1989).

## References.

1. H H Johann, *Z Phys*, 69, 185-206 (1931).
2. C De Michelis and M Mattioli, "Soft-X-Ray Spectroscopic Diagnostics of Laboratory Plasmas", *Nuclear Fusion*, 21(6), 677-754 (1981).
3. C De Michelis and M Mattioli, "Spectroscopy and Impurity Behaviour in Fusion Plasmas", *Rep Prog Phys*, 47, 1233-1346 (1984).
4. Proc of 33rd SUSSP on "Astrophysical and Laboratory Plasmas", St Andrews 1987, (R Brown and J Lang, Ed), 415pp, Publ by SUSSP (1988).
5. M von Laue, *Ann d Physik*, 41, 971 (1913).
6. W L Bragg, *Proc Camb Phil Soc*, 17, 43 (1912).
7. C G Darwin, *Phil Mag*, 27, 315; 27, 675 (1914).
8. P P Ewald, *Ann d Physik*, 49, 117 (1916); 49, 1 (1916); 54, 519 (1917).
9. J A Prins, *Zeit f Physik*, 63, 477 (1930).
10. A H Compton and S K Allison, "X-rays in Theory and Experiment", Publ D Van Nostrand, New York, p295-8 (1935).
11. R Hall, Ph D Thesis, University of Leicester (1980).
12. A J Burek, *Space Sci Instrum*, 2, 53-104 (1976).
13. K D Evans and B Leigh, *Space Sci Instrum*, 2, 105-123 (1976).
14. R Barnsley, K D Evans, N J Peacock and N C Hawkes, *Rev Sci Instrum*, 57(8), 2159 (1986).
15. K D Evans, R Hall, M Lewis, D Underwood and B A Cooke, *Space Sci Instrum*, 2, 313 (1976).
16. R Barnsley, K D Evans, N J Peacock, J Dunn and N C Hawkes, "Basic and Advanced Diagnostic Techniques for Fusion Plasmas", Varenna, Italy, September 1986, Publ Int School of Plasma Physics, Piero Caldirola Milano (1986).
17. J D Kilkenny, R W Lee, M H Key and J G Lunney, *Phys Rev A*, 22, 2746 (1980).
18. L von Hamos, *Ann d Physik*, 17, 716 (1933).
19. E Källne, J Källne, E S Marmar and J E Rice, *Physica Scripta*, 31, 551-64 (1985).
20. M de Broglie and F A Lindeman, *C R Acad Sci (Paris)*, 158, 944 (1914).
21. N J Peacock, R J Speer and M G Hobby, *J Phys B*, 2, 7698; Culham Report CLM-P197 (1969).
22. H Gordon, Ph D Thesis, University of Essex (1982).
23. R Barnsley, (private communication) (1983).
24. T Johansson, *Zeit f Physik*, 82, 507-28 (1933).
25. R Barnsley, J E Bateman, K D Evans, M J Forrest, W G Griffin, N C Hawkes and N J Peacock, JET Diagnostic Design Study (unpublished) (1982).
26. G W F Drake (private communication) (1987).
27. P J Mohr, *At Data Nucl Data Tables*, 29, 453 (1983).
28. J D Garcia and J E Mack, *J Opt Soc Am*, 55(6), 654-85 (1965).
29. R D Deslattes, J L Torgesen, B Paretzkin and A T Horton, *Advances in X-ray Analysis*, 18, 315 (1965).

30. D M Barrus, R L Blake, H Felthausen, E E Fenimore and A J Burek, AIP Conf No.75, "Low Energy X-ray Diagnostics, D T Attwood and B L Henke (Ed), 115-23 (1981).
31. R W G Wyckoff, Crystal Structures, 2nd Ed, Interscience (1965).
32. M Bitter, S von Goeler, M Goldman, K W Hill, R Horton, W Roney, N Sauthoff and W Stodiek, in "Temperature, its Measurement and Control in Science and Industry", J F Schooley (Ed), 5, 693-703, AIP, New York (1982).
33. A E Sandström, "Experimental Methods of X-Ray Spectroscopy: Ordinary Wavelengths", in Handbuch der Physik, S Flügge, Ed, 30, 78 Springer-Verlag, Berlin (1957).
34. Micro-Controle (UK), 4320 First Avenue, Newbury Business Park, London Road, Newbury, RG13 2PZ.  
The following commercial components were used from the above manufacturers:

(1) TR-80S, low profile rotation stage with locking of fine adjustment (Catalogue No. 338-324). Two units were required; for the crystal and detector angle alignment.

(2)  $\theta\theta$ -80, 2-axis adjustment orientation stage, compatible with TR-80S rotation stage, (Catalogue No. 133-143). One unit required for adjusting crystal surface tilt.

(3) MR 50-16, translation unit (Catalogue No. 338-066). Ideally two units, mounted perpendicularly to give XY positioning, would be used to align the crystal pole on the rotary stage axis. In practice one unit is sufficient.

From crystal platform, mounting sequence is rotation stage, orientation stage, adaptor plate, translation stage and crystal jig body.

From detector platform, mounting sequence is rotation stage, adaptor plate then film plate.

35. Ealing Electro-Optics, Greycaine Road, Watford WD2 4PW.  
Assorted "Continuous Cast" iron triangular optical benches were used for alignment and a 0.5m length (Catalogue No. 44-5163) was an integral part of the R=0.5m Johann instrument.
36. M Hart, (private communication) (1987).
37. K W Hill, S von Goeler, M Bitter, L Campbell, R D Cocan, B Fraenkel, A Greenberger, R Horton, J Hovey, W Roney, N R Sauthoff and W Stodiek, Phys Rev A 19(4), 1770-9 (1979).
38. H Hsuan, M Bitter, K W Hill, S von Goeler, B Grek, D Johnson, L C Johnson, S Sesnic, C P Bhalla, K R Karim, F Bely-Dubau and P Faucher, Phys Rev A, 35, 4280-5 (1987).
39. K Feser and A Faessler, Z Phys, 209, 1 (1968).
40. R Bartiromo, R Giannella, M L Apicella, F Bombarda, S Mantovani and G Pizzicaroli, Nucl Instr Meth, 225, 378 (1984)
41. F Bombarda, R Giannella, E Kallne, G J Tallents, F Bely-Dubau, P Faucher, M Cornille, J Dubau and A H Gabriel, Phys Rev A, 37(2), 504-22 (1988)
42. P Platz, J Ramette, E Belin, C Bonnelle and A H Gabriel, J Phys E: Sci Instrum, 14, 448-51 (1981).
43. A Hauer, J D Kilkenny and O L Landen, Rev Sci Instr, 56(5), 803-5 (1985).
44. B L Henke, H T Yamada and T J Tanaka, Rev Sci Instr, 54(10), 1311-30 (1983).
45. Yu I Mikhailov, Lebedev Physical Institute, USSR Academy of Sciences, Moscow, USSR (private communication) (1987).
46. "A Device for Bending Beams" by Leonardo da Vinci, (circa 1488).  
See for example, "The Literary Works of Leonardo da Vinci", edited by J P Richter, 3rd Edition, 2 vols, London and New York, (1970).

47. S Timoshenko and D H Young, "Elements of Strength of Materials", Publ by Van Nostrand Company, Princeton (1968).
48. Newport Corporation, 18235 Mt Baldy Circle, Fountain Valley, CA 92078 USA. Micrometers (Catalogue No. SM-05) four required.
49. Mitutoyo U K Ltd. Micrometer (Catalogue No. 148-201) one required.
50. S G Lipson and H Lipson, "Optical Physics", 239-242, Publ by Cambridge, 494 pages (1969).
51. C E K Mees, "From Dry Plates to Ektachrome Film", Publ by Ziff-Davis, New York (1961).
52. T H James (Ed), "The Theory of the Photographic Process", 4th Edition, Publ by MacMillan, New York (1977).
53. E Hecht and A Zajac, "Optics", 336, Publ by Addison Wesley, Mass, USA (1974).
54. R Barnsley, (private communication) (1989).
55. M Lewis, Ph D Thesis, University of Leicester (1982).
56. R Willingale, Ph D Thesis, University of Leicester (1979).
57. A J Bearden and F N Huffman, Rev Sci Instrum, 34(11), 1233-4 (1963).
58. K J H Phillips, J W Leibacher, C J Wolfson, J H Parkinson, B C Fawcett, B J Kent, H E Mason, L W Acton, J L Culhane and A H Gabriel, Astrophys J, 256, 774 (1982).
59. M Hart, Jn Cryst Growth, 55, 409-427 (1981).
60. R L Blake and W D Wick, Rev Sci Instrum, 44(8), 985-7 (1973).
61. Y Okaya and R Pepinsky, Acta Cryst, 10, 324 (1957).
62. A A Khan and W H Baur, Acta Cryst, B29, 2721 (1973).
63. J M Laming, C T Chantler, J D Silver, D D Dietrich, E C Finch, P H Mokler and S D Rosner, in "Atomic Spectroscopy and Highly Ionised Atoms", H G Berry, R Dunford and L Young (Eds), Nucl Instrum Meth, B31, 21-3 (1988).
64. Lange's Handbook of Chemistry, J A Dean (Ed), 13th Edition, Publ McGraw Hill (1985).
65. D T Cromer and D Liberman, J Chem Phys, 53, 1891-8 (1970).
66. Société Quartz et Silice, 8 Rue d'Anjou, 75 - Paris 8. Supplied by Nuclear and Silica Products Ltd, 44-46 The Green, Wooburn Green, High Wycombe, Bucks, HP10 OEU.
67. P Beiersdorfer, S von Goeler, M Bitter, K W Hill, R A Hulse and R S Walling, Rev Sci Instrum, 60(5), 895-906 (1989).
68. P Beiersdorfer, M Bitter, S von Goeler, S Cohen, K W Hill, J Timberlake, R S Walling, M H Chen, P L Hagelstein and J H Scofield, Phys Rev A, 34(2), 1297-1315 (1986).
69. A J Lieber, S S Wojtowicz and K H Burrell, Preprint GA-A17636, GA Technologies (1984).
70. B L Henke, J Y Uejio, G F Stone, C H Dittmore, F G Fujiwara, J Opt Soc Am, B3(11), 1540 (1986).
71. C Tuttle, J Opt Soc Am, 12, 559-565 (1926).
72. K S Weaver, J Opt Soc Am, 40(8), 524-536 (1950).
73. F K Richtmeyer and F W Warburton, Phys Rev, 22, 539-545 (1923).
74. "Photon Cross-sections from 0.1keV to 1MeV for Elements Z=1 to Z=94", W M J Veigele, At Dat Tabl, 5, 51-111 (1973).

75. X-ray Data Booklet, D Vaughan (Ed), Lawrence Berkely Laboratory, University of California (1986).
76. R L Kelly and L J Palumbo, "Atomic and Ionic Emission Lines Below 2000Å: Hydrogen Through Krypton", NRL Report 7599, June (1973).
77. G K Wertheim, M A Butler, K W West and D N E Buchanan, *Rev Sci Instrum.* **45**(11), 1369-71 (1974).
78. P Richard, M Stöckli, R D Deslattes, P Cowan, R E LaVilla, B Johnson, K Jones, M Meron, R Mann and K Schartner, *Phys Rev A*, **29**(5), 2939-42 (1984).
79. J Tudor Davies and J M Vaughan, *Astrophys J*, **137**, 1302 (1963).
80. E G Chowanietz, D H Lumb and A A Wells, *SPIE X-Ray Instrum Astron*, **597**, 381 (1985).
81. D H Lumb, Department of Physics, University of Leicester, Leicester, LE1 7RH, (private communication) (1989).
82. R Mewe, *ibid*<sup>4</sup>, 129-184 (1988).
83. H Van Regemorter, *Astrophys Jn*, **136**, 906-15 (1962).
84. A H Gabriel and C Jordan, in "Case Studies in Atomic Collision Physics", Vol 2 , E W McDaniel and M R C McDowell (Ed), (Amsterdam:North-Holland), 209-91 (1972).
85. A H Gabriel, *Mon Not R astron Soc*, **160**, 99-119 (1972).
86. J Dubau and S Volonté, *Rep Prog Phys*, **43**, 200-51 (1980).
87. R W P McWhirter, in "Plasma Diagnostic Techniques", R H Huddlestone and S L Leonard (Ed), Academic Press, New York, 201 (1965).
88. D R Bates, A E Kingston and R W P McWhirter, *Proc R Soc London, Ser A***267**, 297 (1962).
89. J D Lawson, *Proc Phys Soc*, **70**, 6 (1957).
90. E Speth, *Rep Prog Phys*, **52**, 57-121 (1989).
91. S Witkowski, *Nuclear Fusion*, **25**, 227 (1985).
92. L R Grisham, *Science*, **207**, 1301 (1980).
93. M Bitter, S von Goeler, R Horton, M Goldman, K W Hill, N R Sauthoff and W Stodiek, *Phys Rev Lett*, **42**(5), 304-7 (1979).
94. L Spitzer, "Physics of Fully Ionized Gases", Publ Interscience, New York, 170 pages (1962).
95. G E Bromage, R D Cowan, B C Fawcett and A Ridgeley. *J Opt Soc Am*, **68**(1), **48** (1978).
96. F Bombarda, R Gianella, E Källne and G J Tallents, *J Quant Spectr Rad Trans*, **41**(4), 323-33 (1989).
97. F P Keenan, S M McCann, R Barnsley, J Dunn, K D Evans and N J Peacock, *Phys Rev A*, **39**, 4092 (1989).
98. F P Keenan, S M McCann, R Barnsley, J Dunn and N J Peacock, to be published.
99. N C Hawkes and N J Peacock, *Nuclear Fusion*, **25**(8), 971-80 (1985).
100. P46110 CCD monochrome camera, specified without a window. Supplied and manufactured by: EEV English Electric Valve Company Limited, Chelmsford, Essex, England.
101. R Bartiromo, "Basic and Advanced Diagnostic Techniques for Fusion Plasmas", Vol 1, International School of Plasma Physics, Varenna, 227 (1986).

102. The same CCD detector has been operated by the author as an x-ray pinhole camera and in conjunction with a small R=300mm Johann PET (002) spectrometer. These were used for laser experiments on the SPRITE UV laser at the Rutherford Appleton Laboratory, during October and November 1989. The x-ray images were recorded on a 8-bit frame store. Background noise levels were extremely low (1→4 levels of grey out of 256 levels) away from the x-ray image for the pinhole camera. However, horizontal bands of thermal noise ( ~30→40 levels of grey) would build up on the frame if the CCD was left on for 30 minutes or longer.
103. "Laser Plasma Interactions", R A Cairns and J J Sanderson (Eds), SUSSP Publications, (1980). There are other books in this series.
104. "Annual Report to the Laser Facility Committee", Central Laser Facility, Rutherford Appleton Laboratory, RAL-89-045 (1989).
105. A L Schawlow and C H Townes, "Infrared and Optical Masers", Phys Rev, 112(6), 1940-9 (1958).
106. In "Lasers, Light Amplifiers and Oscillators", D Röss, Academic Press, London (1968).
107. E Snitzer, Phys Rev Lett, 7, 444 (1961).
108. N G Basov and O N Krokhin, "The Conditions of Plasma Heating by the Optical Generator Radiation", 3rd Quantum Electronics Conference, Paris, 1963, N Bloembergen and P Grivet (Eds), Columbia University Press, NY (1964).
109. R L Kauffman, Jn de Phys, 49, 145 (1988).
110. T P Hughes, *ibid*<sup>103</sup>, 1-90 (1980).
111. M H Key, *ibid*<sup>103</sup>, 219-322 (1980).
112. M H Key, *ibid*<sup>4</sup>, 385 (1988).
113. M H Key, Jn de Phys, 49, 135 (1988).
114. H R Griem, "Spectral Line Broadening by Plasmas", Academic Press, New York (1974).
115. H R Griem, M Blaha and P Kepple, Phys Rev A, 19, 2421 (1979).
116. R W Lee, J Phys B, 11, L167 (1978); J Phys B, 12, 1129-44 (1979).
117. R J Tighe and C F Hooper, Phys Rev A, 14, 1514 (1976).
118. B Yaakobi, D Steel, E Thorsos, A Hauer and B Perry, Phys Rev Lett, 29, 1526 (1977).
119. R W Lee, J Quant Spectr Rad Trans, 40, 561 (1988).
120. N J Peacock, *ibid*<sup>103</sup>, 711 (1980).
121. F E Irons, J Quant Spectr Rad Trans, 22 1-44 (1979).
122. J F Holtzrichter, *ibid*<sup>103</sup>, 497 (1980).
123. J Dunn, R Barnsley, K D Evans and N J Peacock, Annual Report to LFC, SERC Rutherford Appleton Laboratory, RAL-88-042, A7.3, 146-149 (1988).
124. D Brown, P A Norreys, E Wooding, J Dunn, R Barnsley, M H Key, G J Tallents and H A Baldis, Annual Report to LFC, SERC Rutherford Appleton Laboratory, RAL-88-042, A2.3, 58-62 (1988).
125. G J Tallents, M H Key, P Norreys, D Brown, J Dunn and H A Baldis, Phys Rev A, 40(5), 2857-9 (1989).
126. D Duston, J E Rogerson, J Davis and M Blaha, Phys Rev A 28(5), 2698-80 (1983).
127. L A Vainstein and U I Safronova, At Data Nucl Data Tables, 21, 49 (1978).

128. N J Peacock, M G Hobby and M Galanti, *J Phys B: At Mol Phys*, 6, 298-304 (1973).
129. L A Vainshtein and U I Safronova, *Phys Ser*, 31, 579 (1985).
130. V A Boiko, A Ya Faenov, S A Pikuz and U I Safronova, *Mon Not R astr Soc*, 181, 107-120 (1977).
131. F P Keenan and A E Kingston, *Mon Not R astr Soc*, 220, 493-500 (1986).
132. T Holstein, *Phys Rev*, 72, 1212 (1947).
133. A C G Mitchell and M C Zemansky, "Resonance Radiation and Excited Atoms", Publ Cambridge University Press (1961).
134. C D Lin, W R Johnson and A Dalgarno, *Astrophys Jn*, 217, 1011-15 (1977).
135. F E Irons, *Aust J Phys*, 33, 283-301 (1980).
136. B Sylwester, P Faucher, J Jakmiec, V V Krutov, V V Korneev, R W P McWhirter, J Sylwester, M Tomczak, S Volonté and I A Zhitnik, *Solar Physics*, 103, 67-87 (1986).
137. V A Boiko, S A Pikuz and A Ya Faenov, *J Phys B: At Mol Phys*, 12,(11), 1889-1910 (1979).
138. D Duston and J Davis, *Phys Rev A*, 21(3), 932 (1980).
139. A Audebert, J P Geindre, J C Gauthier and C Popovics, *Phys Rev A*, 30(2), 768-772 (1984).
140. J G Lunney, RAL Ann Rep RAL-84-049, A3.4 (1984); *J Phys B: At Mol Phys*, 16, 283-87 (1983).
141. J M Bañon, L L Sánchez-Soto and E Bernabeu, *J Phys B: At Mol Opt Phys*, 22, 199-210 (1989).
142. J M Bañon, L L Sánchez-Soto and E Bernabeu, *J Phys B: At Mol Opt Phys*, 22, L309-313 (1989).
143. J P Apruzese, D Duston and J Davis, *J Quant Spectr Rad Trans*, 36(4), 339-344 (1986).
144. F P Keenan, S M McCann and A E Kingston, *J Phys B: At Mol Phys* 19, L803-806 (1986).
145. C D Lin, W R Johnson and A Dalgarno, *Phys Rev A*, 15(1), 154-161 (1977).
146. F P Keenan, Queen's College, Belfast, Northern Ireland, (Private Communication) (1989).
147. I L Beigman, V A Boiko, S A Pikuz and A Ya Faenov, *Sov Phys JETP*, 44(3), 511-515 (1976).
148. A V Vinogradov, I I Sobelman, and E A Yukov, *Fiz Plasma*, 3, 686 (1977).
149. V L Jacobs and M Blaha, *Phys Rev A*, 21, 525 (1980).
150. V I Bayanov, V A Boiko, A V Vinogradov, S S Gulidov et al, *JETP Lett*, 24, 319 (1976).
151. J F Seely, *Phys Rev Lett*, 42, 1606 (1979).
152. I Martinson, Proc of 33rd SUSSP on "Astrophysical and Laboratory Spectroscopy", St Andrews 1987, (R Brown and J Lang Ed), 339-365, Publ by SUSSP (1988).
153. "Fast Ion Beam Spectroscopy", (E J Knystautas and R Drouin, Ed), *Nucl Instrum Meth*, 222, 1-402 (1982).
154. "The Physics of Highly Ionised Ions", (J D Silver and N J Peacock, Ed), *Nucl Instrum Meth*, B9, 359-787 (1985).
155. "Atomic Spectroscopy and Highly Ionised Atoms", (H G Berry, R Dunford and L Young, Ed), *Nucl Instrum Meth*, B31, 1-375 (1988).

156. E H Pinnington, *ibid*<sup>154</sup>, 549-556 (1985).
157. J M Laming, University of Oxford, Clarendon Laboratory, Parks Road, Oxford (private communication) (1987).
158. K X To and R Drouin, *Nucl Instrum Meth*, 160, 461 (1979).
159. M P Stöckli, and P Richard, *ibid*154, 727-731 (1985).
160. W E Lamb and R C Retherford, *Phys Rev*, 72, 241 (1947).
161. W E Lamb and R C Retherford, *Phys Rev*, 86, 1014 (1953).
162. G W Erickson, *J Phys Chem Ref Dat*, 6(3), 831-853 (1977).
163. G W F Drake, *Adv At Mol Phys*, 18, 399 (1982).
164. P Indelicato, *ibid*<sup>155</sup>, 14-20, (1988).
165. R D Deslattes, R Schuch and E Justiano, *Phys Rev A*, 32(3), 1911-1913 (1985).
166. H F Beyer, R D Deslattes, F Folkmann and R E La Villa, *J Phys B: At Mol Phys*, 18, 207-215 (1985).
167. R D Deslattes, H F Beyer and F Folkman, *J Phys B: At Mol Phys*, 17, L689-L694 (1984).
168. J Désesquelles, Ph D Thesis, University of Lyons (1970). S Bashkin, *Appl Opt*, 7, 2341 (1968).
169. J Gordon, Ph D Thesis, University of Leicester (1984).
170. E Träbert, I A Armour, S Bashkin, N A Jelley, R O'Brian and J D Silver *J Phys B: At Mol Phys*, 12(10), 1665-1676 (1979).
171. E Träbert and B C Fawcett, *J Phys B: At Mol Phys*, 12(15), L441-L447 (1979).
172. J P Mosnier, R Barchewitz, M Cukier, R Del-Cas, C Senemaud and J Bruneau, *J Phys B: At Mol Phys*, 19, 2531-2546 (1986).
173. A B C Walker and H R Rugge, *Astron Astrophys*, 5, 4 (1970).
174. A B C Walker and H R Rugge, *Astron Astrophys*,164, 181 (1971).
175. J Dunn, R Barnsley, K D Evans and N J Peacock, *Phys Lett A*, 126(4), 253-257 (1988).
176. J M Laming, J D Silver, R Barnsley, J Dunn, K D Evans and N J Peacock, *Phys Lett A*, 126(4), 253-257 (1988).
177. G W F Drake, *Astrophys J*, 158, 1199 (1969).
178. G R Blumenthal, G W F Drake and W H Tucker, *Astrophys J*, 172, 205 (1972).
179. C T Chantler and J D Silver, *ibid*<sup>155</sup> 59-69 (1988).
180. I A Sellin et al, *Phys Lett A*, 61, 107 (1977).
181. J M Laming and J D Silver, *Phys Lett A*, 123(8), 395-398 (1987).
182. R D Deslattes, *ibid*<sup>155</sup>, 51-58 (1988).
183. D D Dietrich, G A Chandler, R J Fortner, C J Hailey and R E Stewart, *ibid*<sup>154</sup>, 686-688 (1985).
184. E V Aglitsky, P S Antsiferov, S L Mandelstam, A M Panin, U I Safronova, S A Ulitin and L A Vainshtein, *Phys Scr*, 38, 136-142 (1988).
185. J D Silver, A F McClelland, J M Laming, S D Rosner, G C Chantler, D D Dietrich and P O Egan, *Phys Rev A*, 36(3), 1515-1518 (1987).
186. R D Deslattes, *ibid*<sup>154</sup>, 668 (1985).

187. M Bitter, S von Goeler, S Cohen, K W Hill, S Sesnic, F Tenney, J Timberlake, U I Safronova, L A Vainshtein, J Dubau, M Loulergue, F Bely-Dubau and L Steenman-Clark, *Phys Rev A*, 29(2), 661-74 (1984).
188. Yu I Grineva, V I Karev, V V Korneev, V V Krutov, S L Mandelstam, L A Vainshtein, B L Vasilyev and I A Zhitnik, *Solar Physics*, 29, 441-6 (1973).
189. I Martinson, *Rep Prog Phys*, 52, 157-225 (1989).
190. J P Briand, P Indelicato, M Tavernier, O Gorceix, D Liesen, H F Beyer, B Liu, A Warzak and J P Desclaux, *Z Phys A*, 318(1), 1-5 (1984).
191. E S Marmar, J E Rice, E Källne, J Källne and R E LaVilla, *Phys Rev A*, 31(1), 774-7 (1986).
192. W R Johnson and G Soff, *At Data Nucl Data Tables*, 33, 405-46 (1985).
193. L Schleinkofer, F Bell, H D Betz, G Trollman and J Rothermel, *Phys Scripta*, 25, 917 (1982).
194. R Barnsley, K D Evans, N C Hawkes and N J Peacock, *Jn de Phys*, 49, 207-10 (1988).
195. "Dimensional Stability of Kodak Ester Base Films for the Graphic Arts", Pamphlet No. Q-34, Eastman Kodak Company, Rochester, NY 14650.
196. E Källne, J Källne and J E Rice, *Phys Rev Lett*, 49, 330 (1982).
197. A V Vinogradov, I Yu Skobelev and E A Yukov, *Sov J Plasma Phys*, 3, 389 (1977).
198. G J Tallents, *J Phys B: At Mol Phys*, 17, 3677-91 (1984).
199. N N Ljepojevic, R J Hutcheon and R W P McWhirter, *J Phys B: At Mol Phys*, 17, 3057-73 (1984).
200. N N Ljepojevic, R W P McWhirter and S Volonté, *J Phys B: At Mol Phys*, 18, 3285-97 (1985).
201. J Dubau, A H Gabriel, M Loulergue, L Steenman-Clark and S Volonté, *Mon Not R astro Soc*, 195, 705 (1981).
202. G W F Drake, *Phys Rev A*, 3, 908 (1971).
203. G Breit and E Teller, *Astrophys J*, 91, 215 (1940).
204. J M Allen et al, *Plasma Physics and Controlled Fusion*, 28, 101 (1986).
205. R Prentice, Culham Laboratory Report CLM R179 (1978).
206. E Källne, J Källne, P Richard and M Stöckli, *J Phys B*, 17, L115-20 (1984).
207. R Bartiromo, F Bombarda and R Gianella, *Nucl Instrum Meth*, B9, 679-81 (1985).
208. J P Briand, J P Mossé, P Indelicato, P Chevallier, D Girard-Vernhet, A Chetioui, M T Ramos and J P Desclaux, *Phys Rev A*, 28(3), 1413-7 (1983).
209. H F Beyer, R Mann, F Folkmann and P H Mokler, *J Phys B*, 15, 3853 (1982).
210. J F Seely and U Feldman, *Phys Rev Lett*, 54(10), 1016-9 (1985).
211. H D Dohmann, D Liesen and E Pfeng, Proc 13th Int Conf on "The Physics of Electronic and Atomic Collisions", Berlin 1983. Abstracts of contributed papers, J Eichler (Ed), p467 ICPEAC, Berlin, (1983); GSI Scientific Report No. 1982, p155, unpublished (1983).
212. C J Hailey, R E Stewart, G A Chandler, D D Dietrich and R J Fortner, *J Phys B*, 18, 1443-8 (1985).
213. J P Briand, M Tavernier, P Indelicato, R Marrus and H Gould, *Phys Rev Lett*, 50, 832 (1983).

214. F Bombarda, R Gianella, E Källne, G J Tallents, F Bely-Dubau, P Faucher, M Cornille, J Dubau and A H Gabriel, Phys Rev A, 37(2), 504-22 (1988).
215. J Dunn, R Barnsley, K D Evans and N J Peacock, Jn de Phys, 49, 91-4 (1988).

## **Abstract.**

# **High Resolution X-Ray Spectroscopy of Laboratory Sources.**

**James Dunn.**

A detailed programme of research is presented to design, build and operate a high resolution  $\lambda/\Delta\lambda \geq 5000$  curved crystal Johann-type x-ray spectrometer for the waveband below  $13\text{\AA}$ . The spectrometer is used to observe line emission features from different laboratory x-ray sources. Characteristics of the Johann geometry are described with emphasis given to the properties of sensitivity, dispersion, resolving power and waveband. The tolerance of the instrumental parameters is defined for successful high spectral resolution operation. The key feature of the spectrometer is the unique crystal bending device which can generate a high quality cylindrical curvature of radius  $R=150 \rightarrow 5000\text{mm}$ . The crystal focusing alignment and testing procedures are evaluated. Choice of crystals suitable for the observation programme is discussed together with analysis techniques for interpretation of the x-ray spectral line profiles.

The instrument is optimised for time-integrated and time-resolved ion temperature measurements of UKAEA DITE Tokamak at the Culham Fusion Laboratory. X-ray line emission results from medium Z He-like and H-like impurity ions are presented for different plasma conditions.

Density sensitive He-like and Li-like Aluminium ion satellite emission features are studied for intense transient laser produced plasmas at the Central Laser Facility, SERC Rutherford Appleton Laboratory. The peak plasma electron density of 0.1 times solid density is estimated from these line intensity ratios and is in good agreement with Stark line width measurements.

X-ray emission from beam-foil interactions is observed on the Folded Tandem accelerator of the Nuclear Physics Department, Oxford University. The proposed improvement in the intrinsic spectral line broadening due to the accelerator is investigated by high resolution axial beam measurements of the He-like Silicon and H-like Neon  $n=2$  transitions.

The Lyman- $\alpha$  intensity  $\beta$ -ratio and wavelength separation  $\Delta\lambda_{FS}$  is studied for the fine-structure of Hydrogenic Neon, Magnesium, Aluminium and Silicon. The fine-structure separation is compared with the Dirac theory and other experimental data, while the possible mechanisms giving rise to the non-statistical value of the  $\beta$ -ratio are analysed.